The University of Hull

DEVELOPING A NOVEL SPHEROID-ON-CHIP MICROFLUIDIC

DEVICE FOR INVESTIGATIONS INTO METASTASIS

Being a Thesis Submission for the Degree of Doctor of Philosophy at

the University of Hull

By

Thomas Charles Collins

BSc- University of Chester

MRes- University of Birmingham

May 2019

Abstract

One in two people born after 1960 will develop cancer, with 90% of all cancer deaths arising from metastasis. Conventional 2D *in vitro* metastasis models do not fully replicate tumour complexity. *In vivo* models can address tumour complexity, but do not fully represent human tumour biology. Multicellular spheroids are widely used 3D models of cancer. Spheroids contain internal zonal differentiation of oxygen, metabolite, and nutrient gradients, associated with regions of proliferative, quiescent, and necrotic cells. Current *in vitro* static spheroid methodologies do not recapitulate factors of cellular spread including continuous flow or shear stress. Therefore, better 3D *in vitro* models to investigate metastasis represent an area of unmet need. This research aims to develop spheroid-on-chip models, providing a novel strategy to investigate cancer spread. The microfluidic devices used in this study feature weirs for spheroid inclusion, and a borosilicate base coverslip for optical clarity. The devices feature an access port allowing direct access to the microwell. Spheroids derived from established cancer cell lines, MCF7 and U-87 MG, were formed off-chip and incorporated into the device by pipetting, before being perfused with complete media at 3 µL min^{-1} for 72 h. Cell viability was assessed in effluent, using the CytoTox Glo assay, demonstrating spheroid viability is robustly maintained on-chip. *In situ* analysis of cell viability, through FDA/PI live/dead staining indicated an increased proportion of viable cells and decreased dead cells on-chip compared to off-chip. VEGF (Vascular Endothelial Growth Factor) ELISA showed that VEGF secretion, as evaluated by its presence in conditioned media, was comparable across all testing conditions. The chip model has been further developed to allow spheroids to be embedded in ECM (extracellular matrix)-like matrices. VEGF ELISA and IL-6 ELISA showed that both VEGF and IL-6 secretion, as evaluated by its presence in conditioned media, was comparable across all testing conditions. ELISA also showed that IL-6 and VEGF was increased in the on-chip models within hydrogel conditions. The device has also allowed the direct imaging of spheroids on chip over 72 h. The analysis of U-87 MG spheroids on chip showed that invasion through Matrigel was comparable to the off-chip static models. Whilst migration on chip, through collagen analysis, was increased over the off-chip counterparts. The work shown offers a novel insight into cancer metastasis; on a more replicative model than the current conventional *in vitro* techniques.

Acknowledgements

Thank you Dr Isabel Pires and Professor Nicole Pamme. Your constant support, feedback (which most the time was difficult to read!), knowledge, wisdom and help has guided me to where I am today. You are two inspirational women whom are making a positive difference to the world.

Thank you, Dr Alex Iles and Dr Martin Christensen. Martin you were the person whom I first met from Chemistry and showed me how to make all the bits and bobs of microfluidics (and did all the simulations - Thank you!). You've been a supporting friend and colleague. Dr Alex Iles, you've put up with a lot during my time here, you're a highly skilled and talented individual, whom can seemingly fabricate anything anyone thinks of! You've been fundamental in this project, and specifically making all the generations of devices, so from the bottom of my heart, thank you.

A final thank you to all the Biomicrofluidics group, for the support, friendship and ideas you've given me throughout.

To my family: Alex I am the real doctor now… Mom and Dad. Thank you. Your love, support, investment and unwavering faith have stood as a solid foundation in life, allowing me to get to this point. Four years ago, lying brain damaged in a hospital bed, we never expected this to be possible. Well, here we are.

Rachael, you know how I feel, thanks.

To everyone else, especially my Grandparents, Lee, the Cartwrights, Steven and Joe, Dr Munford, you know who you are, thanks for believing in me. Even if I didn't myself.

I'm still going strong!

'There can be no greater gift than that of giving one's time and energy to help others without expecting anything in return.'

Nelson Mandela

'We all die. The goal isn't to live forever, the goal is to create something that will.'

Chuck Palahniuk

Table of Contents

List of figures

List of Tables

List of abbreviations

2D – Two dimensional

3D – Three dimensional

5-FU – Five fluorouracil

ADAM - A-disintegrin-and-metalloproteinase

AMF - Autocrine motility factor

APS – Ammonium persulfate

ARNT - Aryl hydrocarbon receptor nuclear translocator

ATCC - American Type Culture Collection

ATP - Adenosine triphosphate

BCL - B-cell lymphoma 2

BCNU - Bis-chloroethyl nitrosourea

BMDC - Bone marrow derived cells

BSA - Bovine serum albumin

CAF – Cancer associated fibroblasts

CAIX – Carbonic anhydrase 9

cAMP – Cyclic adenosine monophosphate

CCNU - Lomustine

CD (44) – Cluster of differentiation

CDX- Cell Line Derived Xenograft Models

CNC – Computer numerical control

CO_2 - Carbon Dioxide

CTC - Circulating tumour cells

CV – Cellular viability

CXCR4 - C-X-C chemokine receptor type 4

DAB - 3,3'-diaminobenzidine

DMEM – Dulbecco's modified eagles' medium

DMSO - Dimethyl sulfoxide

DNA - Deoxyribonucleic acid

DOX – Doxorubicin

ECACC - European Collection of Authenticated Cell Cultures

ECM – Extracellular matrix

EGFR - Epidermal growth factor receptor

ELISA - Enzyme-linked immunosorbent assay

EMT – Epithelial mesenchymal transition

FAK - Focal adhesion kinase

FBS – Foetal bovine serum

FDA – Fluorescein diacetate

FLM - Final luminescent measurement

H&E – Haematoxylin and Eosin

HCL – Hydrochloric acid

HES1 - *Hairy and enhancer of split 1*

HIF – Hypoxic inducible factor

HMVECs - Human microvascular endothelial cells

HRE - Hypoxic responsive elements

HRP – Horse radish peroxidase

HSP – Heat shock protein

HUVECs – Human umbilical vein endothelial cells

IARC – International agency for the research of cancer

IHC - Immunohistochemistry

IL – Interleukin

ILM - Initial luminescence measurement

LDH – Lactate dehydrogenase

LOX - *Lysyl oxidase*

MCTS – Multicellular tumour spheroids

MET – Mesenchymal epithelial transition

MMP – Matrix metalloproteinases

NK – Natural killer

O_2 - Oxygen

OCT -Optimal Cutting temperature

ODD - Oxygen-dependent degradation

OTS – Octadecyltrichlorosilane

Pa - Pascal

PAGE – Polyacrylamide gel electrophoresis

PAP - Peroxidase-Antiperoxidase

PBS – Phosphate buffered saline

PDGF – Platelet derived growth factor

PDK1 - *Pyruvate dehydrogenase kinase*

PDMS - Polydimethylsiloxane

PDX - Patient-Derived Xenograft

PEG – Polyethylene glycol

PHD - Prolyl hydroxylases

PI – Propidium iodide

PIMO - Pimonidazole

PLA - Polylysine adhesion slides

PMMA - Polymethyl methacrylate

PTFE - Polytetrafluoroethylene

PTX - Paclitaxel

PVDF - Polyvinylidene fluoride

RANKL - Receptor activator of nuclear factor kappa-B ligand

RNA - Ribonucleic acid

ROI – Region of interest

RPMI - Roswell Park Memorial Institute

RT-PCR – Real time polymerase chain reaction

SDS - Sodium dodecyl sulfate

SHH – Sonic Hedgehog

SLUG - Snail Family Transcriptional Repressor 2

SNAIL - Zinc finger protein

STAT-3 - Signal transducer and activator of transcription 3

TBS - Tris Buffered saline

TBST – Tris buffered saline tween

TCF4 - Transcription factor 4

TEMED - Tetramethylethylenediamine

TF – Tissue factor

TGF-β - Transforming growth factor beta

TIC - Tumour initiating cells

TMZ - Temozolomide

TNF-α - Tumour necrosis factor

TWIST - Twist related protein 1

ULA – Ultra low adherence

UTB – Urea Tris Buffer

VEGF – Vascular Endothelial Growth Factor

VHL - Von Hippel-Lindau

WNT - Wingless and the name Int-

ZEB - Zinc finger E-box binding homeobox 1

Chapter 1- General Introduction

1.1 Cancer Biology overview

Cancer is a condition characterised by the uncontrolled growth and division of cells in a particular region in the body (Weinberg, 2013). There are over 200 types of cancer which can affect humans, with the most common types in the UK being breast, bowel, prostate and lung, in total accountable for 46% of deaths (Murphy, 2016). In 2008, the international agency for research on cancer (IARC) reported that by the year 2030, 27 million new cancer cases and 17 million cancer deaths will occur annually. Similarly, cancer was responsible for 9.6 million deaths in 2018 (Bray *et al*., 2012; World Health Organisation., 2018). Moreover, a report by cancer research UK showed that there were 163,000 deaths in the UK in 2014 attributed to cancer, equating to 447 deaths per day (Murphy, 2016). Importantly, another report from 2015 showed that 50% of individuals born after 1960 will develop cancer (Ahmad *et al*., 2015). These reports highlight why more research is required into the devastating condition.

The understanding of the biology of cancer is fundamental for the development of new diagnostic and therapeutic strategies. In 2000, Robert Weinberg and Douglas Hanahan postulated that the progression into cancer requires the acquisition of key characteristics, or hallmarks, which are shared by all tumours alike (Weinberg & Hanahan, 2011). These hallmarks of cancer encompassed biological capabilities: sustaining proliferation signalling, evading growth suppressors, and resisting cell death, inducing angiogenesis, enabling replicative immortality, activating invasion and metastasis (Weinberg & Hanahan, 2011). In 2011, two further hallmarks, immune destruction avoidance and deregulation of cellular energetics, were added, as well as two enabling characteristics, genomic instability and inflammation (Weinberg & Hanahan, 2011). Importantly, metastasis, one of the hallmarks, is accountable for 90% of deaths caused by cancer (Mehlen & Puisieux, 2006). Therefore, understanding of the biological processes underlying its progression is a very active and important research topic in cancer biology.

1.2 Metastasis

Metastasis is the process of a primary tumour migrating to, and establishing, a secondary, tertiary, or quaternary tumour at a distant site within the body. Whilst metastasis accounts for approximately 90% of all cancer deaths, with survival rates being <30% for metastatic tumours, it is a very inefficient process. For example, a tumour composed of 10^9 cells can release 10^6 cells a day. But only <0.01% of these tumour cells that enter into circulation will form metastases at a distant site (Talmadge & Fidler, 2010). Specific types of primary cancers (such as breast) are associated with metastasising to certain secondary sites (e.g. bone or lung), that is, following specific tropisms and re-establishing a growing tumour (Lu & Kang, 2010). It was originally postulated that the primary tumour mass would invade the local blood vessel network. Developing a second cancer at locations directly linked to the first, through the vasculature. However, theories and hypotheses into where primary cancer spreads, changed. Meaning much work has focussed on the specificity of metastasis and the locations where the primary tumour spreads towards. Although different cancers metastasise to different locations, most tumours appear to initially undergo a similar metastatic process, designated as the metastatic cascade.

1.2.1   The metastatic Cascade

The metastatic cascade (figure 1.1) is a process in which primary tumour cells become more motile and invasive leading to the cancer spreading throughout the body (Mehlen & Puisieux, 2006). The metastatic cascade can be subdivided into a sequential series of steps, which result in the primary cancer becoming more motile, breaking down the local membrane and spreading through the circulation, before stopping at a distance site and invading the local environment. The cancer then grows and develops a secondary tumour in a different location. The steps are: 1) Primary tumour formation 2) Local invasion 3) Intravasation 4) Survival in circulation 5) Arrest at distant site 6) Extravasation 7) Micrometastases development 8) Colony formation
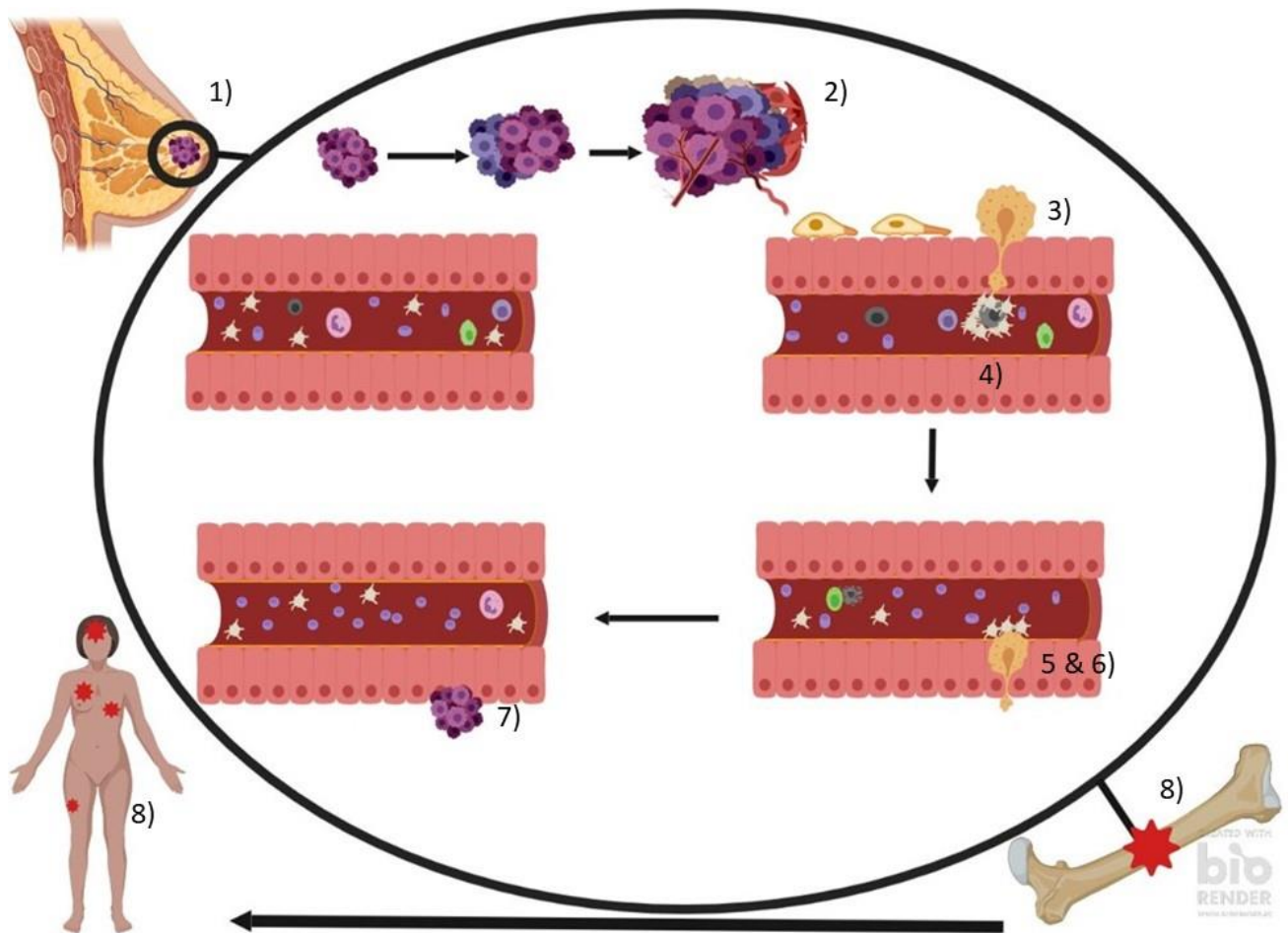
Figure 1.1: The metastatic cascade

The metastatic cascade is a sequential series of steps and details the process of a primary tumour – for example, a breast tumour moving to a secondary site- bone week/month process.1) Primary formation Initially, a tumour will grow over a period (weeks). The larger tumour will continue to grow, being supplied with poorly formed blood vessels (months). 2) Local invasion- The epithelial like tumour cells from the primary tumour acquire a more motile and invasive phenotype. 3) Intravasation-These cells change morphology/ gene expression and intravasate into surrounding circulatory system or lymphatic vessels. 4) Survival in circulation - The circulating tumour cells need to survive within the circulation (surviving the shear stress, turbulence and host immune response) (Minutes). 5) Arrest at a distance site (Minutes) 6) Extravasation - The tumour cells will extravasate at the distant site. (Hours/days) 7) Here, the tumour cells will initially form a micrometastases which, upon increased proliferation and reestablishment of a vascular supply (Months). 8) Colony formation- tumour will grow until a clinically detectable metastatic colony is formed. Diagram created using Biorender.

1, 2 and 3) Epithelial to Mesenchymal Transition (EMT)

One of the initial steps of the metastatic cascade is EMT, step 2 of the previous paragraph. Metastasis is initiated with polarised epithelial-like primary tumour cells acquiring a motile and invasive phenotype, through EMT (Talmadge & Fidler, 2010). In metastatic spread, type three of EMT occurs, as opposed to type 1 and 2 EMT, associated with normal cells and embryogenesis or tissue regeneration (Heerboth *et al.*, 2015). Under static physiological conditions, both epithelial cells and epithelial like cancer cells are polarised and interact with the basement membrane (epithelial phenotype). However, initially during type three EMT, the cancer epithelial cells lose polarity (Brabletz *et al*, 2018)). The polarised epithelial cell surface is anchored to other epithelial cell surfaces through E-cadherin, forming adherens junctions. E-cadherin is highly expressed at the plasma membrane, and the ectodomains of E-cadherin molecules protrude from one epithelial cell and form complexes with the corresponding E-cadherin molecule on a second epithelial cell, giving rise to a homodimeric bridge and thus an adherent junction (Weinberg, 2013). The cytoplasmic tail of E-cadherin is linked to the actin cytoskeleton via β-catenin (Weinberg, 2013). However, during EMT, the loss of E-cadherin leads to the release and trans-location of β-catenin to the nucleus (Yokota, 2000; Bardella *et al.*, 2011). Furthermore, when the cell loses polarity, the loss and degradation of E-cadherin allows the cell to become separated from the neighbouring cells promoting an invasive phenotype. Multiple pathways and components can result in the loss of E-cadherin expression and function; for example, proteolytic cleavage or hypermethylation and histone deacetylation epigenetic silencing through Zeb (Zinc finger E-box binding homeobox 1), Twist (twist related protein 1) and Snail (zinc finger protein), which are transcriptional factors involved in cell maintenance (Paznekas *et al*, 1999). Another example is the inhibition of E-cadherin transport through post translational control by O-glycosylation (Geng *et al.*, 2012). Moreover, the loss of E-cadherin in the cell is mirrored with the gain of N-cadherin (Valastyan & Weinberg,

2011a; Zijl *et al.*, 2011). Cells also present a loss of cytokeratin expression, further loss of polarity and the loss of E-cadherin through the transcriptional repressors Snail, Slug or Twist. Therefore, when cells lose polarity and are unbound to other cells, their phenotypic profile changes to a more stromal and mesenchymal like cell.

3 and 4) Extracellular matrix remodelling and invasion

This mesenchymal phenotype is associated with increased motility, fibroblast like shape, resistance to apoptosis, increased extracellular molecules and glycoprotein production (such as matrix metalloproteinases - MMP2 and 9 or fibronectin), mesenchymal gene expression and invasiveness and migratory capabilities. Mesenchymal-like cells increase Matrix Metalloproteinase (MMP)- 2 and -9 secretion, fibronectin and Platelet Derived Growth Factor (PDGF) receptor expression. These secreted factors are critical in the progression of motility of cells. MMPs for example, can cleave and degrade components of the extracellular matrix, basement membrane and cell-cell junctions. MMP1 and 2 can degrade collagen, whilst MMP 7 and 9 can degrade fibronectin, laminin and gelatin. MMPs can further promote the invasiveness of cells through the ability to catalyse the cleavage E-cadherin. E-cadherin can be cleaved by α-secretase, which is catalysed by MMP 3,7, 9, 14 and a disintegrin and metalloproteinase (ADAM) 10 or 15. The cleavage of E-cadherin occurs at the ectodomain resulting in a soluble E-cad fragment which can induce invasion and proliferation through epidermal growth factor receptor (EGFR) signalling (David & Rajasekaran, 2012). The initial primary epithelial like cells are now more motile, fibroblastic, are presenting a mesenchymal gene expression and are secreting factors that break down the ECM/ basement membrane. The cancer cells will then invade/intravasate the local blood vessel vasculature.
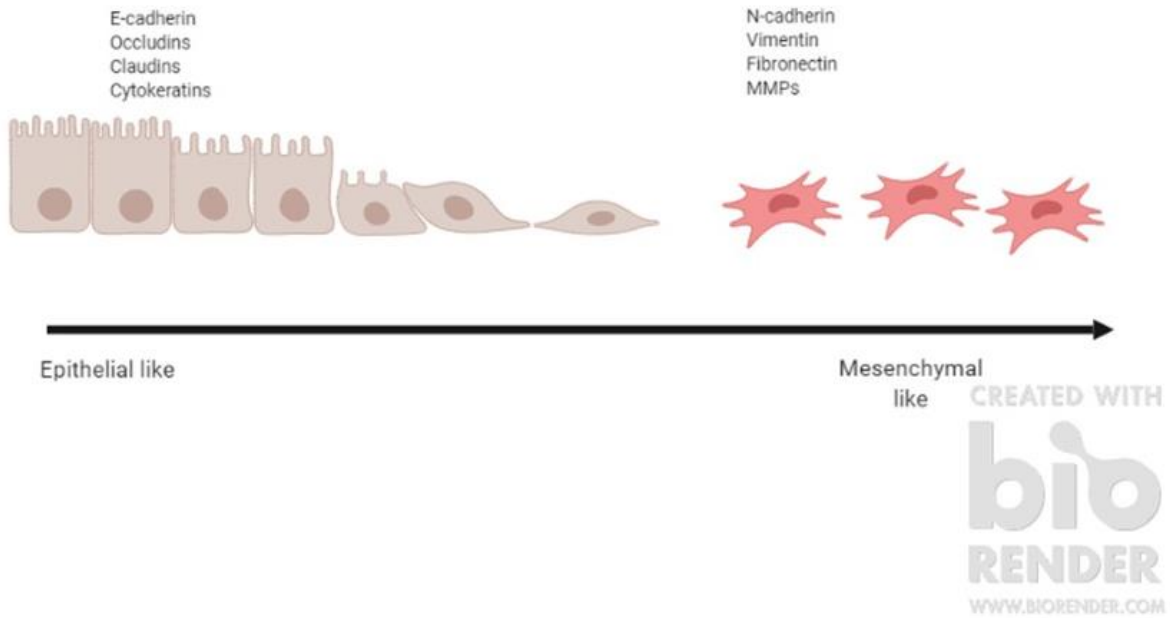
Figure 1.2   Epithelial mesenchymal transition schematic

EMT is characterised by the change of epithelial like tumour cells losing their polarity and shifting to a more motile and invasive phenotype. Change of factors include: Loss of E-cadherin, being replaced by N-cadherin. Loss of Occludin, Claudins and cytokeratin. Gain of Vimentin, MMP expression and fibronectin.

4 and 5) Intravasation and survival in circulation

Once cancer cells invade the local vessel network, they only reside there for a short period of time. This is possibly due to the size dimensions and restrictions of cancer cells in comparison to human anatomy. Most carcinoma cells have diameters that are too large to pass through capillaries and capillary beds (breast cancer cells - MCF7 are 15- 25 μm) (Khaitan *et al.*, 2006), resulting in them becoming trapped within a matter of minutes post invasion. However, upon full invasion into the blood flow, cells are subjected to shear stress, high velocities and immune responses from the host, for example natural killer cells (NK) can induce cancer cell death (Labelle & Hynes, 2012). Therefore, circulating tumour cells (CTC) need to reduce the amount of time they are present within the vasculature, resulting in the CTC being in circulation being very quick. Moreover, tumour cells possess the abilities to mask themselves from the immune response and shield their presence. An example of this trait is platelets forming aggregates around the cancer cell. CTCs can secrete tissue factor (TF), leading to the coagulation, formation and activation of platelets and thrombin. Activated platelets present in the aggregates can be bound to tumour cells through fibrin and P-selectin ligand interactions with integrins on the cell surfaces These aggregations can physically shield and mask the CTCs from the immune cells and act as protection against turbulence and shear stress. The coagulation and shielding exhibited on CTCs has been shown to impair NK cell mediated killing, through PDGF suppressing NK function and downregulation of NK gene complex 2D (NKG2D) by platelet derived (transforming growth factor beta) TGFβ (Labelle & Hynes, 2012). Once the aggregate (emboli) is formed and the CTCs have survived the initial minutes in the blood flow, the emboli needs to arrest and stop at a distant site. Passive trapping may occur due to the size of the embolus in comparison to capillaries but trapping at specific sites (tropisms) irrelevant of size also occurs.

5 and 6) Pre-metastatic niche formation, extravasation, and metastatic colonisation

It is thought that primary tumours secrete specific soluble factors which prime distant sites, enhancing a pre-metastatic niche. These factors can activate E-selectin and focal adhesion kinase (FAK) on the endothelium of distant sites, promoting the adhesion of the CTC emboli to these areas. The emboli and CTCs bind to the adhesion molecules now present, promoting cell rolling and arrest. The activated endothelium, coupled with the secreted factors from the primary tumour, can recruit bone marrow derived dendritic cells (BMDCs) to the distant site. Further enhancing the premetastatic niche, promoting inflammation, survival, growth and support for the CTC emboli (Labelle & Hynes, 2012). Once present in the premetastatic niche, CTCs need to undergo a reversal of the EMT process. The cancer cells need to regain the phenotype of epithelial like cells and re-express molecules that facilitate the attachment of cells to the new tissue. Thusly the cells undergo Mesenchymal Epithelial Transition (MET). The cells reversal from EMT to MET is thought to be controlled epigenetically, through a complex interplay between Twist, (Wingless and int-1) Wnt, (micro RNA) miRNAs (namely 34c, 200, 205), hypermethylation and long non-coding RNAs (lncRNA). Once the cells have undergone MET, they form micro-metastasis at a distant site. A long process (weeks, months, years) of forming a secondary detectable colony occurs. The cells which are 'founding' the secondary colony must possess a high self-renewal rate to generate large growths, such cells are called tumour initiating cells (TIC) (Valastyan & Weinberg, 2011; Labelle & Hynes, 2012). It is believed that only a subpopulation of TICs exists in the primary tumour. These TICs must disseminate, survive circulation, arrest and adhere at a distant site and then survival the foreign environment. This is before self-renewing at a rapid rate. If the TICs overcome the host obstacles and divide, then a secondary detectable metastatic colony can occur. These secondary colonies represent the final step in the metastatic cascade (Valastyan & Weinberg, 2011b). Table 1.1 shows typical locations primary tumours metastases towards.

Table 1.1: Primary tumours metastatic sites *Adapted from information from Martin et al., 2013)*

Primary Tumour	Metastatic site
Melanoma	Bone, brain, liver, lung, skin, muscle
Ovary	Liver, lung, peritoneum
Pancreas	Liver, lung, peritoneum
Prostate	Adrenal gland, bone, liver, lung
Rectal	Liver, lung, peritoneum
Stomach	Liver, lung, peritoneum

1.2.2 Hypoxia

Hypoxia corresponds to decreased oxygen tension in tissues, where the concentration of oxygen is between 5-10 mmHg – 0%-2% oxygen (Scanlon & Glazer, 2015). Hypoxia is a common characteristic of tumours, relating to a poor prognosis, and decreased overall survival and distant metastasis free survival (McKeown, 2014). Hypoxia can arise due to the imbalance of oxygen delivery and consumption within the tumour (Lee *et al*., 2014). It has been suggested that 50-60% of tumours contain regions of hypoxia or anoxia – absence of oxygen (Scanlon & Glazer, 2015). Hypoxia is associated with metastasis, angiogenesis and invasion of tumours, through the regulation of survival responses, metabolic shift, increased genomic instability and the promotion of stem-like phenotypic properties. Furthermore, hypoxia has been suggested to impede drug delivery and immune response against tumours (McDonald *et al*., 2016).

1.2.3 Hypoxia Inducible Factor (HIF)

The key transcription factor in hypoxic biology is the hypoxia inducible factor (HIF) (Masoud & Li, 2015). HIF is a heterodimer, with an α and a β subunit, also called ARNT (aryl hydrocarbon receptor nuclear translocator) (Palazon *et al*., 2014). HIF has three isoforms: HIF-1, HIF-2 and HIF-3 ((Masoud & Li, 2015). The stability of the HIF-α subunit is regulated in an oxygen-dependent manner, whilst the HIF-β subunit is constitutively expressed. During

normoxia, prolyl hydroxylases (PHDs) hydroxylate prolines 402 and 564 on the HIF-α oxygen-dependent degradation (ODD) domain using oxygen as a substrate (Ziello *et al*., 2007). The Von Hippel-Lindau (VHL) E3-ligase recognises the hydroxylated HIF-α, resulting in its poly-ubiquitylation and targeting for proteasomal degradation (Masoud & Li, 2015). Where hypoxia occurs, the absence of oxygen prevents HIF-α hydroxylation and subsequent ubiquitylation, resulting in its rapid stabilisation (Masoud & Li, 2015). HIF-α then translocates to the nucleus, dimerises with HIF-1β, and the HIF heterodimer can then can bind to hypoxic responsive elements (HREs) in the promoters of target genes, mediating gene transcription, potentiated by transcriptional coactivators such as p300 (Wang & Semenza, 1993; Ziello *et al*., 2007; Greer *et al*., 2012; Masoud & Li, 2015b). HIF-1α and HIF-2 α can activate hundreds of genes, including those coding for VEGF, β1 integrin, and MMPs, which are involved in pathways such as angiogenesis, survival and proliferation, invasion and metastasis, and glucose transport and glycolysis (Wei *et al*., 2012; Masson & Ratcliffe, 2014; Rankin & Giaccia, 2016).

1.2.4   Hypoxic control of metastasis

Metastasis can be promoted by the presence of hypoxia (Rankin & Giaccia, 2016). HIF-1α plays an integral role in the progression of metastasis at each of the cascade stages, and the survival of tumours (Masoud & Li, 2015; Rankin & Giaccia, 2016).

Hypoxic regulation of EMT and early metastatic cascade stages (1 and 2)

Hypoxia mediates the upregulation of *zinc finger protein SNAI1* (SNAIL), *Zinc finger E-box-binding homeobox 1 and 2* (ZEB1 and, 2), *twist related protein 1* (TWIST) and TCF4 (*transcription factor 4*) in a HIF-1α dependent manner, therefore regulating EMT (Rankin & Giaccia, 2016). HIF is able to further promote EMT indirectly through increasing expression of Notch target genes such as HES1 (*hairy and enhancer of split 1*),TGFB1 (*transforming*

growth factor beta), *Hedgehog* (SHH) and Wnt family genes (Chen *et al*., 2010; Rankin & Giaccia, 2016). Resulting in EMT progression by activating factors such as SNAIL.

Hypoxic regulation of local invasion and intravasation (3)

Hypoxia can also mediate the disruption of the basement membrane, extracellular matrix (ECM) and stroma. HIF has been shown to upregulate *lysyl oxidase* (LOX), which in turn post translationally modifies collagen and elastin, increasing *focal adhesion kinase* (FAK) (Cox *et al*., 2013). HIF promotes the induction of autocrine motility factor (AMF), which can enhance proliferation, migration and angiogenesis (Ziello *et al*., 2007; Masoud & Li, 2015a). HIF-1α targets MMP1 and MMP2, which breaks down the ECM (Lu & Kang, 2010; Rankin & Giaccia, 2016).

Hypoxic regulation of survival in circulation (4 and 5)

Hypoxia also promotes immune system evasion (Palazon *et al*., 2014). HIF signalling stabilisation promotes the resistance of tumour cells to lysis from cytotoxic T-lymphocytes and regulates the degradation of natural killer derived granzyme B in autophagosomes (Wang & Semenza, 1993; GL., 2014). Furthermore, hypoxic and HIF signalling increases the expression of *programmed death ligand 1* (PD-L1) on tumour cells and myeloid derived suppressor cells (MDSCs) which promotes resistance against T-cell mediated killing (Barsoum *et al*., 2013). Hypoxia promotes the inhibition of the function, proliferation, cytokine secretion and expansion of tumour-infiltrating lymphocytes through accumulating extracellular adenosine (Palazon *et al*., 2014; Noman *et al*., 2015; Rankin & Giaccia, 2016).

Hypoxic regulation of metastatic niche and final metastatic cascade stages (6, 7 and 8)

Hypoxia and HIF target VEGF-α to stimulate the recruitment and proliferation of endothelial cells, building a blood network to supply the secondary site and the growing micrometastases (Hoeben *et al*., 2004). LOX also promotes the formation of the pre-metastatic niche (Cox *et*

al., 2013). Hypoxia can also recruit T cells, which express NP-1 and chemokine receptor 10, which promote angiogenesis and immune tolerance (Rankin & Giaccia, 2016). Hypoxia recruits MDSCs and macrophages to the microenvironment, which in turn secrete VEGF, which promote tumour progression and immune tolerance (Valastyan & Weinberg, 2011a). HIF-1α also targets *pyruvate dehydrogenase kinase* (PDK1), which represses mitochondrial function and as such affect's glycolytic mechanisms in the tumour. It is thought that secondary tumours have an increased level of PDK1 in comparison to the primary tumour and thus the primary tumour and hypoxia can facilitate metastasis through creating a preferential niche for tumours (Valastyan & Weinberg, 2011; Wilson & Hay, 2011; Zijl *et al*., 2011; Rankin & Giaccia, 2016).

In order to study hypoxia biology and metastasis, the different ways of modelling cancer and the tumour microenvironment need to be considered. One such technique are multicellular 3D models of cancer, such as spheroids.

1.3   Cancer models

There are many cancer models aiming to address different aspects of tumour and cancer questions. These models range from *in vivo* using animals, being translated into human cancer, using creatures such as Zebrafish or mice (Holen *et al*., 2017), to *in vitro*, based in the laboratory away from animal culture (Pickle & Ries, 2009). However due to the complexity of human and mammalian cancer many models are not fully representative, therefore different types of modelling must occur (Imamura *et al*., 2015). For example, much *in vitro* work is completed on a 2D planar surface, which does not replicate cancer found in humans, whilst *in vivo* work is done in three dimensions, but requires immunocompromised organisms, which differ to humans, therefore is not fully representative (Imamura *et al*., 2015; Zhou, 2016). However, both types of models, both *in vitro and in vivo*, 2D and 3D models have benefits and drawbacks in comparison to one another.

1.3.1   2D models vs 3D models

Two-dimensional cancer models are flat models and include the cell monolayer. These models and the cell monolayer have traditionally allowed the investigation into stem cell differentiation, molecular biology, protein presence and many other factors thought to be important in cancer development (Sutherland, 1988; Mehta *et al.*, 2012). Whilst initially seeming useful for biological questions, within the 2D model there are many differences to what is seen in mammalian tumours (Hongzhou *et al.*, 2013; Edmondson *et al.*, 2014). In 2D there is a homogenous acquisition of nutrients and removal of waste. 2D culture allows homogenous and uniform concentrations of cytokines, growth factors and nutrients to be present, surrounding the cell (Sutherland, 1988; Mehta *et al.*, 2012). Cell monolayers observe an exponential growth pattern (which is different from *in vivo* tumours), where they can continually proliferate until they reach the constraints of the culture plastics (Hongzhou *et al.*, 2013). However, the artificial conditions of 2D culture result in the cells becoming elongated with a flat morphology, and can give rise to genetic aberrations, totalling a 30% difference in genetic and protein expression patterns in 2D cultures, compared to the tissue origin (Edmondson *et al.*, 2014). This is reflected in the upregulation of genes responsible for growth and proliferation and the repression of genes that limit growth and proliferation, when compared to the original site of the cell line, demonstrating why the monolayer exhibits exponential growth (Mehta *et al.*, 2012; Edmondson *et al.*, 2014). Moreover, in 2D, the ECM and cell interactions are reduced, resulting in limited mass transport of molecules and differences in integrin binding. An example of this being an issue is the testing of therapeutics (Mehta *et al.*, 2012). When a new drug is tested, the concentration used on a 2D platform is homogenous across the whole culture and every cell. When this is then transitioned to an *in*

vivo 3D model, the drug doesn't uniformly affect each cell, due to the diffusion gradients present, resulting in a disparity between the two studies.

The homogenous access to nutrients and waste removal is not observed in 3D cell cultures. Instead, 3D culture models demonstrate heterogeneous access to nutrients, gases, and metabolite distribution (Chandrasekaran & King, 2012). Solid tumours have leaky blood vessels and therefore a poor blood flow. The tumours attempt to quickly divide and demand nutrients to grow. The tumour is highly metabolically active and attempts to acquire as much nutrients as possible, whilst removing excess waste such as CO_2 and lactate (Weinberg and Hanahan, 2011). To do this, human cancers are highly angiogenically active. The tumour will rapidly form new blood vessels through a complex interaction of tip cells, endothelial cells, cytokines and other pro-angiogenic factors. However, as the blood vessels are being rapidly formed, they are not well formed hence the blood vessels are often 'leaky' and poorly shaped. This results in differences in concentrations of nutrients and waste, including oxygen (DeBerardinis & Chandel., 2016). Oxygen can only diffuse 100-200 μm into the tumour (Mehta *et al*., 2012). Therefore, the cells present at the edge of the tumour are the closest to the blood vessels and have the highest concentration and best acquisition of nutrients. The central region of the tumour has different characteristics, specifically: the oxygen tension decreases, waste metabolites increase, and hypoxic and anoxic regions are formed. Hypoxia starts to occur in the cells where the oxygen concentration is less than 10mmHg. This phenotype results in reduced sensitivity to chemotherapy, increased resistance, increased invasive potential and poorer patient survival rates (Zhou, 2016).

1.3.2 *In vivo vs In vitro*

There are many different types of *in vitro* models used in cancer research, including monolayers, clonogeneics, spheroids, scratch assays and transwell based assays. Models have been used for tumour kinetics, drug screening, invasion and angiogenesis. *In vitro* models typically use cancer cell lines, due to availability, ease of growth and direct comparisons to human tumours (Mehta *et al*., 2012; Edmondson *et al*., 2014)

An example of an *in vitro* model used in cancer research is the scratch or wound healing assay. The wound healing assay is a simple assay, using a monolayer of cells, inflicted with a wound, situated through the centre of the monolayer to assess the ability of cells migrate back across the space created by the wound (Liang *et al*., 2007). Another model is the transwell based assay (Justus *et al*., 2014). Transwell based can be used to study migration, invasion, various aspects of the metastatic cascade and drug screening. An example of transwell based assays is the seeding of cells onto a porous membrane and studying the movement of cells to a lower chamber within the culture dish; combination of drugs, chemoattractants and cytokines can be added to investigate different aspects of cancer spread (Justus *et al*., 2014). These assays are low cost and have a high throughput, however, they are of low physiological relevance due to the static nature of the culture. Plus, the invasion data can conflict between experiments and can only assay single cell motility. Further examples of *in vitro* models include cell monolayers and co-culture models (Mehta *et al*., 2012).

In vivo models are cancer models which use animals to study tumours. These models can be used for drug screening, invasion, growth kinetics and migration (Muthna *et al*., 2016; Nunes *et al*., 2018). These are more complex than the *in vitro* models, require ethics and are relatively low throughput. One such example of an *in vivo* model is one of the simplest models, the cell derived xenograft (CDX) model. This model requires human tumour cells being subcutaneously implanted into an immunocompromised mouse (Holen *et al*., 2017). Whilst it

is fast, cheap and includes human tumour cells, it does not include all tumour subtypes. The host is immunocompromised and can only model advanced disease states. The sample is added subcutaneously and is not at the same site where the tumour is within a human. Moreover, there are ethics involved and it requires the sacrifice of animals. Another example of an *in vivo* model is the patient derived xenograft (PDX). Again, these models use human tumour fragments, but are costly. They require an immunocompromised host, namely athymic nude mice, severely immunocompromised mice, nonobese diabetic mice, before a fresh tumour sample from the patient is added into the host and the mouse stroma will replace human cells within time. Moreover subcutaneous PDX models rarely produce metastasis and struggle to simulate the initial tumour microenvironment (Holen *et al.*, 2017).

Whilst brief, these examples demonstrate the complexity of cancer modelling. For example, the 2D *in vitro* experiments are more cost effective, are high throughput and require reduced ethics but fail to recapitulate the physiological relevance of the 3D *in vivo* model. On the other hand, *in vivo* models are costly, lower throughput, and requires animal testing, and therefore strict training and ethical constraints. With these factors in mind, alternative 3D *in vitro* models can be used (Holen *et al*., 2017).

1.3.3   *In vitro* 3D models

Limitations regarding low throughput, cost, direct application and ethics of *in vivo* work can be attempted to be overcome by using *in vitro* and *ex vivo* 3D models (Chandrasekaran & King, 2012).

Ex vivo models, such as tumour biopsies embedded into extracellular like matrices (ECM), such as collagen, are used to investigate the tumour microenvironment and spread (van de Merbel *et al*., 2018) The complexity and human heterogeneity of cellular populations is maintained,   whilst   keeping   host   cell   interactions.   The   model   does   not   use

immunocompromised animals or risks having cells from a different host present. However, the vasculature of these models is not perfusable and the models themselves have only been used for drug sensitivity and to determine tumour growth kinetics. Migration through the ECM is possible but can be difficult. An alternate higher throughput, lower cost alternative *in vitro* model that can be used for similar applications is the multicellular tumour spheroid (MCTS) (Li *et al*., 2012;Katt *et al*., 2016)

1.3.4   Spheroids as cancer models

Spheroids are 3D models of cancer that are formed where cell suspensions are grown in non/low adherent conditions, resulting in cells self-aggregating to form a sphere like structure (Sutherland, 1988; Mehta *et al*., 2012). Spheroids have been used in cancer research for the past 60 years, first being used in the 1950s (Sutherland, 1988). The term spheroid was first coined in the 1960/70s when a research team observed near spherical shapes being formed from V79 hamster lung cells (Sutherland, 1988).

Spheroids typically tend to share common characteristics with mammalian tumours. It has been very heavily documented that multicellular tumour spheroids contain distinct zones, namely a core, a layer of quiescent cells, and an external layer of proliferative cells (Figure 1.3) (Hamilton, 1998; Horning, 2008; Mehta *et al*., 2012; Gong *et al*., 2015). This structure results through the heterogeneous acquisition of nutrients, and oxygen diffusion (Mehta *et al*., 2012). The diffusion gradient of oxygen through cells and the proportion of cells present within the spheroid give rise to a centralised region of necrosis with surrounding layers of proliferating and quiescent cells (Chandrasekaran & King, 2012; Mehta *et al*., 2012). This is like similar zoning in some tumours. As oxygen has a diffusion limit of 100-200 µm, the cells at the external layer of the spheroid can access it and nutrients (Olive *et al*., 1992; Grimes *et al*., 2014). These cells can proliferate and remove catabolites into the surrounding media. In contrast, cells which are over 200 µm from the spheroid edge have limited access to the

nutrients and oxygen, and limited waste removal. This therefore creates chemical and nutrient gradients mirroring regions found within human tumours (Sutherland, 1988). The gradients give rise to the central cells of the spheroid (the core) having the smallest level of access to nutrients and oxygen, meaning these cells become hypoxic and void of ideal growth conditions (Sutherland, 1988; Olive *et al*., 1992).

This coupled with the inability to removal catabolites, results in an acidic and necrotic core being present at the centre of the spheroid. In between the core of the spheroid and the proliferative layer of cells, is a layer of quiescent cells. The quiescent cells are in a G0 phase of cell growth, which is attributed to the limited oxygen and nutrient supply (Chandrasekaran & King, 2012; Mehta *et al*., 2012). Overall this diffusion and chemical gradient gives rise to a structure in 3D cell cultures being more similar to tumours *in vivo* (Sutherland, 1988).
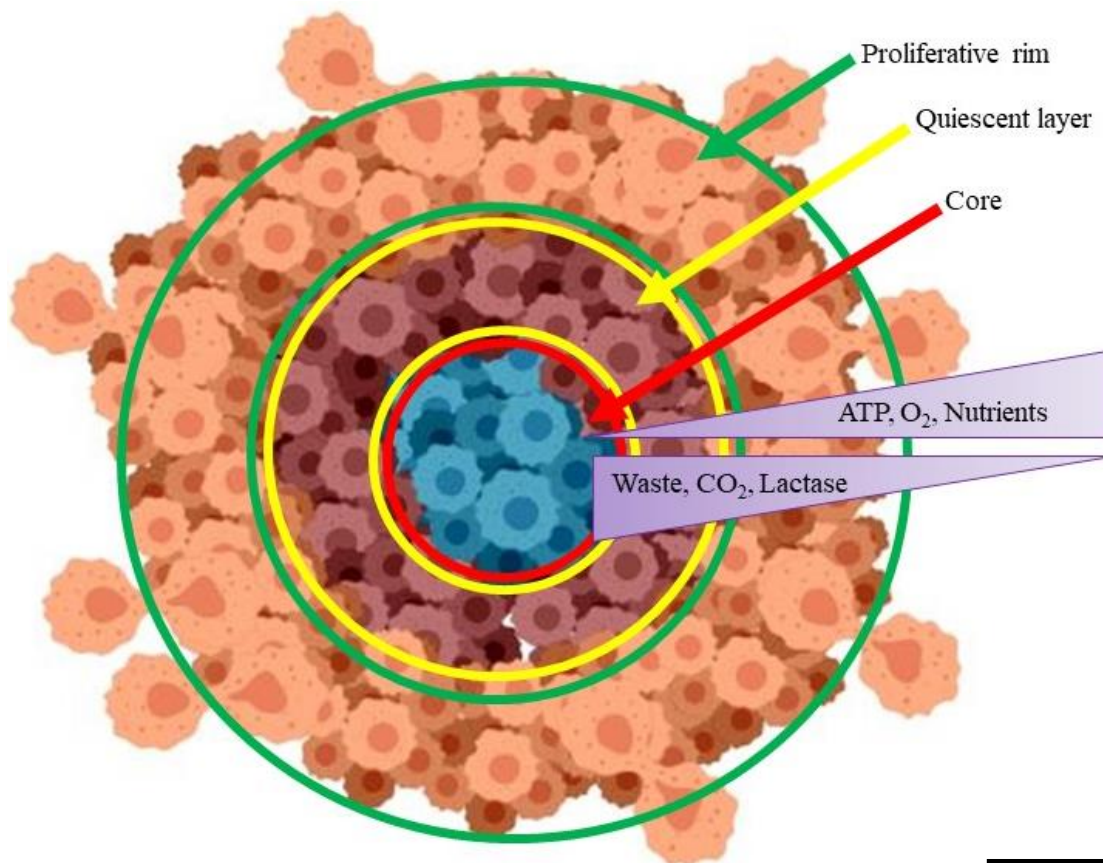
Figure 1.3: Tumour spheroids zones

A spheroid has distinct zones (core, quiescent cells and proliferating cells), which arise due to the diffusion limits of nutrients and oxygen. The build-up of catabolites, waste, CO_2 and lactase results in the central zone of the spheroid being more acidic, hypoxic and anoxic, containing apoptotic and necrotic cells. The external layer of cells has the highest percentage of O_2, ATP and nutrients. This results in the cells being proliferative and able to divide. The layer between this external rim and central core has limited acquisition of nutrients and limited removal of waste, therefore these cells are in a quiescent state or within the G0 phase of cell cycle growth. Made using Biorender. Scale = 200 μm.

Spheroids can be seeded and formed at different sizes, correlated to the cell function, transport, drug efficacy and migration (Katt *et al*., 2016). Where spheroids are between 200 – 500 μm, gradients can develop. Larger than this (typically 400 – 600 μm) secondary necrosis can develop in the central core of the spheroid, something which is thought to be more representative of mammalian tumours (Chandrasekaran & King, 2012; Mehta *et al*., 2012).

Spheroid application

Spheroids can be used of a variety of applications, tumour growth kinetics, cell proliferation, migration, drug screening, immune cell interactions and invasion (Sutherland, 1988).

As previously detailed, the genetic profile and protein expression of spheroids in comparison to 2D cultures showed that spheroids better resemble *in vivo* tumours than 2D culture (Katt *et al*., 2016). Invasive potential of cancer and the migratory capabilities of cells have been studied by using spheroids embedded within hydrogels and ECM like matrices, identifying key factors released and direct measurement of cells moving away from the primary mass (Yuan *et al*., 2019).

Spheroids have also been used to measure the immune response, by co culturing spheroids with immune cells (NK or macrophages), the immune response and infiltration into the cancer mass has been observed (Ayuso *et al*., 2019).

Another application and probably the most common use of spheroids is drug screening (Edmondson *et al*., 2014). It is estimated that $1.3 billion is required to get a new pharmaceutical agent through clinical trials (Edmondson *et al*., 2014). However, most pre-clinical evaluation *in vitro* is conducted using 2D cell cultures, which do not fully reflect the tumour microenvironment and associated therapy-resistance phenotypes (Edmondson *et al*., 2014). In an example, ovarian cancer cells were treated with the chemotherapy agent paclitaxel, leading to an 80% reduced cellular viability (Loessner *et al*., 2010). However, when the same

paclitaxel concentration was used on a 3D cancer cell model, it led to only 40-60% loss of viability. These type of studies do not take the tumour microenvironment into consideration and therefore some therapeutic agents fail during clinical trials (Loessner *et al.*, 2010; Edmondson *et al.*, 2014). Specifically, as detailed previously, hypoxia is associated with radio- and chemo-resistance, decreased apoptotic potential, increased genomic instability, impaired DNA repair, and reduced drug availability. These later issues with drug delivery to 3D models can be overcome using by several techniques such as using liposomes or nanoparticles (Mehta *et al.*, 2012; Edmondson *et al.*, 2014).

These brief examples demonstrate the applicability of spheroids as alternate *in vitro* models of cancer. However, there are other factors related to metastatic spread and invasion (such as interstitial flow, the tumour microenvironment and shear stress) that spheroids cannot model. The spheroid fails to recapitulate shear stress, continuous perfusion, the full microenvironment, cytokine signalling and interstitial flow. Therefore, it is necessary that hybrid models are used to attempt to tackle the complexity of cancer biology and metastasis. Such as being able to replicate shear stress, continuous perfusion and chemical gradients into account.

1.4   Microfluidic devices

Microfluidic devices, also called Lab-on-a-Chip devices, are systems that can process or manipulate microscopic amounts of fluids (10^{-9} to 10^{-18} L), through the use of micro-meter sized flow channels and networks (Whitesides, 2006). They have been applied to biological and biomedical research, as well as chemical synthesis and analysis (Hsiao *et al.*, 2009; Ong *et al.*, 2017; Michael *et al.*, 2018; Yuan *et al.*, 2019). These devices require only small quantities of reagents and samples, resulting in reduced cost, quicker experimental time and have the potential for lower environmental impact (Whitesides, 2006). Microfluidic devices

can be designed and fabricated in a multitude of ways, often involving computer aided design packages (Ren *et al*., 2013). Commonly employed materials include paper, silicon, glass and polydimethylsiloxane (PDMS), shown in table 1.2 (Daw & Finkelstein, 2006; Whitesides, 2006). For cell culture and spheroid applications on-chip, PDMS or glass are generally used (Ma 2018; Park *et al*., 2019), owing to the characteristics listed in the table below (Iliescu *et al*., 2012; Ren *et al*., 2013).

Table 1.2: Microfluidic device materials commonly used. Advantages/disadvantages associated with different materials (based on information from Ren et al., 2013)

Material	Benefit	Limitation
Paper	Inexpensive Fast Easily transportable	Too simple for complex analysis Fragile Cannot get wet
Glass	Biological analysis able Sterilisation Non gas permeable Transparent	Easily Breakable Rough More expensive than plastic Non malleable
PDMS	Malleable Transparent Cheap Fast production	Gas Permeable Difficult to clean and sterilise Smooth Limited heat resistance
Silicon	Thin membranes (thermal benefits) Low cost Fast production	Application breadth Poor heat resistance Brittle
PMMA (polymethyl methacrylate)	Malleable Unlimited colour options High resistance to UV Unlimited colour options	Limited heat resistance Cracking under load Limited chemical resistance Poor impact resistance
Ceramic	Multilayer ceramic is well established Slow heat transfer Chemical resistance and stability	Breakable Non-malleable More expensive than plastic

1.4.1 Microfluidic devices and cancer research

Microfluidic devices are currently being used in cancer research for various applications (Ma 2018; Park *et al*., 2019). These are desirable for biological and cancer analysis due to the abilities to control the internal and external temperature, have precise control over nutrients, and present laminar flow and shear stress (Ip *et al*., 2016). These controllable factors are key

in cancer research models to mimic those conditions found within patient tumour tissue whilst saving resources.

Zhang & Nagrath (2013) reviewed microfluidic device models, suggesting future roles, gaps and applications that microfluidic devices could be used for. The areas they identified concluded that spheroids within microfluidic device were a useful avenue for cancer research, as such this was further reviewed by Ma and more recently Park. The authors focused on isolation of circulating tumour cells, size-based separation, molecular analysis of cancer, drug screening, high throughput approaches and migration assays (Zhang & Nagrath, 2013). (Ma 2018; Park *et al.*, 2019). The controllable factors possible in biological microfluidic devices, such as temperature, can be further combined with the 3D models mentioned previously, including spheroids. A spheroid could be generated at 500 microns to generate a hypoxic core (Cai *et al.*, 2013; Ma *et al.*, 2016) and these two models can be combined to further bridge the gap between *in vitro* and *in vivo.* By mixing 3D cultures incorporated into microfluidic devices, these issues can be addressed and have been adopted by various groups (Das *et al.*, 2013; Kuo *et al.*, 2014; Bender *et al.*, 2016; Ip *et al.*, 2016; Shang *et al.*, 2019). Table 1.3 shows examples of this breadth of work. The table focusses on examples of microfluidic devices being used for different components of the metastasis cascade; for example, confinement on cancer cells (experienced when metastatic cell clusters are flowing through the circulation), extravasation (stage 6 on the previous diagrams, with an example figure of a device used that combines primary cell cultures and hydrogels), shear stresses influence on cellular spread (with an example image of the device used to generate relevant shear stress values on-chip) and spheroid formation on-chip. Within these examples, it possible to see that most authors focus on the latter stages of the metastatic cascade, and similarly, those whom focus on early metastasis, use single cells and drugs to impede this.

Table 1.3: An overview of microfluidic devices and their uses in biological research

Study	Design	Results	Reference
Extravasation in the metastatic cascade	The three layered PDMS device was coated using Collagen IV, lined with an endothelial cell monolayer. Kuhlbach used a flow of 0.8-1.2 µl, over the 72 h period	Endothelial cells within the device acted similarly to *in vivo* endothelial cells. Cells were able to be imaged live within the device	(Kühlbach *et al*., 2018)
Extravasation in the metastatic cascade	A PDMS microfluidic device coated in collagen and HUVECs*	(MDA-MB-231) have enhanced matrix invasion when in the presence of HUVECs, whilst MDA-MB-231 cells have significantly decreased invasion without HUVECs.	(Blaha *et al*., 2017).
Cell migration	PDMS microfluidic device, coated in ECM-Matrigel	Chaw found that 40% of the MDA-MB-231 cells invaded the Matrigel over 5 days at a rate of 7 µm/h, whilst none occurred in the MCF7 cell line. The MDA-MB-231 cells rotated 2-3 radians over this time.	(Chaw *et al*., 2007)
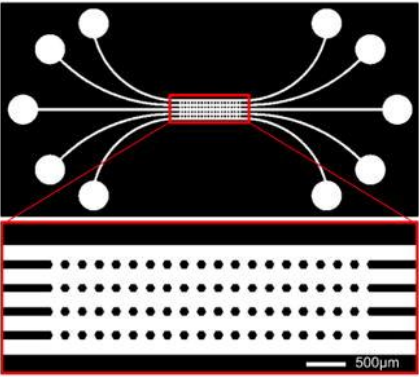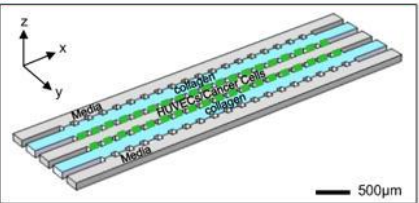
Cell interaction and shear stress	PDMS device	At 0.50 and 2.50 dyne cm^{-2} shear stress, circulating MDA-MB-231 cells adhere to regions of endothelium treated with TNF-α compared to untreated regions. TNF-α upregulated CXCR4 and 7, whilst CXCL12 upregulated CXCR4 in HDMECs. From this they demonstrated that CXCR4 and 7 increased adhesion to endothelium of MDA-MB-231 cells and cancer cells were preferential CXCL12 treated endothelium within a microfluidic device	(Song *et al*., 2009)
Cell migration, intravasation and hypoxia	Multilayered PDMS device lined with type I collagen	PANC-1 cells grown on-chip at 1% O_2 had a 50% lower growth rate than the same cells on-chip at 5% O_2. Both conditions showed the cells were viable for 8 days. Moreover, When no oxygen gradient was present on-chip, fewer cells migrated into collagen. When a gradient was present, 1% O_2 in one channel and 21% in another, the cells migrated 10 x higher.	(Acosta *et al*., 2014)

Replicating the blood brain barrier	PDMS microfluidic device	reductase family 1 B10 (AKR1B10) was higher in metastatic lung cancers, although AKR1B10 downregulated MMP2 and 9. Silencing of AKR1B10 suppressed extravasation in the microfluidic device.	(Liu, 2019).
Metastatic potential of cells	Dual material microfluidic device out of glass and PDMS	Were able to capture 10-500 cells/ml in 50% of the patients and circulating tumour emboli in 10% of the samples	(Kulasinghe *et al*., 2019).
Confinement on cancer cells and drug testing	PDMS microfluidic device, comprised of four arrays with 50 channels	Confinement alone was able to drive migration.MDA-MB-231 cells migration appeared to be the fastest across the cell lines investigated. Migration rate was reduced after subjecting the cells to Taxol and Nocodazole	(Irimia & Toner, 2009)
Cancer cell migration through confinement of tight blood vessel, how different angles (between 1 and 40 degrees) affected migration of cancer cells	Glass	MDA-MB-231 cells had a 480% rate of permeation into the smaller channel at all angles, in comparison to the non-cancerous cell lines used. Taxol treatment reduces the percentage of cancer cell migration	(Mak *et al*., 2013)
Confinement on cancer clusters	ULA plate cluster chip	90% of clusters migrated through narrow constrictions and, as the cancer clusters approached the narrowing of the channel, these were able to unfold into a chain	(Au *et al*., 2016)

		like structure and pass through the narrowest point. As the cells exited, the cancer clusters were able to re-cluster from the chain into their original shape	
Confinement on cancer cells	microfluidic device containing a comparator region and a liquid interface	Stiffness of cells that affect the migration speeds of	(Khan & Vanapalli, 2013)
Physiological shear stress (15-30 dynes per cm^2)	Three channel PDMS with collagen lining*	Flow promoted an amoeboid and a mesenchymal phenotype with evenly distributed actin filaments	(Ma *et al*., 2017)
Co-cultured cell migration	'm' chip	Whilst under flow, MCF7 were consistently trapped in comparison to the MDA-MB-436. Both cell types had decreased size after separation, however. Enriched populations of SUM149 cells had greater cytoskeletal and nucleoskeletal motility gene expression	(Zhang *et al*, 2012)
Drug testing	PDMS	Cells were maintained at 90% viability. Increased migratory ability of MDA-MB-231 cells was relative to IL-6 secretion.	(Mi, 2016).
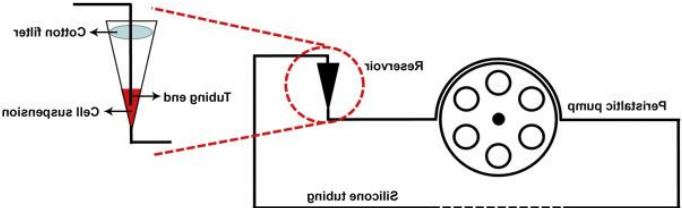
		HMEpiC morphology was altered and both drugs inhibited cell migration.	
Fluid patterns on cell migration	PDMS device that contained four regions, housed two PDMS pillars that contained the ECM regions. One of the regions was used to allow a different hydrogel to be present within the device, enabling the flow to be altered and limited without hindering cell migration	interstitial velocity of 10 μm s^{-1} was relevant in acute inflammation and tumour microenvironments, in comparison to the normal levels of 0.1 -1 μm s^{-1}. Interstitial flow increases migration speed of 20% of cells and migrational persistence. Interestingly, they noted cells migrated faster without direction upstream, in comparison to migrating slower with higher directness with flow	(Haessler *et al.*, 2012)
Cancer EMT	PDMS	EMT phenotypes, demonstrated by E-cadherin and vimentin expression, were shown in mixed cell spheroids. This phenotype showed different drug sensitivity, which was improved through inhibitors of TGF-β. Moreover, invasion assays showed spheroids had fibroblast led movement	(Khawar *et al.*, 2018)
Spheroid formation on chip	PDMS device	Over 9000 spheroids were being generated per device, giving rise to	(Hardelauf *et al.*, 2011)

		the ability to rapidly increase output of spheroids over a 96 h period and accommodating high-throughput analyses	
Spheroid formation on-chip	Gravity-driven cell aggregation and balanced droplet dispensing system on a PDMS device	Possible to generate uniform spheroids (>90%) across a range of sizes (58 µm – 400 µm). However, the size of these spheroids was too small to contain substantial hypoxic and necrotic regions	(Kim *et al.*, 2012)
Spheroid formation on-chip	PDMS device	Possible to form spheroids (MCF7 cells) within a microfluidic device	(Wu *et al.*, 2008)
Spheroid formation on-chip	PDMS device	Possible to form MCF-7 spheroids and a tubular mammary duct	(Young, 2013)
Extravasation and micrometastases	PDMS microfluidic device, containing 3 media channels and 4 independent gel channels	The channels were 150 mm deep and coated with poly-D-lysine hydrobromide (PDL), to promote matrix adhesion. Collagen and Matrigel were used as coating layers to simulate the ECM. The authors used this device to study MDA-MB-231 invasion towards CXCR2 bone chemokines	(Bersini *et al.*, 2014)
Cell-cell interaction	PDMS device	Hockemeyer observed that CAFs induce dispersion of spheroid tumour cells into the matrix, which is mimicked by CXCL12, whilst NAFs induce aid single cell	(Hockemeyer *et al.*, 2014)

		migration into the environment. CXCL12 did not produce the same effects.	
Cell-cell interactions and drug testing	PDMS device	Invasion under normal conditions and under MMP inhibitors (specifically the broad MMP inhibitor GM6001 CAFs promoted cell invasion, in a spheroid fashion, and that MMP inhibitors can prevent this effect	(Liu et., 2010)
HUVEC distribution in HEPG2 spheroids	PDMS device	They then added (pro-angiogenic) VEGF and b-FGF to the spheroids to look at HUVEC migration over a period of 72 HUVECs formed lumen structures within the spheroids when treated with VEGF and β-FGF over a period of 72 h	(Patra *et al*., 2014)
Spheroids and drug testing	PDMS device	Finding that no significance was seen when using drugs responsible for converting cytochrome peroxidases. They concluded that HepG2 are limited as a 3D liver model	(Fernekorn *et al*., 2015)
Spheroid formation	PDMS device	Developed a process of forming OV90 and TOV112D cell enriched spheroids ranging in sizes from 230-530 μm	(Marimuthu *et al*., 2018)

Spheroid formation	Droplet based microfluidic device	Capable of generating 1000 droplets per minute, which encapsulated cancer cells to form spheroids ranging from 50-245 μm. They explained that viability was maintained on chip for over a two week period	(Kwak *et al.*, 2018).
Cell-cell interactions	Device lined with Collagen	The study found that T47D cells stimulated with macrophage colony stimulating factor (M-CSF) and MDA-MB-231 cells could polarise monocytes into tumour associated macrophages (TAMs), increasing cell migration	(Yuan *et al.*, 2019)
Drug testing on spheroids	PDMS, silicon wafer and glass microfluidic device	Generated coculture spheroids from SUDHL-10 and HS-5 cells, before testing the effects of lenalidomide drugs on the proliferation of the spheroids, concluding there was an inhibitory effect on cell proliferation	(Sabhachandani *et al.*, 2019)
On-chip formation and drug treatment	Paper based microfluidic device, utilising a wax patterning print with photoinduced surface modification	The device was used to culture MCF7 and 1058Sk coculture spheroids on chip. The chip showed the spheroids were stable for 10 days and the group were able to perform both ELISA assays and drug testing on chip	(Michael *et al.*, 2018).

On-chip spheroid formation and drug testing	PDMS based screening device, capable of testing 1032 MCF7, SUM157 and Mia PaCa spheroid models simultaneously with 8 drugs. The device comprised of 28 drug combinations, 7 mixing ratios and controls, all with 6 replicates	They showed that drug concentration ratios of $1:10^6$, 1:100, 1:10, 1:1, 10:1, 100:1 and $10^6:1$ were achieved on-chip. The drugs used were cisplatin, docetaxel, doxorubicin, gemcitabine, irinotecan, oxaliplatin and 5-FU. These drugs were used on the MIA- PaCa-2 spheroids formed on chip, which were reproducibly formed at 328 μm. Showing that 4 combinations of drugs showed synergistic effects, to match literature conclusions	(Zhang *et al*., 2018).
On-chip spheroid formation and drug testing	Microfluidic device with a pillar array	90% of spheroids ranged from 175 – 225 μm in diameter. They found that spheroids expressed higher levels of CD133 and nucleic HIF-1α. And the spheroids had a higher doxorubicin resistance than the cell monolayers	(Lim *et al*., 2018)

As table 1.3 shows there are many different examples of biological research within a microfluidic device. As previously stated, combining spheroids and microfluidic devices offers a useful avenue for researching cancer *in vitro*. There are two manners to conduct this. One is to form spheroids on-chip, whilst the other is generation of the spheroids off-chip.

1.4.2 Spheroid formation on chip

Ong *et al* reported a spheroid on chip 3D printed microfluidic device, printed using stereolithography and PolyJet to immobilise and form HepG2 and oral squamous cell carcinoma cells to form spheroids on chip (Ong *et al*., 2017). The device was a pump free perfusion system utilising gravity driven flow (Ong *et al*., 2017; Park *et al*., 2019). The device seeded cells at a flow rate of 0.15 ml h, with wall shear stress being 0.8 dynes cm^{-2}. However, the shear stress was decreased to 0.0025 and 0.88 Pa within the cell chamber compartment. They found that metastatic and patient derived parental spheroids were able to be maintained on chip for a period of 72 h, with good viability. Similarly, Chen *et al* developed a technology to recreate 3D cell cultures using a specially designed open plate, utilising naked liquid marble techniques (Chen *et al*., 2019). The plate was coated using a superhydrophobic layer to allow the natural formation of mouse olfactory ensheathing cells (mOECs-GFP) spheroids. The plate was coated using a hydrophobic coating of methyl isobutyl ketone, butyl acetate and mineral spirits and acetone. Using this technique, spheroid formation was uniform and over a 24 h period the spheroids increased in size by 125%, showing good viability (Chen *et al*., 2019). A further demonstration of spheroid on chip formation was conducted by Lee and Cha, which used a PDMS microfluidic device with double flow-focusing to allow the formation of MCF7 cells cocultured with macrophages of fibroblasts, 3T3 or RAW264.7, within a microgel – methacrylic gelatin (Lee & Cha, 2018). A further device from Imaninezhad *et al* aimed to form U251 spheroids from oil and a 4-arm PEG-Ac, DBTA solution within a T-junction microfluidic device (Imaninezhad *et al*., 2019). The research focused on the initial formation of spheroids

by flowing the solutions at varying speeds (5 - 60 µl/min for PEG and 0.5- 1 ml/hour for water), before testing PTX, DOX, BCNU, CCNU and TMZ on the spheroids (Imaninezhad *et al*., 2019). Imaninezhad detailed that PEG hydrogel was degraded a lower rate in the presence due to water percentage differences. Moreover, they showed that spheroid viability was maintained at high levels (>90%) for 7 days on-chip. They further showed that in the presence of CCNU and TMZ, spheroids were more susceptible to chemotherapeutics when within PEG hydrogels. Cheng developed a high throughput single cell derived tumour sphere microfluidic device to track over 10,000 cells on chip. A PDMS chip coated with F108 was used to form breast cancer spheroids on chip (Cheng *et al*., 2016). Their device had a >60% capture rate for cell suspensions of 2.5×10^4 to 1×10^5 ml, whilst a 76.5% capture rate was seen for cells of 5×10^4 ml. Spheroids were monitored of 14 days on-chip, and they concluded that small SUM-159 cells had a higher sphere forming potential over T47D and SUM-149 cells. Rogers *et al* engineered a two layered PDMS microfluidic bioreactor to look at 3D breast tumour environment. Type I collagen and Matrigel was added to the microfluidic device before externally grown MDA-MB-231 spheroids of 60,000 cells were added to the microfluidic device after 3 days. HMVECs and NIH-3T3s were also added to test the interactions with the breast cancer spheroid. They found spheroids were viable within the device for a period of 15 days (Rogers, 2018). The overall finding shows that many applications are using microfluidic devices to form spheroids on-chip, but these are being generated at sizes too small to be comparable to *in vivo* tumours.

1.4.3   Spheroid formation off chip

An alternative to the formation of spheroids on chip is the formation of spheroids off chip and then being introduced into the device as was conducted by Christoffersson *et al*. Here, cardiac spheroids of 2500 cells, 250 µm in diameter, were formed before introducing them into a polymer based microfluidic device treated with laminin (Christoffersson *et al*., 2018).

Following this the group tested drugs on the spheroids to investigate cellular spread (Christoffersson *et al*., 2018). They showed by using doxorubicin and endothelin-1, it was possible to decrease cells surrounding the spheroids. On the other hand, it was possible to increase the number of cells present around the spheroid by using phenylephrine and amiodarone. Choi and colleagues used a microfluidic device (shown in figure 1.4) to look 3D models of early stage breast cancer. The authors used MCF10, mammary fibroblasts and HMT-3522 cells to form spheroids in a ULA plate, before introducing them into a Matrigel and fibronectin coated PDMS multilayered microfluidic device after 3 days. The study tested the effects of paclitaxel on cells through LDH assays, concluding a reduction in size was seen on the size of treated spheroids in comparison to the untreated conditions (Choi *et al*., 2015).

1.4.4   Metastasis on chip

To perform this effectively, the various stages of the metastatic cascade need to be considered in relation to the cancer model.

1.4.5   EMT and shear stress (early stage metastasis)

Lee and colleagues developed a PDMS microfluidic device compromising of 7 channels, lined with type I collagen coupled with PANC-1 cells. They aimed to look at the formation of PANC-1 tumour spheroids on chip, to further assess the EMT related markers and proteomic expression analysis, before treating them with Gemcitabine. The study concluded that the survival on chip was maintained and that cocultured spheroids expressed more EMT markers than their monoculture counterparts (Lee *et al*., 2018). Like Lee, Mina *et al* looked at the effects of shear stress on EMT and tumour endothelial cell interaction. The authors developed a PDMS 3D culture microfluidic device, housing type I collagen and glycosaminoglycans (GAGs), to recapitulate 1 dyne/cm^2 (Mina *et al*., 2017). HUVECs were seeded in a collagen MDA-MB-231 spheroid through on chip formation (Mina *et al*., 2017). Mina found that under low shear stress and in the presence of ECM, EMT was upregulated. They showed that mesenchymal
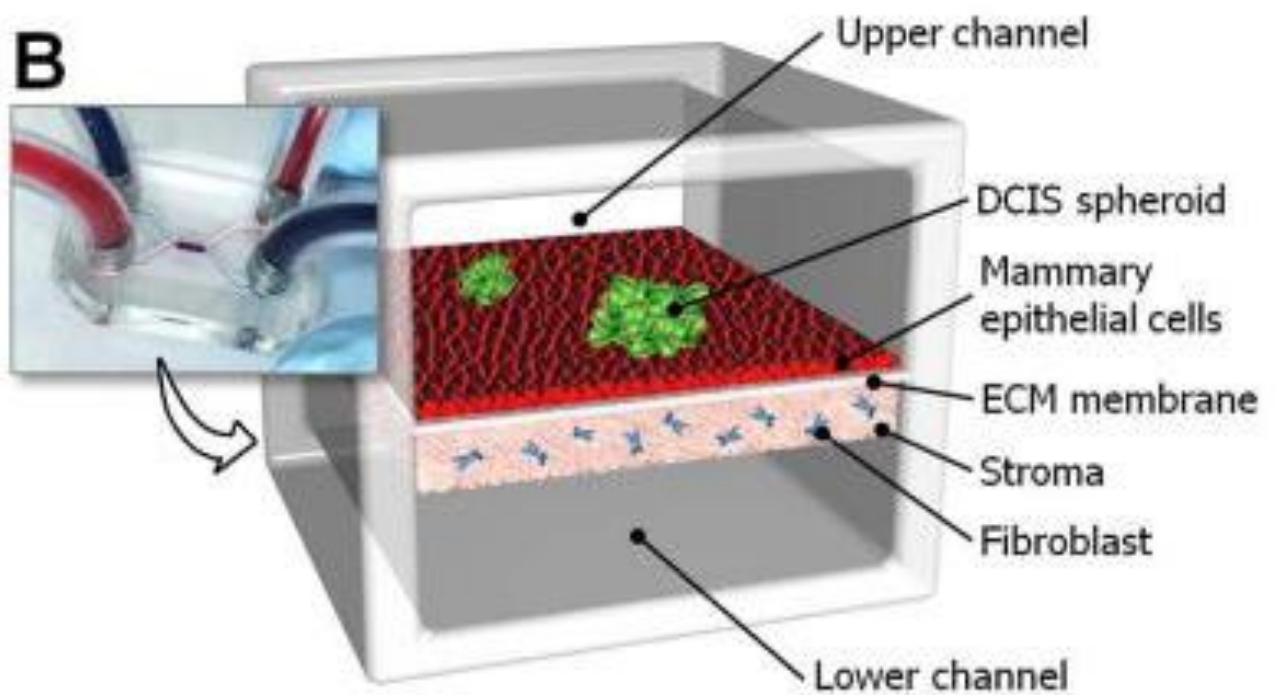
Figure 1.4: Microfluidic device for mimicking early stage breast cancer taken from(Choi et

al., 2015)

A microfluidic device used to mimic early stage breast cancer, as used by Choi et al. The device is comprised of upper and lower cell chambers separated by an ECM membrane. The group used MCF10, mammary fibroblasts and HMT-3522 cells to form spheroids in a ULA plate, before introducing them into a Matrigel and fibronectin coated PDMS multilayered microfluidic device after 3 days.

markers including *Snail* was upregulated, whilst endothelial marker proteins, including VE-cadherin, was downregulated. They stated that for the first time, it was demonstrated that breast cancer spheroids are dependent on shear stress. Moreover, Zhang reported a PDMS microfluidic device to separate and enrich a mix of MDA-MB-436 and MCF7 cells, and a SUM149 population by mechanical manipulation and micro barriers. The authors trapped the cells on chip (named m chip) and forced them to separate, concluding that SUM149 cells showed increased motility, expression relevant genes to demonstrate this (Zhang *et al*., 2012).

1.4.6   Stromal interactions

Peela *et al* developed a PDMS oxygen plasma and poly-d-lysine treated microfluidic device, to investigate the effects of suberoylanilide hydroxamic acid on breast cancer cells interactions with stroma. Using SUM-159 and CAF cells with a Matrigel, type I collagen mix this was achieved. This group looked at the drug diffusion patterns through COMSOL modelling and also real time imaging of single cell migration through the chip, concluding that cells migrated slower in the presence of SAHA (Peela *et al*., 2017).

1.4.7   Local invasion, intravasation and circulating tumour cells

Toh *et al* developed a PDMS based microfluidic device to try and mirror cancer cell migration and invasion on a basement membrane (Toh *et al*., 2018). They engineered a 3D culture using MX-1 cells, including collagen as a basement membrane, which were shown to be highly metastatic in comparison to MCF7 cells (Toh *et al*., 2018). Toh showed that MX-1 cells could invade through collagen over a 45 h period, having a migratory velocity of 6.6 and 13.5 μm/h. Like Toh, Nagaraju and colleagues were interested in looking at early stage metastasis, specifically breast cancer cell invasion and intravasation. A three layered PDMS culture device, treated with Poly-D-lysine, was used to create vasculature (Nagaraju *et al*., 2018). HUVECs, triple negative MDA-MB-231 and ER/PR$^+$ MCF7 cells were transfected and used coupled with

collagen and fibrin. They concluded that MDA-MB-231 invasion was enhanced in vasculature (Nagaraju *et al*., 2018).

A further example of spheroid on chip for metastatic research was conducted by Soldati *et al*. Soldati *et al* looked at microfluidic device to investigate metastasis, through the use of liquid biopsy to detect circulating tumour cells present within a sample (Soldati *et al*., 2018). They showed that the device would allow a 90.2% accuracy when classifying acid droplets from both healthy and cancer patients. Furthermore, they also demonstrated that white blood cell expression of CD45 could be predicted at 82.9%. A further example of circulating tumour cells and metastatic research was conducted by Bersini. Bersini *et al* used a PDMS microfluidic device bonded to glass coverslip, treated with oxygen plasma to look at cellular spread. The authors developed a bone mimicking environment and vascular bed within the device to investigate CTC endothelium and secondary site interactions, as well as tropisms with triple negative MDA-MB-231 cells to investigate extravasation (Bersini *et al*., 2018). The study further focussed on MMP and ADAM expression through microarrays and ventured to the invasion of T24 and OVCAR-3 cell lines, concluding that T24 possess the most migratory potential and OVCAR-3 the lowest (Bersini *et al*., 2018). Moreover, Obermayr and colleagues aimed to identify circulating tumour cells from primary tumours within patient blood samples using the microfluidic Parsortix cell separation system (Miller *et al*., 2018). RT-PCR was used to investigate gene markers from enriched blood samples from gynaecological cancer patients and metastatic breast cancer patients, moreover they used ovarian cancer cell lines- TOV21G and CaOV3 as an alternative comparison (Obermayr *et al*., 2017).

1.4.8   Cancer and immune interaction/evasion

Ayuso *et al* were interested in a PDMS device design treated with oxygen plasma and bound to glass to investigate MCF7 spheroids interactions with NK cells within a collagen hydrogel. They focussed the research on the immune response of NK cells and their abilities to target

cancer spheroids (Ayuso *et al*., 2019). Ayuso showed that antibodies perfused in the lateral lumens, rapidly diffused through the ECM matrix, whilst tumour cell junctions lowered this penetration into the spheroid. They also demonstrated that NK cells were able to penetrate the spheroids faster and deeper than antibodies. By combining these therapies, cytotoxicity was increased, but NK cells were mostly located at the spheroid edge.

1.4.9   Cancer cell clusters in circulation and identification

Babahosseini and colleagues created a microfluidic device for the identification of single metastatic cells from a sample. A PDMS and glass microfluidic chip was developed for this purpose featuring constrictions, deformation and relaxation zones, to focus on 184A1, MCF10, MDA-MB-231 and MDA-MB-468 cells (Babahosseini *et al*., 2017), shown in Figure 1.5. The study concluded that metastatic cell resistance decreased in comparison to non-metastatic increased, after each relaxation period (Babahosseini *et al*., 2017).

1.4.10 Cancer tropisms and migration patterns

Hao *et al* were interested in researching the metastasis of breast cancer cells to bone. The authors created a 3D bone-on-chip microfluidic device to investigate this due to the frequency of bone metastasis from breast cancer (70%) (Hao *et al*., 2018). In the study, a PDMS microfluidic device with a glass coverslip to grow MC3T3-E1 cells on was constructed, coupled with MDA-MB-231 and MDA-MB-231 BRMS cells (Hao *et al*., 2018). Moreover, a 3D mineralised bone tissue was formed over 720 h on chip, co-cultured with the cells mentioned (Hao *et al*., 2018). Hao was able to form an 85 μm mature osteoblastic tissue on-chip, in the absence of differential agents. They also detailed that breast cancer cell interactions seen in the *in vivo* environment was also demonstrated on-chip. Another example of migration to specific locations on-chip was conducted by Sleeboom. In order to investigate oxygen
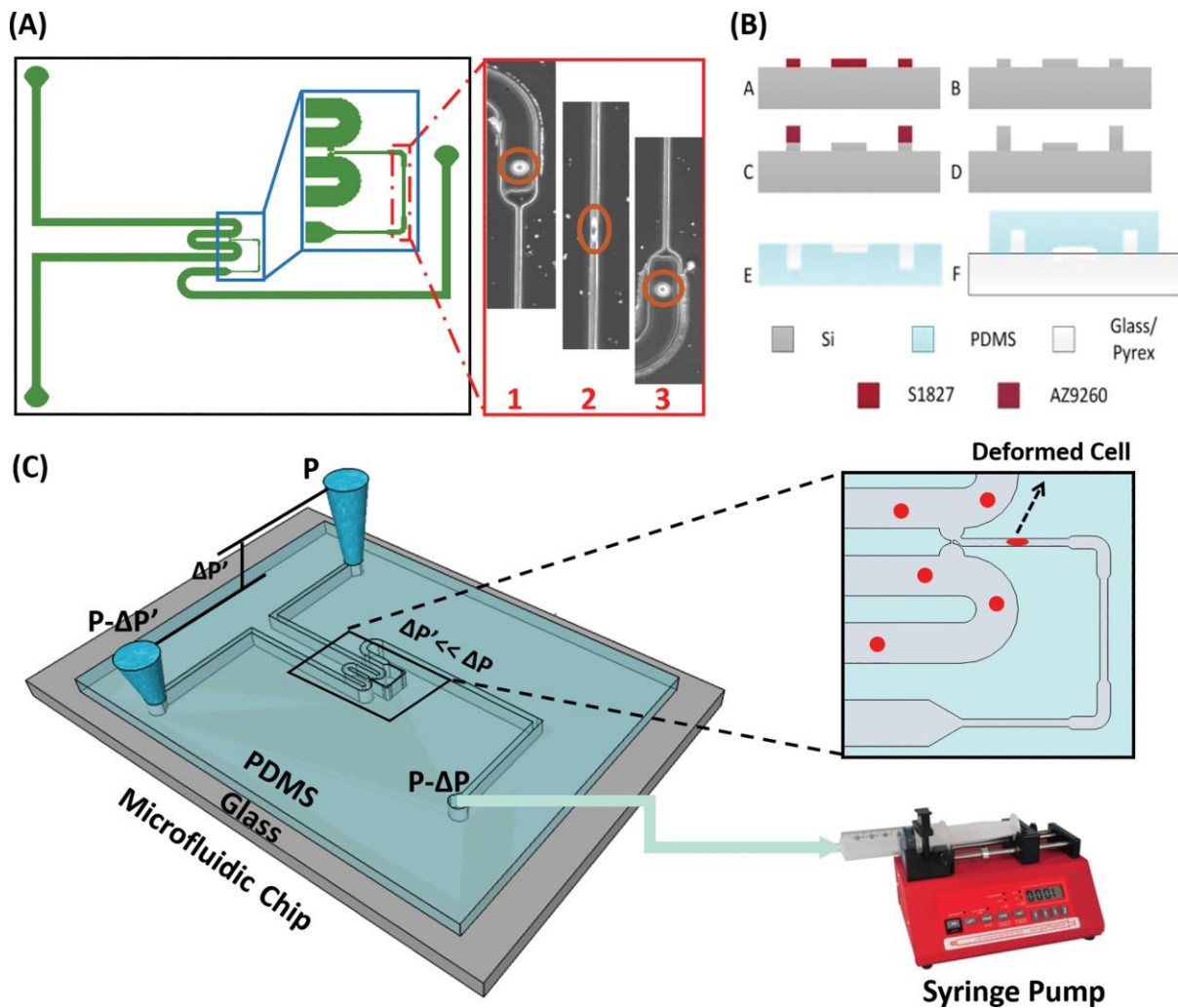
Figure 1.5: Microfluidic device for breast cancer migration taken from *(Babahosseini et al.,*

2017)

A PDMS and glass microfluidic chip was developed for this purpose featuring constrictions, deformation and relaxation zones a), to focus on 184A1, MCF10, MDA-MB-231 and MDA-MB-468 cells. b) shows a cross section of the chip, demonstrating which materials are in which locations, whilst c) details a drawing of the microfluidic device connected to a syringe pump, focussing on the constrictions, deformation and relaxation zones present.

gradients on migratory behaviour of breast cancer cells and breast cancer stem cells, namely MDA-MB-231 and stem cells derived from these, Sleeboom *et al* constructed a PDMS and a PMMA microfluidic device. (Sleeboom *et al*., 2018). The device contained a chamber that could simulate the 1.3% oxygen seen in cancerous breast tissue and 6.8% seen in healthy breast tissue. The PMMA component of the device acted as an oxygen diffusion barrier. Moreover, the group simulated the oxygen gradient and diffusion using COMSOL (Sleeboom *et al*., 2018). They tracker CSCs from MDA-MB-231 cells, between 17.5 and 24 h post adhesion. Showing that the migration patterns correlate to those of 'normal' MDA-MB-231 cells. They did show that cells migrate to lower oxygen levels, however.

1.4.11 Opportunity within the literature

There is a clear gap in the research which this project aims to fill. The current gap in the research is a lack of understanding and knowledge regarding the early stages of the metastatic cascade and how external factors such as shear stress, the tumour microenvironment and continuous perfusion contribute to cancer spread *in vitro*. This research aims to use a glass microfluidic device to replicate *in vivo* conditions within an *in vitro* environment. The device will be used to look at both brain and breast cancer spheroids to investigate the early metastatic spread of tumours.

1.5 Context and Significance of this study

Traditional *in vitro* models used for studying cell migration are unable generate real time monitoring of cancer, therefore lack information on migration and invasion. They do not allow precise manipulation and control over the local environment. *In vivo* and *ex vivo* models have been developed to try and overcome these issues. But these models are difficult to reproduce/perform, with large ethical constraints. Furthermore, these models are within a different environment to the primary tumour (such as being a human tumour in a mouse). *In*

vitro 3D models, such as spheroids, have been designed to attempt to overcome some of these issues. Spheroids mirror the cell-cell interactions, nutrient gradients, drug resistance and microenvironments seen *in vivo*. They are highly controllable and reproducible, allow co-culturing, giving rise to heterogeneous populations, like those seen *in vivo*. They potentially bridge the gap between *in vitro* and *in vivo* but are still limited by some issues. Spheroids in trans-well plates are unable to replicate interstitial flow, shear stress and perfusion culture. Therefore, a highly controllable, more replicative *in vitro* cancer model to investigate cell migration and invasion, is needed. Microfluidic devices fit this premise, as they are fast, sensitive, cheap, portable, highly controllable, and reproducible models. Microfluidic models allow real-time monitoring of factors within the device; they offer highly controllable gradients of chemicals and nutrients, all whilst using small quantities of reagents and biological material, such as cells. Microfluidic devices have been coupled with spheroids as shown, allowing precise manipulation of the external environment around the spheroids.

The majority of work conducted on spheroids within a microfluidic device had focussed on generation of spheroids within the device (West, 1989; Hardelauf *et al*., 2011; Kim *et al*., 2012; Das *et al*., 2013; Kuo *et al*., 2014; Bender *et al*., 2016; Ip *et al*., 2016; Marimuthu *et al*., 2018; Zhang *et al*., 2018; Shang *et al*., 2019), across a variety of cell lines. These examples then used the spheroids to test drug responses *in vitro*. However, much like the work conducted by Kim *et al*, the spheroids ranged from a small size (58 µm – 400 µm). The size of these spheroids was too small to contain substantial hypoxic and necrotic regions, which is seen *in vivo* (Mehta *et al*., 2012). To generate larger spheroids, giving rise to hypoxic and anoxic regions, necrosis and larger chemical gradients, other groups generated spheroids out of the device before placing them within (Kuo *et al*., 2014; Kwapiszewska *et al*., 2014; Chen *et al*., 2015). These groups again placed the spheroids into microfluidic devices but used them to test common chemotherapeutic drug efficacy on the culture (Das *et*

al., 2013; Ruppen *et al*., 2014; Kwapiszewska *et al*., 2014; Chen *et al*., 2015; Choi *et al*., 2015; Sabhachandani *et al*., 2019). To determine and assess the viability of spheroids within culture the groups used different methods, including: manual counting through spheroid dissociation and manual counting using trypan blue, fluorescent labelling of cells, LDH assays and, company bought viability assays (Choi *et al*., 2015; Kwak *et al*., 2018; Lee & Cha, 2018;Rogers, 2018; Chen *et al*., 2019). Many authors noted that viability was increased on-chip in comparison to off-chip counterparts, for periods of 3-14 days (Acosta *et al*., 2014; Kwak *et al*., 2018; Michael *et al*., 2018; Chen *et al*., 2019). Some stating that viability of over 90% for one week was shown on-chip (Mi, 2016; Imaninezhad *et al*., 2019)

1.6   Aims and objectives of this study

A novel approach will be adopted to investigate cancer cell migration and invasion spheroids within a microfluidic device as an improved *in vitro* model of metastasis. By combining spheroids with a microfluidic device, the real time invasive and migratory capabilities of tumours will be able to be investigated. This novel approach will thus allow the factors associated with tumour spread and cell migration, such interstitial flow, shear stress and the tumour microenvironment to be precisely controlled and manipulated, giving key insight to the process of metastasis. The new model using spheroids within a microfluidic device will therefore be optimised to allow the investigation of tumour spread and ultimately metastasis to be conducted.

This study has an overarching hypothesis. It **hypothesises** that is possible to mirror the early stages of metastasis in a microfluidic device. It will be possible to recreate and drive EMT and invasion of cells in spheroids within a microfluidic device.

The overarching **aim** of this study is to design and optimise a microfluidic device capable of harbouring a characterised cancer spheroid, in order to mirror characteristics that are linked to

metastatic potential and spread, in a spheroid-on-a-chip platform. The investigation of metastatic biomarkers released from the primary spheroid mass will be identified.

The specific hypotheses and aims of this research study are to:

Hypothesis 1: It is possible to generate reproducible and reliable cancer spheroid *in vitro*. The spheroids will follow literature convention.

1. **Aim: To generate and characterise the best cancer spheroids to incorporate in a microfluidic device**

   - *Generate a panel of spheroids to investigate growth kinetics*

   - *Characterise spheroid size profiles*

   - *Characterise spheroid regions*

   - *Assess if there are any morphological and phenotypical differences between spheroid seeded at different sizes*

Hypothesis 2: It is possible to design and fabricate a microfluidic device that will harbour a cancer spheroid. The tightly bound spheroids will be placed within and its viability will be comparable to current off-chip work.

2. **Aim: To design and validate a microfluidic device for spheroid incorporation and maintenance**

   - *Design and fabricate a microfluidic device*

   - *Incorporate a spheroid into a microfluidic device and assess spheroid viability*

   - *Investigate for the presence of components of migration*

Hypothesis 3: The spheroids within the device will show an increased migratory and invasive capability than monolayer and off-chip models.

3. **Aim: To improve the microfluidic device design for analysis of pro-metastatic phenotypes in spheroids**

- *Advance design to allow easier access to microwell*

- *Advance design to image spheroids directly on-chip*

- *Incorporate hydrogel(s) into microfluidic device and embed spheroids*

- *Investigation of potential secreted biomarkers of cell migration/invasion, such as VEGF or IL-6*

- *Evaluate cell migration patterns of spheroids on-chip*

Chapter 2   Methodology

2.0   Methodologies

2.1   General methods

2.1.1   General Reagents and consumables

General chemicals used in this study were purchased from Sigma (Gillingham, UK), VWR (Lutterworth, UK), or Fisher Scientific (Loughborough, UK), unless otherwise noted. General plastics used in this study were purchased from VWR (Lutterworth, UK), Fisher Scientific (Loughborough, UK), or Starlab (Milton Keynes, UK), unless otherwise noted. Tissue culture specific plastics were purchased from VWR (Lutterworth, UK), Fisher Scientific (Loughborough, UK), BD Bioscience (Oxford, UK) or Starlab (Milton Keynes, UK), unless otherwise noted.

2.2   Cell culture

2.2.1   Tissue Culture

Five cell lines were initially used for testing in this study: U-87 MG (glioblastoma), HCT116 and HT29 (colorectal cancer), and MCF7 and MDA-MB-231 (breast cancer). This number was decreased to three however as the research progressed. The three used throughout were U-87 MG; a robust spheroid model, used as a control throughout this research, whilst breast cell lines (MCF7 and MDA-MB-231) were used to test differences between epithelial and mesenchymal like cell spheroids. The cell lines were obtained from obtained from ATCC (Teddington, UK) and EACC (Salisbury, UK) as indicated in Table 2.1. The cells were cultured in high glucose complete Dulbecco's Modified Eagle Medium (DMEM) (Corning, Amsterdam, Netherlands), supplemented with 10% foetal bovine serum (FBS) (Gibco, Life Technologies, Loughborough, UK), 1% Sodium pyruvate from lab stock (PAA) (GE Healthcare Life Science, Buckinghamshire, UK) and 1% Penicillin / Streptomycin from lab stock (Lonza, Castleford, UK) in an incubator (Nuaire, UK) at 37°C, with a humidified atmosphere with 5% CO_2. Cells were passaged at specific rations (1:4 – 1:12) depending on the cell line in order to maintain exponential growth upon reaching 65-80% confluency. Spent medium was removed from the

cells before being washed with 1x Phosphate-Buffered Saline (PBS) without calcium and magnesium (GE Healthcare Life Science). 1x Trypsin (Lonza) was then added to the cells and these were incubated at 37°C and 5% CO_2, reflecting conditions found in mammalian tissue. Detached cells were re-suspended in fresh DMEM before a volume of cell suspension (a fraction of the original amount) was transferred into a fresh culture flask with fresh media. Cells were regularly tested negative for mycoplasma infection.

Table 2.1 – Characteristics of the cell lines used in this study (information from ATCC/ECACC)

Cell line	MDA-MB-231	MCF7	U-87 MG	HT29	HCT116
Disease	Adeno-carcinoma (metastatic)	Adeno-carcinoma (metastatic)	Glioblastoma; Astrocytoma (primary)	Colorectal adenocarcinoma (primary)	Colorectal Carcinoma (primary)
Origin	Pleural effusion	Pleural effusion	Brain	Colon	Colon
Classification	Basal	Luminal A	IV	Unknown	unknown
Age (years)	51	69	44	44	unknown
Ethnicity	Caucasian	Caucasian	Caucasian	Caucasian	unknown
Sex	Female	Female	Male	Female	Male
	ATCC	ATCC	ATCC	ECACC	ECACC

2.2.2 Freezing and thawing of cells

Cell stocks were frozen at early passage and stored in liquid nitrogen. At 65-80% confluency the cells were trypsinised as detailed in section 2.2.1, before being re-suspended in the relevant media and centrifuged at 338 x *g*. The cell pellet was re-suspended in 1x PBS, centrifuged and re-suspended in freezing media, which comprised of 10% dimethyl sulfoxide (DMSO) and 90% FBS (Gibco). The cell suspension was aliquoted into cryovials (Nunc, ThermoFischer Scientific, Loughborough, UK) and placed into a Mr Frosty freezing container (ThermoFischer

Scientific), which was placed at -80°C for gradual cooling of the cells. After 24 h, cells were transferred into liquid nitrogen (-120°C) for long-term storage. When cells were thawed, the cryovial was brought to room temperature quickly and the cells were transferred into pre-warmed complete media, containing FBS, L-glutamine and sodium pyruvate. This suspension was centrifuged, and the supernatant discarded to remove DMSO. The cell pellet was gently re-suspended in fresh media and transferred into a T25 flask before being transferred into a T75 flask when 65-80% confluency was reached. Once in a T75 flask the cells were grown as detailed in section 2.2.

2.2.3 Exposure to Hypoxic conditions

Incubation of cells in low oxygen (hypoxic) conditions was performed using a H35 Hypoxystation hypoxia chamber (Don Whitley Scientific, UK). Oxygen concentrations were set to 2% prior to experimentation, with humidity (75%), CO_2 (5%) and temperature (37°C) set and monitored throughout. Normoxic controls were kept at 80% humidity at 21% oxygen, 5% CO_2 and 37°C.

2.2.4 Drug treatment of cells

Gemcitabine (Sigma, UK) stock solutions (100 mM) were prepared in sterile dH_2O and stored at -20°C. Immediately before treatment, gemcitabine stock solution was diluted to 100 nM in fresh DMEM, and gemcitabine-containing media was used to treat spheroids or cell monolayers for the timings noted for specific experiments. Untreated controls corresponded to cells incubated with complete DMEM added to the wells

2.3 Spheroid Biology

2.3.1 Spheroid formation

Cells were seeded in ultralow adherence (ULA), round bottom, 96-well plates at different cell densities (typically 2.5×10^4 or 3.5×10^4 cells per well) (Costar, Sigma-Aldrich, UK) following the established protocol by Vinci *et al.* (Vinci *et al*., 2013). Once the cell suspension

was pipetted into the micro-wells, the plate was transferred to a 37°C, 5% CO_2 incubator and left undisturbed for 96 h, allowing the cells to aggregate into spheroids.

2.3.2 Measurement of spheroid diameter

Spheroids were imaged using a GelCount instrument (Oxford Optronix, Oxford, UK). Spheroid diameter was determined from the obtained images, using ImageJ analysis software (National Institute of Health, Maryland, USA). The software's 'measurement tool' was employed to determine the longest and shortest diameter across the spheroid (Figure 2.1). The average of these two values was taken to determine the overall average spheroid diameter.

2.3.3 Measurement of spheroid growth curve

U-87 MG and MCF7 (3.5×10^4 cells per well) spheroid growth analysis was performed over a period of 18 days. The ULA plate, with the cell suspension, was incubated at 5% CO_2 and 37°C and left undisturbed for 48 h. After 48 h, and subsequently every 24 h for 18 days, the plate was imaged on a GelCount imager. Spheroid average diameter (largest and shortest diameters divided by two) were analysed using ImageJ software in the same manner depicted in Figure 2.1. Spheroid media was refreshed every 24-48 h using fresh complete DMEM, in order to maintain nutrient levels, present in the micro-well.

2.3.4 Determination of distinct visible spheroid zones

Spheroids contain three distinct zones; a central necrotic core, a layer of quiescent cells and a viable rim of cells at the outer spheroid edge. The cell populations within the spheroid affects the cellular interactions present, and further indicates the length of time the spheroid is viable for testing (Vaithilingam *et al*., 1991). A semi-quantitative approach was adapted from a protocol developed by Monazzam and colleagues (2005) to investigate how the core and viable rim of cells present in a spheroid changes over a period of time (Monazzam A *et al*., 2005). U-87 MG and MCF7 spheroids (seeded at 3.5×10^4 cells per well) were left undisturbed overnight. At 48 h, and subsequently every 24 h, the spheroids were imaged under bright-field settings on
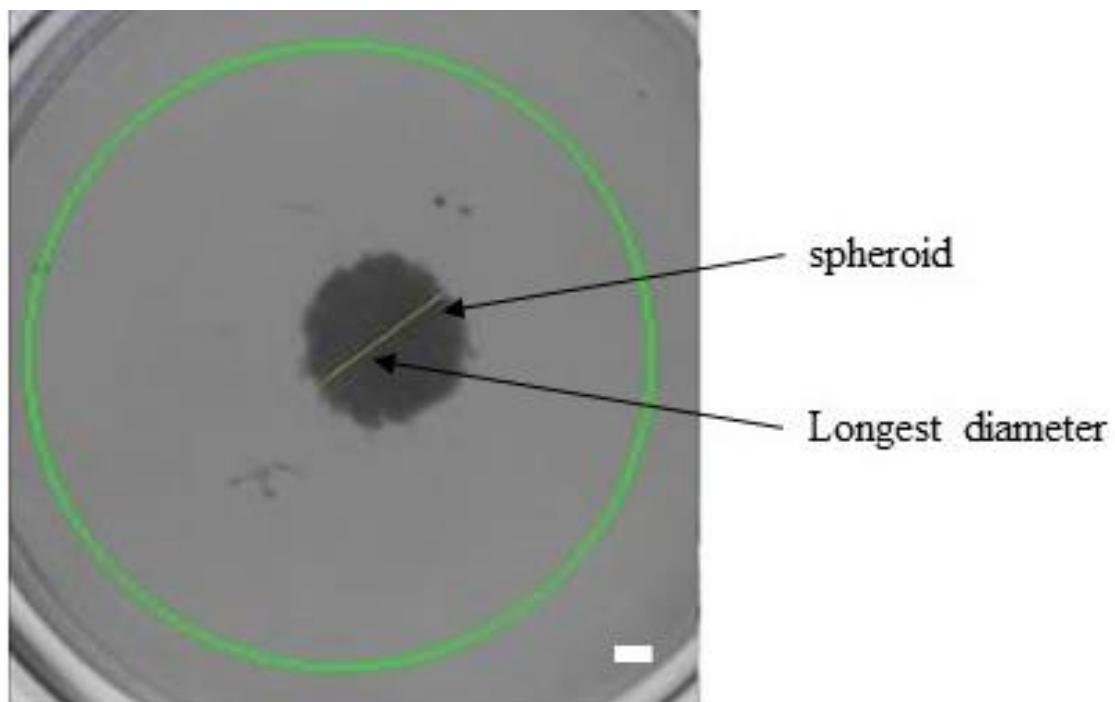
Figure 2.1: Spheroid size measurement from Gelcount panel image using ImageJ analysis software.

ImageJ toolbar with 'measurement tool' was selected to analyse the example image of a Gelcount Image; with an MDA-MB-231 spheroid seeded with 5 x 10^4 cells per well. The scale was internally set against the scale measure on the Gelcount – 1 pixel unit =42.3 μm. Two measurements of diameter were taken. The longest and shortest. The yellow line indicates the longest diameter taken. The diameters were divided by two to generate an average. Scale = 200 μm.

a Zeiss inverted microscope (Zeiss, Germany) at 5x magnification. Figure 2.2 shows an example image, where two distinct zones can be seen and classified; either as a viable rim of cells or a core (including quiescent cells), this was repeated for each spheroid of the same size to generate an average spheroid size. ImageJ software was used to measure the spheroid core and the total spheroid area, using the 'polygon' selection tool (Figure 2.2). ImageJ was also used to determine the dimensions of the total spheroid and cellular rim areas. The dimensions of the core were determined as a percentage of the total spheroid area.

2.3.5 Migration and Invasion assays

To determine the invasive and migratory capabilities of cells in spheroids, migration and invasion assays were performed (Vinci *et al*, 2013). Spheroids were formed as detailed in section 2.3.1. 50 µl of hydrogel (shown in table 2.2) were transferred to a flat bottom or ULA 96 well plate and left for the determined period in Table 2.2. Flat bottom plates were used for investigations into cell migration, whilst the ULA plates were used for investigations into invasion. The spheroids were pipetted in 200 µl DMEM onto the surface of the hydrogel and left for 20 min to adhere. Spheroids were then immediately imaged at t = 0 min and subsequently every 24 h for 72 h on a brightfield microscope (Zeiss) to determine the levels of cellular spread from the original spheroid mass over time.

Table 2.2: Hydrogel dilution, temperature and time taken to set.

Matrices	Concentration	Temperature	Time
Gelatin	2% v/v (dH$_2$O)	4°C	45 min – 1h
Fibronectin	1 µg/ml	37°C	1 h – 2h
Collagen	3 mg/ml	Room temperature	1 h
Matrigel	10 mg/ml	On Ice/Set at room temp	15 min
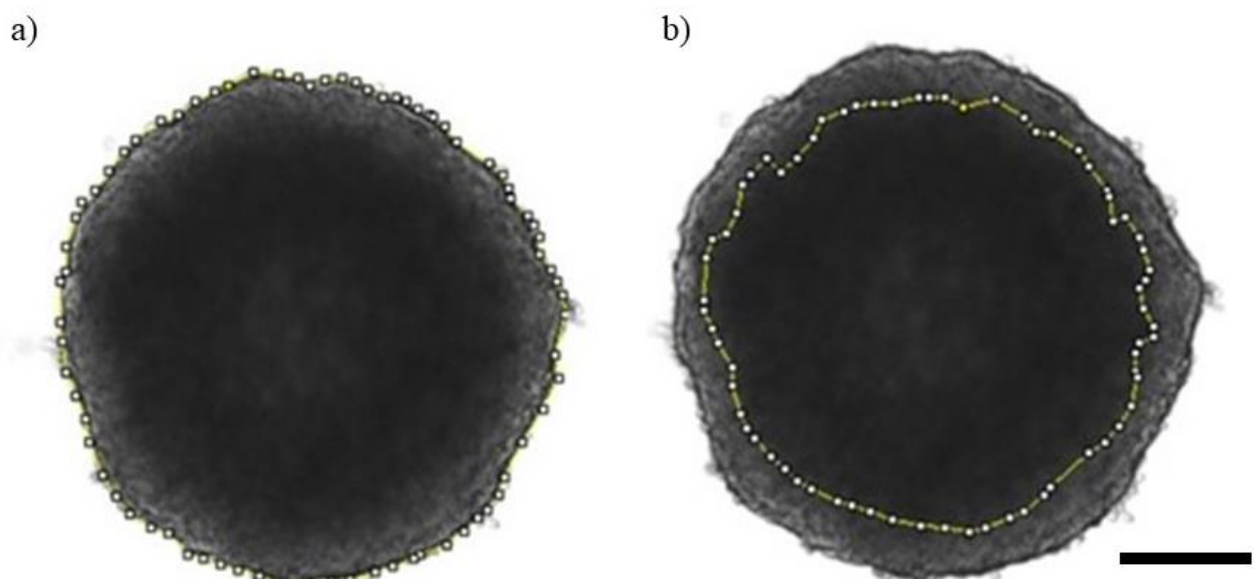
Figure 2.2: Spheroid core and viable rim measurement using ImageJ analysis software.

Figure 2.2 shows a spheroid where two distinct zones can be seen; a viable rim of cells or a core (including quiescent cells). The polygon selection tool was used in ImageJ software to closely measure around the spheroid edge. Similarly, the polygon selection tool was also used to draw around the core and the quiescent cells, in which the darker areas present was determined to be core/quiescent cells. a) Example of a MCF7 (3.5×10^4 cells per well) spheroid image (5x magnification) with the total spheroid area mapped b) An example of the core mapped (yellow line indicates the area border of the core and quiescent cells).Repeats of this measure were conducted multiple times. Scale = 200 μm

2.4 Cell viability Assays

2.4.1 CytoTox Glo Assay

The Cyto-Tox Glo cytotoxicity assay (Promega, G9290) measures the extracellular activity of an intracellular protease (dead-cell protease), which is released by cells with compromised cellular membranes. This is achieved through the addition of a luminogenic cell-impermeant peptide substrate (AAF-amino luciferin). When cells undergo cytotoxic stress, they release the intracellular protease, which cleaves the added AAF-substrate, resulting in luminescence. The luminescence directly correlates to the percentage of cells undergoing cytotoxic stress as the AAF-substrate cannot pass through the intact membrane of live cells, resulting in no appreciable signal. Media was collected from each sample (spheroids in ULA plate and monolayers), by pipetting the media from the 96 ULA plate into an Eppendorf, whilst the media was collected from the collecting vessel used in the microfluidic device (spheroids within a device) through pipetting. Once all media was collected from cells and spheroid-based experiments, it was stored at 4°C (for fresh analysis) or-80°C (for frozen analysis). Media samples were transferred to a white 96 well plate (Nunclon) in triplicate per sample. The CytoTox-Glo protocol was followed (as per manufacturer's instructions); in brief the media samples were collected from the testing conditions and added to a 96 well plate. The assay buffer and the AAF-substrate were mixed and added to the media samples. The plate was measured in two luminescence plate readers (due to access restrictions): Fluoroskan (ThermoFischer Scientific) or Tecan (BMG, Florida, USA), after 15 min of incubation. A second addition stage was conducted on controls allowing for the indirect determination, which used digitonin (20 mg mL^{-1}) as a lysis buffer, which lysed the entire cell population, before the plates were read again. This would give an indication of how much luminescence would be present when the entire cell population was lysed. The luminescence value determined the value of protease present within the conditioned media, suggesting the level of dead cells present across the three conditions.

Cellular viability (CV) of controls was determined by subtracting the initial luminescence measurement (ILM) from the final luminescent measurement (FLM) (equation 1).

$$CV = FLM - ILM \qquad\qquad \textbf{equation 1}$$

2.4.2 Fluorescein diacetate (FDA) and Propidium iodide (PI) live dead assay

Spheroid cell viability *in situ* was assessed using the fluorescent-based FDA-PI live-dead assay (Jones and Senft, 1985). FDA (ThermoFischer Scientific) stains viable cells, through a process where the FDA is converted into a green fluorescent metabolite, fluorescein. Cell viability is indicated through the intensity of the green fluorescent signal produced, as the conversion of FDA to fluorescein is esterase dependent. PI (ThermoFischer Scientific) stains the nucleic acids of dead cells after passing through the disordered cellular membrane, resulting in these cells having red florescence , it is not possible for PI to stain live cells as the PI is unable to penetrate membrane of live cells (Boyd , Cholewa and Papas 2008). Spheroid media for specific samples was carefully pipetted and discarded, before the spheroids were washed in 1X PBS, in order to remove all traces of media. Spheroids were stained using an FDA (5 mg mL^{-1}) – PI (2 mg mL^{-1}) solution in phenol red free Roswell Park Memorial institute (RPMI) media.

PBS was removed and then the FDA/PI staining solution was added to the wells. The plate was incubated in the dark for 5 min and the solution removed, the spheroids were washed in PBS three times. PBS was further added to the wells and the spheroids imaged. Spheroid images were acquired using an epifluorescence microscope (Zeiss, Germany) with pre-set filters for Texas Red for PI (excitation 596 nm/emission 614 nm) and Fluorescein isothiocyanate for fluorescein (excitation 495 nm/emission 517 nm).

2.4.3 Fluorescence Quantification

ImageJ analysis software was used to quantify the fluorescence signal produced from both the PI and FDA separately for each image, using an adapted method from Burgess (2010) and McCloy (2014). Original greyscale spheroid images were opened in ImageJ software (Figure 2.3). The '*area', 'integrated density'* and '*mean grey value'* options were selected in the 'analyse' tool bar menu. The '*polygon*' tool was selected to draw around the spheroid or region of interest (ROI). ImageJ was then used to automatically measure the parameters pre-set earlier. A background signal measurement (away from the ROI) at the same size as the ROI was taken. Where the background size could not be taken at the same size of the ROI, a sample without interference was taken and the value divided by the area taken, before being multiplied by the total area of the region of interest. To give a more reliable result, the fluorescence intensity was calculated per unit area. The equation used to generate corrected total spheroid fluorescence (CTSF) was as follows:

$$Corrected\ total\ spheroid\ fluorescent\ (CTSF) =$$

$$Integrated\ density - area\ of\ spheroid\ ROI\ background\ fluorescence$$

(equation 2)

2.5 Biochemical Assays

2.5.1 Cell lysis and protein extraction

Protein extraction was performed on both spheroids and cell monolayers. For cell monolayers, cells were seeded in tissue culture dishes (Nunc, Thermo Scientific), before being incubated in their corresponding experimental conditions. Media was then removed, and cells washed in 1X PBS. Cells were scraped into 1X PBS using a cell scraper (Starstedt, UK), before being
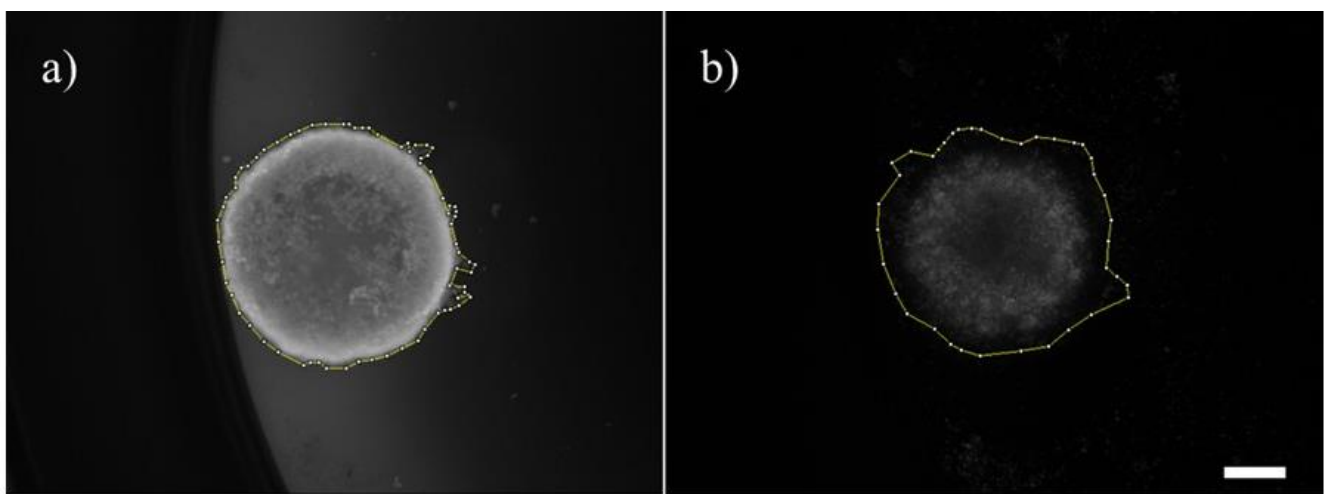
Figure 2.3:   Method used to quantify FDA-PI fluorescence in spheroids

FDA/PI quantification of grey scale images was performed using ImageJ. The measurement settings were area, mean gray values and integrated density selected (ImageJ →Analyse → Set measurements). a) Example of a spheroid original image (FDA image), with the ROI drawn around the spheroid b) Example of ROI on PI spheroid. The Measurement output from Image J using IntDen values were used for the spheroid fluorescence signal and background signal. Equation 2 was used to give final CTSF values. Scale = 200 μm.

centrifuged at 20,000 x g. Supernatant was removed, and the pellet was resuspended in an appropriate volume of UTB lysis buffer (9 M Urea; 75 mM Tris-HCl pH 7.5; 0.15 M β-mercaptoethanol). The lysate was either frozen at -20°C for temporary storage, of processed further. For this, lysates were sonicated in a Bioruptor (Diagenode, Belgium) for 5 min with 30 s intervals on the high setting. Samples were transferred and centrifuged at 20,000 x g at 4°C for 15 min, with the supernatant being transferred to new microcentrifuge tubes and stored for quantification. For spheroids, the spheroids were collected into microcentrifuge tubes, washed in 1x PBS and resuspended in UTB. The same process of sonication and centrifugation was then conducted.

2.5.2   Protein quantification and sample preparation

Clarified lysates were quantified using a Nanodrop Light Spectrophotometer (Thermo Scientific), using the protein absorbance (A280) 1 mg mL^{-1} setting. The samples were diluted using UTB lysis buffer to match protein sample concentrations and volume across each testing condition in order to each sample to have 30 ug protein. Sample buffer (3.3% SDS, 6 M Urea, 17 mM Tris-HCl pH 7.5, 0.01% bromophenol blue, 0.07 M β-mercaptoethanol) was added per sample, before being heated at 95 °C for 5 min in a heating block.

2.5.3   Sodium dodecylsulfate polyacrylamide gel electrophoresis (SDS PAGE)

Protein samples were separated using SDS PAGE, prior to western blot analysis using a 10% acrylamide gel (See recipes in Table 2.3) (1.5M Tris-HCl pH 6.8, 30% v/v acrylamide/0.8% bis-acrylamide, 10% w/v SDS, 10% v/v TEMED and 10% w/v APS in the appropriate volumes). A cassette containing the gels was assembled and filled with 1x running buffer (Recipe in Table 2.3), and samples were loaded, alongside a pre-stained colorimetric molecular ladder (Geneflow, UK). Electrophoresis was performed for 60-120 min at 100-120 V, until the

sample migration front reached the base of the gel (1 cm away from base) and the electrophoresis was stopped.

2.5.4   Western blot

A polyvinylidene difluoride (PVDF) (GE Healthcare) membrane was cut to size and activated in 100% methanol for 10-15 s. The protein samples within the separating gel were then transferred to the PVDF membrane. For this, two sponges and blotting membranes (Millipore) were soaked in 1x blotting buffer (see recipe in Table 2.3) for 5 min, before a cassette sandwich was assembled. The cassette sandwich was placed in a tank (BioRad) and filled with 1x blotting buffer. The transfer was then conducted at 100 V for 90 min. If it was required that the PVDF membrane was tested for successful transfer prior to the next steps of western blot, then the membrane was placed in Ponceau stain (Sigma, UK) for 15 min before being washed with 5% milk TBST (10% 10X TBS (Tris-Buffered Saline) (88 g NaCl; 24 g Tris base; pH 7.4 in a final volume of 1 L MilliQ water and 0.1% Tween 20 diluted in MilliQ water)) on a plate rocker.

After transfer, the PVDF membrane was blocked for 1 h in 5 % milk in 1X TBST (See recipe in Table 2.3). The membrane was then incubated at 4°C in primary antibody (in 1% milk in 1X TBST) overnight. Antibody dilutions are available in Table 2.4. After incubation with the primary antibody, the membrane was washed in 1X TBST for 3x 10 min before being incubated at room temperature for 1 h in the appropriate HRP-conjugated polyclonal secondary antibody (Dako, Denmark) at 1:2000 dilution in 1% milk TBST. The membrane was further washed for 3x 10 min in TBST and incubated in Clarity ECL developing solution (1- luminol enhancer, 2-peroxidase solution) (BioRad) for 1 min. The membrane was imaged on a ChemiDoc XRS+ with Image Lab software (BioRad).

Table 2.3: Running and Blotting buffer composition

	Running	Blotting
Tris-base	30.20g	30.20
Glycine	144g	144g
Milli Q water	Fill to 1L	Fill to 1L
SDS	10μg	

Table 2.4: List of antibodies commonly used in western blotting

Target	Manufacturer	Origin	Dilution	Band size kDa	Clonality
α-tubulin	Abcam	Rabbit	1:4000	50	Poly
β-actin	Santa Cruz	Mouse	1:10000	42	Mono
E &N-Cadherin	Cell signalling	Rabbit	1:1000	135	Mono
GAPDH	Ambion	Mouse	1:5000	36	Mono
Vimentin	Cell signalling	Rabbit	1:1000	57	Mono

2.5.5 Coomassie blue stain

In order to stain proteins in an SDS-PAGE gel, gels were incubated with Coomassie blue stain

('*Instant Blue',* Expedeon, UK) at room temperature for 2 h, and the gels were then washed

with MilliQ water and imaged on the ChemiDoc XRS+ using the Image Lab software (BioRad).

2.5.6 VEGF and Il-6 (Vascular endothelial growth factor & interleukin 6) Enzyme linked immuno sorbent assay

A sandwich ELISA for VEGF and IL-6 (Novex, UK) was conducted to quantify secreted VEGF, as per manufacturers instruction. In brief, conditioned media samples were obtained from media incubated with 2D or 3D cell cultures, and added to the wells of the ELISA plate, and antigens present became bound to the immobilised antibody at the bottom of the plate. A secondary biotinylated antibody was added which bound to the antigen that is captured on the well surface. A streptavidin-HRP enzyme was introduced to the system which bound to the detection antibody. Finally, a provided substrate is added, which becomes cleaved by the bound enzyme resulting in a colorimetric reaction. The colour is directly proportional to the amount of VEGF present in the samples. The colour signal was measured using a spectrophotometer plate reader (BioTek ELx800) (BioTek, UK) at 450 nm. VEGF secretion levels are normalised as picogram (pg) of 3.5×10^4 cells. The secretion levels are normalised to this number as this is the number of cells present in both the spheroids and monolayers at the time of seeding. Therefore, to normalise the data to one another, allowing it to be comparable, the levels of VEGF were normalised to 3.5×10^4 cells. This was done by:

1. producing a standard curve from known concentrations.

2. Rearranging Y=MX+C to individualise X (X=(y-C)/M)

3. Input the data to find X, before identifying volume differences between conditions

4. The calculated VEGF concentration were normalised to the appropriated start volume for each sample.

5. The cell number noted for the volume collected

6. The normalised volume was divided by the number of cells present

7. Final answer produced for concentration (X) for 2.5 or 3.5 x 10^4

For a worked example, see figure 7.3 in the appendix.

2.6 Microscopy and staining

2.6.1 Spheroid fixation and embedding

Spheroids were collected after 96 h and carefully washed in 1x PBS. PBS was aspirated, before the spheroids were incubated for fixation in 10% formalin (in PBS) for a minimum of 1 h at room temperature or overnight at 4°C. Formalin was discarded, and fixed spheroids were incubated in a 30% w/v sucrose solution in 1x PBS and allowed to equilibrate at room temperature for 1-3 h, until the spheroids sank to the bottom of the microcentrifuge tube. Spheroids were then pipetted onto a cork mat in the smallest possible volume of sucrose solution. The excess sucrose solution was aspirated without disturbing the spheroids. A small volume of optimal cutting temperature compound (OCT) was added on top of the spheroids for embedding. Embedded spheroids in OCT were quickly and carefully transferred to -80°C to solidify and for storage prior to cryosectioning.

2.6.2 Spheroid Cryosectioning

Cryostat (Leica, UK) was set at -20°C (+/- 3°C). Embedded spheroids in OCT were cut into sections between 8-12 µm and sections were transferred to Polylysine adhesion slides (PLA) by rapidly inverting the slides over the samples and allowing surface tension to bind the sample to the PLA slide. The slides were then left to air dry for 20 min on a flat surface, before being stored at -20°C.

2.6.3 Haematoxylin and Eosin staining (H & E)

H&E staining is utilised in histology and pathology to differentiate cell components, resulting in the ability to visualise the overall tissue structure. Haematoxylin stains basophilic/acidic structures, such as nucleic acids, blue, whilst eosin stains acidophilic/basic structures, such as cytoplasm, red. H&E staining was used to analyse spheroid structure. Pre-prepared slides (section 2.6) were taken from the -20 $^{\circ}$C freezer and left to thaw for 20 min at room temperature. They were then cleared using 100% histoclear (National Diagnostics, UK) for 3 min. Clearing is the process of replacing the dehydrant (formaldehyde) with a miscible substance such as histoclear or xylene. The clearing agent has the same refractive index as the proteins in the sample, resulting in the tissue/sample becoming transparent. Slides were then subjected to a series of alcohol solutions of descending concentrations (100, 95, 45, 25 % v/v) for 30 s each, before being immersed in 30mL Delafield's haematoxylin solution (haematoxyline, ethanol 95% v/v, ammonium alum solution, glycerin, methyl alcohol) for 3 min. The slides were rinsed in water for 6 min, before being incubated in ascending alcohol concentrations (25, 45, 75, 95%) for 30 s each. The slides were then immersed in eosin Y solution (eosin, ethanol and glacial acid) for 10 s. Depex mounting media (>=90% Toluene, >=30-50% xylene and >=2.5%-> 10%) (Sigma, UK) was dropped onto the sample and covered with a coverslip, before being left to set prior to microscopy.

2.6.4 Preparation of cells for immunocytochemistry

Cells were pelleted at 180 x g for 5 min. Following this, they were washed in PBS before being centrifuged again, counted and resuspended at 5 x 10^6 cells per mL in 10% w/v formalin. The cells were left to fix for 20-30 min in a class 2 biosafety cabinet. The cells were then centrifuged (180 x g 5 min) and resuspended in sterile PBS. Polylysine adhesion slides (PLA, Fisher

Scientific) were cleaned with 100% methanol, before 10, 000 cells of cell solution was spotted on each PLA slide at three or more independent sites. The PLA slides were left to air dry for a period of 1-2 h, before being wrapped in saran wrap and stored at -20 °C. The PLA slides were removed from -20 °C and left to defrost for 20 min at room temperature. The saran wrap was then removed.

2.6.5 Common process for immunocytochemistry and immunohistochemistry

A hydrophobic/diamond miniature PAP pen (Fisher Scientific) was used to mark around the cells/sample to be stained. The slide was immersed into 100% ice-cold methanol in a coplin jar (Fisher Scientific) on ice for 15 min. The slides were removed and placed face up into a moisture chamber. 1X Tris-buffered saline (TBS) was used to wash the slides with the excess being carefully removed using dry tissue. Primary antibody was diluted in 1X TBS based upon values shown in Table 2.5. 0.5mg/ml primary antibody solution was added to the appropriate sample. An isotype species control was also used. The slides were incubated for 1 h in the dark at room temperature. After this, the slides were washed with 1X TBS to remove any antibody/isotype solution. An HRP-conjugated anti-species IgG antibody was added to the sample and incubated for 30 min at room temperature. The samples were washed with 1X TBS and 3,3'-diaminobenzidine (DAB) substrate detector reagent (Dako) was added to each sample. The slides were incubated for 5 min and then washed with water. 1:5 Lille's modification of haematoxylin was added to each sample as a counterstain. Excess haematoxylin was removed by washing the slides in deionised water. The slides were mounted in DPX mountant (Sigma, UK) and imaged on an Olympus colour microscope.

Table 2.5: Antibody dilutions used for immunocyte/histochemistry and immunofluorescence

Antibody	Species	Dilution
CAIX	Mouse	1:50
Ki-67	Mouse	1:100
E-cadherin	Rabbit	1:100
B-actin	Mouse	1:100
Pimonidazole	Mouse	1:100

2.6.6 Pimonidazole (PIMO) treatment and staining

To detect hypoxia presence within samples, PIMO incubation and staining was conducted. Immunofluorescence analysis was adopted to visualise PIMO staining. Briefly, pimonidazole binds to cellular thiols present in hypoxic conditions in tumours, and the remaining pimonidazole is degraded in water, shown in Figure 2.4.

For pimonidazole staining, spheroids were seeded at 2.5×10^4 cells per well in a ULA plate and left for 96 h in an incubator. At 96 h, 200 μMol of pimonidazole HCL was diluted in saline solution (0.9% w/v NaCl in dH_20). Spheroids were collected and placed in a microcentrifuge tube, spent DMEM was removed and spheroids were washed three times in 1X PBS. Spheroids were incubated with Pimonidazole diluted in saline for 90 min, before being washed three times in PBS and then incubated in 1X PBS for 30 min. Following the removal of PBS, spheroids were fixed in 10% formalin in 1X PBS for 1 h, left in 30% sucrose in deionised water for a further 30 min and then placed in OCT as described section 2.6.1. Spheroids were then cut and stained using immunofluorescence techniques as noted in section 2.6.6.
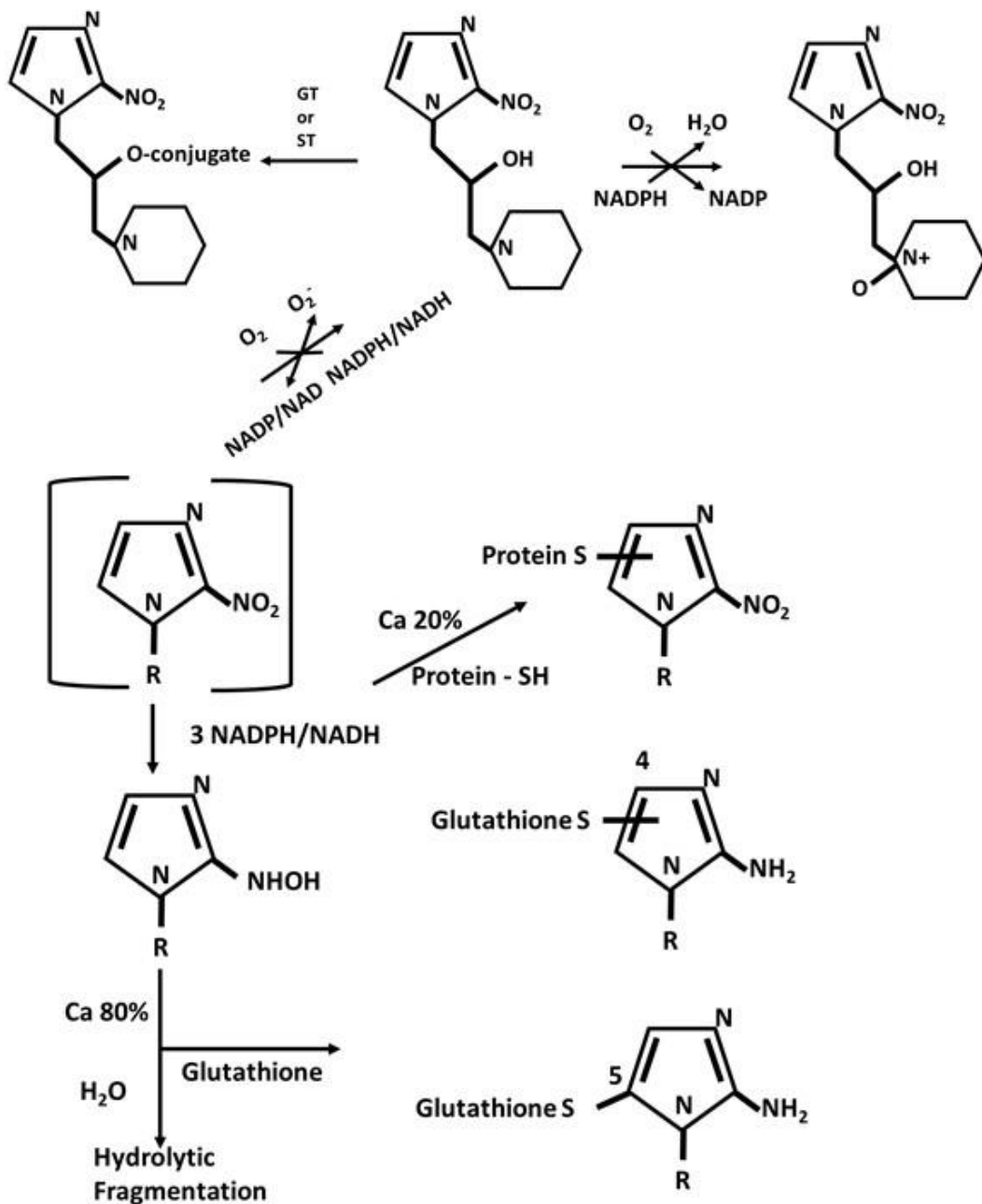
Figure 2.4: Pimonidazole mechanism of action

Pimonidazole mechanism of action for the staining of hypoxic tissue and tumour regions. Briefly, pimonidazole binds to cellular thiols present in hypoxic conditions, and the remaining pimonidazole is degraded in water (redrawn from Hypoxyprobe example).

2.6.7   Immunofluorescence

Spheroid sections were obtained in the manner depicted in section 2.6.6. Sections were taken from -20ºC and left to thaw for 15 min at room temperature. The slides were permeabilised for 10 min in 1X PBS 0.5% Triton X-100 before being blocked in 2% bovine serum albumin (BSA) in 0.1% Tween in 1X PBS for 2 h at room temperature. Afterwards, the slides were washed in 1X PBS and a hydrophobic PAP pen (Sigma, UK) was used to draw around the sample. Primary antibody diluted in TBS at the concentration noted in Table 2.5 was added to the section and left to incubate overnight at room temperature. The following day, sections were washed thoroughly in TBS and incubated for 90 min at room temperature in fluorochrome/fluorophore conjugated anti-species secondary antibody diluted at 1:250 in TBS. Prolong gold antifade nuclei counterstain (ThermoFischer, UK) was added to the sections, which were then covered with coverslips. The slides were imaged on a Zeiss fluorescence microscope as previously noted (Section 2.6.6).

2.7 Initial flow cell ('gen 1')

2.7.1 Microfluidic Device design and fabrication

The initial device design for this study needed to allow the passage of cell culture media and spheroids of varying sizes into and out of the microfluidic device. It was envisaged to entrap spheroids within a specific zone, whilst allowing media to continually perfuse over the spheroid for a prolonged period. Effluent media was to be collected for further analysis. Furthermore, it was desirable to have a non-gas permeable device that would be readily machinable, reusable, and inexpensive to produce. Schott B270 glass was chosen as the device material to fit these characteristics and functions, coupled with available techniques and machinery. The device was designed in discussion with Dr Iles, based on a previous model used within the University of Hull. The fabrication was also carried out by Dr Iles. The design was drawn in SolidWorks (Waltham, USA) (Figure 2.5) and milled with a Computer Numerical Controlled (CNC) machine (Datron, Germany) using a diamond milling tool of 1 mm diameter (Eternal Tools,

a)
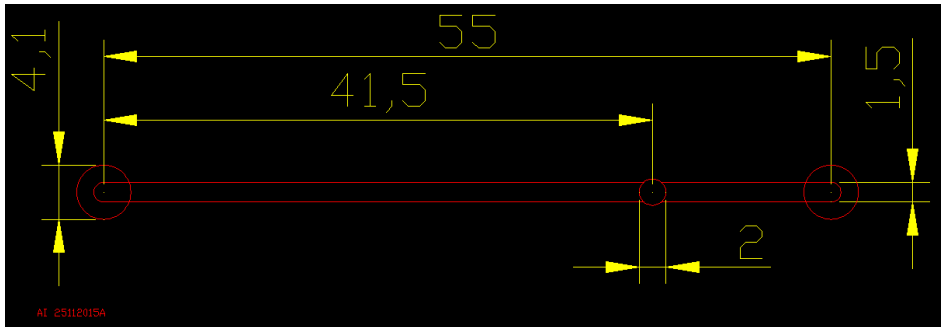
b)
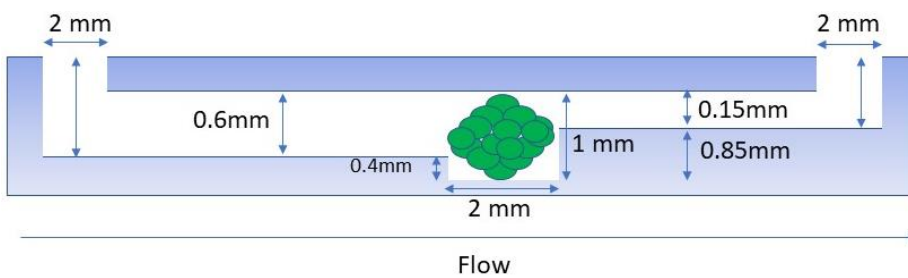
Figure 2.5: Generation 1 microfluidic device panel image (schematic and a cross sectional drawing)

The generation 1 microfluidic device schematic (in mm) used for CNC milling purposes a), Generation 1 microfluidic device cross sectional drawing with an example spheroid in the micro-well b)(2 mm radius on the inlet and outlet are shown in the cross sectional drawing in b)

UK). A second glass slide was thermally bonded to enclose the channel structure. The microfluidic device contained a 2 mm wide inlet and outlet port, with a deep channel at a depth of 0.6 mm and a width of 1.5 mm, leading to a microwell of 2 mm x 1 mm (width x depth) and a shallow channel of 0.15 mm depth and a width of 1.5 mm. Overall the channel length was 55 mm from the inlet to the outlet and the entire device was designed to contain one spheroid under continuous perfusion culture.

2.7.2 Device inlet and outlet tube assembly

Two 5 mL disposable syringes (BD, Oxford, UK) were inserted into the inlet and outlet holes, before being cut with a scalpel at the base, leaving just the nozzle of the disposable syringes left in the inlet and outlet holes. These were trimmed to size using a scalpel, to create a snug airtight fit. Araldite Rapid glue (RS Components, UK) was then carefully applied around the inlet and outlet ports, with the nozzle base attached, and left in a 37°C incubator for 2 h to solidify and set. 200 μl pipette tips were cut at approximately 1 cm from the base. Two pieces of PTFE tubing (polytetrafluoroethylene) (ColeParmer Natural, Item # WZ-06605-27, i.d. 1.6mm, o.d. 3.2mm, wall thickness 0.8mm) were cut at about 12 cm in length and a further two 1 cm sections of larger Tygon (STI VWR bioprocessing 2375, i.d. 3.2 mm, o.d. 6.4mm)tubing was also cut. The larger diameter tubing was fed over the smaller diameter tubing and inserted into the pipette tip. This resulted in the thicker tubing being at the tip of the pipette. Araldite Rapid glue was applied to ensure the tubing would stick to the pipette tip. The tubing was selected based on their biocompatibility properties and methodological use.

This was mirrored on the alternate end of the PTFE tubing; however, the tip was the opposite way around, so it could be attached to a disposable syringe. A second tubing set was made without a pipette tip on one end, leaving an exposed PTFE tube ending, to allow effluent to flow out into a collect vesicle. This was repeated so there were multiple sets of tubing, for both the inlet and out ports, as can be seen in Figure 2.6.
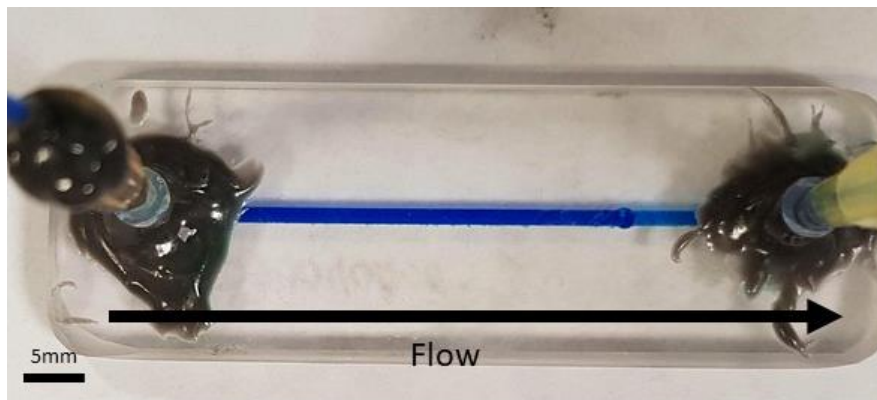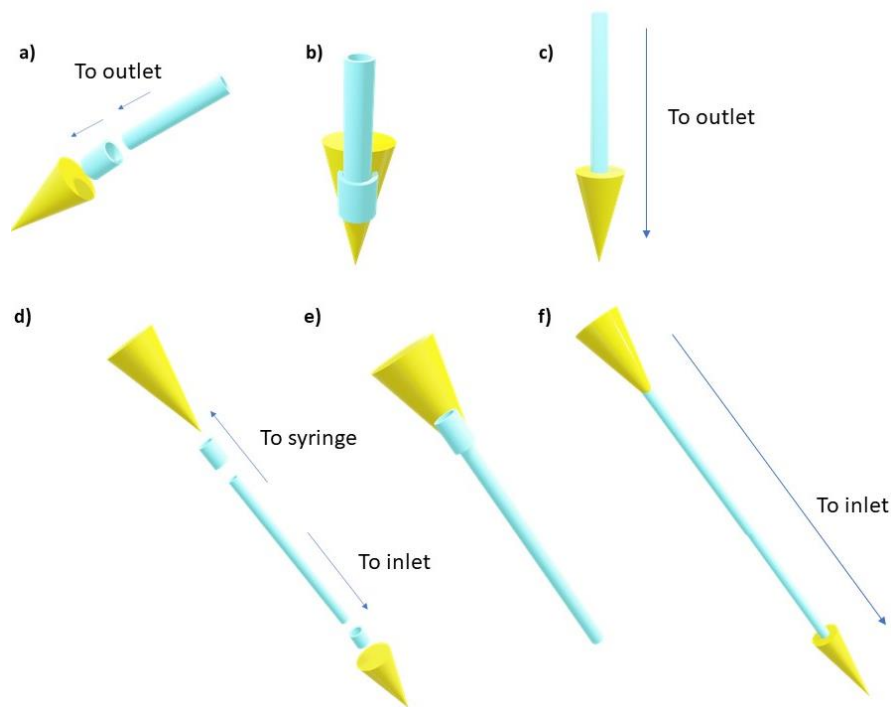
Figure 2.6: Generation 1 inlet and outlet tubing and the microfluidic device image

Outlet PTFE tubing assembly. a, b) The pipette tip has a thicker piece of PTFE inserted into its base to create a snug fit, before a thinner piece of PTFE with an open end is inserted, c) the pipette tip is inserted into the outlet to allow media to flow out. d, e) The inlet tubing is the opposite of the outlet tubing; however, the PTFE tubing has a pipette tip on each side, this will allow the syringe to be attached to the f) upper pipette tip whilst the lower is attached to the inlet. The flow for leaks was tested and the gen 1 microfluidic device photo from above with brilliant blue dye flowing from the deep channel, through the micro-well and into the shallow channel is shown below. Scale bar represents 5 mm

2.7.3 Device integrity assessment

To ensure the free flow and passage of fluids through the microfluidic device uninterrupted, 3 mL of brilliant blue dye solution (SigmaAldrich, UK) was pumped from a 10 mL disposable syringe (BD) by hand, thus the speed of infusion was variable. This allowed the identification of any leaks or holes present, which could compromise future experiments. The microfluidic device was then imaged on an inverted microscope, at 10x magnification with a handheld camera. Once the integrity of the device was ensured, media was flown through the device in the same manner as detailed above and imaged.

2.8 Experimental procedures for initial flow cell design

2.8.1 Incorporation of spheroids into the generation 1 microfluidic device

Spheroids were carefully collected, using a P1000 pipette, from the 96 ULA plate and placed into labelled collection tubes. The inlet tubing was placed in the outlet port, whilst the outlet tubing was place in the inlet port (shown in Figure 2.7). The spheroids were drawn into the microfluidic device, which was then placed in an egg incubator (Covatutto 24 eco, Novital, Italy) see Figure 2.8, which was set to 37 $^{\circ}$C. The tubing was set up to a 10 mL disposable syringe filled with DMEM. The disposable syringe was placed in an electronic syringe pump (Harvard apparatus) and set to 3 µL per h for a total of 72 h per experiment.

2.8.2 Treatment of microfluidic device to decrease cell adherence for generation 2

To prevent the adherence of cells to the microfluidic device glass surface, glass modification experiments were performed (Tarn 2011). These treatments were performed to render the microfluidic device resistant to cell adhesion, which would be beneficial to both the current
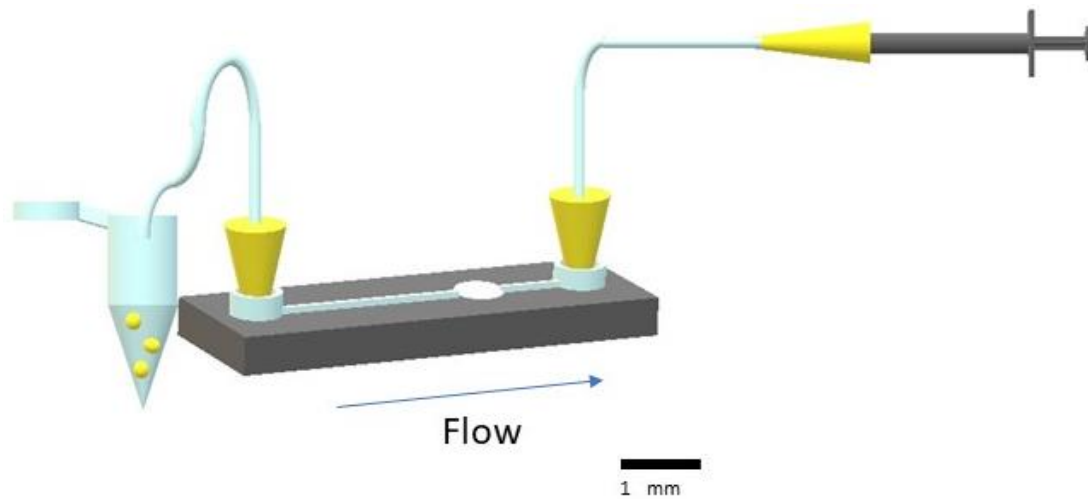
Figure 2.7: Setup used for the placement of spheroids into microfluidic device*.*

Spheroids (96 h post seeding) were transferred into a collecting tube. The tubing was arranged as shown above. A disposable syringe was used to draw the spheroids into the device in the manner denoted by the arrows. Upon a successful placement of a spheroid in the microfluidic device, the tubing was reversed back (so the inlet and outlet tubing were attached to the inlet and outlet ports). A disposable syringe filled with 10 mL DMEM was placed in an electronic syringe pump and was set to a flow rate of 3 μL min^{-1} for 72 h.
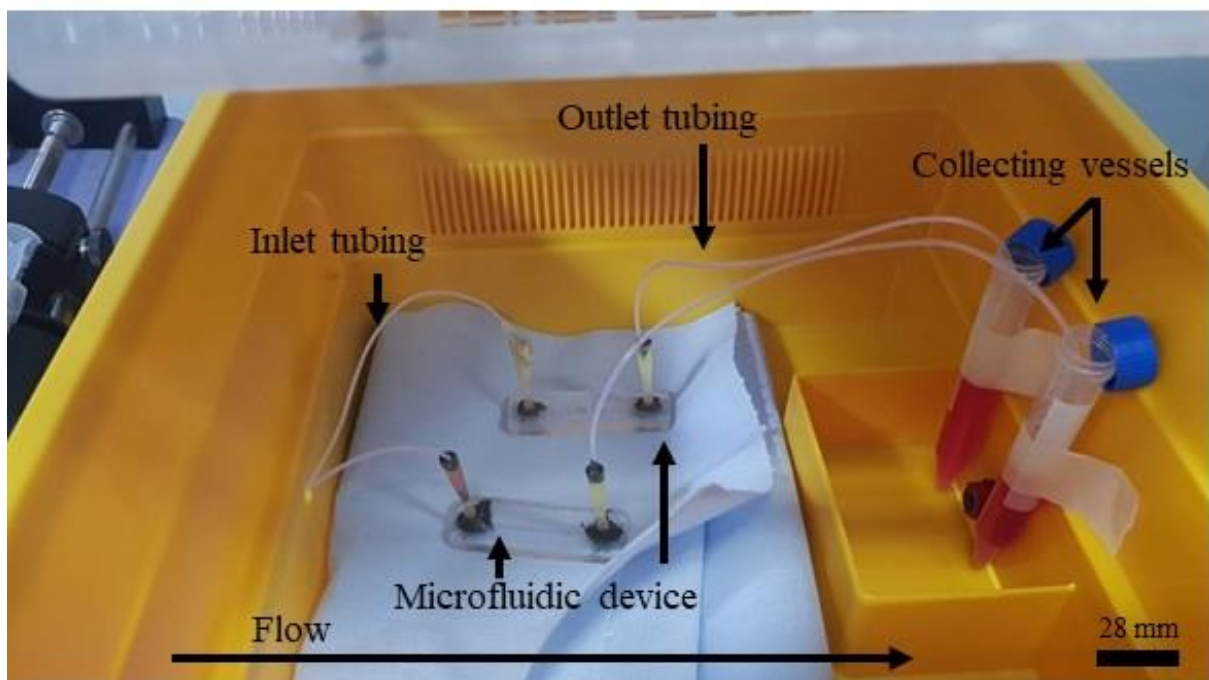
Figure 2.8: Egg incubator and microfluidic device set up

Disposable syringes filled with complete DMEM is connected to a microfluidic device placed inside an egg incubator (Covatutto 24 eco, Novital, Italy). The flow rate is set to 3μl min^{-1} and the spent media collected in a 15ml collection vesicle. After 24 h the vesicles are replaced.

and future microfluidic device design and functionality (Corey *et al.* 2010). To prepare a surface with decreased cell adhesion, silanisation of the microfluidic device glass surface was performed, followed by treatment with the PEG tri-co-polymer F108 (1g per 100 ml) (Sigma, UK). Silanisation is the process of covering (surface treating) a surface (glass) with organofunctional molecules to prevent the absorption of solute to glass surfaces, resulting in the increasing of its hydrophobicity (Seed 2001). The silanisation step is necessary as F018 can only bind to hydrophobic surfaces and has been shown to lead to decreased cell adhesion (Corey *et al*. 2010).

2.8.3 Silanisation of generation 2 microfluidic device and treatment with PEG F108

The silanisation agent chosen was octadecyltrichlorosilane (OTS) (Sigma, UK) OTS as it has been shown to render the glass surface hydrophobic (Lee and Sung 2005, Tarn 2011). For the silanisation, the glass device or slide to be treated, were initially cleaned in piranha solution (30% hydrogen peroxide and 99.9% sulfuric acid, 1:3), before being cleaned in a furnace (500 °C for 6 – 12 h) with no tubing attached. After this time, the device and glass slides were flushed and washed with acetone, before being dried and flushed with air. These steps were critical as they would remove the presence of water from the glass surfaces, as these could result in powered residues and by products which could block the microfluidic device channels. A 1% v/v silane solvent solution (comprised of 90% v/v octadecyltrichlorosilane, 99 % v/v hexane and 99% v/v chloroform formed in a 1% v/v solution in 4:1 of Hexane: Chloroform) was flushed through the device and over the slide. The device and slide were immersed in the solution for at least 10 min to allow the solution to react. Afterwards, the glass was washed with acetone and water once more allowing it ready for use. OTS was stored in a desiccator for 2-3 weeks when not in use to reduce the amount of water present, as this can cause the formation of powdery residues. OTS features a silane group with four substituents and a -R group. Shown in figure 2.9.
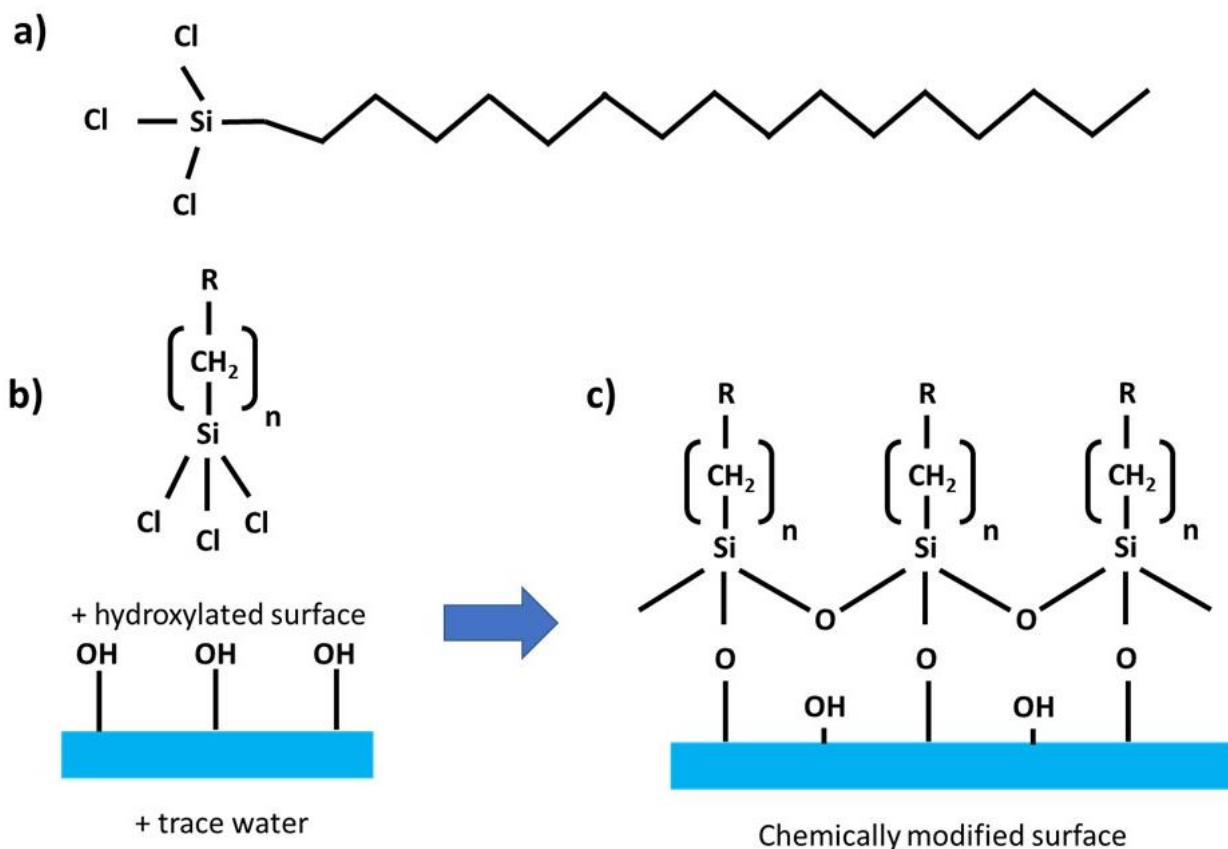
Figure 2.9: Octadecyltrichlorosilane chemical structure and glass surface modification

Octadecyltrichlorosilane chemical structure a). A modification of the glass surface from b) to c). A 1% v/v silane solvent solution (comprised of 90% octadecyltrichlorosilane, 99 % hexane and 99% chloroform) was formed in a 1% solution in 4:1 of Hexane: Chloroform) was flushed onto a glass surface. OTS features a silane group with four substituents and a -R group responsible for causing the glass to become hydrophobic. The chlorine present in OTS reacts hexane in the solvent to produce an alkoxy silane and hydrochloric acid, meaning the silanizing agent works due to hydrolysis. The chlorine (-Cl) present in OTS was used to link the silane to the surface.

responsible for causing the glass to become hydrophobic. The chlorine present in OTS reacts hexane in the solvent to produce an alkoxy silane and hydrochloric acid, meaning the silanizing agent works due to hydrolysis. The chlorine (-Cl) present in OTS was used to link the silane to the surface. After the glass surface was turned hydrophobic, the microfluidic devices (including the filled channels) were incubated for 12 h at 55 °C in PEG tri co polymer F108, to turn the surface resistant to cell adhesion (Corey *et al* 2010).

2.8.3.1 Silanisation within microfluidic devices

To silanise the microfluidic device, the devices were treated in a similar manner to the glass slides. Like the microscope slides, a 1% OTS solution was prepared as before, before 10 ml was flowed into the channels by hand using glass syringes. Following this, 10 ml of OTS was added into the devices from both the inlet and outlet port simultaneously to ensure all channels were filled. The solution left within the devices to incubate for 20 mins. After this time. The devices were flushed with air three times, before 10 ml of F108 was added into the inlet and outlet channels in the same process described for OTS. The F108 was left incubated within the microchannels for 12 h overnight at 55°C.

2.8.3.2 Contact angle measurements for generation 2

To demonstrate whether the silanisation and surface treatment of the glass surface was successful in increasing the hydrophobicity, contact angles were measured. The contact angle of a water droplet in relation to the glass surface can denote the levels of hydrophobicity present (Cras *et al*. 1999); where a contact angle is greater than 90°, it indicates a hydrophilic surface; where it is less than 90°, the surface is hydrophobic.

The contact angles were measured using a droplet of 20 µL of water on multiple testing slides. An untreated glass slide was used as a hydrophilic control, and a p-nitrile surface was used as

a hydrophobic control, by using lab glove surface stretched over a slide. These two conditions were used to demonstrate how water droplets would form and allow a comparison of the contact angles of water in both a water repelling and water loving surface. Three further microscope slide conditions were tested: (1) an untreated glass slide, (2) an OTS silanised glass slide and (3) an OTS silanised slide following F108 treatment. The slide was placed on a shape drop analyser (Kruss, Germany). 20 µl of deionised water was pipetted on at least four separate locations on the slides. The droplet was imaged and analysed on the shape drop analyser, with the angle between the water and slide surface being determined automatically by the Kruss analyser. This was repeated at least two further times with separate slides.

2.8.4 Testing of surface treatment

As F108 PEG tri-co-polymer treatment has been shown to lead to decreased cell adhesion (Corey *et al*. 2010). The efficacy of this treatment needed to be determined prior to implementation in the microfluidic devices. In order to do so, an experiment was conducted using cell monolayers and four variations of treated microscope slides, namely (1) an untreated glass slide, (2) a glass slide treated with polylysine (PLA) which is known to promote better cell adhesion, (3) a glass slide with OTS and (4) a glass slide silanised with OTS and further coated with 1% w/v F108. The slides were cleaned with 70% ethanol and stored a sealed Tupperware container until further use. MCF7 and U-87 MG cells were prepared in a cell suspension of 5×10^6 cells mL^{-1}. The four variations of microscope slides were placed in separate tissue culture dishes. The MCF7 and U-87 MG cell suspensions were pipetted over the top of the slides, DMEM added and the dishes placed in an incubator at 5% CO_2 and 37 $^\circ$C for 24 h to allow cells to adhere. After 48 h, the slides were removed and placed into a clean and sterile tissue culture dish. The dishes were immediately taken to a microscope set at 5 x magnification (Zeiss, Germany) and imaged in random locations over the slide, to study the adherence of cells across the different treatments.

2.8.5 Hydrogel incorporation into generation 2 and 3 microfluidic devices

Several hydrogels and ECMs were chosen for this study, namely; Collagen, Fibronectin, Matrigel, Gelatin and Peptigel as these hydrogels offered different elements of the extracellular matrix and have been previously used for migration and invasion assays (Vinci *et al*, 2013). Before all hydrogel incorporation, the microfluidic device was cleaned with 100% ethanol at least three times and further perfused with 1X PBS, using 50ml of each solution perfused by hand. The device was then flushed with PBS to ensure the channels and microwells were wetted. Two disposable syringes (BD, Plastipak, UK) were attached at the inlet and outlet ports and the plungers pressed to the base, ensuring that no air remained within the channels or microwells. Gel solutions were prepared as summarised in table 2.2. 10 µl of gel solution was added directly to the microwell using a pipette, ensuring no air bubbles were present. The microfluidic device was then left for a period to air dry at varying temperatures (see table 2.2 for conditions). The device was imaged on a microscope at 5x magnification (Zeiss, Germany), before brilliant blue solution (Sigma, UK) was flowed into the device and imaged in the same manner to study whether the hydrogel was incorporated successfully.

2.8.6 Cell migration

Cell migration is a critical process within metastasis. The migration process involves complex interactions between host cells, proteins, cell junctions and the ECM. Therefore, it was essential to try and recapitulate this *in vivo* process *in vitro*. To mirror this within the microfluidic device, hydrogels and ECM were adopted to simulate the migration process. Several hydrogels and ECMs were chosen for this study, namely; Collagen, Fibronectin, Matrigel, Gelatin and Peptigel, as they were readily available, offered different elements of the ECM and have been previously used for transwell migration assays.

2.9   Access port device (gen 2)

2.9.1   Device design and fabrication

Several issues were found in the initial 'generation 1' microfluidic device design. Although the generation 1 device allowed for incorporation of spheroids, continuous prefusion of media and collection of effluent, the device lacked the ability to directly image the spheroids on-chip. It was not possible to collect an intact spheroid post 72 h incubation as they were found to be broken, disaggregated and disrupted. There was the risk of the spheroids becoming entrapped, lost or disaggregated when initially pumping the spheroid into the fluidic device as was observed for several cell lines.

Taking these limitations into account, a new design was developed with the input of Dr Alex Iles. The generation 2 microfluidic device was designed with the same geometry as the generation 1 device and was again fabricated in Schott B270 glass. One alteration to the geometry was a 70 μm weir, which was milled at the entrance of the shallow channel, to prevent any through flow of spheroids out of the microfluidic device. A hole was also milled directly above the micro-well, which would allow the direct pipetting of spheroids into and out of the micro-well, pipetting of ECM-like matrices and hydrogels into the micro-well, as well as direct imaging of the micro-well itself. Removable transparent poly dimethyl siloxane (PDMS) plugs, (3 mm wide) were fabricated and moulded to exactly fit into the hole above the micro-well to prevent leakage of the microfluidic device. The PDMS plug was produced by mixing a 10:1 ratio of plastiser (Sigma) to curing agent (Sigma), and allowing it to be centrifuged at 1700 x *g* for 10 min. The mixed liquid PDMS was poured into a plastic mould and left to set for 2 days at room temperature. The plugs were then pushed out after 2 days and placed into the microfluidic device port to test the size fit. The generation 2 microfluidic device design can be seen as a schematic (Figure 2.10A), as a cross sectional side profile (Figure 2.10B) and as a photo (Figure 2.10). To further prevent spheroid disaggregation and cell sticking all devices were silanised with OTS and treated with F108 as detailed in previous sections 2.8.2.

2.9.2 Generation 2 device integrity assessment

Like the generation one microfluidic device, the second device needed to be assessed for leaks and free passage of fluids. The variation in design, the microwell access port, meant that there was a much higher percentage of leaks due to a third hole being introduced. Furthermore, the access port above the microwell would not be bound with glue and an inlet interface tubing device, it would be sealed with a PDMS plug interface, resulting in a higher chance of the fluid being able to free flow out into the external environment. To ensure the free flow of fluids through the generation two microfluidic device, 3 mL of brilliant blur dye solution (SigmaAldrich, UK) was loaded into and pumped from a 10 mL disposable syringe (BD) by hand as was done previously with the generation one device. The microfluidic device was imaged in the same manner on a zeiss microscope at 10x magnification. The device was then imaged using a handheld camera and shown in figure 2.10.

2.9.3 Generation 2 device spheroid integration

Spheroids were incorporated into the generation two microfluidic device through the microwell access port. Spheroids, U-87 MG and MCF7, were seeded at 2.5 and 3.5 x 10^4 cells per well in a 96 well plate as detailed previously. A single spheroid was pipetted in a p1000 pipette and the pipette was carefully placed over the microwell through the access port. The spheroid was gently released into the base of the microwell, ensuring most of the liquid was ejected as to not

a)
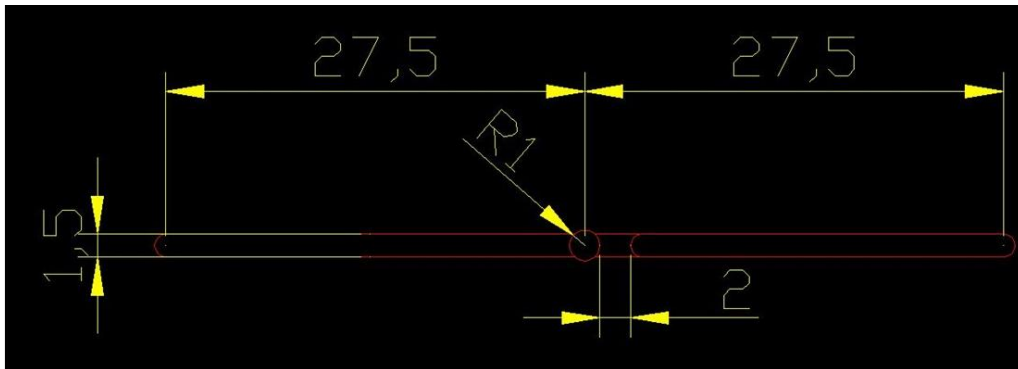
b)
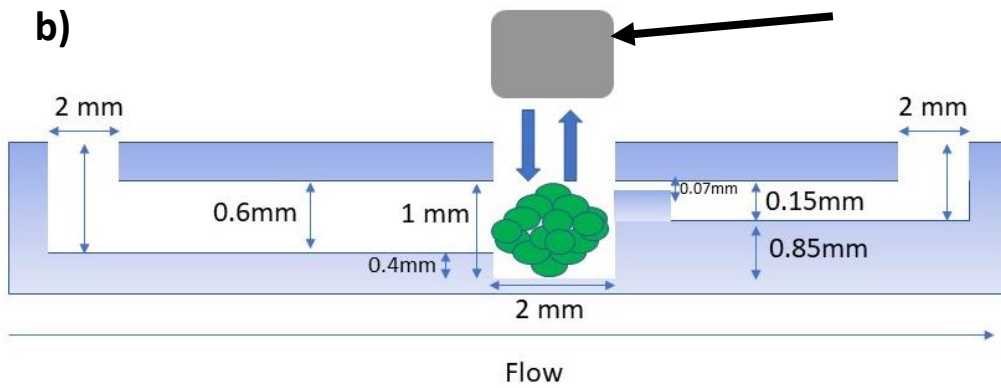
Figure 2.10: Generation 2 microfluidic device panel image - schematic, cross sectional drawing and photo

Generation 2 microfluidic device schematic (in mm) used for CNC milling purposes a), Generation 2 microfluidic device cross sectional drawing with an example spheroid in the micro-well and a grey PDMS plug with arrows denoting the removability of its b) Access port device
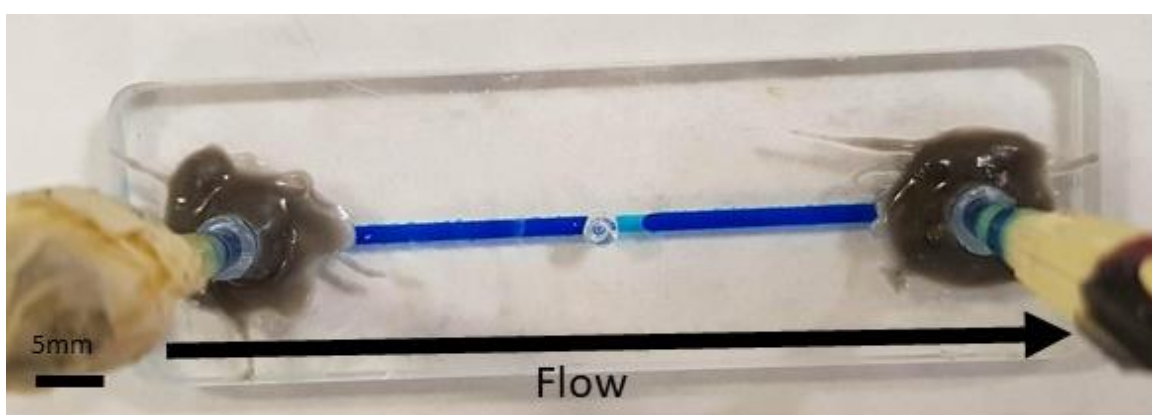
Figure 2.11: Generation 2 microfluidic device panel image

A photo from above with brilliant blue dye flowing from the deep channel, through the micro-well and into the shallow channel. Scale bar represents 5 mm

disturb the spheroid. The PDMS plug was then placed over the top of the access port and the device connected to the disposable syringes for experimentation.

2.9.4 Device design and fabrication

The second-generation device, although an improvement upon on the first design, still resulted in several problems. The device did not allow the spheroid to be imaged as clearly as required, with the rough microwell base refracting and reflecting light unevenly. This meant that the spheroids could not be imaged within the device under flow as desired. It was desired as hydrogel incorporation and subsequent migration of the spheroids needed to be monitored. Therefore, a further advancement on the device design was proposed and constructed with the help of Dr Alex Iles. The advancement would allow real time spheroid monitoring and migration through the addition of a glass coverslip at the base of the microwell. The device for generation three was designed with the same geometry as the generation two device and was again fabricated in Schott B270 glass. However, a borosilicate glass coverslip was thermally bonded to the base to allow better clarity and imaging of the spheroids when inside the device. The generation three microfluidic device design can be seen as a schematic (Figure 2.12) and as a cross sectional side profile (Figure 2.12).

2.10 Statistical analysis

Experiments were repeated in triplicate (internal replicate of 3) with a minimum of n of 3 (intra experimental) unless otherwise noted within the figure legend. Standard error was calculated on graphed data and statistical significance was determined using a two-way ANOVA using GraphPad Prism (California, USA). Significance was determined if $p<0.05$. Error bars represent Standard Error of the mean (SE), unless otherwise noted, p values denote values being less than * 0.05, ** 0.01 ***0.005 ****0.0001.
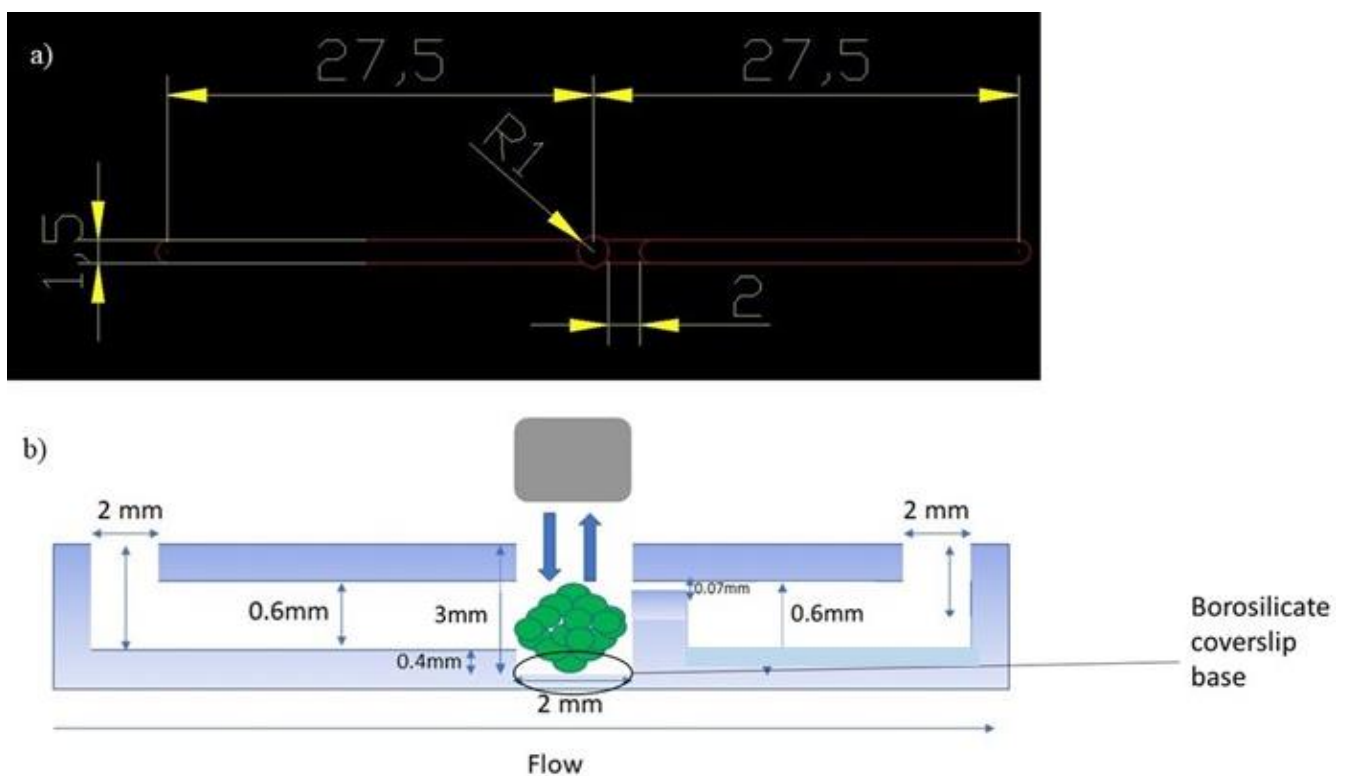
Figure 2.12: Generation 3 microfluidic device panel image (schematic and cross sectional)

Generation 3 microfluidic device schematic used for CNC milling purposes a), Generation 3 microfluidic device cross sectional drawing with an example spheroid in the micro-well and a grey PDMS plug with arrows denoting the removability of its b). The microwell base features a borosilicate glass coverslip bounded externally to the glass of the overall device. This allows direct better viewing of the spheroid mass.

Chapter 3. Characterisation of cancer spheroids for incorporation into a microfluidic device

3.1 Introduction

3.1.1 Spheroids as cancer models

Following on from section 1.3.4 in the introduction, a cancer cell line spheroid can be defined as an amalgamation or agglomeration of cells from a cancer cell line formed into a spherical structure (Weiswald *et al*., 2015). Spheroids are attractive models for cancer research due to their morphology, which gives rise to a more realistic representation of mammalian tumours (Sutherland, 1988). The diffusion gradient of oxygen, nutrients, metabolites, and catabolites in tissues is 200 μm, generating heterogenous chemical and nutrient gradients (Mehta *et al*., 2012). This results in distinct, clearly defined internally differentiated zones (figure 3.1). The zones are well characterised, with a central region of necrosis with an acidic pH, low waste removal and poorer nutrient acquisition, surrounded by layers of proliferating and quiescent cells in the G0 phase of cell cycle and growth (Chandrasekaran & King, 2012; Mehta *et al*., 2012). Spheroids have been shown to be advantageous over 2D cultures, including work by both Vinci *et al* and Imamura *et al.*, showing how spheroids can be used to form both heterogeneous cell populations and microenvironmental conditions, in comparison to those of 2D cultures (Vinci *et al*., 2012; Imamura *et al*., 2015). However, it must be noted that spheroids (MTCS) lack the complexity of *in vivo* models, being a singular cancer cell type, in comparison to a complex mixture of primary cells, immune cells and basement membrane mix. This is the spheroids largest caveat.

3.1.2 Spheroid types and generation techniques

All spheroids can be classified into four main different subtypes, originating from different sources and generated using different techniques. The subtypes are multicellular tumour spheroid (MCTS), tumourspheres, tissue-derived tumourspheres, and organotypic multicellular spheroids (Raghavan *et al*., 2016).
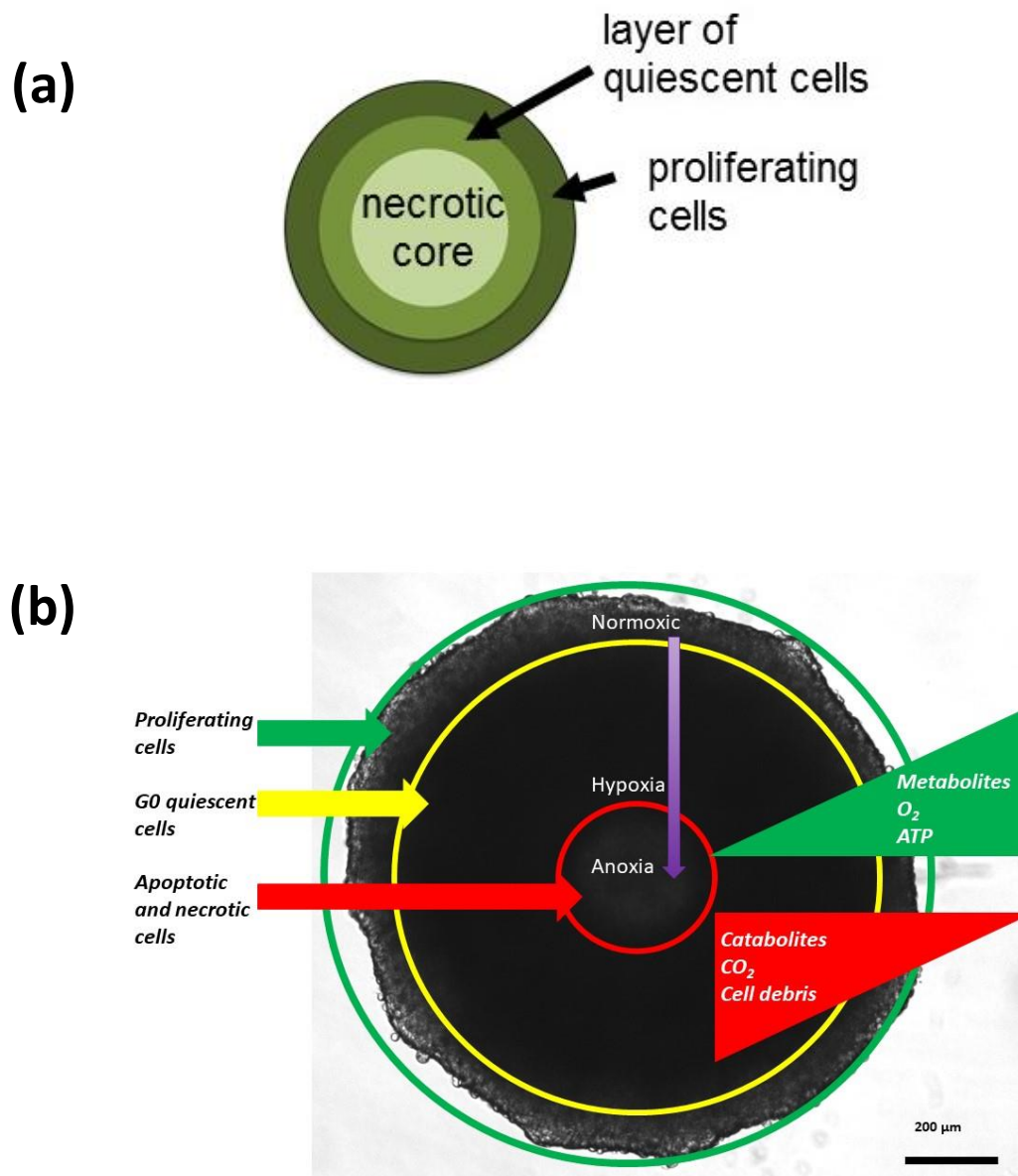
Figure 3.1: **Spheroid composition**

(a) Schematic of spheroid zones; proliferating cells on the outside are surrounding a layer of quiescent cells and a necrotic core. (b) Example of a microscope image of a spheroid showing the internal zones formed from diffusion gradients, coupled with oxygen content (Adapted from Zanoni et al., 2016)

MCTS are formed from cell lines and rely on the propriety of cells to bind to one another as opposed to the culture plate. The techniques used to generate MCTS include hanging drop, liquid overlay technique which includes ULA (ultra-low adherence) aggregation, and a more recent technique using microcapsules with membranes contained within methylcellulose (Weiswald *et al*., 2015;Raghavan *et al*., 2016). The liquid overlay technique produces reproducible and uniform spheroids (Vinci *et al*., 2012). In this process, single cell suspensions are grown in non/low adherent conditions, such as being grown in plates coated with agarose, that prevents cell adhesion, resulting in cells aggregating to one another instead of the plastic base (Weiswald *et al*., 2015).

Tumourspheres, on the other hand, are formed from individual cells suspended in an ECM-like matrix and represent individual colonies. Tumourspheres are formed from one cancer stem cell, proliferating to form a spherical, solid and round structure. Tumourspheres range from <50 μm to 250 μm and are distinguishable from aggregated single cells (such as MCTS) due to their structure. The structure of tumourspheres appear to be a dense, solid mass with no distinguishable space between cells, whilst MCTS appear to be larger, the cells are distinguishable from one another and are not one solid mass. The original cancer cell is grown in serum free and non-adherent conditions. However, only certain cancer cell lines can form cancer tumourspheres, such as MCF7, BT474 and primary mammary tumour cells from *neu* Mice (Johnson *et al*., 2013).

Tissue-derived tumourspheres are formed from cancer tissue samples which are partially dissociated and aggregated in non-adherent environment. Tumour derived spheroids are grown in a similar manner to MCTS, *i.e.* in low adherent conditions, resulting in free floating spheres. Tumour derived spheroids are an *in vitro* model of cancer used to evaluate cancer stem cells (CSC), with stem cell related characteristics. They are a high throughput method, with non-

tumour niches present that can be genetically manipulated. (Mehta *et al*., 2012; Weiswald *et al*., 2015).

Organotypic multicellular spheroids are cultured in a similar method to the tissue derived spheroid, but the dissected tumour is cultured with low percentage agar media and cultured for 2 to 3 weeks, with a media changed once a week. This model allows more realistic testing conditions of tumours, especially as it directly from a patient (Weiswald *et al*., 2015). The cancer tissue can either be enzymatically or mechanically dissociated, and the cancer itself will maintain histological features and heterogeneity seen from within the host. Organotypic multicellular spheroids contain cancer cells, stromal components, and non-cancer cells, and are intended to accurately reproduce the tumour microenvironment. Several cell lines have been described to be used to generate spheroids indicating the availability, robustness and reproducibility of the spheroid model. (West, 1989; Chandrasekaran & King, 2012; Mehta *et al*., 2012; Vinci *et al*., 2012; Imamura *et al*., 2015). A breakdown of spheroids is shown in table 3.1.

3.2 Rationale and aim of this chapter

The rationale underpinning the work in this chapter is that incorporation of relevant spheroid models within a microfluidic device would allow researchers to explore what effects the internal forces acting within the microfluidic device would have on cancer migration and spread, using relevant 3D *in vitro* models. It was essential to characterise the spheroids thoroughly to ensure they were following observations shown in the literature. This would allow us to be confident that any differences noted post incorporation were a result of the microfluidic device.

Therefore, the key aim of this chapter was to characterise and establish which spheroids would be suitable for introduction into a microfluidic device. In order to do this, the objectives of this

series of experiments was to establish and characterise spheroid formation, growth kinetics, structure, and invasive/migratory potential off chip.

Table 3.1 – Types of 3D spheroid models

3D cancer models	Multicellular tumour spheroids	Organotypic multicellular spheroids	Tumour-derived spheroids
Source	Cancer cell line	Tumour tissue	Tumour tissue
Clonality of tumour cells	Monoclonal	Polyclonal	Poly/monoclonal
Histological preservation of original tumour	-	+	+
High throughput	+	-	-
Genetic manipulation	+	+	+
Non-tumour niche cells	-	+	-
CSC like cells	+	-	+

3.2 Experimental design

3.2.1 Spheroid growth characterisation

To investigate spheroid growth in a variety of cell lines, a cell line panel was used. Several cancer cell lines, U-87 MG (glioblastoma), MDA-MB-231 and MCF7 (breast), and HCT116 and HT29 (colorectal), were seeded in ULA plates at a range of cell densities (5×10^3, 2.5×10^4, 3.5×10^4, and 5×10^4 cells per well), and spheroids were generated as previously detailed (Section 2.3.1). Spheroids were then imaged on the Zeiss microscope, and diameters determined using ImageJ. A growth pattern analysis/curve was conducted for U-87 MG and MCF7 cells. The spheroids were seeded at 2.5×10^4 and 3.5×10^4 cells per well and imaged using brightfield settings every 24 h post formation, for 2 - 3 weeks. The diameters were measured via Image J.

3.2.2 Spheroid zone and histological structure characterisation

The viable rim of cells at the spheroid extremity should remain at 60-200 µm due to the diffusion limits of nutrients, particularly oxygen, whilst the spheroid core should vary in size due to the increased toxic metabolic waste and inability to gain essential nutrients (Mehta *et al*., 2012). A semi-quantitative approach was adapted from a protocol developed by Monazzam *et al.* to investigate how the core and viable rim of cells present in a spheroid changes over a period of time (Monazzam *et al*., 2005). MCF7 and U-87 MG pheroids were formed and imaged over a period of 3 weeks on a brightfield microscope and the zones plotted on ImageJ.

In order to evaluate the histological structure, spheroids were fixed with formalin, embedded in OCT, and sectioned through the protocol detailed in sections 2.6.2, prior to staining through conventional immunofluorescence and immunocytochemistry techniques. To assess structural

integrity of spheroids, Haematoxylin and Eosin staining was conducted, as per section 2.6.5. In order to evaluate other biochemical biomarkers of proliferation and the presence of hypoxia, MCF7 and U-87 MG spheroid sections were stained for KI-67 (proliferation marker), CAIX (hypoxia-inducible protein) and β-actin (as a positive control). The presence of hypoxic regions was also further evaluated indirectly using the Hypoxyprobe (Pimonidazole) dye (as per M&M section 2.6.3).

3.2.3 Spheroid migrative and invasive capability characterisation

To investigate spheroid migration and invasive potential, MDA-MB-231, U-87 MG, and MCF7 spheroids were embedded in various hydrogels, specifically gelatin (0.1% in dH_20), collagen (1-3 mg) and Matrigel (10 mg mL^{-1}), as previously described (Vinci *et al*, 2013). Spheroid plates were then imaged every 24 h for 3 days and analysed for the total area shown in section 2. 3.

3. 3 Results

Spheroid diameter is an important measure. It will denote seeding densities to be used for further experimentation. It can be observed in Figures 3.2 – 3.5 that spheroid diameter increased concurrently with an increase in seeding density, for all cell lines used. Almost all cell lines, excluding MDA-MB-231 cells, used in this study formed very similar sized spheroids when seeded at the same densities; which was the case for all cell densities (approximately 1,000 µm when seeded at 2.5 x 10^4 cells per well) (Figure 3.4). Spheroids were considered dense if they had a compact appearance and did not disintegrate upon pipetting. However, when compared to the other cell lines tested, MDA-MB-231 cells formed spheroids that were much larger, for example 60-70% larger than MCF7 and U-87 MG spheroids, less dense and more loosely formed (Figure 3.3). The smallest MDA-MB-231 spheroids had an average diameter of 881 µm (5 x 10^3 cells per well), and the largest 1,810 µm (5 x 10^4 cells per well). The corresponding cell density spheroids for MCF7 cells, for example, were smaller, with a respective average diameter of 793 µm and 1,300 µm. Spheroids generated from the HT29 and HCT116 colorectal cancer cell lines were larger than their MCF7 and U-87 MG counterparts. Importantly, these data also showed that spheroid generation was reproducible. U-87 MG and MCF7 spheroids were chosen to further evaluate growth kinetics and establish whether they could be integrated within the microfluidic device. It was hypothesised that as time increases so does the spheroid size and that spheroids seeded at 2.5 x 10^4 and 3.5 x 10^4 cells per well will be more suited for entrapment within the microfluidic device micro-well.
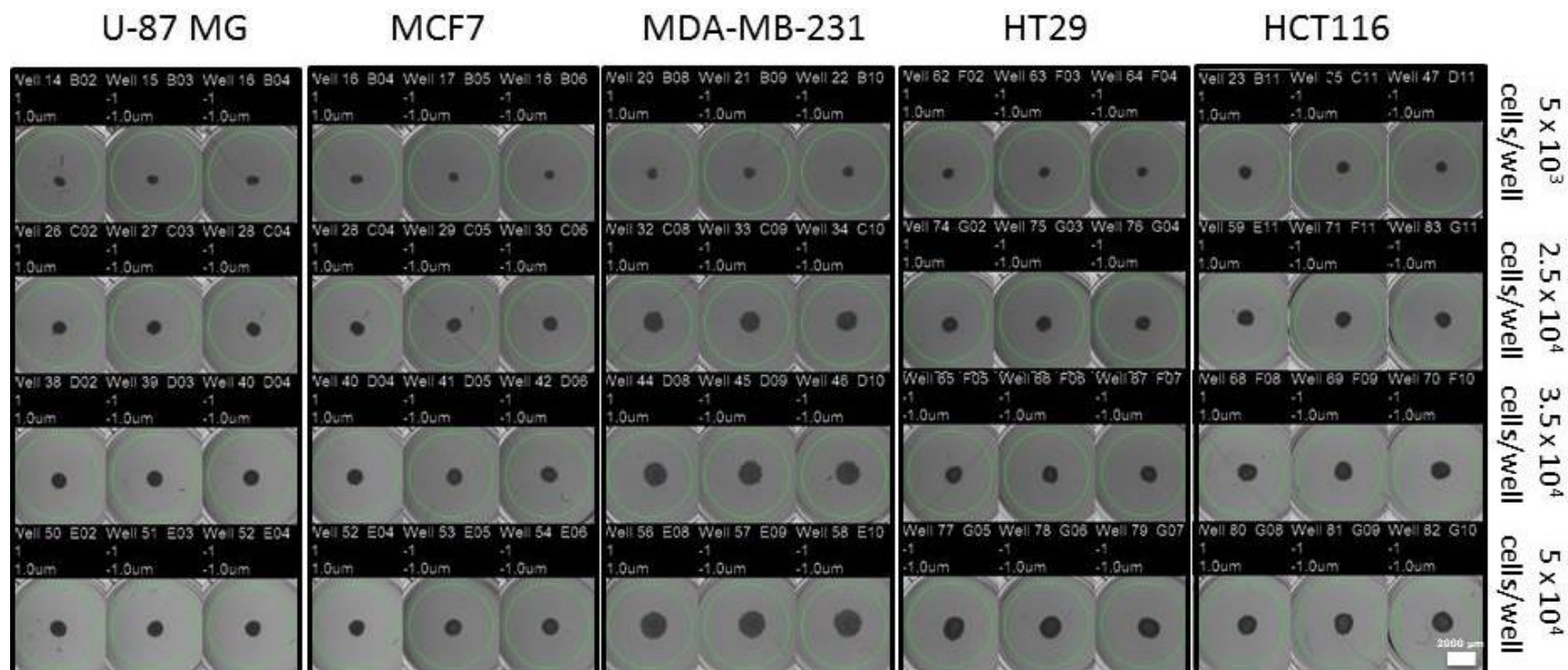
Figure 3.2: **Evaluation of optimal spheroid seeding densities.**

Spheroids were generated as described in Materials and Methods (section 2.3). In brief, spheroids for U-87 MG (a), MCF7 (b), MDA-MB-231 (c), HT29 (d), and HCT116 (e) cancer cell lines in ULA plates in triplicate wells at four seeding densities ($5x10^3$, $2.5x10^4$, $3.5x10^4$, and $5x10^4$ cells per well). Image shown is a representative example of the images obtained from the GelDoc images, and of n=3 experimental repeats in triplicate. Scale bar = 2000 µm.
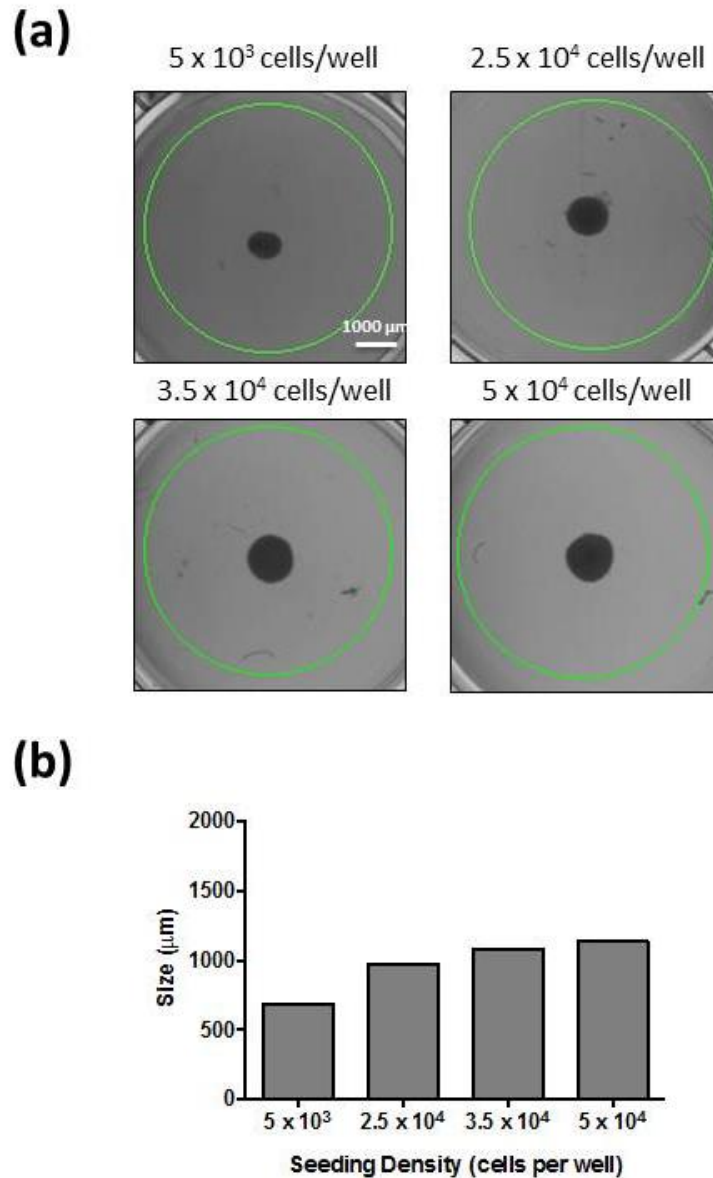
Figure 3.3: **Evaluation of optimal spheroid seeding densities: U-87 MG.**

Spheroids were generated as described in Materials and Methods (section 2.3). In brief, spheroids for U-87 MG glioblastoma cell line were generated in ULA plates at four seeding densities ($5x10^3$, $2.5x10^4$, $3.5x10^4$, and $5x10^4$ cells per well). (a) Image shown is a representative example of spheroids for each cell density at 4 days post seeding. (b) Histogram represents average U-87 MG spheroid size (diameter) in μm, measured 4 days post seeding. Error bar depicts SE. Scale bar = 1000 μm. n=3 experimental repeats in triplicate.
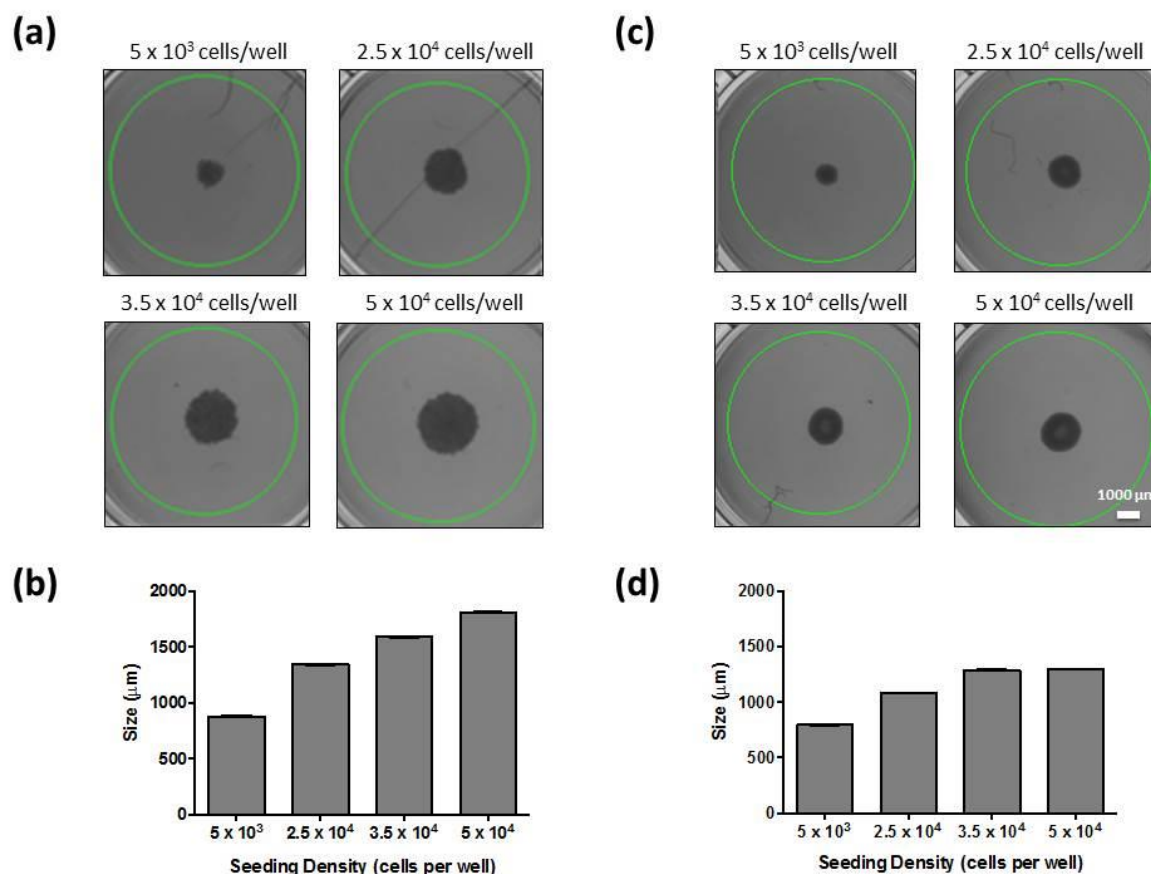
Figure 3.4: **Evaluation of optimal spheroid seeding densities: MDA-MB-231 and MCF7.**

Spheroids were generated as described in Materials and Methods (section 2.3). In brief, spheroids for MCF7 and MDA-MB-231 breast cancer cell lines were generated in ULA plates at four seeding densities ($5x10^3$, $2.5x10^4$, $3.5x10^4$, and $5x10^4$ cells per well). (a, c) Images shown are a representative example of spheroids for each cell density at 4 days post seeding for MDA-MB-231 (a) and MCF7 (c). (b, d). Histograms represent average spheroid size (diameter) in µm for MDA-MB-231 (b) and MCF7 (d), measured 4 days post seeding. Error bar depicts SE. Scale bar = 1000µm. n=3 experimental repeats in triplicate.
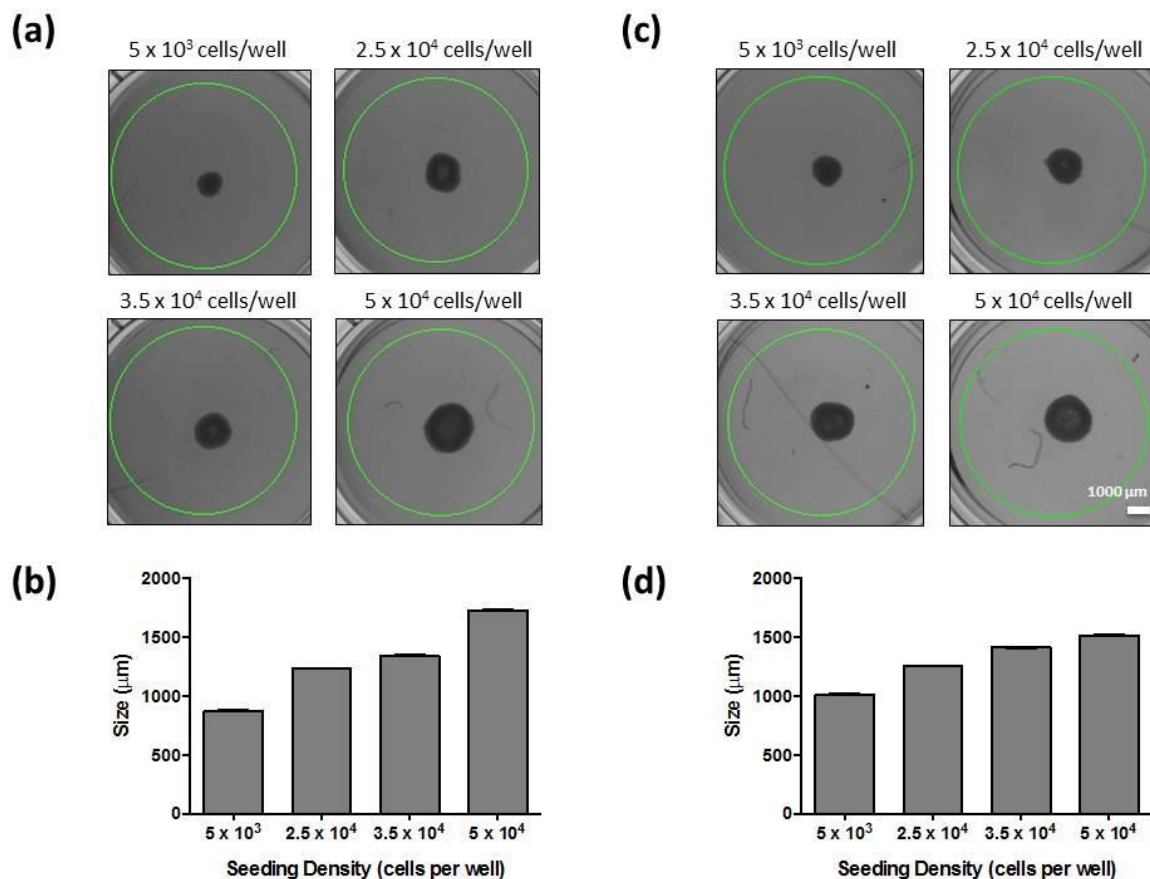
Figure 3.5:   Evaluation of optimal spheroid seeding densities: HT29 and HCT116.

 Spheroids were generated as described in Materials and Methods (section 2.3). In brief, spheroids for HT29 and HCT116 colorectal cancer cell lines were generated in ULA plates at four seeding densities ($5x10^3$, $2.5x10^4$, $3.5x10^4$, and $5x10^4$ cells per well). (a, c) Images shown are a representative example of spheroids for each cell density at 4 days post seeding for HT29 (a) and HCT116 (c). (b, d). Histograms represent average spheroid size (diameter) in μm for HT29 (b) and HCT116 (d), measured 4 days post seeding. Error bar depicts SE. Scale bar = 1000 μm. n=3 experimental repeats in triplicate.

3.3.1 Evaluation of spheroid growth pattern

As large multi-cellular spheroids (>200 µm in diameter) contain distinct zones (Figure 3.1), measurement of spheroid size as a function of time is an important consideration for suitability as models. A typical growth patterns is illustrated in figure 3.6. The results obtained here are shown in figure 3.7. Initially, single cells were observed to self-assemble to form spheroids through intercellular interactions and merge (day 1-2). These cells coalescence, eventually leading to the formation of dense spheroids (day 3-4). After the formation stage, the U-87 MG spheroids (Figure 3.7) were seen to increase in size from 706 µm on day 4 to 1,039 µm on day 10, before a plateau and slight decrease in size toward the 18th day.

3.3.2 Spheroid Zones characterisation (Core and Proliferative rim)

A semi-quantitative approach was adapted from a protocol developed by Monazzam *et al.* to investigate how the core and viable rim of cells present in a spheroid changes over a period of time (Monazzam A *et al*., 2005). The method is based on defining two zones, the core and proliferative rim. MCF7 spheroids seeded at 2.5×10^4 cells per well largely followed the expected growth patterns noted previously (Figure 3.6). The single cell suspension aggregate decreased in total area size by day 4, seemingly when the cell suspensions form a compact and dense spheroid. From day 4 the spheroid grew and increased in size, as the proliferative rim of cells continued to proliferate. The spheroid therefore increased in overall size until the final timepoint of 19 days, being nearly double the total area from the 4th day of initial spheroid formation.
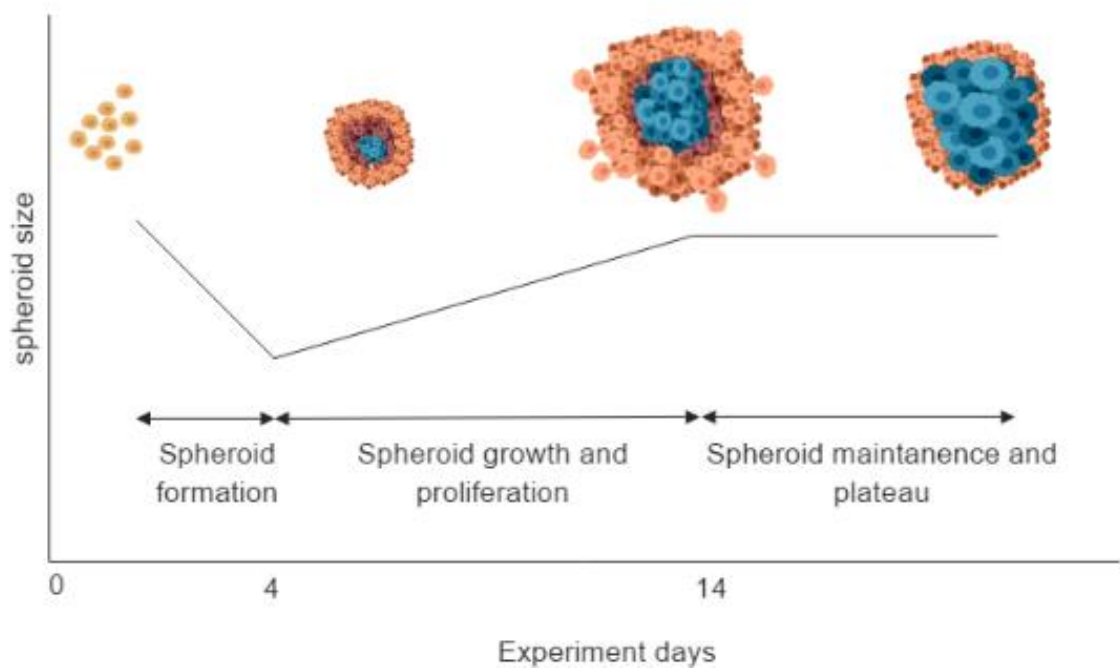
Figure 3.6   ***Spheroid growth patter and structural zoning***

Growth curves typically feature three phases: (1) Within 2-4 days from seeding, spheroids are expected to form from the cell suspension. The spheroid becomes more compact, and therefore a reduction in size is typically observed during this formation phase. (2) This is then followed by a period of growth in size, indicating the successful proliferation of cells. The spheroid size is strongly correlated with the cellular functions present within the spheroid. (3) Finally, the spheroid growth is expected to plateau/decrease. The plateau/decrease is due to increasing proportion of non-proliferating (quiescent) and necrotic cells present. The proportion of non-proliferating cells equals the level of proliferative cells, resulting in a decreased growth rate, before reaching a growth plateau. The necrotic core further increases in size, whilst the proliferating cell layer on the outside decreases. Created with Bio render.
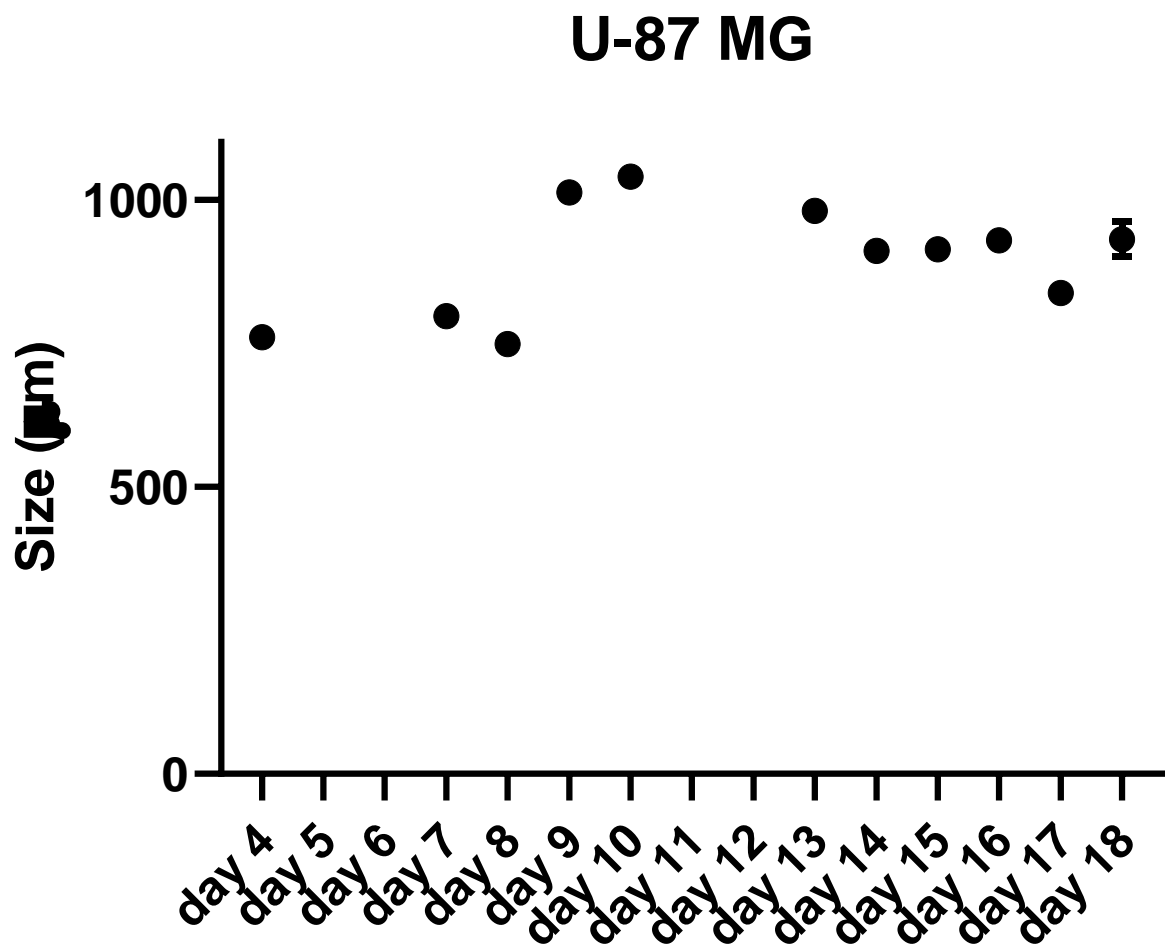
U-87 MG

Figure 3.7: **U-87 MG spheroid growth pattern**

Spheroids were formed from U-87 MG cell suspensions of 3.5 x 10 ^{4} cells per well as previously described (section 2.3). Plates were left undisturbed for a period of 96 h to allow for aggregation, and subsequently the spheroids were imaged every 24 h for 18 days. Scatter plots represent the average diameter in μm. Error bars depicts SE. n=3 experimental repeats in triplicate.
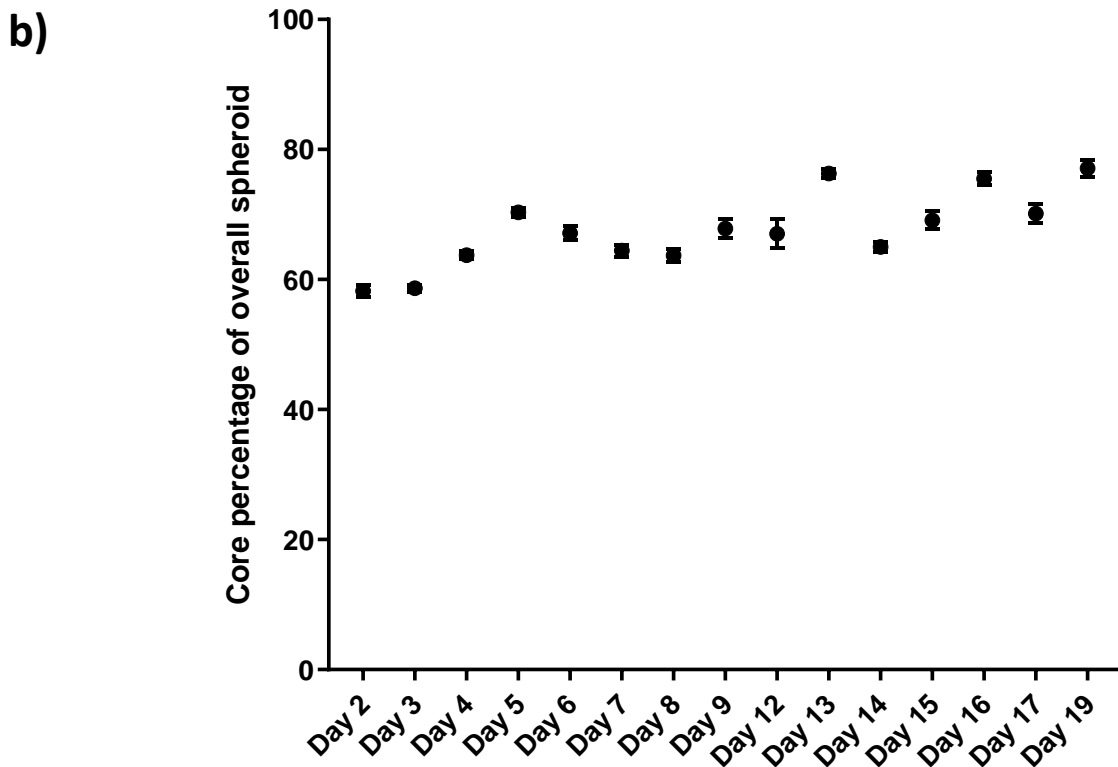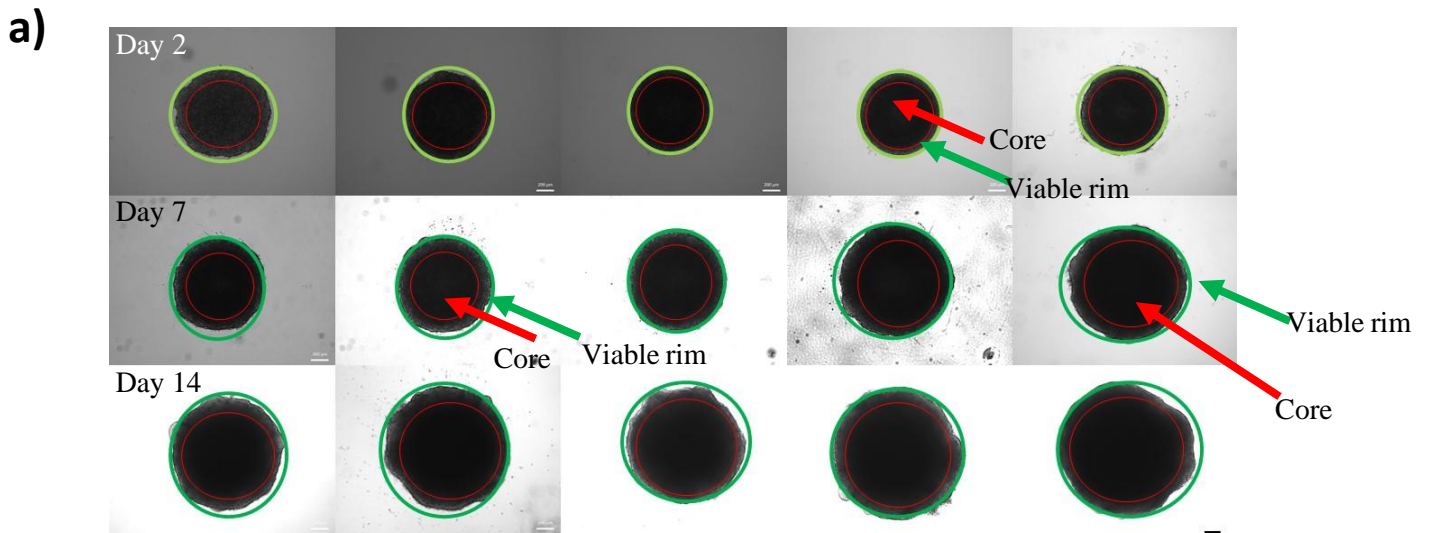
Figure 3.8: *MCF7 spheroid core images over time a) and plot of spheroid core as a percentage of the total area b).*

MCF7 Spheroids were formed from cell suspensions of 2.5 x 10 ^{4} cells per well. The wells were left undisturbed for a period of 96 h, and subsequently the spheroids were imaged every 24 h for 19 days, using a Zeiss inverted microscope at 5x magnification. For each spheroid, ImageJ analysis software was used to plot the spheroid core and the total spheroid area. The percentages calculated were of the core and proliferative rim. On the representative images the red circle denotes the core and quiescent cells, whilst the green circle denotes the proliferative rim. Scale = 200 μm. n=3 experimental repeats in triplicate.
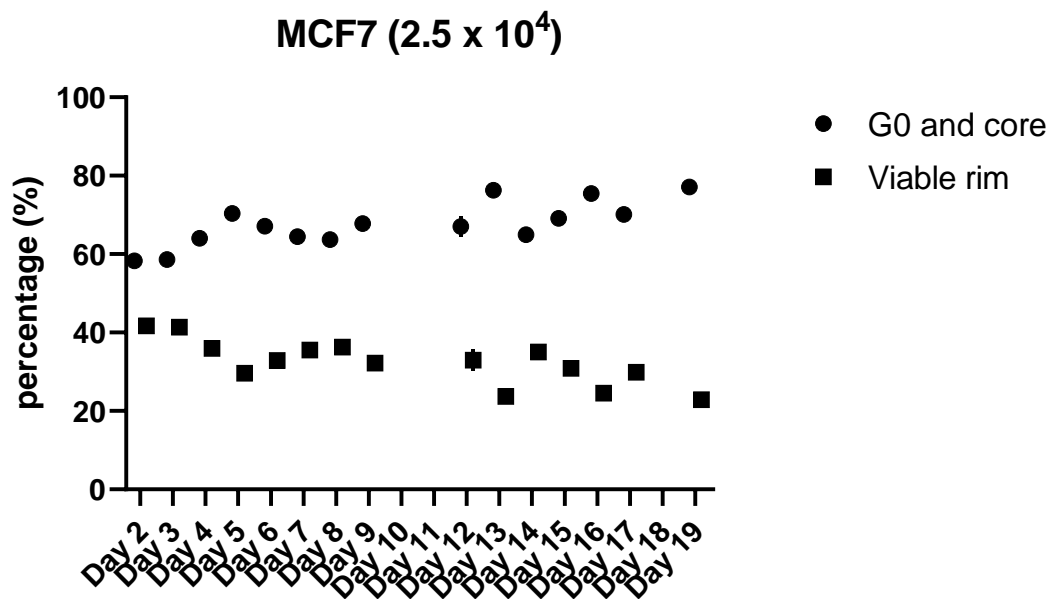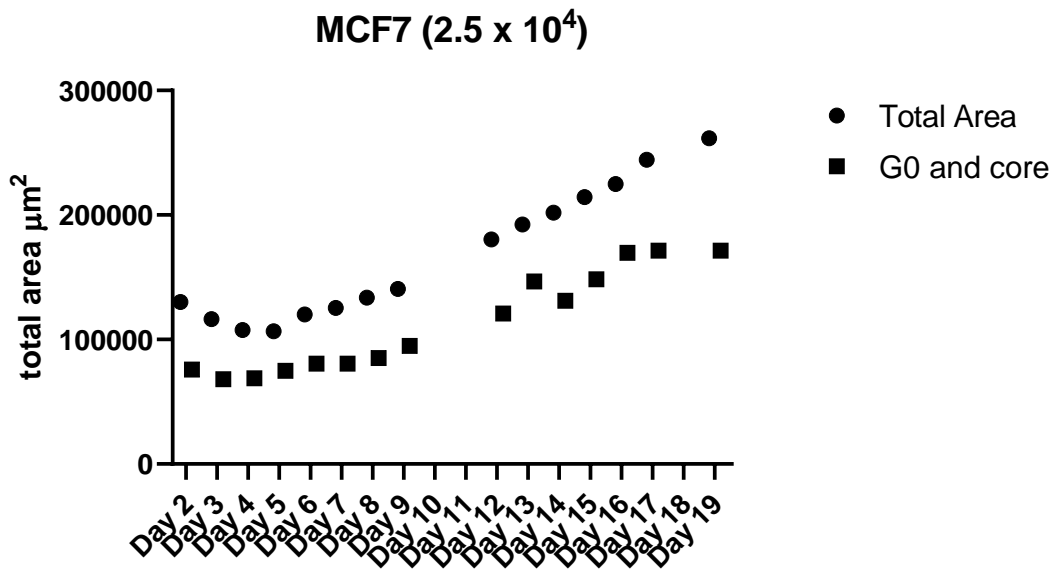
Figure 3.9:   *2.5 x 10 ^{4} MCF7 spheroid total area and area of core and quiescent cells a) core and viable rim as a percentage of the total area b).*

MCF7 Spheroids were formed from cell suspensions of 2.5 x 10 ^{4} cells per well. The wells were left undisturbed for a period of 96 h, and subsequently the spheroids were imaged every 24 h for 19 days, using a Zeiss inverted microscope at 5x magnification. For each spheroid, ImageJ analysis software was used to plot spheroid core area and total spheroid area. The percentages calculated were of both the core (a) and proliferative rim of cells (b) against the total spheroid size. Error bars depicts SE. n=3 experimental repeats in triplicate.

The percentage change of the spheroid core zone increased from 60% to 75% at its maximum on day 19. Similarly, the external rim of cells decreased from 40% to 20%. The only disparity to the trend was day 13 which showed an increased level of quiescent cells and spheroid core size. The viable rim decreased in size over time whilst the total area increases throughout the whole experimental period.

The total area of the 2.5 x 10^4 MCF7 spheroids increased over time (Figure 3.9). Similarly, the 3.5 x 10^4 spheroids (Figure 3.10) followed the same trend. The 2.5 x 10^4 spheroid increased in size throughout the two-week period. The total area of the spheroid increased from approximately 100, 000 to 225, 000 μm^2 (Figure 3.9). The core and quiescent cells occupied 60% of the initial spheroid mass, in comparison to 75% at day 15. On the other hand, the viable rim occupied 40% of the spheroid mass initially and decreased to 25% by the end of the 14 days. Interestingly, the spheroids seeded from 3.5 x 10^4 cells (Figure 3.10) increased by 125% from their initial size over the period of 15 days, whist the spheroids seeded from 2.5 x 10^4 cells increased by 201% over 19 days. These results also show that the spheroids seeded at a larger seeding density have a slower growth rate over the same period, being a 101% growth rate in spheroids seeded at 2.5 x 10^4 and 25% growth rate in the spheroids seeded at 3.5 x 10^4.

3.3.3   Evaluation of spheroid structure and integrity

To evaluate spheroid integrity and structure, spheroids generated from MCF7 and U-87 MG cells were fixed, embedded in OCT, sectioned, and stained with H&E (as noted in section 2.6).
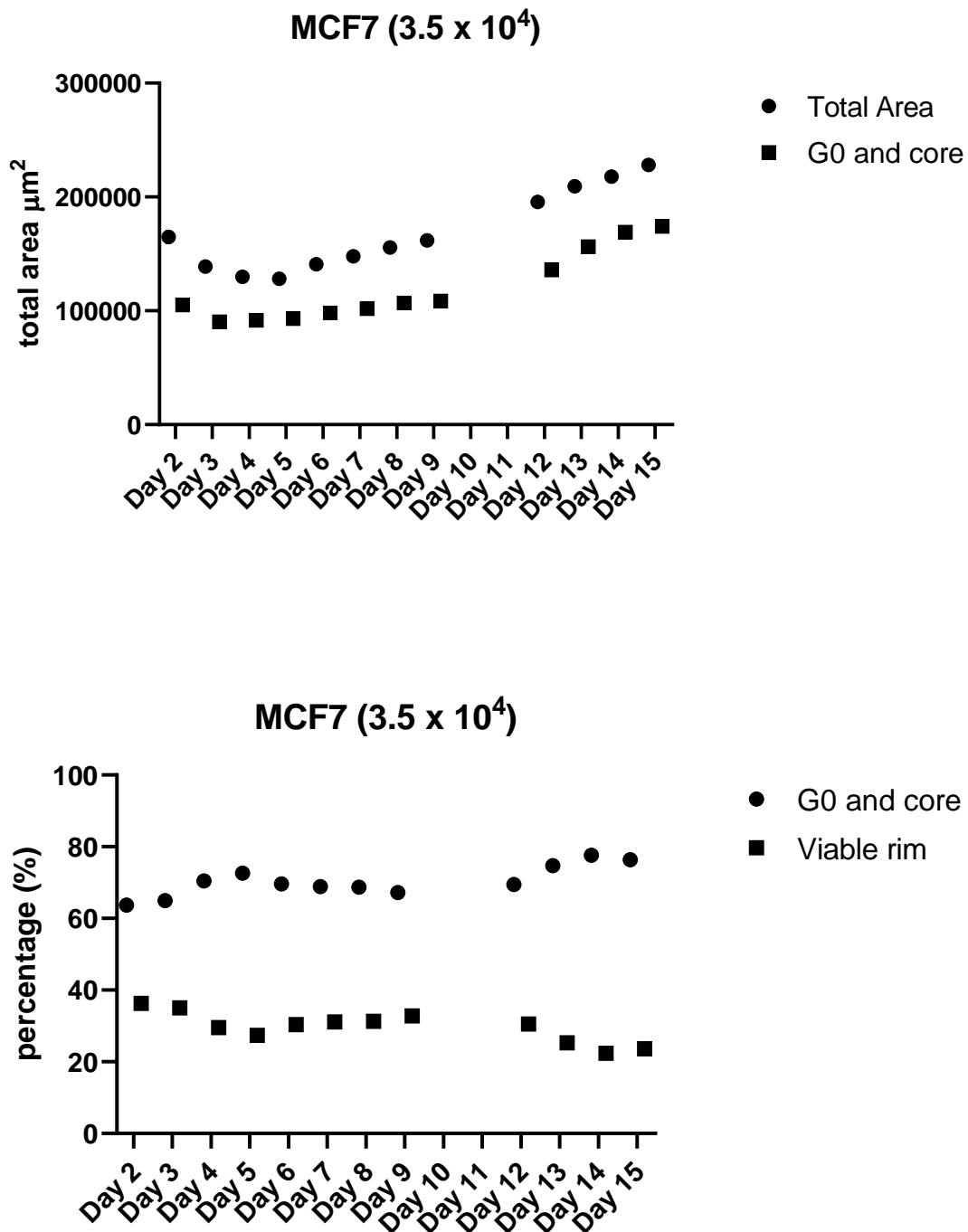
Figure 3.10: *3.5 x 10 ^{4} MCF7 spheroid total area and area of core and quiescent cells a) core and viable rim as a percentage of the total area b)*

MCF7 Spheroids were formed from cell suspensions of 3.5 x 10 ^{4} cells per well. The wells were left undisturbed for a period of 96 h, and subsequently the spheroids were imaged every 24 h for 15 days, using a Zeiss inverted microscope at 5x magnification. For each spheroid, ImageJ analysis software was used to plot the spheroid core and the total spheroid. The percentages calculated were of both the core (a) and proliferative rim of cells (b) against the total spheroid size. The standard errors of the experiments are presented on the graph. n=3 experimental repeats in triplicate.

Figure 3.11 depicts H&E stained sections for MCF7 (3.11) and U-87 MG (3.11) spheroids $(3.5 \times 10^4$ cells per well). It can be observed that both the MCF7 and U-87 MG spheroids had similar structures. There was intense dark blue staining around the extremity of both spheroids, suggesting there was a large volume of nucleic acids/acidophilic structures present. The larger level of acidophilic structures suggests that there was a higher level of cellular turnover and therefore that this was the viable rim of cells. These data show that the spheroids generated had the expected structure for these type of 3D models.

3.3.4 Immunocytochemical analysis of spheroids

3.4.4.1 Optimisation of staining protocol: β-actin control in spheroids

β-actin, a cytoskeletal protein, is an abundant protein frequently used as a loading or housekeeping control (Eaton *et al* 2013). In this report, β-actin was used to test the IHC methodology on the spheroid sections. In Figures 3.12 and 13, it can be observed that samples incubated with the β-actin antibody had an intense brown staining, whereas all control samples (isotype, secondary, TBS and cell only controls) showed no brown precipitate indicating there was no staining present. This indicates that the method was suitable for further testing.
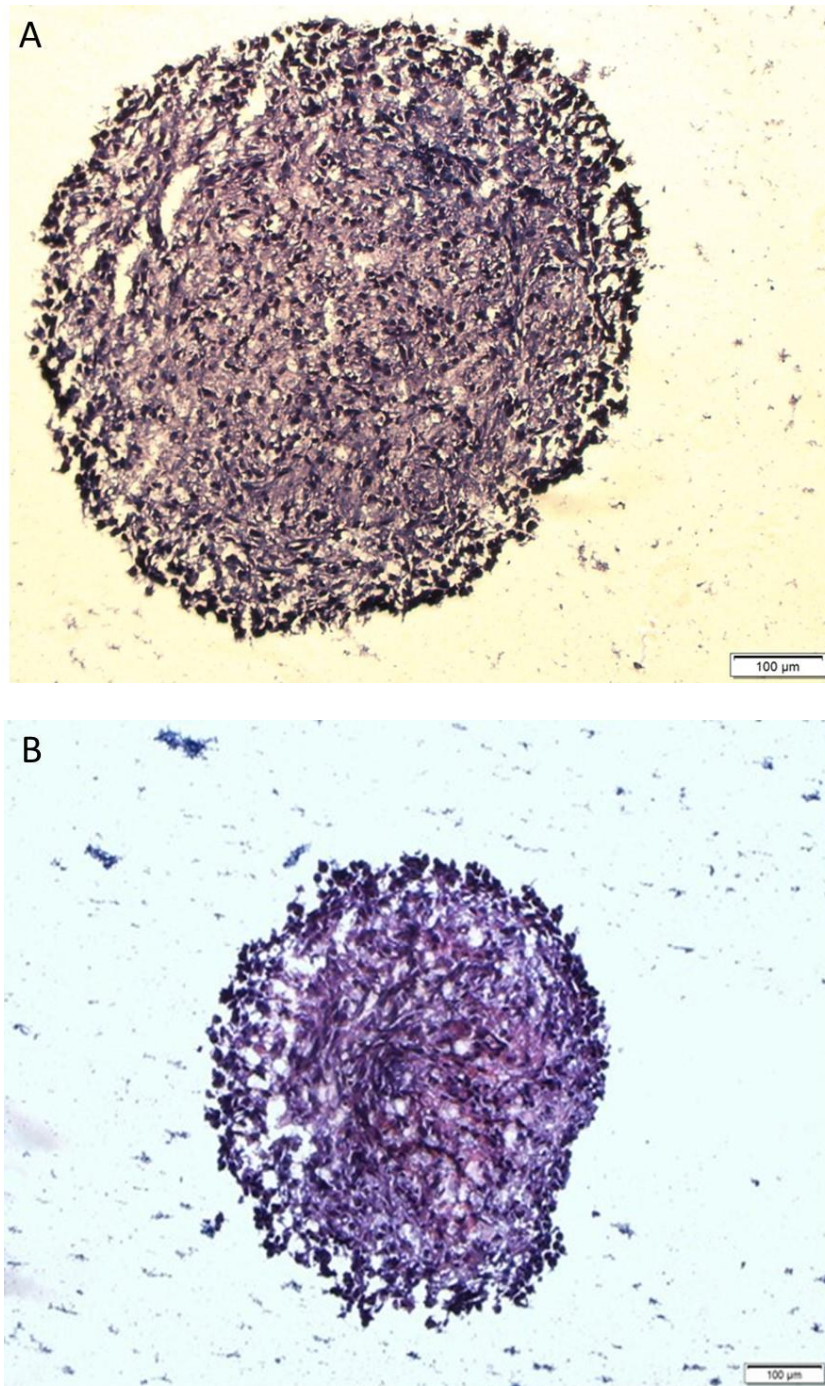
Figure 3.11: H&E staining for MCF7 and U-87 MG spheroids

H&E stained (A) MCF7 and (B) U-87 MG spheroid (3.5x10^4 cells per well), processed as noted in section 2.6. Haematoxylin stains basophilic/acidic structures, such as nucleic acids, blue. Eosin stains acidophilic/basic structures, such as cytoplasm, red. Scale bar is 100 µm. n=3 experimental repeats in triplicate.
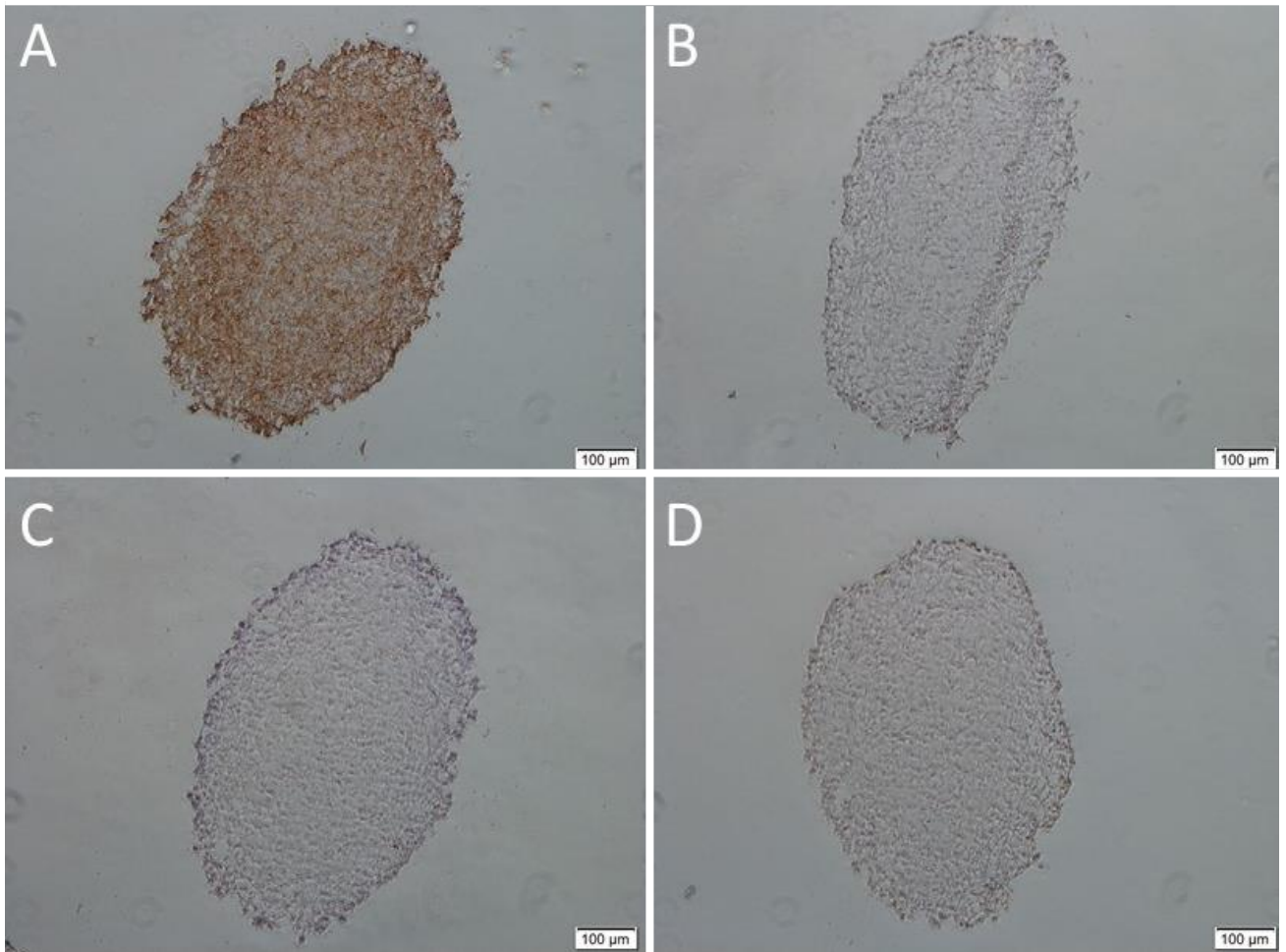
Figure 3.12: MCF7 spheroid β-actin IHC

MCF7 spheroid (seeded at 3.5 x 10⁴) cryo-sections stained for β-actin, as described in section 2.6. Key: β-actin antibody diluted 1:100 (A) Mouse Isotype IgG1 Mopc-21 antibody control diluted 1:100 (B) Secondary mouse HRP conjugated antibody diluted 1:100 (C) TBS only (D) Scale bars represent 100 μm. n=3 experimental repeats
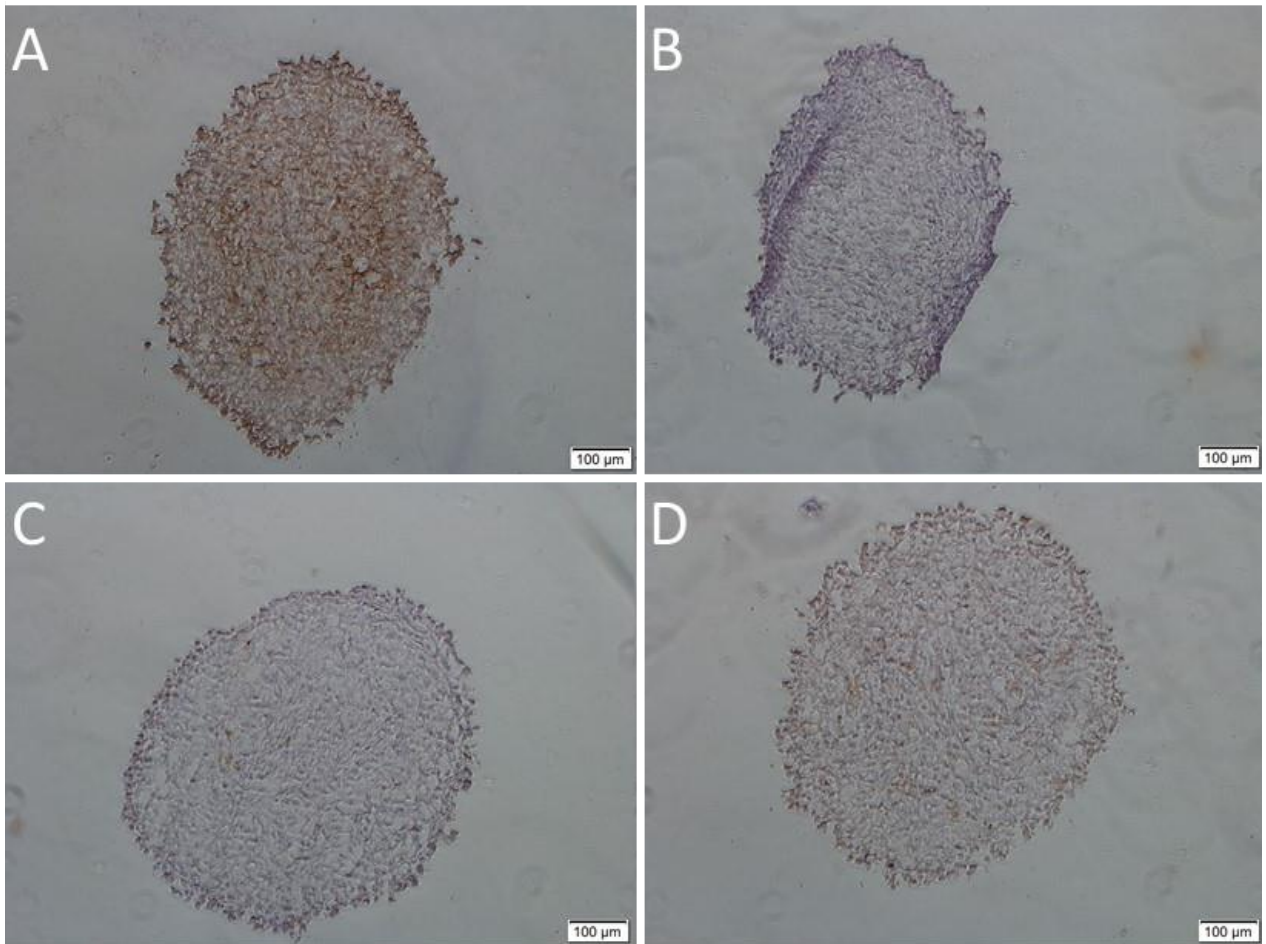
Figure 3.13: U-87 MG spheroid β-actin IHC

U-87 MG spheroids (seeded at 3.5 x 10⁴) cryo-sections stained for β-actin, as described in section 2.6. Key: β-actin antibody diluted 1:100 (A) Mouse Isotype IgG1 Mopc-21 antibody control diluted 1:100 (B) Secondary mouse HRP conjugated antibody diluted 1:100 (C) TBS only (D) Scale bars represent 100 μm. n=3 experimental repeats.

3.4.4.2   Optimisation of staining protocol: CAIX

One of the most readily inducible proteins of HIF is carbonic anhydrase IX (CAIX) (Kuijper *et al.*, 2005). CAIX expression was therefore tested in spheroid sections as an intrinsic marker of hypoxia. CAIX IHC was performed on MCF7 and U-87 MG spheroids (Figures 3.14 and 3.15). Sections incubated with CAIX (Figures 3.14 and 15) had brown precipitate present across the whole section of the spheroid, whereas the relevant controls all showed no staining. It would be plausible that CAIX should be present in the spheroids due to the diffusion limit of oxygen (200 μm) (Grimes *et al.*, 2014; Zanoni M *et al.*, 2016). Therefore, it was predicted that a centralised ring of CAIX staining approximately 200 μm from the spheroid edge should have been present (Kuijper *et al.*, 2005). However, the intense brown staining observed throughout the samples was unexpected, as the staining was predicted to be restricted to a central hypoxic core, indicating CAIX might not be an ideal hypoxia marker for these samples. Therefore, an alternate hypoxic marker was considered.

Hypoxyprobe is a nitroimidazole with hypoxic sensitivity, making it an ideal hypoxia specific dye (Varia *et al*, 1998). Hypoxyprobe is reduced in hypoxic cells and binds -SH containing groups (thiols) in hypoxic cells (Varia *et al*, 1998). In order to evaluate this marker, MCF7 spheroids were seeded at 2.5 x 10^4 cells per well and incubated with 5 μM Hypoxyprobe and processed as before. Samples were stained for the presence of Hypoxyprobe using immunofluorescence (Figure 3.16). Intense green staining was observed at the central region of the spheroid, indicating Hypoxyprobe binding and localisation. The distance was approximately 100 μm from the lower right-hand edge, and about 200 μm from the upper left section of the spheroid, which is consistent with the oxygen diffusion distances in the literature (Mehta *et al.*, 2012). These data indicate that Hypoxyprobe treatment can be used as a hypoxia marker in these models.
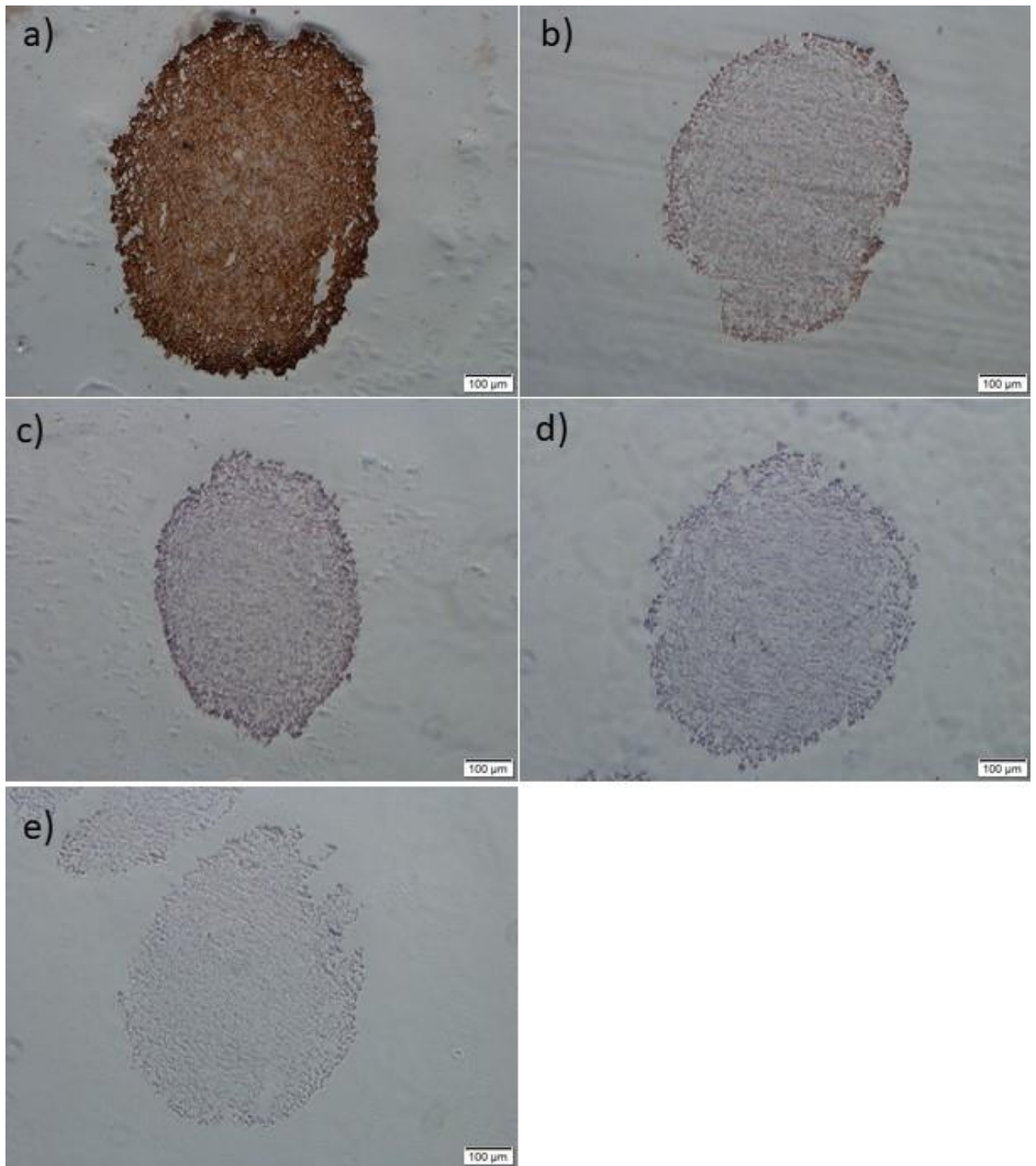
Figure 3.14: MCF7 spheroid CAIX Immunohistochemistry

MCF7 spheroids (seeded at 3.5 x 10^4) cryo-sections stained for the hypoxic marker CAIX as described in section 2.6. Key: CAIX antibody diluted 1:100 (A) Mouse Isotype IgG1 Mopc-21 antibody control diluted 1:100 (B) Secondary mouse HRP conjugated antibody diluted 1:100 (C) TBS only (D) and Cell only (E) Scale bars represent 100 μm. n=3 experimental repeats.
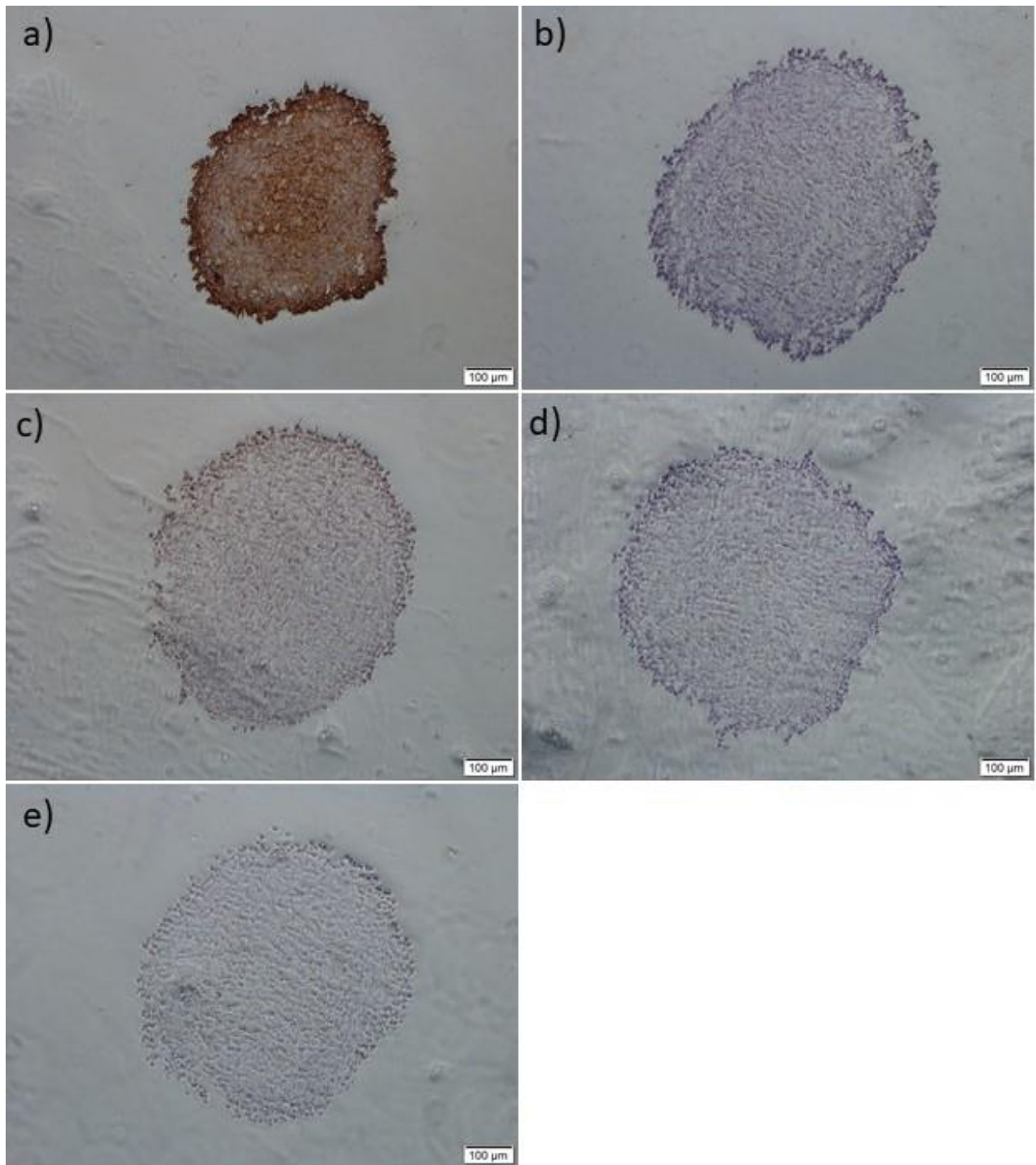
Figure 3.15: U-87 MG spheroid CAIX Immunohistochemistry

U-87 MG spheroids (seeded at 3.5 x 10⁴) cryo-sections stained for the hypoxic marker CAIX as described in section 2.6. Key: CAIX antibody diluted 1:100 (A) Mouse Isotype IgG1 Mopc-21 antibody control diluted 1:100 (B) Secondary mouse HRP conjugated antibody diluted 1:100 (C) TBS only (D) and Cell only (E) Scale bars represent 100 µm. n=3 experimental repeats.
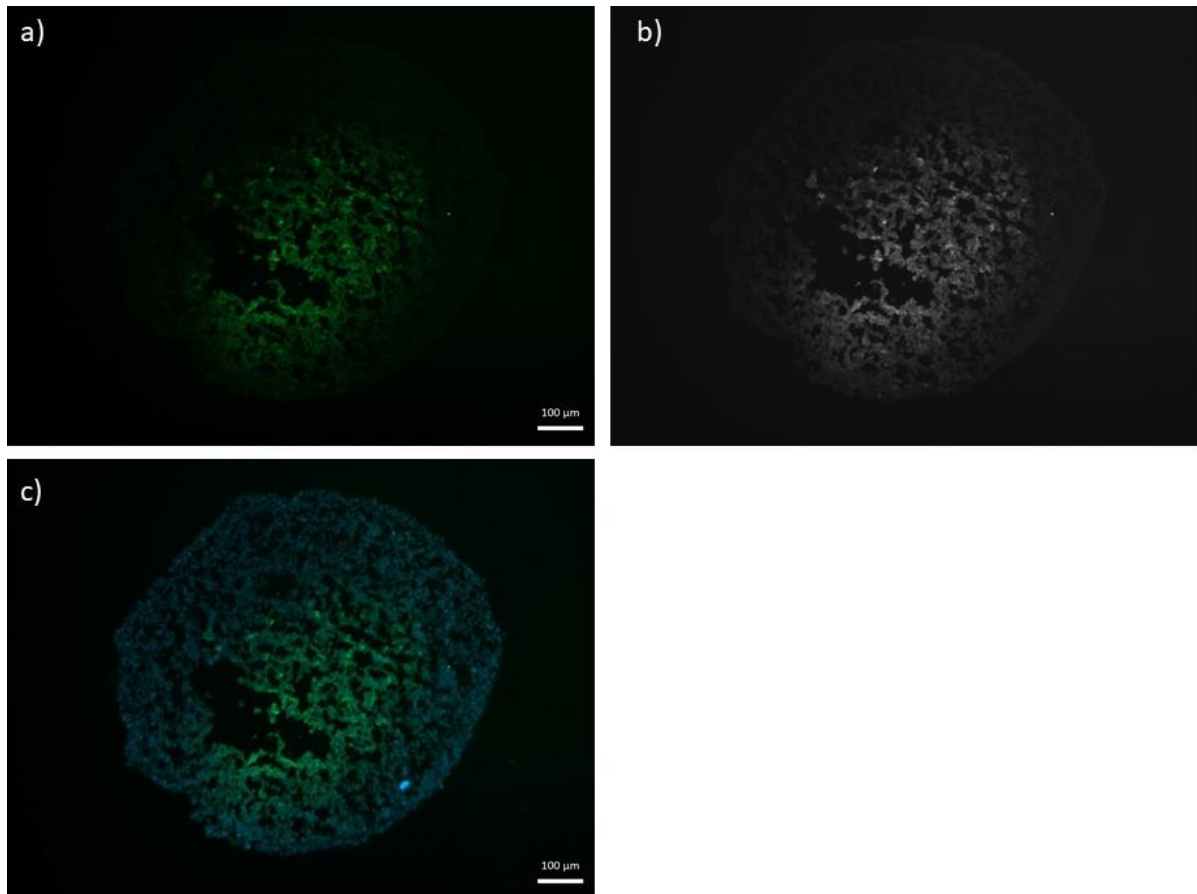
Figure 3.16: MCF7 spheroid Hypoxyprobe immunofluorescence variability

MCF7 spheroids (seeded at 2.5 x 10^4) cryo-sections stained for the hypoxic marker Hypoxyprobe (PIMO) as described in section 2.6. In brief MCF7 spheroids were incubated with 200 μMol Hypoxyprobe PIMO for 90 mins before being washed in PBS and stained using IF as described in section 2.6. (a) Alexa 488 green Hypoxyprobe stain (b) greyscale PIMO stain (c) Merge image. Green fluorescence indicates positive hypoxyprobe stain, blue fluorescence corresponds to nuclei counterstain positivity (DAPI stain). Scale bar represents 100 μm. n=5 experimental repeats

3.3.5 Assessment of the proliferative rim within spheroids through Ki-67 staining

To evaluate the spheroid proliferative rim, immunofluorescence analysis of a proliferative marker, Ki-67 was adopted. Ki-67 is a cellular marker of proliferation found exclusively within the nucleus of cells during interphase (Scholzen, 2000). Sections of MCF7 spheroids seeded at different densities were stained for Ki-67 (figure 3.17). The green Ki-67 and blue DAPI counterstain can clearly be seen with the green fluorescence localised to the extremity/rim of the spheroids. This was observed for all seeding densities. The fluorescence appeared to be throughout most of the spheroid on the lower seeding density sections (except for the core), whilst the remainder of the sections showed Ki-67 staining at approximately 50 μm at and from the spheroid edge.

Overall, these data indicate that the chosen spheroid models present the characteristic spheroid structure zones, including a hypoxic core (as shown by the Hypoxyprobe staining) and proliferative rim (as shown by the Ki-67 staining).

3.3.6 Analysis of migrative and invasive capability of spheroids on hydrogels

To validate the methodologies to evaluate the migration and invasive potential of the spheroid models in preparation for on-chip work, invasion and migration assays were conducted using different hydrogels, *i.e.* Matrigel, collagen and hydrogel. This would allow the determination of the ability of different cell lines to invade and migrate in or over different matrices during a set period time, both in a conventional off-chip environment and in on-chip conditions. As seen in Figure 3.18, the level of cell migration and invasion increased over time for U-87 MG and MDA-MB-231 spheroids. For example, in the U-87 MG spheroids, the migration front increased 400% when incubated in Matrigel over 72 h, whilst there was a 200% increase in area for U-87 MG spheroids incubated in collagen over 72 h.
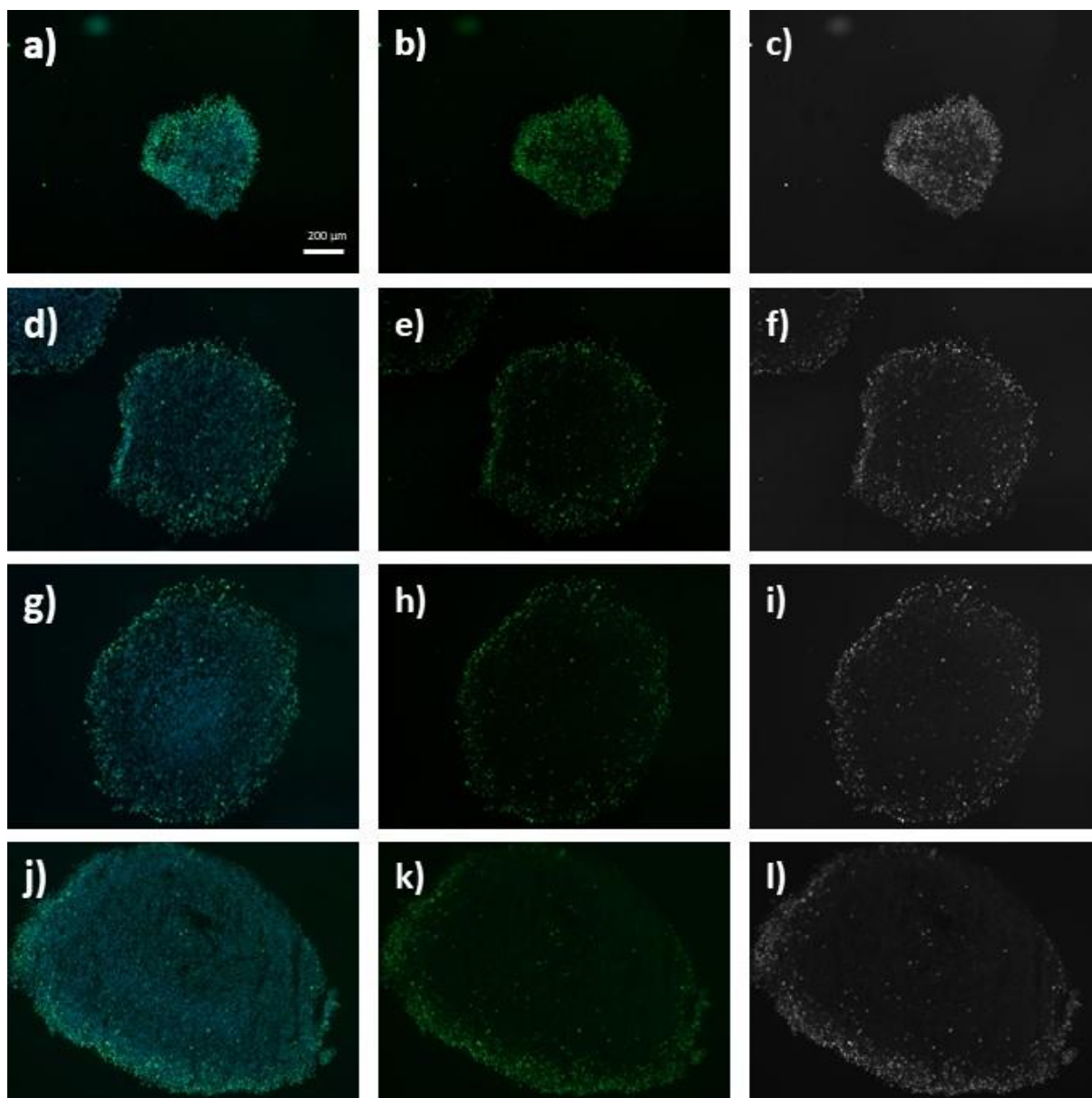
Figure 3.17: MCF7 spheroid Ki-67 Immunofluorescence

MCF7 spheroids (seeded at a) 5 x 10³, b) 2.5 x 10⁴, c) 3.5 x 10⁴ and d) 5 x 10⁴) cryo-sections stained for the proliferative marker Ki-67 as described in section 2.6. Green fluorescence indicates positive Ki67 stain, blue fluorescence corresponds to nuclei counterstain positivity (DAPI stain). a, d, g, j) merge image of DAPI and Alexa 488. b, e, h, k) Alexa 488 only. c, f, I, l) greyscale image of Alexa 488 Ki-67 stain for clarity. Scale bar represents 200 μm. n=3 experimental repeats.
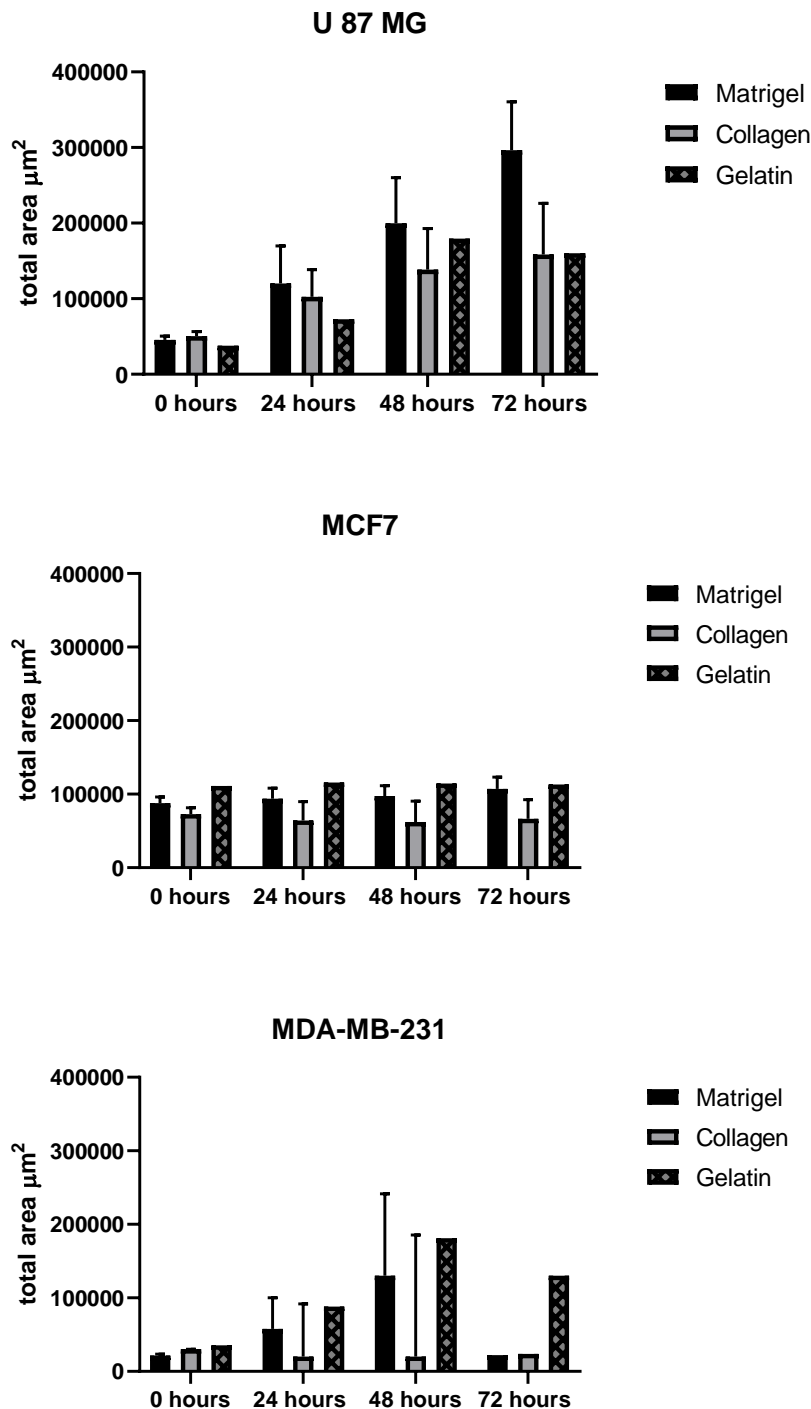
Figure 3.18: U-87 MG, MCF7 and MDA-MB-231 spheroid migration on three hydrogels

U-87 MG a), MCF7 b) and MDA-MB-231 c) spheroids (seeded at 2.5 x 10^4) placed on three hydrogels; Matrigel, collagen and gelatin, and measured for migration (total area in pixels) over a period of 72 h. Migration times equate to t=0, t=24, t= 48 and t=72. SE of n=3 (for Matrigel and collagen). Two way ANOVA shows no significance, similarly no significance was seen between different cell types and hydrogels. See appendix image 7.1..

Moreover, the migration area observed on the images of U-87 MG spheroids increased 4x over 48 h in gelatin; there was a variation at 72 h at which a decrease was observed. The area of the MDA-MB-231 spheroids increased 500% in Matrigel over only 48 h. Moreover, when incubated in gelatin, the MDA-MB-231 spheroids increased in migration to 350% over 48 h. In collagen and gelatin MCF7 spheroids do not migrate or invade, however, when in Matrigel, (Figure 3.18), MCF7 spheroids total area increased by 25%.

Figure 3.19 shows the migratory ability of U-87 MG, MCF7 and MDA-MB-231 spheroids over time when placed on different collagen concentrations. U-87 MG spheroids did not appear to increase their migration front over time when incubated on 1 mg collagen (Figure 3.19). Whilst on 2 mg collagen, U-87 MG spheroids maintained their size over time. However, when incubated on 3 mg collagen the U-87 MG spheroids increased in migration from 200 μm to 750 μm over 72 h. These results support the results seen in figure 3.18, where the U-87 MG spheroids migrated over time in 3 mg collagen. Similarly, the migration front of MDA-MB-231 spheroids increased over time for all concentrations of collagen (Figure 3.21). However, at 1 mg and 2 mg of collagen, the level of increased migration was 50% by 48h incubation, whilst the increased migration in 3 mg was 100% from 0 to 24 h and 300% from 24 to 48 h. Similarly, like the results seen in figure 3.20, where MCF7 spheroids do not migrate, MCF7 spheroids also did not migrate at any time point in different collagen concentrations.
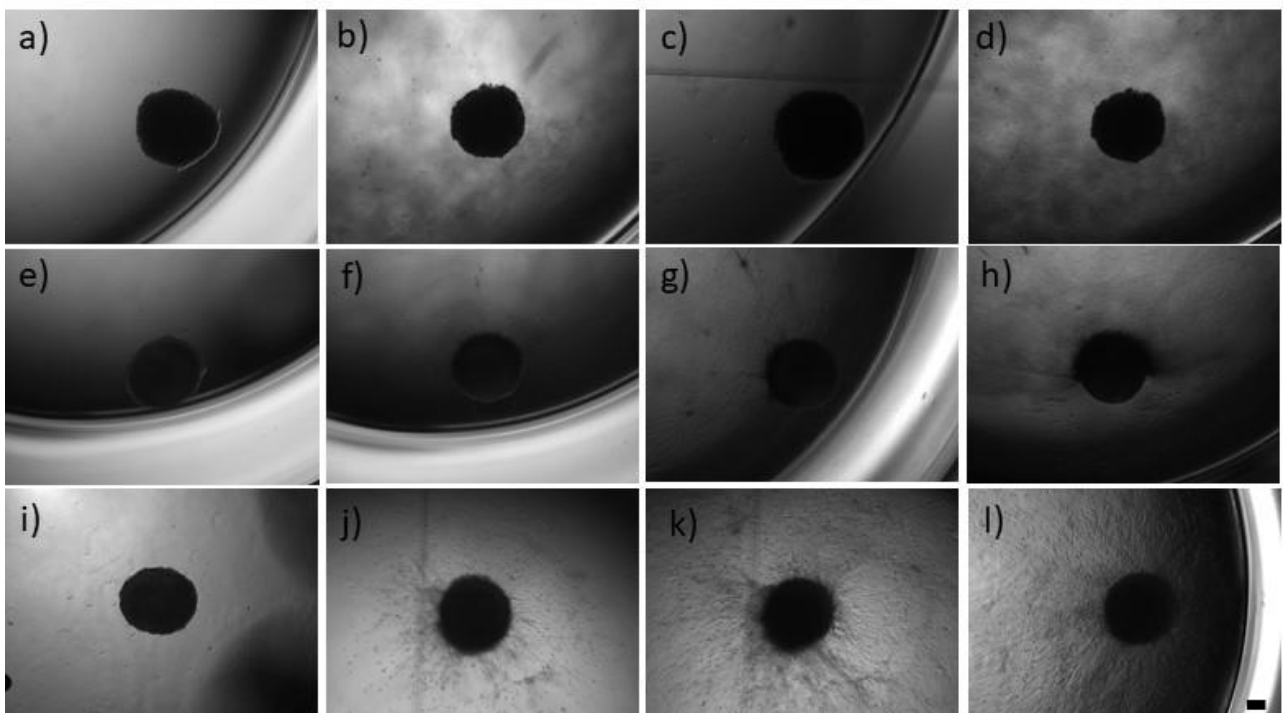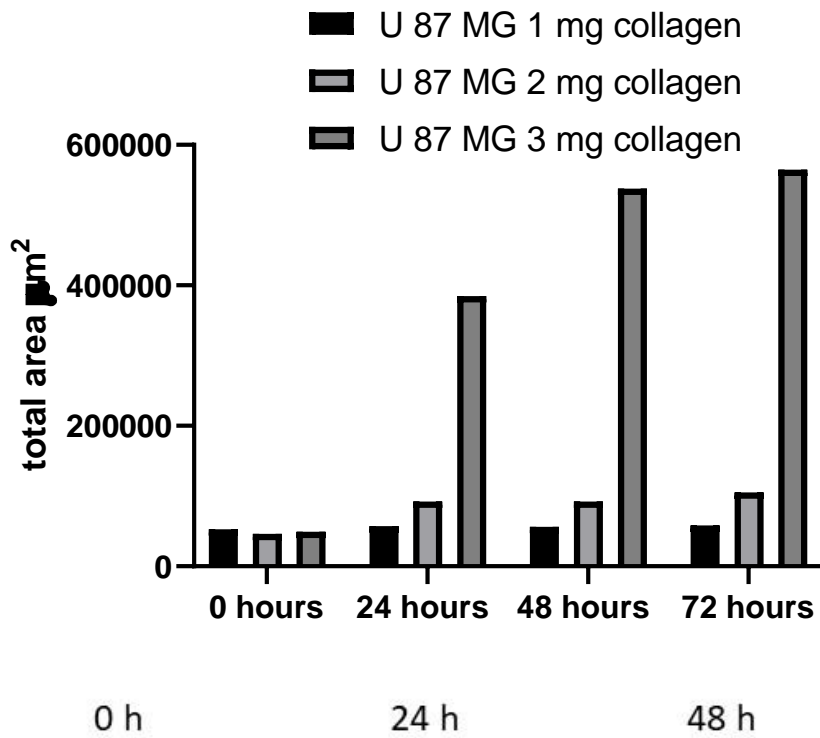
Figure 3.19: U-87 MG spheroid migration on three concentrations of collagen

U-87 MG spheroids (seeded at 2.5 x 10⁴) placed on varying concentrations of collagen. Representative images 1mg a-d), 2mg e-h) and 3 mg i-l) at 0, 24, 48 and 72 h. Spheroids were measured for migration (total area) over a period of 72 h and plotted in a histogram as shown above. Scale = 200 µm. n=1(in triplicate)
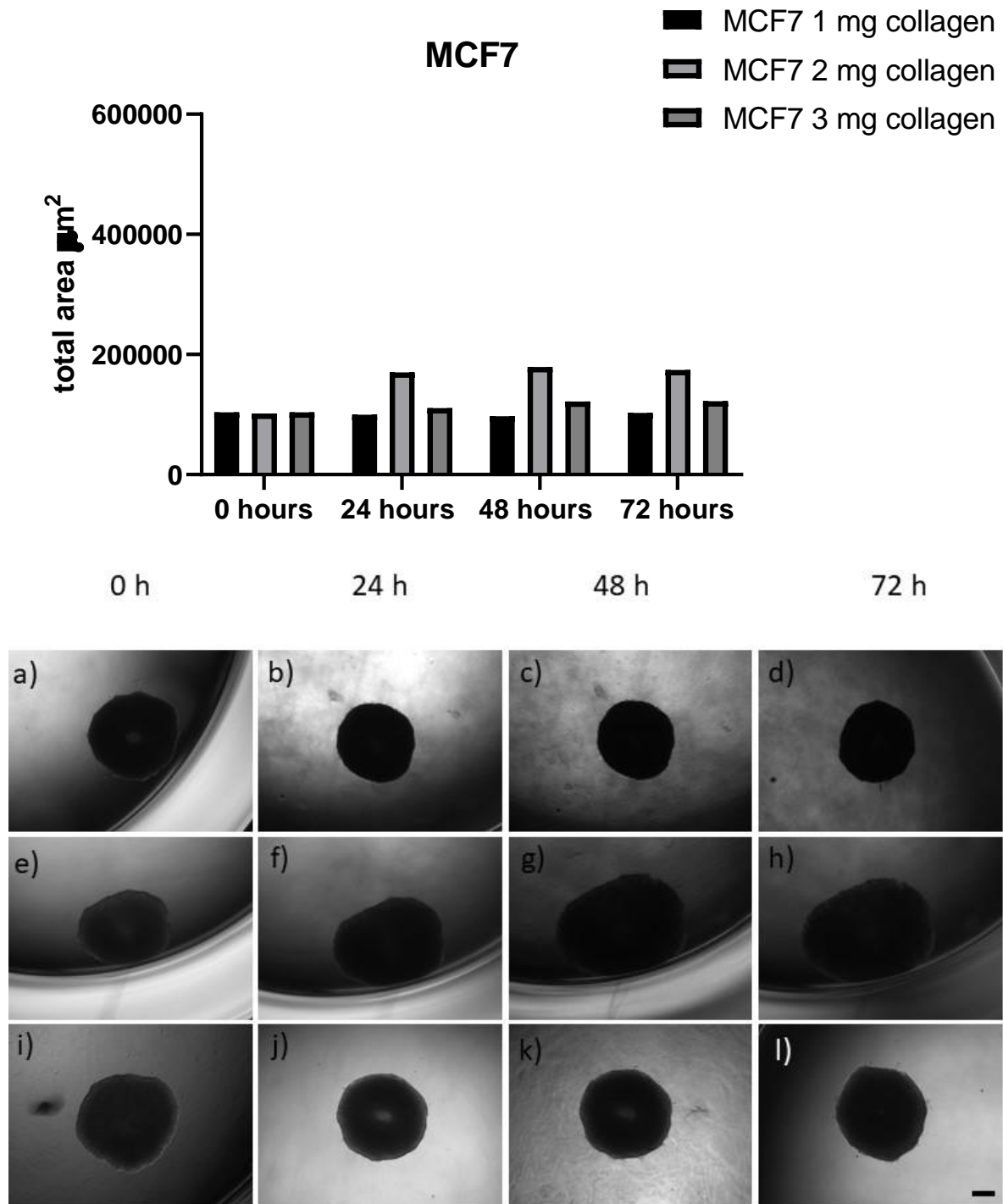
Figure 3.20: MCF7 spheroid migration on three concentrations of collagen

MCF7 spheroids (seeded at 2.5 x 10⁴) placed on varying concentrations of collagen. Representative images 1mg a-d), 2mg e-h) and 3 mg i-l) at 0, 24, 48 and 72 h. Spheroids were measured for migration (total area) over a period of 72 h and plotted in a histogram as shown above. Scale = 200 μm. n=1(in triplicate)
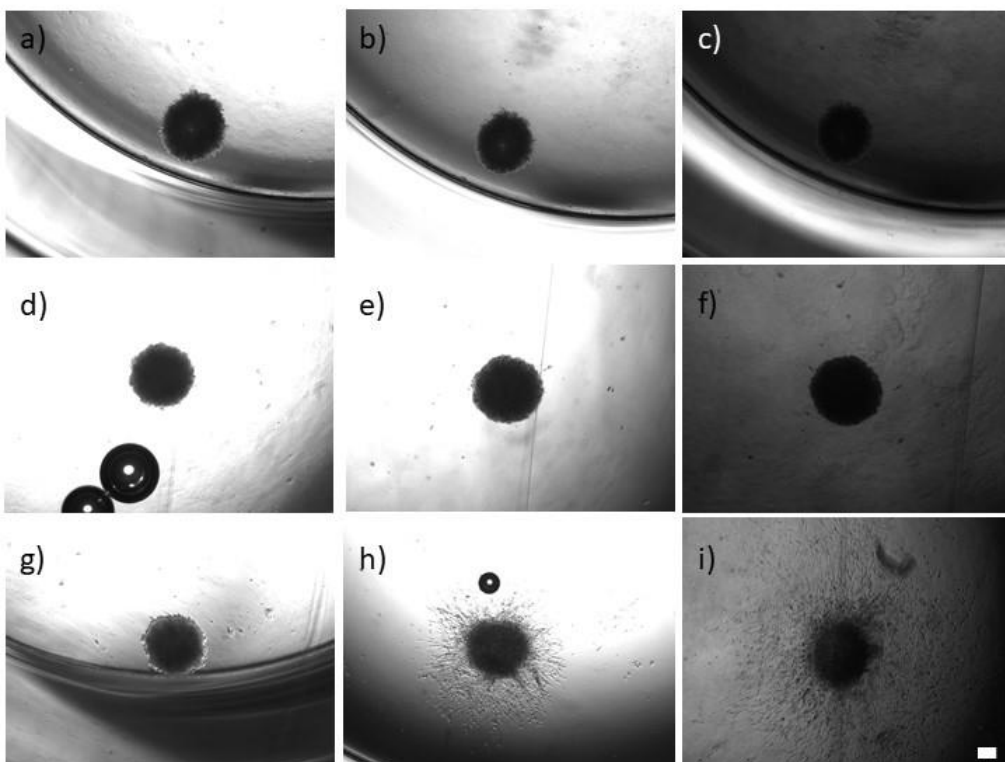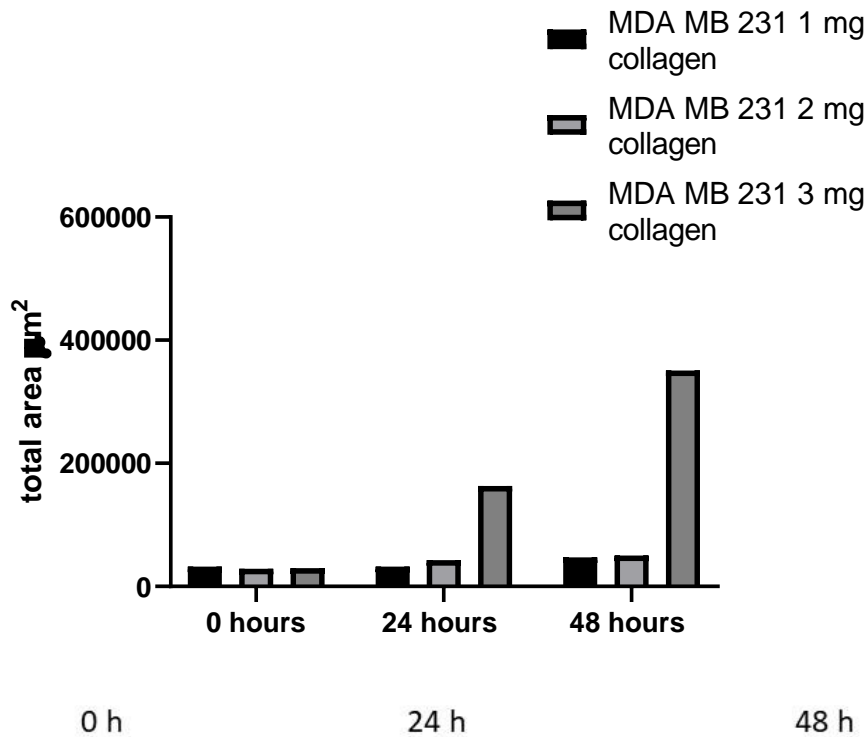
Figure 3.21: MDA-MB-231 spheroid migration on three concentrations of collagen

MDA-MB-231 spheroids (seeded at 2.5 x 10⁴) placed on varying concentrations of collagen. Representative images 1mg a-c), 2mg d-f) and 3 mg g-i) at 0, 24, 48 and 72 h. Spheroids were measured for migration (total area) over a period of 72 h and plotted in a histogram as shown above. Scale = 200 μm. n=1(in triplicate)

Finally, figure 3.22 shows U-87 MG, MCF7 and MDA-MB-231 spheroids in Matrigel, collagen, and a combination of both hydrogels. The data shows that for all hydrogels, U-87 MG spheroids increased in migration and invasion over time (72 h), with the largest increase being in Matrigel at 400%, followed by collagen at 200% and then in both hydrogels together at 150%. The MDA- MB-231 spheroids followed the same trend seen in the U-87 MG spheroids, *i.e.* the spheroids' migration and invasion increased over time. The largest increase was seen in collagen (10 x), followed by Matrigel (9 x) and finally the combination of two hydrogels together. Interestingly, the MCF7 spheroids do not migrate or invade in either of Matrigel or collagen. However, when a combination of Matrigel and collagen was used, the MCF7 spheroids migrated and invaded over time, although very minimally at 28% its original size. When comparing spheroids from different cell lines between hydrogels, at the same time points, no significant differences were found. Except for at 72 h, 1* significance was found between U-87 MG and MDA-MB-231 in Matrigel.
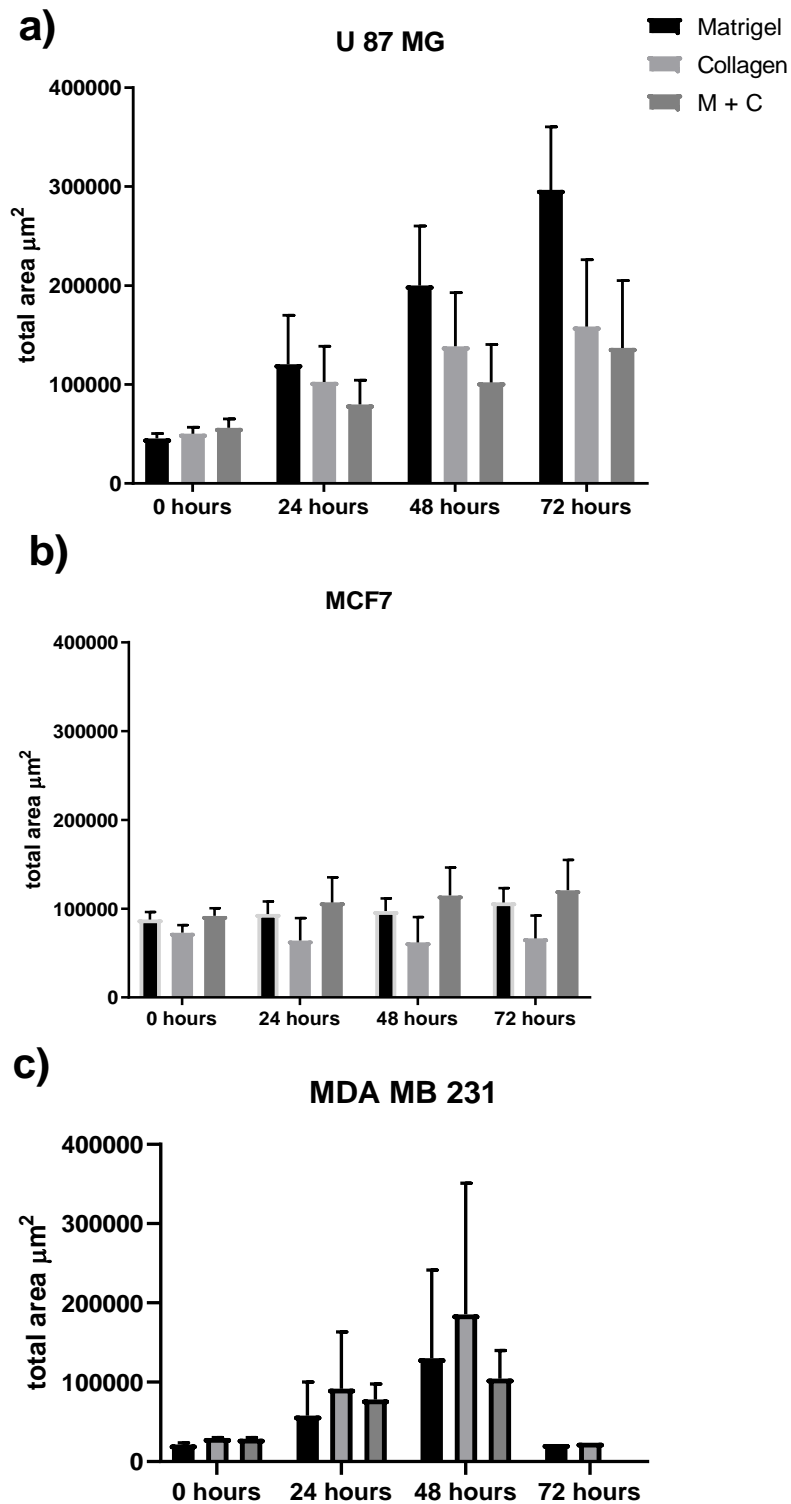
Figure 3.22: U-87 MG, MCF7 and MDA-MB-231 spheroid migration on three concentrations of collagen

U-87 MG a), MCF7 b) and MDA-MB-231 c) spheroids (seeded at 2.5 x 10⁴) placed on various hydrogels; Matrigel, collagen and Matrigel with collagen. Spheroids were measured for migration (total area) over a period of 72 h. Migration times equate to t=0, t=24, t= 48 and t=72. Two way ANOVA was conducted and showed no significance. n=3 experimental repeats in triplicate.

3.4 Discussion

The key aim of this chapter was to establish which spheroids would be suitable for introduction into a microfluidic device. In order to do this, the objectives were to establish and characterise spheroid formation, growth kinetics, structure, and migration/invasion potential.

3.4.1   Key findings:

The key findings of this chapter included the following:

- Spheroids could be grown from all cell lines used. The MDA-MB-231 spheroids were larger than the other cell lines at the same seeding densities. It was demonstrated that spheroids could be generated reliably and reproducibly.

- MCF7 and U-87 MG were tested for their growth pattern, which followed a four phase growth pattern over time.

- Spheroids showed a proliferative rim of cells at their edge and a central hypoxic region in the centre.

- Finally, it was demonstrated that spheroids migrated at different levels over different matrices. MCF7 spheroids did not migrate or invade over time, whilst MDA-MB-231 and U-87 MG spheroids migrated and invaded over the studied period of 72 h.

3.4.2   Characterisation and choice of spheroid models to use in microfluidic device

Spheroid size is correlated to the cell function within, the transport of chemicals, drug efficacy on cells and migration of cells (Vaithilingam *et al*., 1991;Katt *et al*., 2016). Spheroids follow a four-phase system of growth (Mehta *et al*., 2012). As seen in figure 6, U-87 MG and MCF7

spheroids started in the lag phase of growth from day 1 to day 3 or 4, from when the spheroids increased in size to their peak through logarithmic growth over a two to three-week period (Figures 3.7 & 3.9/10). Moreover, all other cell lines tested were found to produce spheroids by the 72-96 h timepoint.

3.5.2.1 Characterisation of spheroid size profiles

Differences in spheroid size were noted amongst all the cell lines used. MDA-MB-231 spheroids appeared to be loosely aggregated, as previously reported (Vinci *et al.*, 2012). It is possible that MDA-MB-231 spheroids are larger than the other spheroids due the actual cell width or diameter. MDA-MB-231 cells are 14-18 μm in diameter, MCF7 are 10-14 μm in diameter and U-87 MG cells are 12–14 μm in diameter (Wagner *et al.*, 2011; Liu *et al.*, 2015). Therefore, it is unlikely that increased MDA-MB-231 spheroid size equates to cell diameters. MCF7 cells form tightly bound spheroids, associated with high levels of E-Cadherin present between the epithelial like tumour cells (like MCF7) (Iglesias *et al.*, 2013). MDA-MB-231 cells are more mesenchymal having undergone the EMT process, expressing factors and proteins associated with an aggressive and motile phenotype, namely N-cadherin. (Holliday & Speirs, 2011). As E-Cadherin has been shown to be a critical factor in breast cancer spheroid formation, decreased levels of E-Cadherin and, lack of binding matrices to form MDA-MB-231 spheroids could result in a loose appearance (Vinci *et al.*, 2012). This observation is also supported by Han, Takayama and Park. (Han *et al.*, 2015) who reported that both MCF7 and HCT116 cells formed tight and compact spheroids (Han *et al.*, 2015).

A key observation of this initial study was that as cell seeding density increased, so did the spheroid diameter, across all cell lines used. The study also showed that spheroid generation was reproducible and reliable. In order to confirm that the spheroids were following the four-phase day of growth as detailed, a growth curve analysis was conducted.

3.5.2.2 Assess ability of different cells to generate spheroids and investigate differences between spheroid sizes

U-87 MG and MCF7 spheroids follow conventional growth patterns (Sutherland, 1988; Gong et al., 2015; Rodriguez et al., 2015). Formation of MCF7 spheroids at an earlier time point was noted in the higher seeding density (3.5×10^4), day 3-4 as opposed to 4-5 in 2.5×10^4 cells per well. Gong et al. reported a 9% growth rate in spheroids seeded at 8×10^3 cells per well in comparison to a 31% growth rate in 2×10^3 cells per well (Gong et al., 2015). In the work presented here, both U-87 MG and MCF7 spheroids were seeded at 3.5×10^4 cells per well, more than four times higher than the cell densities reported by Gong et al. In the larger size of the U-87 MG spheroids, in comparison to Gong et al., the decreased growth could be due to cell apoptosis, resulting through the inability of a higher percentage of cells able to obtain nutrients and oxygen (Mehta et al., 2012). This could account for weaker cell-cell adhesion (Sutherland, 1988). This decreased metabolism results from cellular biochemical interactions. These biochemical interactions modulate energy consumption. Therefore, this process could further influence the fraction quiescent cells and viable rim through modification of O_2 gradients, resulting in a lower growth rate in larger seeded spheroids (Mueller-Klieser W et al., 1986). Overall both MCF7 and U-87 MG spheroids appear to follow the correct phases of spheroid growth (Sutherland, 1988).

3.4.3 Characterisation of spheroid regions

3.4.3.1 *Spheroid core, quiescent cells and proliferative rim*

The size of the necrotic core and the proliferative rim influences the ability of the spheroid to grow (Mehta *et al*., 2012). The data showed that as time increased so did the percentage of quiescent cells and the spheroids core, for both seeding densities tested. The spheroid total area increase showed that the spheroid mass was getting larger over time. This increase in total area could be accounted for by the weaker interactions between cells within cell core. The lack of nutrients and waste build up within the cell core results in necrotic and apoptotic cells. This waste would perpetuate, create toxic metabolic products, resulting in further cell death. This build up could also potentially account for weaker cell-cell adhesion (Sutherland, 1988), meaning a more loosely aggregated cell cluster. Overall spheroids core, quiescent and proliferative cells followed the expected pattern. However, this methodology is only a semi-quantitive method, and to give a better true value, could be repeated by different people, different days or using a threshold limit on imageJ.

3.4.3.2 *Spheroid biological characterisation – spheroid structure*

H&E staining of spheroid sections was essential to determine the overall spheroid structure (Figures 3.11). Spheroids were incubated in 30% sucrose (an isotonic solution to prevent ice crystal formation protecting the spheroid structure in OCT) (McDowall *et al*. 1983; Griffiths *et al*. 1984; McDowall *et al*. 1983). H&E staining showed that there is intense haematoxylin staining at the spheroid edge, indicating a larger volume of nucleic acids, which is the proliferating cell rim presented previously (Sutherland, 1988; Mehta *et al*., 2012; Zanoni M *et al*., 2016). Overall the spheroid structures were consistent with those observed in the literature,

demonstrating the conserved and maintained spheroid structure (Bhave *et al*., 2015; Senkowski *et al*., 2015).

3.4.3.3   Spheroid biological characterisation – hypoxic regions

The most likely target of hypoxia is the transcription factor hypoxia inducible factor (HIF). One of the best characterised downstream targets of HIF is carbonic anhydrase IX (CAIX), which is therefore used as a marker of hypoxia (Kuijper *et al*., 2005). CAIX is shown to contribute to the pre-metastatic niche through its interactions with myeloid derived stem cells (MDSC). Stewart and colleagues reported that CAIX may promote cell invasiveness, migration and angiogenesis (Stewart *et al*., 2014; Chafe & Dedhar, 2015; Chafe *et al*., 2015). A plausible explanation for the intense brown staining seen throughout the spheroid could be due to the accumulation of catabolites, protons and lactate (Chafe *et al*, 2015) resulting in lower pH resulting in increased CAIX expression (Kuijper *et al*., 2005; Chafe & Dedhar, 2015).

Panisova and colleagues demonstrated that CAIX regulation can also be driven by high density normoxic cell culture, resulting in microenvironment aberrations. Furthermore, they demonstrated that lactate increased *CA9* transcription, resulting in the upregulation of CAIX, even in normoxia (Panisova *et al*., 2017). A further study by Lu *et al.* suggest plausible reasons for this phenomenon. Cancer cells display the Warburg effect, where high rates of aerobic glycolysis are present. The end products of glycolysis are pyruvate and lactate. Even in the presence of oxygen (Lu *et al*., 2002). Therefore, spheroids, which are highly dense and tightly packed, can alter the spheroid microenvironment, increasing the transcription of *CA9*, leading to increased CAIX expression, irrelevant of oxygen content (Panisova *et al*., 2017). Moreover, the high turnover of cells at the spheroid edge results in increased glycolysis. This increased glycolysis perpetuates into a higher level of lactate production, again increasing the

transcription of *CA9* and subsequent increased expression of CAIX, even in the presence of oxygen and normoxia. Another explanation for CAIX expression in spheroids is because cells at the spheroid centre are not only hypoxic (resulting in CAIX expression) but also produce high levels of metabolites, waste and lactate. These waste products and metabolites cannot fully diffuse from the spheroid to the external environment. Altering the pH environment within the spheroid causing CAIX expression, and by directly inducing CAIX expression itself through lactate accumulation.

As HIF-1α and CAIX proved non-specific for the hypoxic regions within the spheroid, an alternative marker was used, namely Hypoxyprobe (Varia *et al*, 1998). There was a central zone of green fluorescence in the spheroid sections, indicating positive hypoxyprobe staining in the MCF7 spheroids (Figure 3.16). The staining appeared to be at least 200 μm from the spheroid edge, the entire way around the internal section within the spheroid. It is expected as oxygen can only diffuse 200 μm into the spheroid, meaning the central zone will be low in certain areas and void of oxygen in others. Overall these results confirm the observations seen in the literature. Moreover, they demonstrate that the process of fixation and embedment, cryosectioning, staining and imaging is applicable for spheroids. They also demonstrate that Hypoxyprobe is specific for hypoxia within the spheroids generated. One of the observations seen in the sectioning is an introduced artifact, the slight fragmentation seen at the lower left quarter of the spheroid section would be a microtome blade cut introduced by the user.

3.4.3.4   *Spheroid biological characterisation – Markers of proliferation*

To investigate the proliferative rim, immunofluorescence of Ki-67 was adopted (Figure 3.17). Ki-67 is thought to be involved with cell proliferation and is found exclusively within the nucleus. Ki-67 is present throughout the cell cycle (G1, S, G2, and mitosis) but is not present during cellular quiescence (G0) (Scholzen, 2000). Therefore, the protein and specifically its

location within the nucleus, is used as a marker of cell proliferation (Scholzen, 2000). Figure 3.17 demonstrates the proliferative rim is present around the different spheroids. It shows the proliferative rim is in the external zone of the spheroid, approximately 200μm into the spheroid section, the distance where oxygen and nutrient can diffuse to (Mehta *et al.*, 2012). Overall the spheroids have been shown to follow all expected trends and are proven to have three zones (Sutherland., 19988; Zanoni *et al.*, 2016).

3.4.3.5 *Spheroid biological characterisation – migration and invasion*

U-87 MG cells are grade IV malignant gliomas/astrocytomas which are correlated with poor prognosis (Ahmed *et al.*, 2014). MCF7 are ER/PR+ HER2- luminal breast cancer cells that are of lower metastatic potential than other breast cancer counterparts, they are collected from a pleural effusion and are not as migratory as other breast lines (Comsa, *et al.*, 2015). MDA-MB-231 cells are triple negative basal adeno-carcinoma cells, they are metastatic in nature and mainly spread to bone, bladder and lung (Solinas *et al.*, 2013).

To replicate the process of migration *in vitro* and investigate the difference of spread, collagen, gelatin and Matrigel were used (Weinberg and Hanahan, 2011) designed to mimic conditions found within the human body (Vinci *et al.*, 2012). Matrigel is composed of entactin, laminin, collagen, nidogen, heparan sulfate proteoglycans, proteins and growth factors, and can polymerise to produce a thick 3D gel to study invasion of cells. And is replicative of the human bodies blood vessels in comparison to collagen and gelatin (Rommerswinkel *et al.*, 2014; Jiang *et al.*, 2018). The results demonstrated that only the MCF7 cells are unable to spread and migrate in any of the conditions tested (Figure 3.18). MCF7 cells express low levels of VEGF, especially in comparison to MDA-MB-231 cells (Solinas *et al.*, 2013; Jabłońska-Trypuć *et al.*, 2016). An autocrine loop of VEFG induces MCF7 breast cancer cell migration and invasion,

but as stated, MCF7 cells express low levels of VEGF-A, VEGF- C and even lower levels of VEGF-D. MCF7 cells also express varying levels of VEGFR1 and 2 (Jabłońska-Trypuć *et al*., 2016). Moreover, MCF7 cell *in vivo* models do not induce metastasis and have been shown to have poor angiogenic potential. Whilst increasing VEGF-C concentration causes MCF7 cells to produce invasive tumour subtypes (Bartsch *et al*., 2003). MCF7 cells have been shown to express only MMP 1, 11, 14, 15 and 16. MMP1 is a collagenase which is responsible for collagen degradation, MMP 11 decreases cancer cell sensitivity to natural killer cells, whilst the other MMP's (14, 15 and 16) are responsible for cell adhesion and cell flattering reduction (Bartsch *et al*., 2003; Jabłońska-Trypuć *et al*., 2016). The lack of migration seen in the MCF7 spheroids in the gelatin and Matrigel can be explained by the MCF7's inability to digest and break down the ECM-like matrices. Similarly, the lack of migratory potential, low levels of VEGF and lack of MMP expression explains the low migration and spread seen in the collagen testing condition. Only MMP 1 would break down the collagen hydrogel, however, the cells then do not possess any drive or potential to further spread through the broken-down matrix (Bartsch *et al*., 2003; Jabłońska-Trypuć *et al*., 2016).

In the contrary, MDA-MB-231 and U-87 MG cells can migrate and spread throughout all the hydrogels (Figure 3.18), as previously shown (Shirazi *et al*., 2011; Cosma *et al*., 2015). The triple negative MDA-MB-231 cells have been shown to express MMP 1, 2, 7, 8, 9, 10, 11, 13, 14, 15 and 16, and these MMPs are involved in a range of biological processes; such as EMT and cell migration regarding MMP 13, collagen breakdown in MMP 1 and 10, and further proteolytic activity, cell proliferation and migration. Therefore MDA-MB-231 spheroids can breakdown collagen and gelatin through MMP expression and can breakdown the complex mixture of Matrigel. MDA-MB-231 spheroids then possess the ability to further migrate and proliferate, showing a highly migratory status, something which is seen in *in vivo* models. The levels of MMPs present increases as time increase and therefore ECM-like matrices are further

broken down, without the ability to rebuild, explaining the results shown. U-87 MG cells are from a grade IV malignant glioma/astrocytoma, which is associated with rapid growth and expansion. Astrocytomas and gliomas (U-87 MG cells) express high levels of MMP2 and MMP9. These metalloproteinases can degrade gelatin and collagen, they are also synergistic with one another and further degrade the ECM matrices in the presence of hypoxia, explaining why the U-87 MG spheroids are invasive. Therefore, the observations seen in the U-87 MG spheroid migration are explained in a similar manner to the MDA-MB-231 spheroids, in which the increase level of MMP is increased overtime and accumulate, resulting in the degradation of the ECM like matrices, without the ability to repair. The factors then allow the cells to migrate through the sites opened by the proteolytic activity resulting in increased cell movement and spread over time (Onishi *et al*., 2011; Bernhart *et al*., 2013). Interestingly, when the spheroids were placed on collagen of different concentrations, it was observed that all the different spheroid cell lines spread and migrated more on the highest concentration (3 mg) of collagen. The MCF7 spheroids appeared to be static in spread as reasoned above, whilst the MDA-MB-231 and U-87 MG spheroids appear to spread the most. This is due to the concentration of collagen inducing the higher levels of MMPs. When a higher level of collagen is present, then more MMPs are induced, resulting in more cleavage and proteolytic degradation in the ECM-like matrices, this results in more spread over time. One variation to the expected results was the lower level of migration in Matrigel coupled with collagen, in comparison to collagen and Matrigel alone. However, the concentration of combined Matrigel and collagen is decreased, being 4mg and 1mg respectively, in comparison to 10mg and 3 mg. Therefore, less MMP expression may be present resulting in less degradation and less migration. The error bars are larger and overlapping, and are not statistically significant, so the levels of migration may be more level than expected from the trend and histogram shown.

3.5 Chapter summary and conclusion

To conclude, the results in this chapter have demonstrated that spheroid cell line models chosen for this thesis, MCF7, MDA-MB-231, and U-87 MG, represent suitable models for moving forward to the spheroid-on-chip setting (Chapters 4-5).

These spheroid models have appropriate growth patterns and biological characteristics, including proliferative and hypoxic zoning, and migration/invasion patterns. The following chapters (4-5) will detail the incorporation of spheroids into microfluidic devices to modulate and investigate cellular spread and the tumour microenvironment, and how shear stress, continuous perfusion and hydrogels effect the ability of cancer to spread, mirroring those conditions seen in the human body and mammalian tumours.

Chapter 4   Generation 1 spheroid-on-chip microfluidic device design and validation

4.1 Introduction

Microfluidic devices are systems which can manipulate fluid through micrometer size flow networks, typically processing fluids on the 10^{-9} L to 10^{-18} L scale. Microfluidics continues to expand as a field of research due to its ability to precisely control various conditions at the micrometer scale, such as laminar flow, thermal transport, and diffusion. These microscale devices have been applied in analytical chemistry, cell and biological processes, energy generation, and molecular biology, requiring only small quantities of reagents and samples, resulting in reduced cost, time, and the potential for lower environmental impact (Whitesides, 2006). These devices have the advantage of high throughput standardisation of 3D models with continuous flow conditions, mimicking those seen *in vivo*.

4.1.1 Microfluidic device design and generation techniques

Microfluidic devices can be designed and generated in a variety of ways. Utilisation of computer software packages followed by the fabrication process is the overarching system used, regardless of the material and application required. The application required, *e.g.* cancer biology or analytical chemistry, dictates the material required and subsequently the process of fabrication. Commonly used materials include paper, silicon, plastics, PMMA, polydimethylsiloxane (PDMS), and glass (Daw and Finkelstein, 2006; Whitesides, 2006). PDMS is a common material found in much of microfluidic device research on cancer biology, and it features good optical transparency, can be used for fast prototyping and is gas-permeable (Iliescu *et al*., 2012; Ren *et al*., 2013). Soft lithography is used for producing PDMS devices (Whitesides, 2006). PDMS devices are not easily amenable to mass fabrication and their porosity sometimes causes issues (Iliescu *et al*., 2012; Ren *et al*., 2013). An alternative material is glass, which has good optical transparency properties, is rigid, inert and gas-impermeable. Glass is slightly more expensive than PDMS, PMMA and other plastics for example, but offers

benefits over the other materials such as having the ability to autoclave devices, be none gas permeable and easily cleaned. (Iliescu *et al.*, 2012; Acosta *et al.*, 2014; Lake *et al.*, 2015; Gale *et al.*, 2018; Kühlbach *et al.*, 2018; Ma 2018).

In the work presented in this thesis, the device was drawn in AutoCAD software, before being processed and milled on a CNC machine. The CNC process can cause rough surfaces within the microfluidic devices, so it is not always desirable. An alternative process to prevent the rough surface is wet (acid) etching, dry etching is also possible but again it depends on the application requirements (Whitesides, 2006). Wet etching involves the use of hydrofluoric acid (HF). The pattern is designed on the glass, a masking layer used, and the acid added to clear out the microchannels. However, a consideration is that the rate of etching is affected by the glass composition and oxide content. For example, Corning 7740 has an etch rate of 8 μm min^{-1} at a HF concentration of 49% and quartz is 1.3 μm min^{-1} at the same concentration (Iliescu *et al.*, 2012). Likewise, the masking layer is critical to the pattern and formation of the microfluidic device channels. Defects, tensile stress, and hydrophobicity in the masking layer can cause cracks, pinholes and imperfections in the device resulting in it being unable to be used (Iliescu *et al.*, 2012).

4.1.2 Microfluidics and spheroids

The incorporation of a 3D model of *in vivo* cancer, such as a spheroid, into a highly controllable environment, such as a microfluidic device, is desirable, due to the ability to investigate specific components of cancer cell biology and the hallmarks leading to cancer spread (Weinberg & Hanahan, 2011). As previously detailed in the introduction the 3D model has advantages over 2D cancer models, however, it lacks the ability to be within continuous flow, resulting in waste removal and increased nutrient acquisition (Mehta *et al.*, 2012; Halldorsson *et al.*, 2015). Coupling the two systems together allows the precise control of the external environment surrounding cancer and the control of influential factors related to cancer cell migration and

spread seen within the human body such as continuous perfusion and shear stress (Ip *et al.*, 2016). Recently, the combination of spheroids and microfluidic devices has proved a promising and popular avenue for cancer research, albeit through the formation of spheroids within the microfluidic device, which is the most popular technique for using spheroids and microfluidic devices, or through the testing of drug sensitivity on-chip.

4.1.3   Rationale and aims

The rationale was to fabricate a microfluidic device capable of harbouring a cancer spheroid to better mirror *in vivo* models *in vitro*. The device would need to allow one spheroid to be contained within its microwell and allow effluent to be collected post flow. The device would need to have shear stresses replicative of *in vivo* values as this would allow the investigation to be conducted into what effects the internal forces acting within the microfluidic device would have on cancer migration and spread, within a clinically relevant 3D *in vitro* model. The overall aim of this subsection was to incorporate a spheroid into the microfluidic device, it was necessary to characterise and calculate the shear stress and residence speeds present within the microfluidic device, acting upon the spheroid.

The specific aims of the research described in this chapter were to design and validate a microfluidic device for spheroid incorporation and maintenance. This involved 1) *design and fabrication of the device*, 2) *incorporation of a spheroid*, and 3) *assessment of spheroid viability and migration/invasion potential.*

4.2 Experimental design

4.2.1 Microfluidic device design, interfacing, and set-up

The device needed to have the following characteristics: (i) allow the passage of cell culture media and spheroids of varying sizes into and out of the microfluidic device, (ii) entrap spheroids within a specific zone, whilst allowing media to continually perfuse over the spheroid for a prolonged period, (iii) allow for the collection of the effluent media, (iv) be non-gas permeable and (v) be easy to replicate, readily available, reusable, and inexpensive to produce. The design (**figure 4.1**) was conceived in collaboration with Dr Iles at the University of Hull and fabricated by Dr Iles. Briefly, a deep 600 μm channel, a spheroid housing microwell and a shallow channel are the key features, and CNC milling of Schott B270 glass was done to produce it. A custom inlet and outlet interface was built as shown in section 2.7 employing Araldite glue (type 2000). This set up was mirrored on the second set of tubing as detailed in the methods, figure 2.9.

4.2.2   Spheroid incorporation on-chip

In an initial set of experiments, brilliant blue dye solution was pumped through the device to ensure there are no leaks (fig 4.1 c). Spheroids were then attempted to be incorporated into the device. The spheroids should ideally be sufficiently compact as to not disintegrate upon loading and should be sufficiently large to be retained within the micro-well. Spheroids generated from five cell lines (U-87 MG, MCF7, MDA-MB-231, HCT116, and HT29) at four seeding densities (see section 3.1 for details) were tested for the incorporation. After formation, spheroids were carefully collected and slowly drawn into the micro-well through the deep channel to prevent compression and reduce internal compressive pressure on the spheroid. Once a spheroid was loaded into the micro-well, the device was placed in a Covatutto 24 Eco (Covatutto, Italy) benchtop egg incubator set to 37 °C, and complete DMEM was pumped at 3 μL per h for a
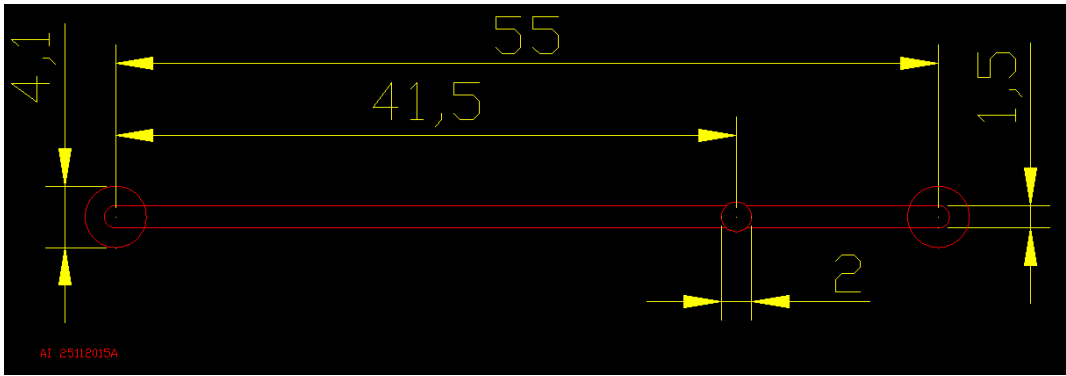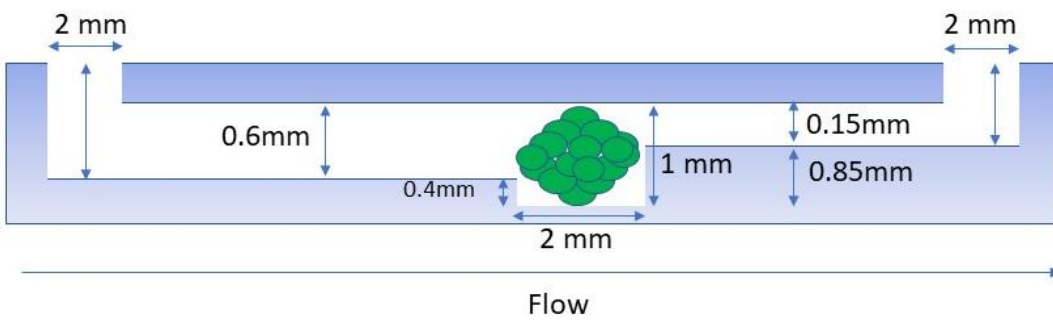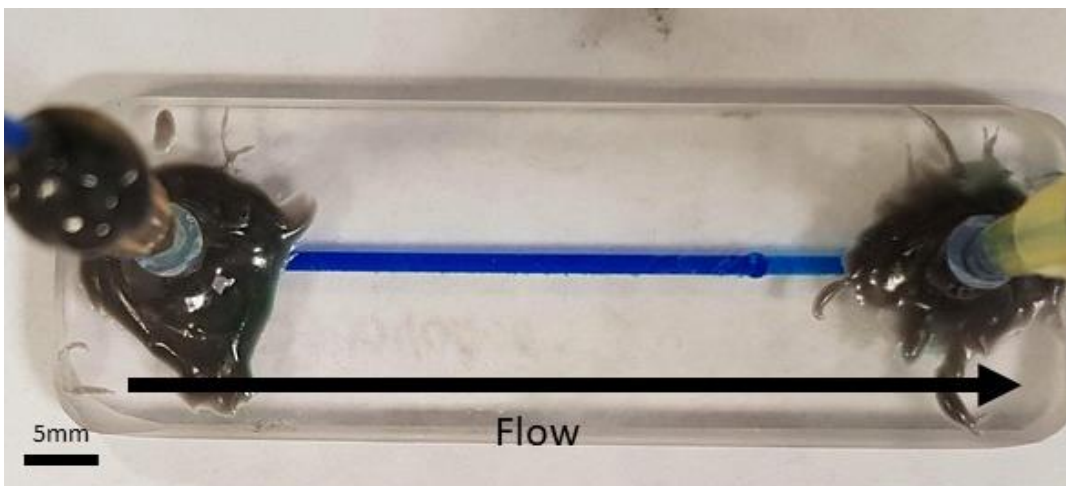
Figure 4.1: Generation 1 microfluidic device design

Generation 1 microfluidic device schematic used for CNC milling purposes (in mm) (A), Generation 1 microfluidic device cross sectional drawing with an example spheroid in the micro-well (B) and a photo from above with brilliant blue dye flowing from the deep channel, through the micro-well and into the shallow channel (c). Scale bar represents 5 mm.

total of 72 h per experiment using a disposable syringe set in a syringe pump (Harvard Apparatus).

4.2.3 Analysis of spheroid viability on-chip

Once a spheroid was incorporated into the micro-well, its viability over time was assessed and compared to spheroids grown off-chip in static conditions. Two methodologies were employed to determine spheroid viability: (1) the CytoTox-Glo cytotoxicity assay (see section 2.4) to assess viability based on markers found within the media effluent; (2) the FDA/PI live/dead staining assay (see section 2.4 of methods) to determine spheroid viability *in situ*.

4.2.4 Determination of viability from effluent media samples

'On-chip' viability was assessed over 72 h via the CytoTox-Glo cytotoxicity assay, which measures the extracellular activity of an intracellular protease. The protease is released by membrane compromised cells into the media or effluent. MCF7 spheroids (3.5×10^4 cells) were either transferred to a microfluidic device or left 'off-chip' in the ULA plate to grow in static conditions. Conditioned media from an MCF7 cell monolayer was also used as an additional control. The samples were stored at either 4 °C or -80 °C, to allow a comparison of assay effectiveness using fresh *vs* frozen media effluent.

4.2.5 Determination of viability *in situ*

To investigate spheroid viability *in situ*, the FDA/PI assay was adopted to determine the levels of live and dead cells present within a MCF7 spheroid mass (3.5×10^4 cells). Spheroid viability was assessed over a period of 72 h in spheroids either on-chip, or in static conditions off-chip. As a positive control for cell death, spheroids were treated using 100 nM of gemcitabine, a clinically relevant cytotoxic agent used in breast cancer treatment (Plunkett *et al*., 1995; National Institute of Health, 2015). Fluorescence quantification was performed using ImageJ analysis software.

4.2.6 Analysis of spheroid structural integrity on-chip

Spheroids were removed by flushing them 'back' through the deep channel in order to assess the structural integrity of the MCF7 spheroids (3.5 x 10^4 cells) following 72 h on-chip. The collected spheroids were then fixed and prepared for H&E staining, as described in section 2.6.

4.2.7 Analysis of metastasis biomarkers in the on-chip spheroid model on-chip

Two strategies were used to preliminarily evaluate markers of metastasis: (1) biomarkers secreted by the spheroids, *i.e.* VEGF and (2) biomarkers within the spheroid *i.e.* E-cadherin and Vimentin.

Firstly, the presence of the pro-metastatic, pro-angiogenic secreted factor VEGF (Vascular Endothelial Growth Factor) was evaluated using a VEGF sandwich ELISA (see section 2.5). To evaluate whether the 3D models, both on- and off-chip can recapitulate the secretion of VEGF in a comparable manner to the 2D monolayers, VEGF secretion was compared between MCF7 (3.5 x 10^4 cells) 2D monolayers, spheroids grown off-chip and on-chip. Detected VEGF amounts were normalised as pg per 3.5 x 10^4 cells.

Secondly, the presence of Epithelial-Mesenchymal Transition (EMT) markers, E-cadherin and Vimentin, was evaluated by Western blotting (as noted in section 2.5). E-cadherin is critical in the EMT transition, being present in epithelial-like cells, such as MCF7. Vimentin is a mesenchymal marker of cells that have undergone the EMT shift. The presence of either E-Cadherin or Vimentin could dictate whether the cells or spheroids have undergone a phenotypic change, identifying any effects the microfluidic device has on cancer spheroids.

4.3 Results

4.3.1 Device flow and shear stress calculations

Shear stress within the human body can vary greatly and table 4.1 shows typical shear stress values for main blood vessels through the human body.

Table 4.1: ***Human blood vessels and typical shear stress (Pa) values*** *(Reneman & Hoeks, 2008)*

Blood Vessel	Shear Stress / Pa
Carotid Artery	1.1-1.3
Brachial	0.4-0.5
Femoral	0.3-0.5
Arterioles	1.0-5.0
Interstitial (primary tumours)	<0.01

As shown, cancer cells and tumours do not typically experience high velocities and stresses, except for when they are in circulation moving to a distant site. Therefore, the shear stresses modelled within a microfluidic device use shear stress values which more closely mirror interstitial flow and stresses experienced by cancer cells *in vivo*, for example being <0.1 dyn/cm^2 in interstitial flow and below. Examples of models using these limits are Mina et al, whom used stresses of 1 dyn/cm^2, whilst Lee et al (0.05), Ip et al (0.01, 0.02, 0.002) and Mitchell and King (0.007 – 0.015) all used shear stress values of 0.007-0.0015 dyn/cm^2.

Shear stress within our generation 1 microfluidic device were therefore calculated to best mimic conditions found within the human body and be comparable to those found above. To calculate and show the shear stresses present, flow rates must first be shown and considered.

Typical flow speeds of human blood vessels can be seen in Table 4.2. Similarly, to before, these velocities are a lot higher than cancer cells and primary tumours experience *in vivo*. Therefore, DMEM was flown at 3 µL min^{-1}, which reflects values seen within the literature to replicate *in vivo* tumours (Kraning Rush *et al*., 2012; Jain *et al*., 2014). Flow rates which are too high may be damaging the spheroid, whereas too low flow rates may leave the spheroid without nutrients, thus not being reflective of a human tumour. The internal speed and residence speeds of DMEM flow through the microfluidic device was calculated using equation 1.

$$speed\ (s) = \frac{volume\ flow\ rate\ (v)}{cross\ sectional\ area\ (A)}$$

equation 1

The flow speed was calculated to be 3.33 mm min^{-1} in the deep channel, 13.33 mm min^{-1} in the shallow channel, and 1.5 mm min^{-1} in the micro-well section of the chip device. The total residence time within the device was calculated to be 18.16 min. These calculations signify that the microfluidic device would be completely replenished with new media three times an hour. Static culture spheroids only have fresh DMEM replenished every 24 to 48 h, therefore replenishing the media three times every h on-chip should be enough time to refresh the spheroid with nutrients and remove waste continuously, offering an advantage over static

culture. By using the flow rates shown, it is possible to demonstrate the shear stress present within the microfluidic device, calculated through equation 2.

Table 4.2: ***Blood vessels and associate blood velocities*** *Blood vessel speeds are shown to give a comparison of the speeds used in this experiment. (Thurston, 1976)*

Blood Vessel	Velocity (mm min^{-1})
Aorta	6.3
Capillaries	0.005
Vena Cava	2.5

Shear stress (τ) has been shown to affect cellular adhesion and metastatic progression (Cezeaux JL *et al*., 1991; Kumar S & V, 2009; Kraning Rush C *et al*., 2012; Jain RK *et al*., 2014) and therefore must be considered in the context of the spheroid study on-chip. Shear stress acts upon the spheroid within the microfluidic device depending on the channel dimensions, viscosities and flow rates employed (equation 2) (Ip *et al*., 2016),

$$\tau = 6\frac{Q\mu}{h^2w}$$

(equation 2)

where τ is the shear stress (Pa), Q is the volume flow rate (m^3 s^{-1}), μ is the dynamic viscosity (Pa s), h is the channel height (m) and w is the channel width (m). As an example, shear stresses acting on blood vessels within the human body is summarised in Table 4.2 (Reneman & Hoeks, 2008).

For an aqueous solution (μ = 8.90 x 10^{-4} Pa s), pumped at 3 μL min^{-1} through the shallow channel (h = 150 x 10^{-6} m, width w = 1.5 x 10^{-3} m), the channel cross sectional area A = w h equals 2.25 x 10^{-7} m^2. The volume flow rate Q therefore equates 5 x 10^{-11} m^3 s^{-1}. Inserted into equation 2,

$$\tau = 6 \frac{5 \ x \ 10^{-11} \ m^3 s^{-1} \ x \ 8.90 \ x \ 10^{-4} \ Pa \ s}{(1.5 \ x \ 10^{-4}m)^2 x \ 1.5 \ x \ 10^{-4}m} = 7.94 \ x \ 10^{-3} \ Pa$$

equation 3

This is commonly expressed in dyn cm^{-2}, where 1 Pa equals 10 dyn cm^{-2}. Therefore, the shear stress in the shallow channel equals τ = **7.91 x 10^{-3} Pa** or **7.91 x 10^{-2} dyn cm^{-2}**.

The same calculation can be carried out to determine the shear stress in the deeper channel (h = 6 x 10^{-4} m, w = 1.5 x 10^{-3} mm) and the micro-well (h = 1 mm, w = 2 mm at its widest point). The values are summarised in Table 4.3. The values within our device are like those shown previously, by Lee, Ip and Mitchell and King - 0.007-0.0015 dyn/cm^2.

Table 4.3:   Shear stress values within the microfluidic device

Microfluidic chip component	Shear Stress / Pa	Shear Stress / dyn cm^{-2}
Shallow Channel	7.91 x 10^{-3}	7.91 x 10^{-2}
Micro-well	1.34 x 10^{-4}	1.34 x 10^{-3}
Deep Channel	4.94 x 10^{-4}	4.94 x 10^{-3}

4.3.2 Spheroid incorporation into microfluidic device

Spheroids from a panel of cell lines at a range of cell densities as noted in section 3.1 were incorporated into the device. Table 4.4 details spheroid incorporation success. Successful incorporation was achieved for U-87 MG and MCF7 spheroids at 2.5×10^4 and 3.5×10^4 cells per well. This was consistently seen across the replicates used. Partial success was seen in HCT116 and HT29 spheroids seeded at 2.5×10^4 and 3.5×10^4 cells per well. However, all the MDA-MB-231 spheroids disaggregated across all seeding densities used. MCF7, U-87 MG, HCT116 and HT29 spheroids either flowed through (when seeded 5×10^3 cells per well) or became lodged and trapped (5×10^4 cells per well) at various other locations, such as the inlet ports and deep channels. Examples are shown in Figure 4.2 & 4.3.

As previously stated, (section 3.1.), MDA-MB-231 spheroids appeared larger than the other cell line counterparts. This is potentially due to the type of cell binding present. MDA-MB-231 spheroids binding is mediated by collagen I and integrin β, with no cadherin involvement as opposed to cadherin binding and thus tight spheroids seen in MCF7 cells (Ivascu & . 2007).

Table 4.4: ***Spheroid incorporation success for the panel of cancer cell lines***
Spheroids were seeded at four cell densities and formed over 96 h. Spheroids were collected at day 4 in separate collecting tubes and tested for incorporation into a microfluidic device (as per section 2.8). minimum of n=3 in triplicate

Cell Line	Spheroid Density (cells per well)	Spheroid approximate diameter (in μm)	Outcome
MCF7	$5x10^3$	700	All spheroids flowed through
MCF7	$2.5x10^4$	1000	Success
MCF7	$3.5x10^4$	1200	Success
MCF7	$5 x10^4$	1300	All spheroids became lodged
MDA-MB-231	$5x10^3$	880	Spheroids disintegrated before entry
MDA-MB-231	$2.5x10^4$	1400	Spheroids disintegrated before entry
MDA-MB-231	$3.5x10^4$	1600	Spheroids disintegrated before entry
MDA-MB-231	$5 x10^4$	1800	Spheroids disintegrated before entry
HCT116	$5x10^3$	1000	All spheroids flowed through
HCT116	$2.5x10^4$	1250	Partial success* (less than 100% spheroids kept in microwell)
HCT116	$3.5x10^4$	1400	Partial success*
HCT116	$5 x10^4$	1500	All spheroids became lodged
HT29	$5x10^3$	850	All spheroids flowed through
HT29	$2.5x10^4$	1200	Partial success*
HT29	$3.5x10^4$	1350	Partial success*
HT29	$5 x10^4$	1750	All spheroids became lodged
U-87 MG	$5x10^3$	700	All spheroids flowed through
U-87 MG	$2.5x10^4$	975	Success
U-87 MG	$3.5x10^4$	1100	Success
U-87 MG	$5 x10^4$	1150	All spheroids became lodged
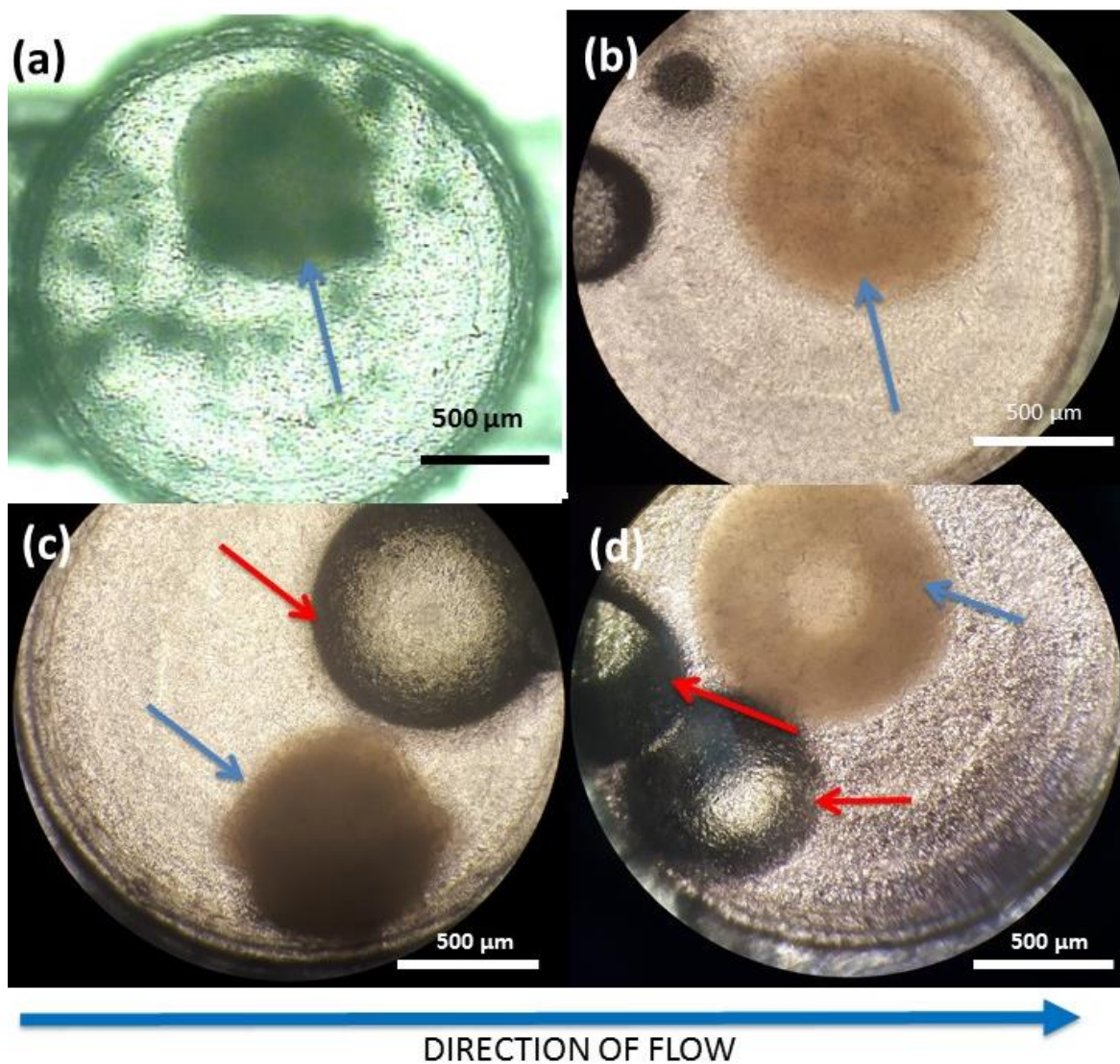
Figure 4.2. Successful spheroid incorporation into the micro-well of the microfluidic device

(a) Representative image of U87MG spheroids seeded at 3.5 x 10⁴ cells per well) and (b) representative image of U87MG spheroids seeded at 2.5 x 10⁴ cells per well. (c) and (d) are two MCF7s spheroids- both 3.5 x 10⁴ cells per well. These were tested in microfluidic devices. The separate images above show the successful incorporation of these spheroids into the microfluidics micro-well. These spheroids were contained within the micro-well for the duration of experimentation, before being flowed out into a collecting vessel. Blue arrows denote spheroids, red arrows denote air bubbles. Flow is from left to right. Scale = 500 μm.

DIRECTION OF FLOW
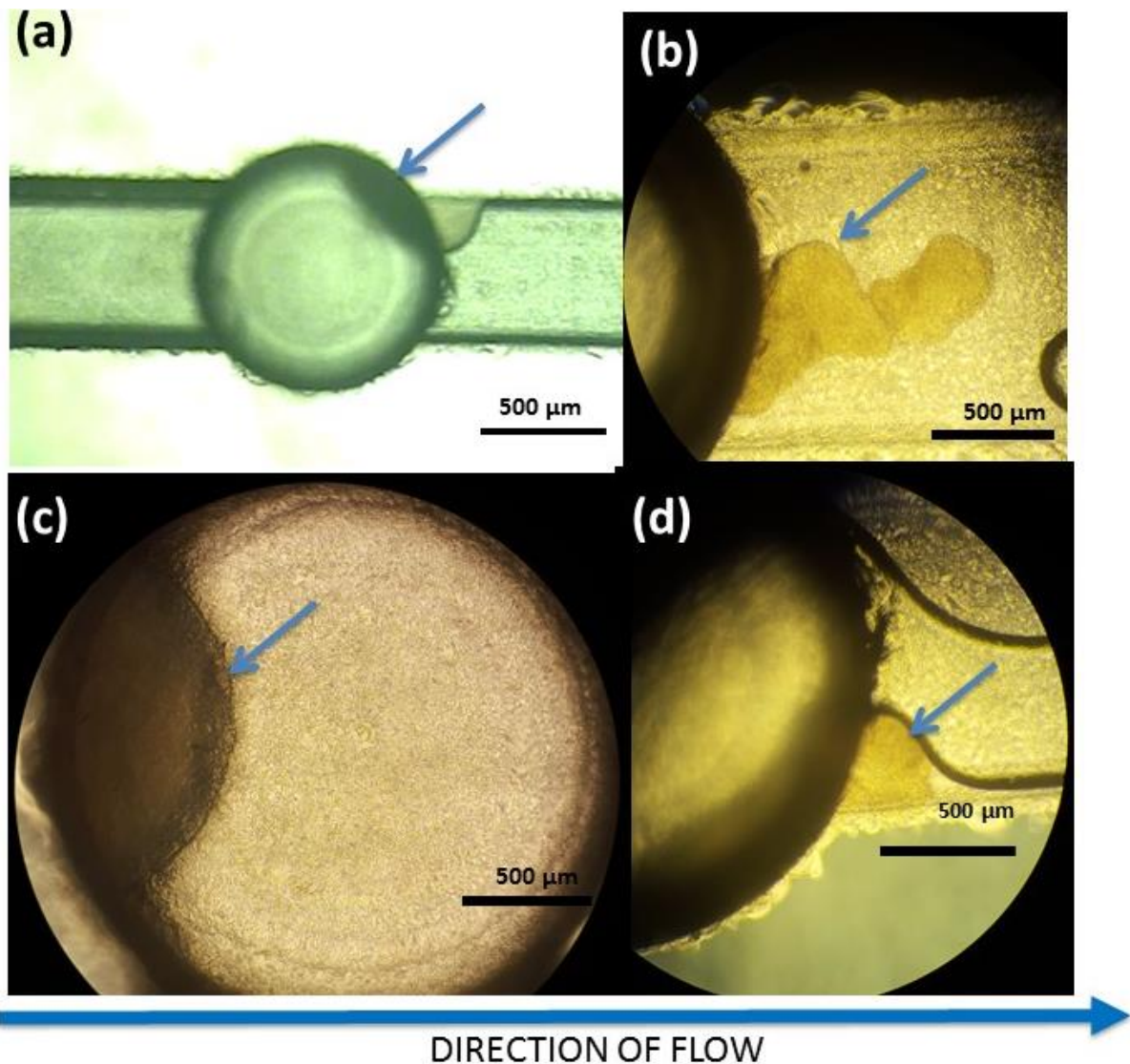
Figure 4.3. Examples of unsuccessful spheroid integration into the microwell of the microfluidic device

(a- b) Images of two U87MG spheroids, seeded at 2.5 x 10^4 cells per well; (c) HCT116 spheroid seeded at 5 x 10^3 cells per well; (d) MCF7 spheroid seeded at 5.0 x 10^4 cells per well. The separate images show the unsuccessful placement of these spheroids into the microfluidic micro-well. Image (a) demonstrates a spheroid becoming 'stuck' to the internal wall of the micro-well, (b) a spheroid being fragmented and passing through the micro-well, (c) a spheroid stuck to the internal edge of the micro-well; (d) a spheroid passing through the micro-well to the device's shallow channel wall. The spheroids were consequently disposed of and the device cleaned. Blue arrows denote spheroids, red arrows denote air bubbles. Flow is from left to right. Scale bar = 500 μm.

Overall the results demonstrate that spheroids seeded at 2.5 x 10^4 and 3.5 x 10^4 cells per well were most suited for incorporation into the microfluidic device, specifically the MCF7 and U-87 MG spheroids, which is likely due to their compact size and tight binding (Vinci *et al.,* 2012).

Once the spheroids were incorporated into the device, the device was placed and set up in an egg incubator set to 37 °C, connected to the syringe pump, shown in figure 4.4. Following this, the spheroids needed to be assessed for their viability in comparison to their off-chip models.

4.3.3 Assessment of spheroid viability on-chip *vs* off-chip: cell death marker in effluent

The first strategy to determine spheroid viability on-chip *vs* off-chip was the CytoTox-Glo cytotoxicity assay for extracellular activity of an intracellular 'death' protease, which is released into the effluent once cell membrane structure is compromised. Figure 4.5 shows that there is not any difference between the experimental conditions. Moreover, there are large overlapping error bars. It is noteworthy that this assay measures protease activity, not a direct measure of viability.

Figure 4.4: Egg incubator and microfluidic device set up

Disposable syringes filled with complete DMEM is connected to a microfluidic device placed inside an egg incubator (Covatutto 24 eco, Novital, Italy). The flow rate is set to 3μl min⁻¹ and the spent media collected in a 15ml collection vesicle. After 24 h the vesicles are replaced. Scale bar is 28 mm, half the microfluidic device width.
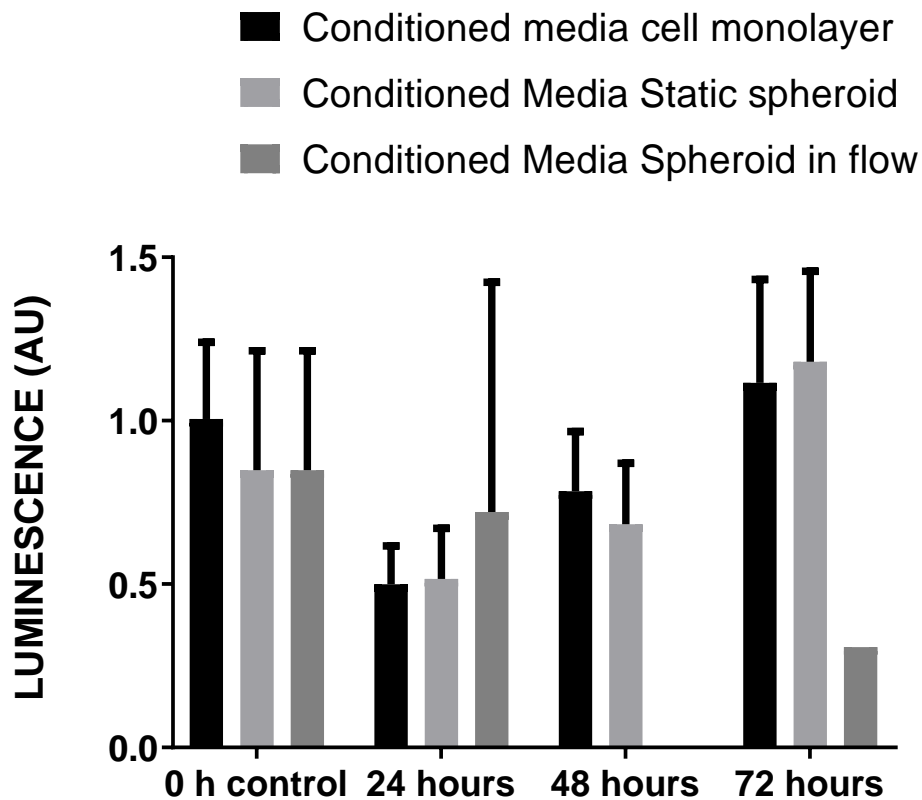
Figure 4.5: *Luminescence histogram shows protease activity in fresh media effluent on the microfluidic device than cellular monolayer and off-chip spheroid*

MCF7 spheroids 3.5 x 10^4 (cells per well) were seeded over 96 h, at 96 h the monolayer and spheroids were seperated into three categories – monolayer, spheroid off-chip and on-chip. MCF7 monolayer and spheroid off-chip were used as controls (3.5 x 10^4). The spheroids were left for 72 h and the media effluent collected at 24, 48 and 72 h timepoints. The effluent was stored at 4°C and tested using CytoTox Glo assay (as per section 2.4). 3 replicate wells were setup per experiment. Histogram representes the average luminescence signal per well of n=3 independent experiments. Error bars are the SE. ANOVA shows no significance.

4.3.3.1 Impact of freezing on sample stability for CytoTox Glo Assay

Cellular viability data from fresh samples (figure 4.6) showed that the lowest protease activity was detected in samples from 24 h on-chip spheroid, with the highest being from the static spheroid. The monolayer and static spheroid samples registered 20 and 38% higher protease activity than the spheroid on-chip condition samples. Similarly, at 48 h, the protease activity in cell monolayer samples was 50% higher than the on-chip condition samples. Likewise, there was a 13% difference in protease activity between static spheroids and on-chip spheroids, with the on-chip spheroids registering lower protease activity. This trend is also observed at 72 h, with on-chip sample protease activity 10% lower than for the other conditions. Therefore, in general, on-chip fresh media samples show the highest viability, as noted by decrease in protease activity.

Protease activity from frozen and the defrosted media is shown in figure 4.7. At 24 h, the protease activity was lowest in the microfluidic device, followed by the static spheroid and then the monolayer. There is a low, approximately 10%, difference between all three conditions. The highest activity at all three time points is seen in the monolayer. At 48 h there is a 6 and 2 fold decrease in protease activity in the static and on-chip spheroid compared to the monolayer, respectively. Finally, at 72 h, the lowest activity is again seen in the on-chip spheroid, being 25% better than the static spheroid and 118% better than the monolayer. Protease activity is an indication of viability. The results suggest there is good viability seen in the on-chip spheroid compared to the static spheroid and even more so compared to the monolayer.

Overall, the data shows that the frozen effluent data has lower protease activity than the fresh samples. However, the values suggest it is best to use the fresh sample effluent to not miss activity from the testing conditions (both 4.6 and 4.7 are from the same samples).

4.3.4 Assessment of spheroid viability on-chip *vs* off chip: *in situ* live/dead assay

In order to evaluate spheroid cell viability *in situ*, the FDA/PI live/dead assay was conducted. The results are presented in Figures 4.8 & 4.9. The intensity of green fluorescence (indicative of live cells) produced was comparable at 24 h in the control (off-chip) and gemcitabine treated spheroids. However, there was a 1.5 fold increase in intensity of red fluorescence (indicative of dead cells) in the gemcitabine treated spheroids than the control. This trend was reflected at 48 h, in which the off-chip spheroids had a 9% increase in green intensity than the gemcitabine conditioned spheroids, with a 25% increase in the proportion of red fluorescence in the gemcitabine spheroids compared to the control. At 72 h the highest intensity of red fluorescence is seen in the gemcitabine spheroids. These spheroids contain 25% and 66% higher intensity than the off-chip and on-chip device spheroids.

The on-chip spheroid shows the lowest intensity of red fluorescence, having 33% less than the control spheroids. Similarly, the highest green intensity is seen in the on-chip spheroids, about 18% and 60% better than the off-chip and gemcitabine spheroids, respectively. These results show that the on-chip contain a higher proportion of live cells and less dead cells than the other two conditions, supporting the cell viability CytoTox Glo data.

Although figure 4.11 is a representative qualitative image, it shows a limitation with the generation 1 microfluidic device design. The MCF7 spheroids which were removed from the device were misshapen and broken, which could be attributed to the cells becoming trapped and stuck to the inner chamber and channel surfaces of the microfluidic device, with the representative image showing the most intact spheroid to be collected from the device across the replicate experiments. The result showed that redesign of the microfluidic device was needed, which will be addressed in Chapter 5.

a)

b)
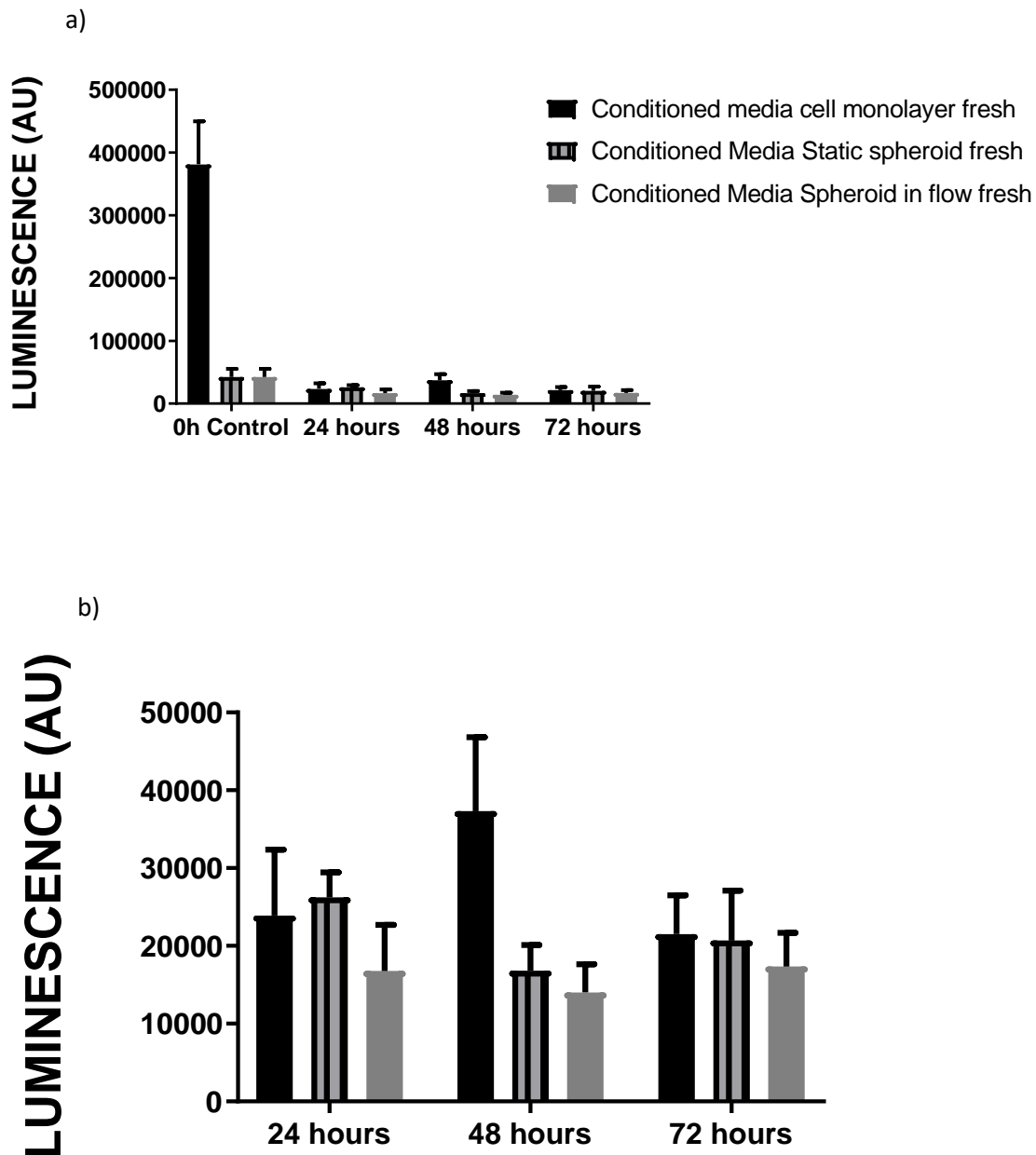
Figure 4.6: ***Luminescence histogram shows protease activity in the fresh media effluent on the microfluidic device, cellular monolayer and off-chip spheroid***

MCF7 spheroids 3.5 x 10 ^{4} (cells per well) were seeded over 96 h, at 96 h the spheroids were seperated into three categories – monolayer, spheroid off-chip and on-chip. MCF7 monolayer and spheroid off-chip were used as controls. The spheroids were left for 72 h and the media effluent collected at 24, 48 and 72 h timepoints. The effluent was stored at 4ºC and tested using CytoTox Glo assay. This indicates cytotoxic stress of the cells present through protease activity. a)Histogram of all conditions including control valuesat 0 h b) Histogram of all conditons without controls (0 hr from) SE of N=3 is represented. ANOVA shows no significance.

Figure 4.7: *Luminescence histogram shows protease activity in the frozen media effluent on the microfluidic device, cellular monolayer and off-chip spheroid*

MCF7 spheroids 3.5 x 10 ^{4} (cells per well) were seeded over 96 h, at 96 h the spheroids were seperated into three categories – monolayer, spheroid off-chip and on-chip. MCF7 monolayer and spheroid off-chip were used as controls. The spheroids were left for 72 h and the media effluent collected at 24, 48 and 72 h timepoints. The effluent was stored at 80 ^{o}C and tested using CytoTox Glo assay. This indicates cytotoxic stress of the cells present through protease activity.a)Histogram of all conditions including control valuesat 0 h b) Histogram of all conditons without controls (0 hr from) SE of N=3 is represented. ANOVA shows one and two star significance. * p<0.05, ** p<0.01
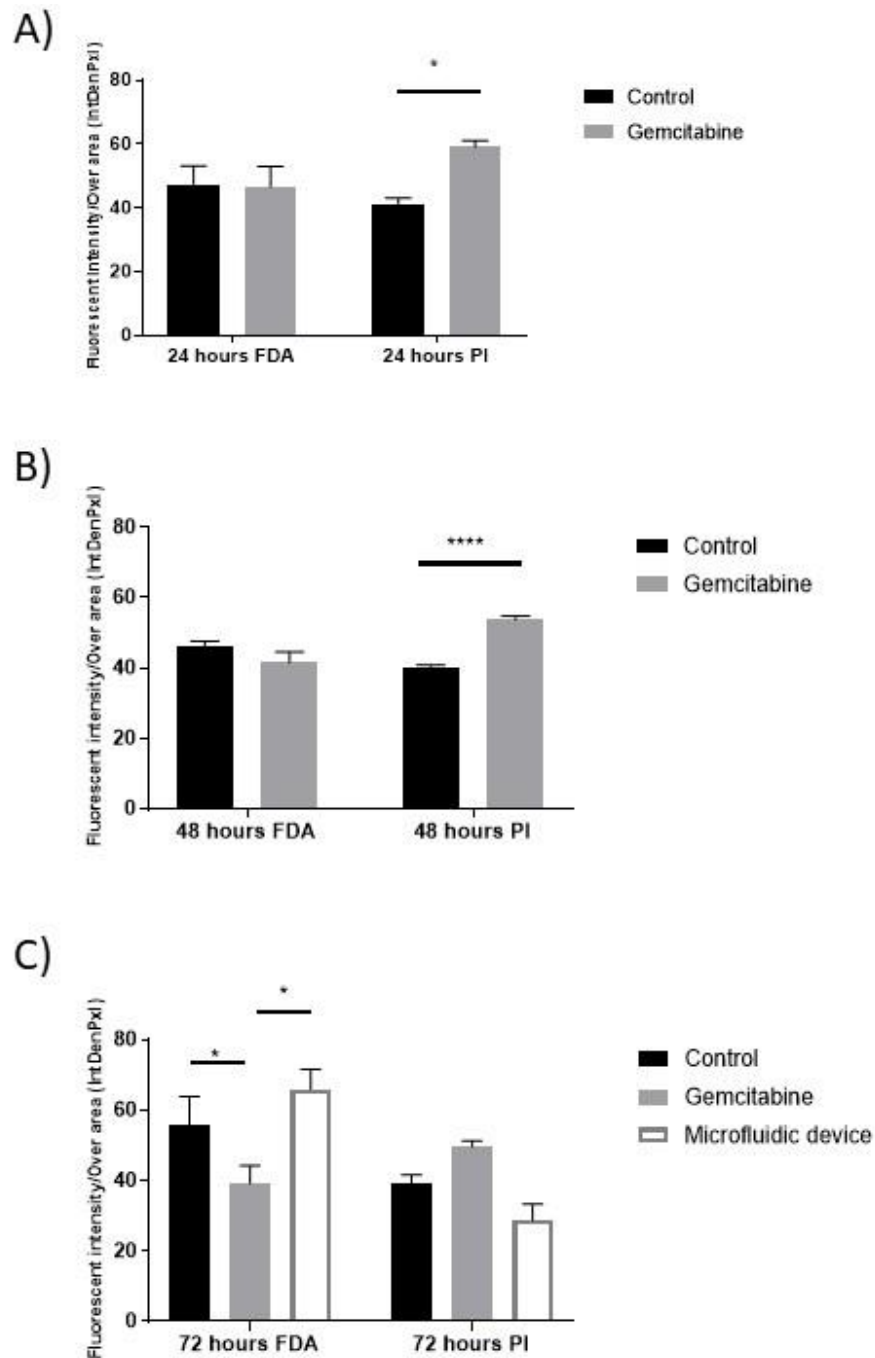
Figure 4.8: FDA-PI fluorescence quantification in spheroids off-chip vs on-chip

*MCF7 spheroids were formed at 3.5 x 10⁴ cells per well. Spheroids were either incorporated into a generation 1 microfluidic device (on-chip) or left in a ULA plate (off chip). A set of off-chip spheroids were treated with 100 nM Gemcitabine. Fluoresce intensity was determined using Image J. Histograms represent the average FDA- and PI- associated fluorescence as a unit of intensity over area for n=3 independent experiments. Raw intensity of original grey scale images of all three spheroid conditions at 24 h (A), 48 h (B), and 72 h (C) is plotted over area. Error bars represent standard error. Two-way ANOVA was performed to test for statistical significance. * p<0.05, **** p<0.0001*

Merge	FDA	PI
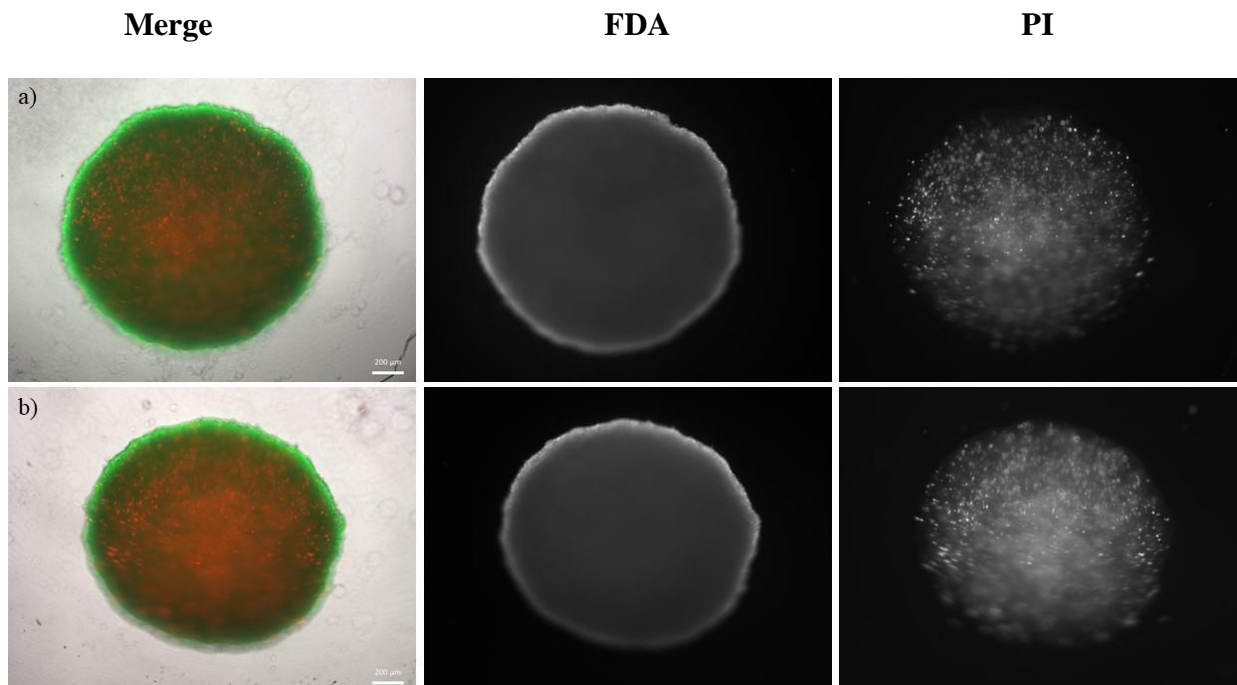
Figure 4.9: Representative images of FDA-PI stained MCF7 spheroids in two testing conditions

Representative FDA/PI live/dead staining images of MCF7 spheroids (3.5 x 10^4 cells per well) at 24 h. (A) Untreated spheroid off-chip; (B) Spheroid treated with 100 nM Gemcitabine for 24 h off-chip Red fluorescence represents PI incorporation and dead cells; green fluorescence represents FDA incorporation and live cells. Scale bar represents 200 µm. n=3 experimental repeats in triplicate.

Merge	FDA	PI
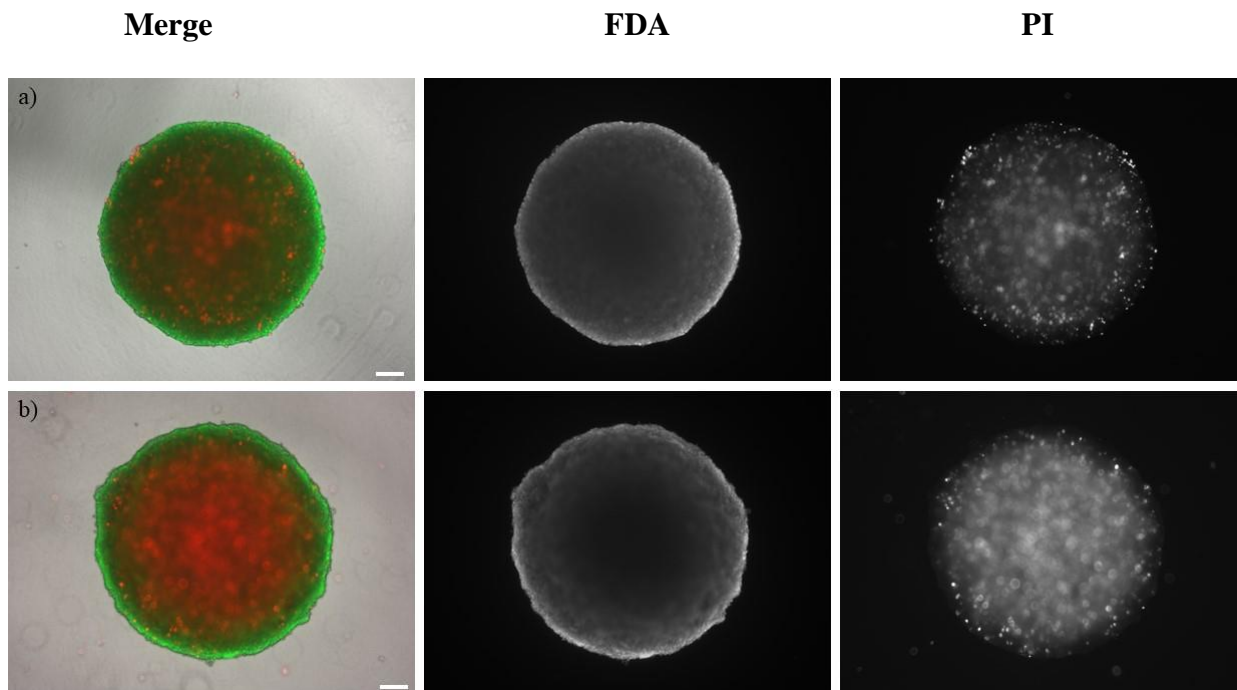
Figure 4.10: Representative images of FDA-PI stained MCF7 spheroids in two testing conditions

Representative FDA/PI live/dead staining images of MCF7 spheroids (3.5 x 10^4 cells per well) at 48 h. (A) Untreated spheroid off-chip; (B) Spheroid treated with 100 nM Gemcitabine for 48 h off-chip Red fluorescence represents PI incorporation and dead cells, green fluorescence represents FDA incorporation and live cells. Scale bar represents 200 μm. n=3 experimental repeats in triplicate.

Merge	FDA	PI
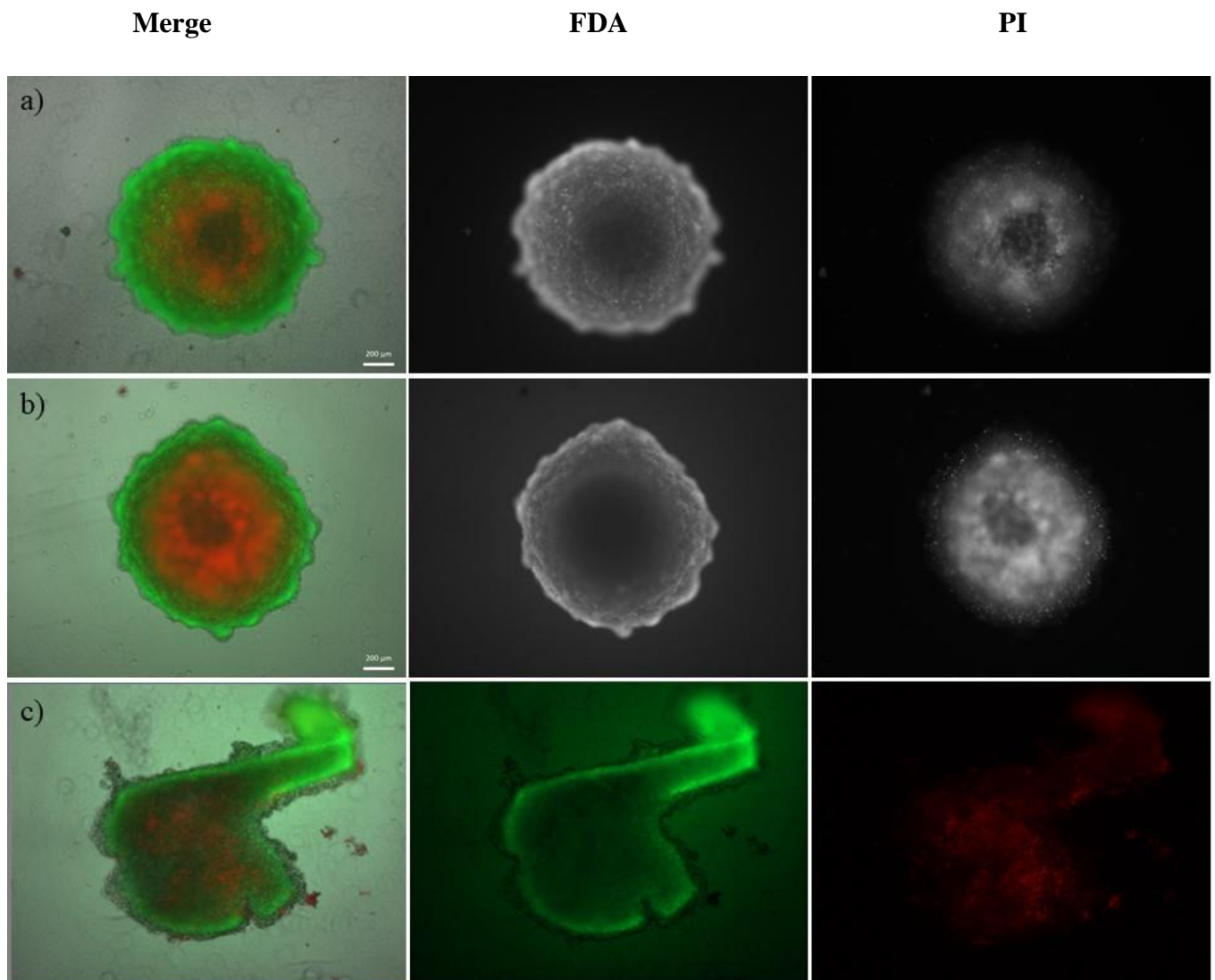
Figure 4.11: Representative images of FDA-PI stained MCF7 spheroids in the three testing conditions

Representative FDA/PI live/dead staining images of MCF7 spheroids (3.5 x 10^4 cells per well) at 72 h. (A) Untreated spheroid off-chip; (B) Spheroid treated with 100 nM Gemcitabine for 72 h off-chip; (C) untreated on-chip spheroid, incorporated into a microfluidic device for 72 h and subsequently removed for staining. Red fluorescence represents PI incorporation and dead cells, green fluorescence represents FDA incorporation and live cells. Scale bar represents 200 μm. n=3 experimental repeats in triplicate.

4.3.5 Evaluation of metastasis biomarkers on-chip *vs* off chip: VEGF secretion

In order to evaluate whether it was possible to analyse secreted biomarkers relevant to metastatic spread using the spheroid on-chip model, the levels of a common pro-metastatic, pro-angiogenic biomarker, the growth factor VEGF, were analysed in the conditioned media effluent in both 2D monolayer, off-chip spheroids and on-chip spheroids (kept under continuous media flow).

Figure 4.12 shows the VEGF levels in the conditioned media or effluent for the various media samples. The results show that at 24 h the highest level of VEGF for U-87 MG samples were observed in the off-chip spheroid samples, approximately 50% more VEGF than for the cell monolayer, samples and 25% more VEGF than on-chip spheroids samples. On-chip spheroid samples contained 40% more VEGF than the monolayer samples. At 48 h there was no clear difference between secreted VEGF levels in all media samples. The data was too high to be recorded at 72 h.

In MCF7 samples, at 24 h the least amount of VEGF was measured in the on-chip spheroid media samples, being 66% less than the off-chip spheroid media samples. At 48 h the VEGF levels was uniform across all samples, meaning the levels increased 6 x in the on-chip conditions from 24 h. At 72 h however, the detected VEGF levels are lowest in the on-chip samples, approximately 25% less than the other samples. Albeit it not statistically significant.

Overall, the results demonstrate that not only is it possible to detect VEGF, but it is identifiable and comparable between media samples from the cell monolayer and both off-chip and on-chip spheroid, albeit with no statistically significance difference between them. Furthermore, the data show that biological markers of metastasis can be collected over a full 72 h from the effluent from the on-chip model, indicating the possibility to detect other secreted biomarkers

A) U 87 MG

B) MCF7
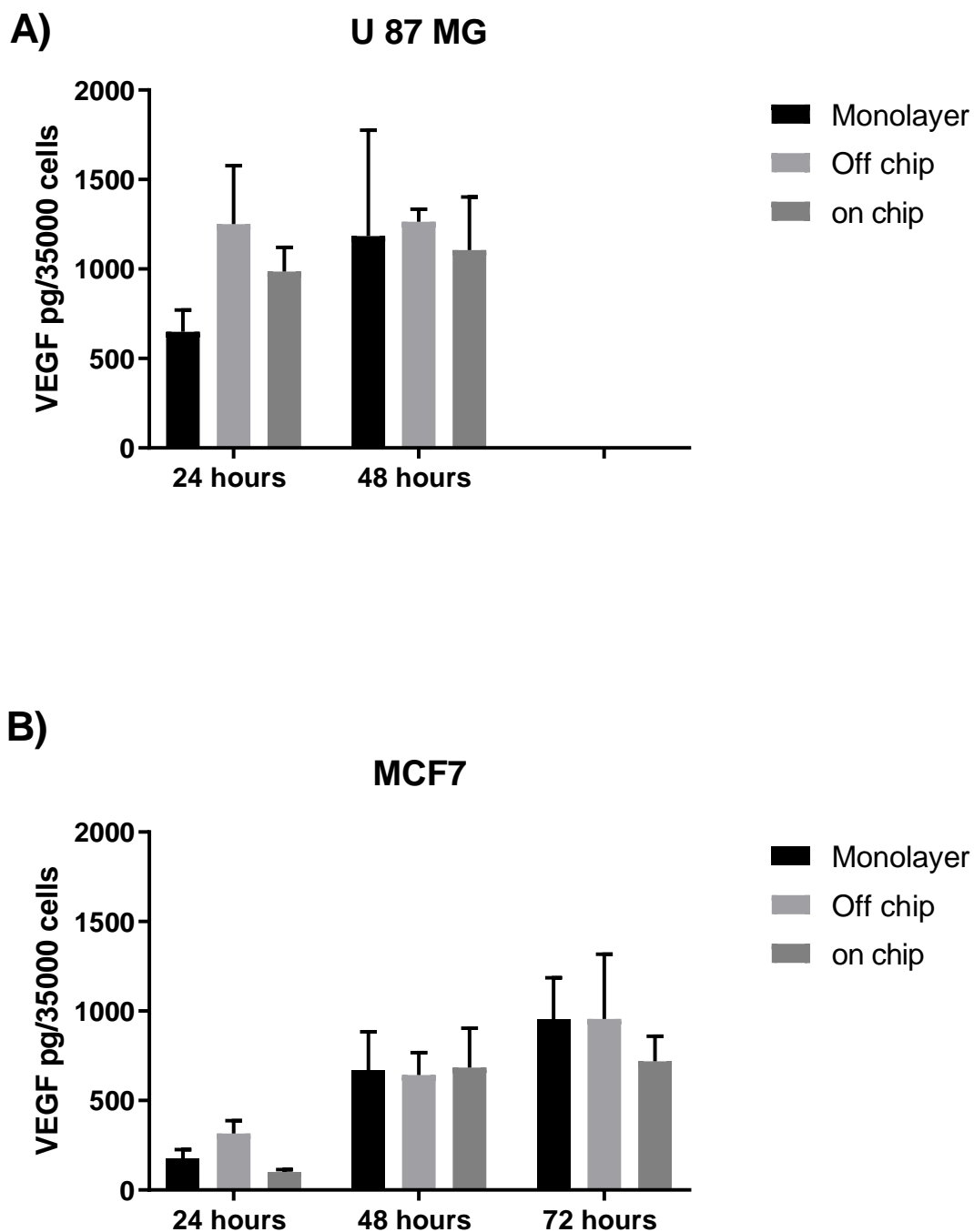
Figure 4.12: VEGF secretion between 2D, 3D off-chip and 3D-on-chip models

U 87 MG (A) and MCF7 (B) spheroids and cell monolayers were formed at 3.5 x 10^4 cells per well. Spheroids were either incorporated into a generation 1 microfluidic device (on-chip) or left in a ULA plate (off chip), and the monolayers were grown in a flat bottom plate. Media was collected at 24, 48, and 72 h, and the presence of secreted VEGF was analysed using a VEGF ELISA (see section 2.5). VEGF concentration was normalised to 3.5x10^4 (as noted in section 2.5). Histograms represent the media from n=3 independent experiments. Error bars represent the SE. Two-way ANOVA was performed to test for statistical significance. ANOVA shows no significance.

4.3.6 Evaluation of metastasis biomarkers on-chip *vs* off chip: protein expression

Expression of biomarkers for epithelial-mesenchymal transition (EMT) was evaluated in MCF7 monolayers, MCF7 spheroids in a ULA plate (off-chip), MCF7 spheroids in a microfluidic device (on-chip), as well as MCF7 and MDA-MB-231 cell monolayer (all seeded at 3.5×10^4 cells per well) in normoxic (20% O_2) and hypoxic controls (2% O_2). Western blots were conducted to assess protein expression between these samples.

MCF7 cells and spheroids were used as opposed to U-87 MG cells and spheroids, to identify if there was a change in epithelial to mesenchymal transition in a epithelial type tumour.

Representative images for the blots at the various conditions can be seen on Figures 4.13. Distinct bands for E-cadherin at 130 kDa were observed in all MCF7 cell line samples. No bands at this molecular weight were visible in the MDA-MB-231 controls. Reciprocally, vimentin was found to be expressed in the MDA-MB-231 control samples, whilst no expression of vimentin was observed the MCF7 samples, as is expected with mesenchymal- and epithelial-like cells, respectively. Interestingly, additional bands were observed exclusively in the MCF7 on-chip spheroid samples when probing for E-Cadherin, specifically at 80 kDa and 30 kDa, suggesting the protein is being cleaved or degraded or there is fragmentation of the junctions between the cells within the spheroids.
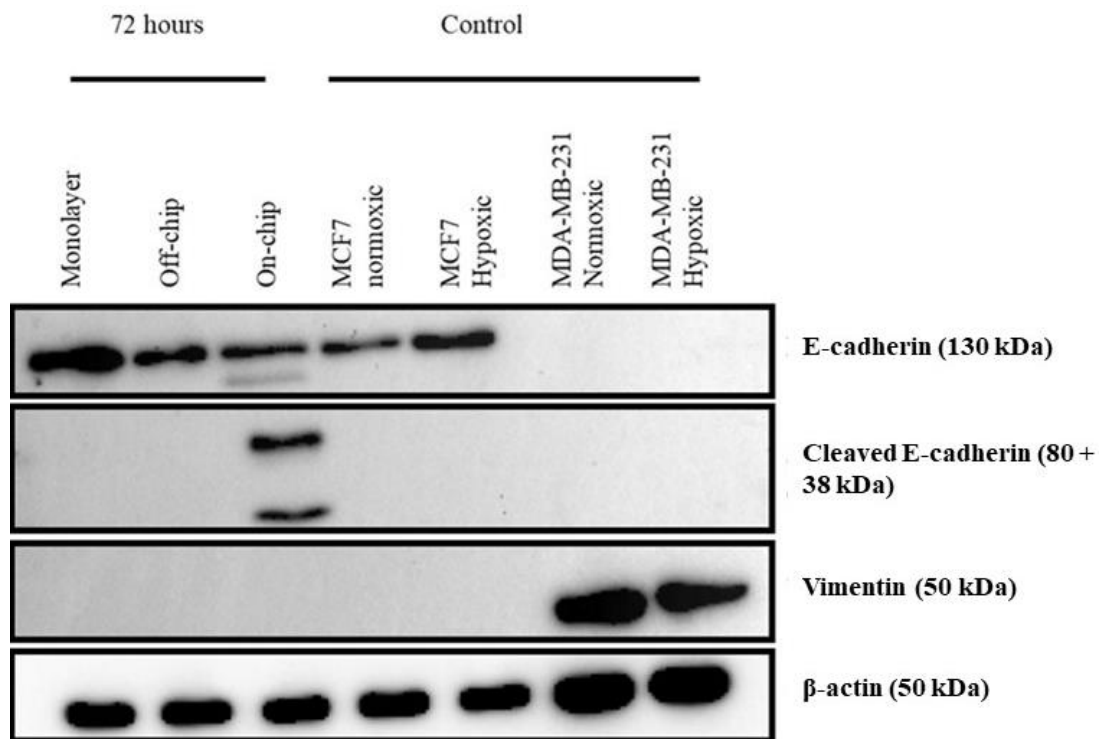
Figure 4.13: Expression of EMT markers in spheroid models (off-chip and on-chip) vs 2D monolayers

Cell lysates were prepared in UTB buffer at 50μg protein from a MCF7 monolayer, MCF7 off-chip spheroid, MCF7 on-chip spheroid (all 72 h), (20% O_2) normoxic and (2% O_2) hypoxic MCF7 monolayer controls and (20% O_2) normoxic and (2% O_2) hypoxic MDA-MB-231 monolayer controls (all samples; 3.5 x 10^4 cells). 50 μg of protein per sample were loaded in an 10% SDS-PAGE gel, separated, and processed for western blotting detection of E-cadherin and Vimentin expression. Loading control was β-actin. Image representative of minimum n=5 experiments.

4.4 Discussion

4.4.1 Key findings

The specific aims of the research described in this chapter were to design and validate a microfluidic device for spheroid incorporation and maintenance. This involved 1) *design and fabrication of the device,* 2) *incorporation of a spheroid*, and 3) *assessment of spheroid viability and migration/invasion potential.*

A microfluidic device (generation 1) was designed and fabricated. Shear stresses present within the device were comparable to those seen within the literature and *in vivo* models. Moreover, spheroids could be incorporated into the device, with U-87 MG and MCF7 spheroids (2.5 x 10^4 and 3.5 x 10^4 cells) being the most suitable. Cell viability was assessed on-chip in comparison to off-chip, which showed the spheroids were able to be maintained viable for 72 h within the microfluidic device. It was also shown that it is possible to detect known secreted factors involved in metastatic spread (VEGF) in the effluent collected from the on-chip model. However, it was noted that the shape of the spheroids retrieved from the chip devices were irregular/non-spherical, which could be a consequence of compression in the slightly too small microwell chamber on the device. This may have resulted in E-cadherin expression being altered. Thus, it was decided to alter the design of the microfluidic device to fully house the spheroid without compression, as discussed below.

4.4.2 Shear Stress

The values calculated for the shear stress within the microfluidic device (between 1.34 x 10^{-4} 7.91 x 10^{-3}) (Table 4.3) were far lower than the values seen in blood vessels (between 0.3 and 5.0 Pa) (Table 4.2), however, shear stress within interstitial flow has been reported as 7 x 10^{-3} to 1.5 x 10^{-2} dyn cm $^{-2}$ (Mitchell & King, 2013). These are like values calculated for the generation 1 the microfluidic device. Increased rates of interstitial flow have been shown to be highly correlated to migration, further supporting how mechanistic forces, such as shear stress,

need to be considered carefully within the microfluidic device (Shields *et al*., 2007; Munson & Shieh, 2014). In a recent study, migration of epithelial ovarian cancer cells were evaluated within a microfluidic device with wall shear stress values of 0.5, 1.0 and 1.5 dyn cm $^{-2}$ (Avraham-Chamik *et al*., 2013) and other groups used 0.002, 0.007 and 0.015 dyn cm^{-2} (Mitchell and King, 2013; Ip *et al*, 2016). It was found that wall shear stress caused cell elongation, fibre formation and microtubule formation, suggesting shear stress may influence cell spreading. For the generation 1 microfluidic device employed here, the shear stress values were within an acceptable range to study cellular migration and spread.

4.4.3   Spheroid Incorporation

The microfluidic device featured a deep channel of 600 μm depth by 1500 μm width, followed by a microwell of 1000 μm depth and 2000 μm. Finally, there was a 150 μm deep, 1500 μm wide shallow channel after the microwell. Therefore, spheroids needed to pass through these dimensions (600 μm x 1500 μm) to reach the central microwell. It was found that U-87 MG and MCF7 spheroids (2.5 and 3.5 x 10^4 cells per well) had the highest success rate for incorporation, followed by HCT116 and HT29 spheroids at 3.5 x 10^4 cells per well (section 3.1). Both U-87MG and MCF7 (2.5 x 10^4 cells per well) spheroids were approximately 1000 μm in diameter, therefore they would need to compress their size by 40% to reach the microwell. This is also similar for the 3.5 x 10^4 seeded MCF7 and U-87 MG spheroids, which would need to compress 50 and 45% respectively, to reach the microwell. This level of compression is reflected in the HT-29 and HCT116 spheroids at 2.5 x 10^4 cells per well, which also needed to compress their size by 50 % to reach the microwell. MDA-MB-231 spheroids completely disaggregated after pipetting. The larger sized spheroids from all cell lines (MCF7, HCT116 and HT-29) would need to compress to 55%, 60% and 65% of their original size to reach the microwell, and all got lodged within different locations at in the deep channel. These observations are explainable, however. Spheroid compression under small levels of

compressive pressure was investigated by Das and colleagues (Das *et al*., 2013). They found

that a 400 µm diameter spheroid was able to compress its shape and squeeze through a 200 µm

wide channel (50% reduction in size) when subjected to small compressive pressures The

MCF7 and U-87 MG spheroids used in the here presented work would need to compress to

about half their size which is similar to the spheroid compression reported by Das. Moreover,

U-87 MG cells have been reported to form rigid, compact spheroids (Günther *et al*., 2003;

Ramis *et al*., 2012; Vinci *et al*., 2013; Aaberg-Jessen *et al*.,2013). This tight-bound, robust

structure will likely allow the spheroids to withstand compression pressures (Vinci *et al*.,

2012).

The 5×10^4 cell per well spheroids may have got lodged, not only due to increased size, but

also due to the microfluidic device properties. The device glass surface is hydrophilic and

negatively charged, so sticking of biomolecules and cells to glass surfaces are common

(Kangning *et al*., 2012). CNC glass fabrication has been shown to result in somewhat rough

channels (Kangning *et al*., 2012). The larger 5×10^4 cells per well spheroids would be very

close to the channel edge and got stuck due to the rough edge. As the highest success rates for

incorporation were seen in MCF7 and U-87 MG spheroids, these were used for subsequent

experiments.

4.4.4   Shear Stress and migration capability

MCF7 and U-87 MG spheroids were incorporated into the microfluidic device and perfused

with media at a flow rate of 3 µL min^{-1} (5×10^{-11} m^3 s^{-1}) (section 2.8). This speed results in the

spheroid being replenished with nutrients three times an hour, specifically once every 18.16

min. Large tumours contain hypoxic and anoxic regions being poorly supplied with structurally

solid blood vessels and therefore have lower blood velocities and shear stress, than the external

tissue and environment (Mitchell & King, 2013). Therefore, the gentle speed within the

microfluidic device mimics the velocity found within *in vivo* tumours. The shear stress values

in interstitial flow ranges from 7 x 10^{-3} to 1.5 x 10^{-2} dyn cm^{-2} (Mitchell & King, 2013). The low levels of shear stress on spheroids was also used by Ip and colleagues. They used shear stress (less than 0.1 dyn cm^{-2}) which closely mimics the level expressed in the peritoneum, on ovarian cancer spheroids (Ip *et al*., 2016). Their findings were that spheroids grown under both 0.002 dyn cm^{-2} and 0.02 dyn cm^{-2}, like the values within the microfluidic device in this project, induced expression of epithelial-to-mesenchymal markers. This suggests that shear stress is associated with the promotion of tumour spread, further reinforcing that the current spheroid-on-a-chip model could be used in future experiments to look at early stage invasion and metastasis. Furthermore, increased rates for interstitial flow have been shown to be highly correlated to increased migration (Shields *et al*., 2007; Munson & Shieh, 2014). Prior to identifying metastatic markers on-chip, the viability of spheroids was assessed, and compared to that of spheroids off-chip.

4.4.5 Evaluation of cell viability maintenance in the spheroid-on-chip model

4.4.5.1 Evaluation of cell viability using effluent biomarkers

To assess cellular viability, the CytoTox glo assay was used. Other groups typically use the LDH assay (Choi *et al*., 2015), trypan blue counting or fluorescent labelling of cells (Kwak *et al*., 2018; Lee & Cha, 2018;Rogers, 2018; Chen *et al*., 2019). However, whilst these studies identify an increase in cell viability on-chip over the static culture or monolayer, supporting trends seen within this data, they are end point assays, requiring the lysis of cells to determine the fraction of viability. In comparison, the CytoTox glo assay used in this work allowed the collection of effluent over time to analyse the presence of protease, to act as an indicator of viability. Meaning it enabled the collection of media from all testing conditions every 24 h without being an endpoint assay (Riss *et al*., 2014). The use of this assay for continued collection of media overtime from on-chip spheroid conditions is something that appears novel. The CytoTox assay results suggested that spheroids on-chip have lower levels of

protease activity than the off-chip counterparts, indicating fewer cells undergoing cell death in the same period. However, a consideration for this assay was that the assay has been designed for monolayers of cells, and at a smaller seeding density, 2.5×10^4 cells (Holden & Horton, 2009) and not for 3D cell models such as spheroids. The protocol outlined specific incubation times (15 min) for the lysis buffer to be able to lyse the control monolayer of cells effectively , not the control spheroids, which may need longer (Holden & Horton, 2009; Edmondson *et al.*, 2014). The viability value was lower in the frozen samples than the fresh samples (section 4.4). At -80 °C proteins should denature, which is a possible reason for the deduction of viability values seen in the frozen samples in comparison to those of the fresh samples (Percival *et al.*, 1999; Sarker *et al.*, 2013).

The control value is very high in comparison to the spheroid controls. The other fresh viability data shows they should be comparable, as both are seeded at 3.5×10^4 cells. The change of machinery (due to a fire) may have affected the data reading and output. If the machine detected the phenol red presence within the media, then this could interfere with the luminescence values. The key observations from all cellular viability data are that viability decreases with frozen media samples in comparison to fresh media. The results demonstrate that the cell monolayer has a lower viability value across all, and spheroids on-chip have a better viability, and the generation 1 microfluidic device allows for successful maintenance of viability for the spheroids on chip.

4.4.5.2   *Evaluation of cell viability in situ*

The FDA/PI assay demonstrated that the spheroid on-chip appeared to have a lower proportion of dead cells than the off-chip conditions, and increased proportion of live cells. The difference between the off-chip and on-chip spheroid viability can be explained by the continuous perfusion of the spheroid and removal of nutrients and waste (Halldorsson *et al.*, 2015). This

continuous flow prevents the accumulation of metabolites and waste in the external environment, potentially contributing to increased cell viability. It is possible that the lower proportion of dead cells is lower in the microfluidic device due to the device design itself, due to either dead cells becoming trapped within the internal channels, or flushed out over the 72 h time period (Whitesides, 2006; Ren *et al.*, 2013). Overall the results did support the observations seen in the CytoTox Glo viability assay.

However, it needs to be noted that the spheroids (repeats) in the on-chip condition all appeared to be broken or misshapen. It is possible to see from figure 4.11, that the spheroid has a leading edge, which appears and is likely to be the section of cells which are flowing through the initial interface between the shallow channel and microwell. This demonstrates that an adaptation to the device design is needed. One plausible approach to assess viability on-chip would be to image spheroids on-chip. However, an amendment to the microfluidic device would be required. This will be covered in Chapter 5.

4.4.6   Evaluation of pro-metastatic biomarkers in the spheroid-on-chip device

To further analyse the biology of spheroids within the microfluidic device, especially regarding pro-metastatic characteristics, spheroids were collected and lysed, in preparation for protein expression analysis. EMT and VEGF were chosen to be looked at, as they are both indicative factors of cancer spread and migration. Therefore, their presence shows that cancer has moved to a migratory and invasive phenotype. As EMT is indicative of invasive cells then the factors associate with EMT were investigated. These factors include Vimentin and E-Cadherin (Weinberg, 2013). Another key aspect of the metastatic cascade that was investigated using the current model is tumour angiogenesis. One key molecule in tumour angiogenesis is vascular endothelial growth factor (VEGF) (Hoeben *et al.*, 2004).

4.4.6.1 *Evaluation of EMT*

E-cadherin is a type-I transmembrane glycoprotein that is localised to the adherens junctions and basolateral membrane in endothelial cells (ECs). E-cadherin consists of a large extracellular domain (comprised of 5 extracellular cadherin domain repeats) (David & Rajasekaran, 2012). The repeats bind calcium ions to form a stiff linear molecule, that bind in a homophilic fashion in trans-interactions (neighbouring cells) and cis-interactions (self), resulting in a 25 nm adherent junction (Perez & Nelson, 2004). E-cadherin also mediates tissue integrity and preservation of tissue function (Jeanes *et al*., 2008; David & Rajasekaran, 2012) and its loss is well characterised in tumour progression

When epithelial like cancer cells (MCF7) undergo a shift towards a motile and invasive phenotype (mesenchymal like), they undergo the process known as epithelial mesenchymal shift (EMT). The cells express different proteins, including the replacement of E-cadherin to N-Cadherin, smooth muscle β-actin, cadherin-11 and vimentin (Alkatout *et al*., 2013; Lima *et al*., 2016). As shown E-cadherin and vimentin was assessed through western blot. The results were expected in which the MCF7 monolayers and spheroids showed E-cadherin, whilst the MDA-MB-231 cell line samples showed no expression, instead MDA-MB-231 showed vimentin expression and the MCF7 samples did not.

Interestingly, the spheroid on-chip model shows three additional bands of E-cadherin. The additional bands could be cleaved E-cadherin fragments at 80 and 38 kDa (repeated at least 5 times). It could be and is more likely to be a result of the microfluidic device design where the rough surface could fragment and damage the spheroid breaking the cell-cell adhesions. This potential artefact of the damaged spheroid or misshapen spheroid is seen in figure 4.11.

4.4.6.2 *Cancer biomarker analysis -VEGF*

Increased VEGF released from the extracellular matrix is mediated by MMPs through a positive feedback loop (Rundhaug, 2003;Hollborn *et al*., 2007). VEGF has been shown to

promote increased endothelial cell proliferation, chemotaxis and vessel permeability (Rundhaug, 2003; Hollborn *et al*., 2007; Saharinen *et al*., 2011). Importantly, the presence of regions of hypoxia are associated with increased VEGF expression, leading to deregulated growth and sprouting of blood vessels (Saharinen *et al*., 2011).

Therefore the presence of secreted VEGF on the effluent media could indicate that the spheroids are shifting towards an invasive phenotype (Hoeben *et al*., 2004). The results show that U-87 MG effluent has a higher level of VEGF than MCF7. A reason for the increased levels of VEGF in U-87 MG conditions may be because U 87 MG is a high-grade stage IV glioblastoma and glioblastomas are typically endothelial rich tumours, relying on a constant blood flow and nutrient supply (Brem *et al*., 1972). VEGF can remodel endothelial cells (Roberts *et al*., 2013). Therefore, glioblastomas express high levels of VEGF to further remodel the basement membrane. Although the simulations confirm that the spheroids can access oxygen, there is a lower concentration within the device than first expected. A decreased oxygen concentration (<2%) within the chip should increase the metastatic potential, as hypoxia is known to drive metastatic progression (Valastyan & Weinberg, 2011; Rankin & Giaccia, 2016). This is important as it demonstrates that the different models of cancer (static spheroid, monolayer and on-chip spheroid) are not greatly changing the expression levels of VEGF, allowing the microfluidic model to be used for further experimentation on metastasis.

4.4.7 Simulations

COMSOL simulations were carried out to study the effect of flow rate, spheroid size and oxygen concentration within the microfluidic device. This work was performed by a PhD student in the Department of Chemistry at the University of Hull, Martin Christensen (Christensen, 2019). He constructed a model of simulation of flow within the generation 1 microfluidic device, in which the computer-generated spheroids of varying size increments of 100 μm ranging from 300 – 1300 μm were placed into the microfluidic device. The simulations

show how a spheroid of 1000-1200 μm diameter would be squeezed as it would not quite fit into the 2000 μm diameter and 1000 μm high cylindrical microwell on-chip. And that a spheroid of 1000-1200 μm diameter would have a core that is 65-75% of the total mass. It is noteworthy that the FDA/PI images (fig 4.11) from spheroids retrieved from the chip device also show evidence of spheroid compression.

Figure 4.14 shows the oxygen concentration at a flow rate of 3μl/min. The highest oxygen concentration (0.2 mM) was found at the neck of the inlet, whilst the lowest oxygen concentration (0.05 mM) at the base of the microwell closest to the outlet of the microfluidic device. The simulation data shows that the spheroid would have good access to oxygen with concentrations of 0.15 - 0.2 mM at its inlet facing side but would have anoxic and hypoxic regions throughout, namely at the microwell base and the outlet; with oxygen concentrations of 0.05 and 0.1 mM. *In vivo* tumours can acquire a median of 3 mmHg (0.39%) O_2. Ranging from 2.0- 32 pO_2, with brain and breast cancer obtaining 1.7 and 1.3 % O_2, respectively (Carreau *et al.*, 2011; McKeown, 2014). Therefore, a spheroid within the device would have access to 0.1-0.2 mM O_2, meaning it would be able to access a hypoxic but adequate amount of oxygen. The simulations clearly shows that the spheroids can acquire oxygen an **<u>acceptable</u>** level within the device. However, these findings supporting the redesign of the microfluidic device as presented in chapter 5.

4.4.8   Further designs

Following these experiments, it was decided to re-design the current device to a generation 2 model device that would allow real-time imaging *on-chip*. It would be advantageous to acquire live/dead data whilst the spheroids are within the microfluidic device, thus allowing the ability
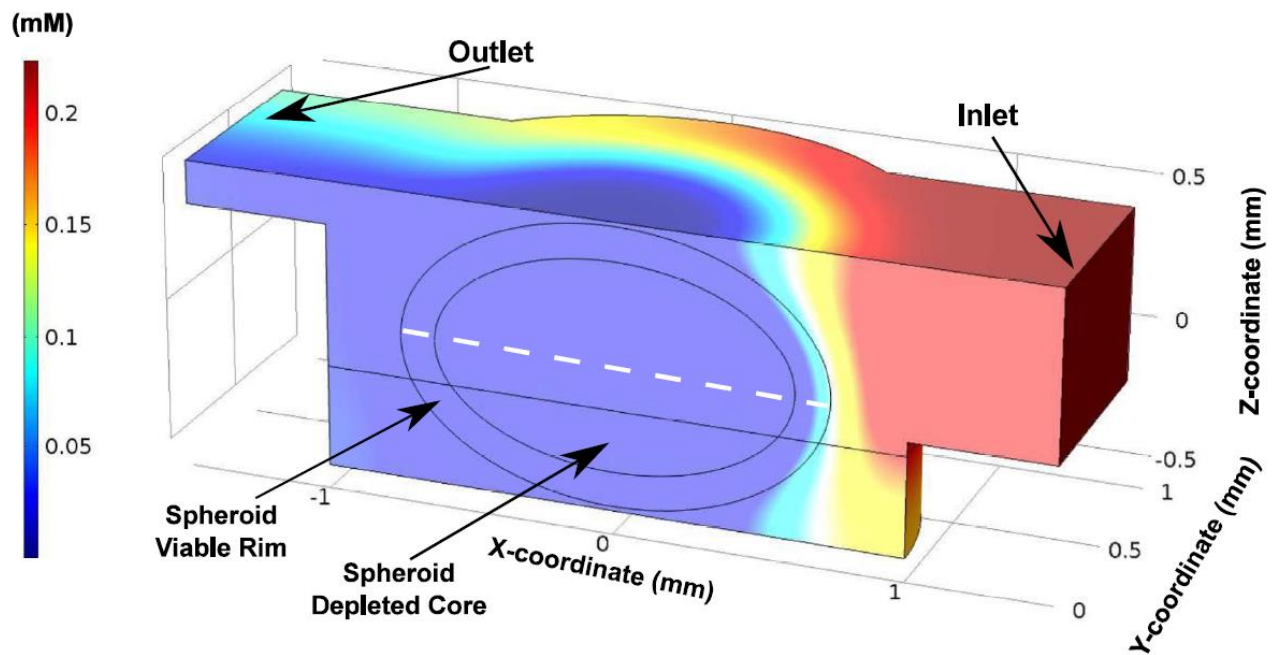
Figure 4.14: Symmetry view of the oxygen concentration   *(Taken from* Christensen, 2019*)*

Volume plot of the spheroid incubation device harbouring a 1300 μm dimeter wide spheroid perfused with an air saturated medium at a flow rate of 3μL min⁻¹. The mid-height cross-sectional line of the spheroid is indicated with a dashed white line. The spheroid was to ease the computational load divided into a viable rim and a depleted core region with higher mesh densities in the viable rim. The thickness of the viable rim is 120 μm.

Table 4.5: Evaluation of the spheroid device for the incubation of spheroids in the diameter range 300-1300μm.

Volume integrals were performed on each spheroid to determine how large of a volume is occupying regions above the necrotic oxygen concentration threshold ($C_{Necrotic}$ 0.00112 μM). (Taken from Christensen, 2019*)*

Spheroid Diameter (μm)	Volume (%) > $C_{Necrotic}$
300	100
400	100
500	84.6
600	69.7
700	58.3
800	49
900	40.3
1000	33.2
1100	28.5
1200	24.9
1300	22.3
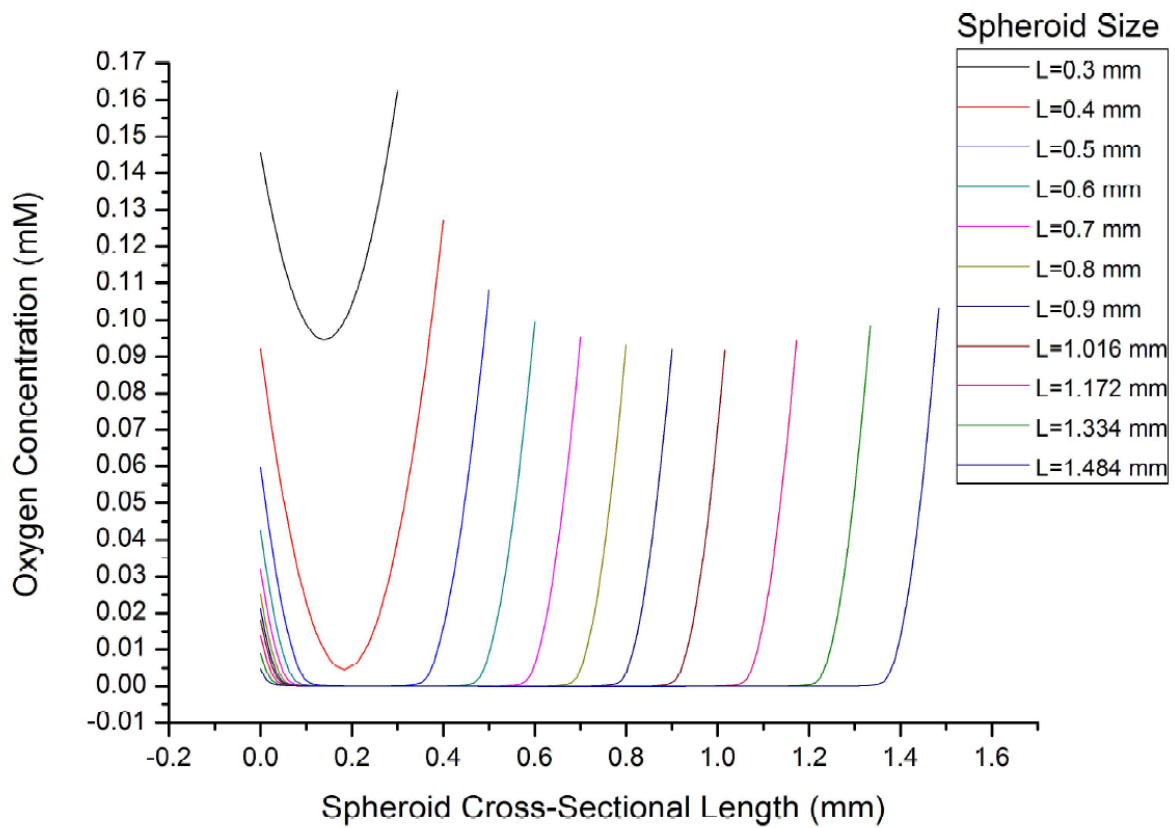
Figure 4.15: Simulation of oxygen tensions within spheroids *(Taken from* Christensen, 2019*)*

Spheroids incubated in the spheroid device as plotted along the cross section going from the outlet towards the inlet. The spheroids have diameter ranging from 300-1300 μm and were perfused with the air saturated medium (225μm) using a flow rate of 3μL min^{-1}.

to monitor the spheroids in real-time. It was also envisaged to introduce ECM matrices and hydrogels such as collagen or Matrigel. Matrigel specifically is made of 60% laminin, 30% collagen and 8% entactin (Kleinman & Martin, 2005). These could surround the spheroid in the micro-well or the spheroid could be directly placed upon the gel substance (Kleinman & Martin, 2005; Hesse *et al*., 2010). This would thus allow the testing of spheroids invasion when within an ECM and perfusion culture.

4.5   Conclusions

The key results of this chapter include; the microfluidic device was able to be fabricated from Schott B270 glass. It was shown that spheroids were able to be incorporated into the device, with U-87 MG and MCF7 spheroids being most applicable. The shear stress was shown to be like literature values and *in vivo* conditions. Live/dead and cell viability assays showed that on-chip spheroids were comparable to off-chip models. However, issues were noted with spheroid structure and spheroid compressing, therefore **advancements are required**.

Chapter 5 –The assessment of migration and invasion of cancer spheroids within an advanced microfluidic device design (generation 2 and 3)

5.1 Introduction

5.1.1 Microfluidic devices for metastasis

Microfluidic devices offer a novel and exciting platform to investigate metastasis and metastatic spread of tumour cells. They offer a highly controllable environment, including factors seen *in vivo*, such as continuous perfusion and shear stress (Whitesides, 2006; Weinberg & Hanahan, 2011). Shear stress has repeatedly been shown to increase the invasive potential of cells and metastatic progression (Rush *et al*., 2012; Jain RK *et al*., 2014). For example, low shear stress has been shown to have led to an increase in migration *in vivo* and *in vitro* in breast cancer cell models (Mitchell & King., 2013; Huang *et al*., 2018). Therefore, microfluidic devices are a desirable model to investigate the metastatic cascade (specifically the early stages- such as local invasion, intravasation and survival in circulation) using a variety of cancer cell lines (Song *et al*., 2009; Blaha *et al*., 2017; Kühlbach *et al*., 2018, Chaw *et al*., 2007; Acosta *et al*., 2014; Liu., 2019). The microfluidic device used in this report focusses on early stage metastasis, specifically local growth invasion and cell shedding from the primary mass. Two examples of metastatic research within a microfluidic device was conducted by Blaha and Hao. Hao's group were interested in latter stage metastatic interactions, namely metastatic breast cancer migration to bone microenvironments. Hao developed a PDMS microfluidic device, containing a glass coverslip. They used the glass coverslip to grow MC3T3-E1, MDA-MB-231 and MDA-MB-231 BRMS cells on. Before forming a 3D mineralised bone tissue over a 1 month period on chip. They noted that osteoblastic tissue, 85 μm in size, was able to be formed without differential agents. Moreover, they concluded that breast cancer cell interactions noted *in vivo* was recapitulated on-chip (Hao *et al*., 2018). Similarly, to Hao is Blaha.

Blaha investigated extravasation, cell-cell interactions and angiogenesis; specifically, endothelial cell and MDA-MB-231 cell interactions, on chip. They developed a PDMS microfluidic device, comprised of five inlets and hexagonal posts, resulting in five lanes. 3 mg/ml of type I collagen was loaded into the device, encapsulating 4×10^6 cells/mL HUVEC cells. To help develop this system COMSOL modelling was adopted, to allow the group to visualise the location of cell presence and hydrogel location within the device. Overall, they developed a platform that allowed the isolation and imaging of cell-cell and cell-matrix interactions, focusing on MDA-MB-231 cells and HUVECs (Blaha *et al*., 2017). Blaha found, through confocal imaging, that HUVECs grow vertically across collagen. Moreover, they concluded that metastatic breast cancer cells have increased migration in the presence of HUVECs in comparison to HUVEC absence. The group quantified MDA-MB-231 cells invade 1 μm (0.61 μm +/- 0.59μm) past collagen without HUVEC presence, whilst they invade 26.7 μm with HUVEC presence (Blaha *et al*., 2017).

5.1.2 Opportunities for device advancement and aims of this chapter

Chapter 4 detailed the development and validation of a 1st generation of a spheroid-on-chip device setup, including evidencing the maintenance of spheroid viability of chip and suitability of the setup for the collection of material/samples relevant for evaluation of metastatic potential. However, specific issues with the device and the spheroid incorporation were also highlighted. Firstly, from figure 4.11 it was possible to see that spheroid shape and structure was changed within the device, potentially due to the rough surface of the microfluidic device glass surface edge formed from CNC fabrication. Secondly, the spheroid incorporation process were not ideal, as the spheroid has to be pumped through the deep channel in order to reach its intended location, which can impact on what spheroids can be incorporated or not. Finally, the

device is not ideal for imaging on a brightfield microscope, again potentially due to the glass thickness and roughness of the channels.

5.1.3 Rationale and Aims

The rationale of this chapter was to advance the microfluidic device to allow hydrogels to be incorporated within, something which was not possible in the generation one microfluidic device. This would allow a more replicative model of *in vivo* cancer within the microfluidic device. Furthermore, it would be desirable to be able to image a spheroid on-chip in real time, so it is possible to monitor cancer spread and migration within the hydrogels. Finally, it will be needed that potential biomarkers of cancer migration and invasion released from the spheroid to be collected. Therefore, the aims of this chapter are to:

To improve the microfluidic device design for analysis of pro-metastatic phenotypes in spheroids

- *Advance design to allow easier access to microwell*

- *Advance design to image spheroids directly on-chip*

- *Incorporate hydrogel(s) into microfluidic device and embed spheroids*

- *Investigation of potential secreted biomarkers of cell migration/invasion, such as VEGF and IL-6*

- *Evaluate at cell migration patterns of spheroids on-chip*

5.2 Experimental set up

5.2.1 Generation 2 spheroid-on-chip device design

As several limitations were found in the generation 1 microfluidic device design, a second device design was constructed with the input of Dr Alex Iles. The advanced microfluidic device

was designed with the same geometry as the initial device (generation 1) and was again fabricated in Schott B270 glass.

The main improvement focused on access for spheroid incorporation. An access port (2 mm wide and 3 mm deep) was milled directly above the micro-well, allowing for direct pipetting and incorporation of spheroids into and out of the micro-well preventing any misshape issues or blockages. It would also allow the pipetting of ECM-like matrices and hydrogels into the micro-well. Furthermore, to prevent any through flow of spheroids out of the microfluidic device, a 70 μm weir was milled at the entrance of the shallow channel.

To maintain continuous flow of DMEM from the inlet to the outlet, removable transparent poly dimethyl siloxane (PDMS) plugs were fabricated and moulded to exactly fit into the hole above the micro-well (section 2.9). The material is transparent and would not impede the direct imaging of a spheroid within the microwell.

Similarly, to the first device design, the advanced microfluidic device did not contain a threaded inlet or outlet so the same custom-built inlet and outlet coupling interface was built and used (same tubing set up as generation 1) as shown in section 2.8

To test the device for leaks and breakages, Brilliant Blue solution was flowed through as shown in section 2.9

5.2.2 Generation 3 spheroid-on-chip device design

The second generation device also had certain issues. The device did not allow the spheroid to be imaged as clearly as required when within the microwell. The spheroid was unable to be viewed correctly as the rough microwell base was refracting and reflecting light unevenly. Therefore, a further improvement on the device was suggested and fabricated. The generation

two microwell was completely drilled through, meaning there was an access port above and below the microwell. Finally, a borosilicate coverslip was added at the base of the microwell. All details are noted in section 2.10.

5.2.3   Spheroid incorporation

U-87 MG and MCF7 spheroids (seeded at 2.5 x 10^4 cells per well) were selected, following the successful incorporation of these spheroids into the microwell. The spheroids were grown in conditions previously detailed (section 2.3) and carefully pipetted directly into the microwell.

5.2.4   Silanisation and PEG treatment

Following issues found in the generation 2 device, it was required that the glass surface be treated to prevent cell adhesion. To prevent cell adhesion, F108 was selected to be used. It has been shown that Pluronic F108 can prevent cell attachment and has been used in previous studies within microfluidic devices (Corey *et al*., 2010; Cheng *et al*., 2016; Zhang *et al*., 2018). To allow the microfluidic device to bind F108 the glass surface needed to be changed to hydrophobic from hydrophilic. The glass surface was chemically modified to change its properties using OTS, allowing a PEG tri-copolymer to be added, as detailed in section 2.8.

To demonstrate whether the silanisation and surface treatment of the glass surface was successful in increasing the hydrophobicity, contact angles were measured. The contact angle of a water droplet in relation to the glass surface can denote the levels of hydrophobicity present (Cras *et al*. 1999). The contact angles were measured using a droplet of water on multiple testing slides. The slide was placed on a shape drop analyser (Kruss, Germany), imaged and analysed on the machinery automatically (section 2.8). As F108 PEG tri-co-polymer treatment has been shown to lead to decreased cell adhesion (Corey *et al*. 2010), the treatment needed to be evaluated prior to adding it to microfluidic devices. Four slides were chosen to test as shown

in section 2.9. MCF7 and U-87 MG cell suspensions were pipetted over the top of the slides before being imaged on a microscope (Zeiss, Germany) in random locations over the slide.

Silanisation within a microfluidic device

To silanise and surface treat the microfluidic devices, OTS and F108 was also used. In brief a 1% v/v OTS solution was prepared and flowed in by hand using glass syringes. The solution was further flowed and left within the devices to incubate for 20 mins before F108 was incubated within the microchannels for 12 h overnight.

The following day, water was added to the device microchannels at a variable flow rate, mainly driven by gravity at 9.81 m s^{-1}. Upon successful water flow within the microchannels, the devices were observed be eye to have a water-air interface and therefore the device was immediately imaged on a microscope (Ziess, UK).

5.2.5 Hydrogel incorporation into the microfluidic devices

Several hydrogels and ECMs were chosen for this study; Collagen, Fibronectin, Matrigel and Gelatin. These hydrogels have been previously used for migration and invasion assays (Vinci *et al*, 2013). Prior to hydrogel incorporation, the microfluidic device was cleaned, and air flushed from the channels or microwells. Hydrogels were added to the microwell through pipetting as described (see section 2.9.4). The microwell was then imaged on a microscope at 5x magnification (Zeiss, Germany). Brilliant blue solution was flowed into the device to test whether the hydrogel was incorporated successfully. Brilliant blue solution was used as it was easily identifiable and was able to stain the hydrogels, allowing the user to know its location.

5.2.6 Evaluation of Spheroid viability

Spheroids were incorporated into the microfluidic devices through direct pipetting into the microwell. Viability was evaluated in situ using the FDA/PI life/dead assay, as detailed in

section 2.4. Fluorescence quantification was performed on the images using ImageJ analysis software.

5.2.7 Evaluation of metastasis potential

Spheroids were added to the hydrogels within the microfluidic device microwell via direct pipetting. In order to evaluate cell migration and invasion *in situ*, the device was imaged at 24, 48 and 72 h. Migration and invasion was quantified for the total spheroid area over time, and its relative change using ImageJ analysis software. Sandwich ELISA for VEGF and IL-6 were used to quantify secreted factor presence in the effluent, as markers of metastatic potential (see section 2.5).

5.3 Results

5.3.1   Design and validation of Generation 2 spheroid-on-chip device

As noted in Chapter 4, several issues were found in the generation 1 microfluidic device design. Firstly, although it was possible to incorporate spheroids into the generation 1 device, allowing continuous prefusion of media and collection of effluent, the device lacked the ability to directly image the spheroids whilst on the microfluidic device. Secondly, the generation 1 device did not allow the collection of intact spheroids at the end of the experiment. Thirdly, there was the risk, for several cell lines, of the spheroids becoming entrapped, lost, or disaggregated during incorporation into the micro-well. This led to a decision not to pursue with the use of these for future experiments, and improve on its design, especially regarding spheroid incorporation and recovery.

Taking these limitations into account, a new design was proposed and constructed Dr Alex Iles. The generation 2 microfluidic device was designed with the same geometry as generation 1 and again fabricated in Schott B270 glass. However, a 70 μm weir was milled at the entrance of the shallow channel, to prevent any through flow of spheroids out of the microfluidic device. An access port was also milled directly above the micro-well, to allow direct pipetting of spheroids into and out of the micro-well, pipetting of ECM-like matrices and hydrogels into the micro-well, as well as direct imaging of the micro-well. Removable transparent poly dimethyl siloxane (PDMS) plugs were fabricated and moulded to exactly fit into the hole above the micro-well to prevent leakage of the microfluidic device.

The generation 2 microfluidic device design is seen as a schematic (Figure 5.1a), as a cross sectional side profile (figure 5.1b) and as a photo (figure 5.1c).
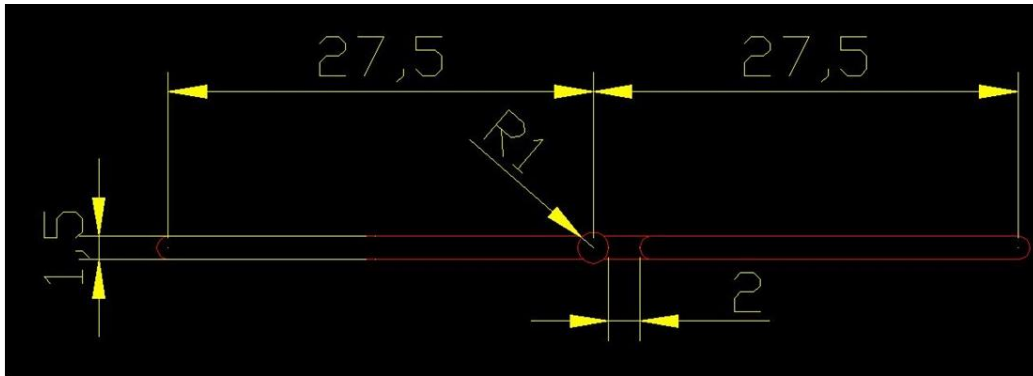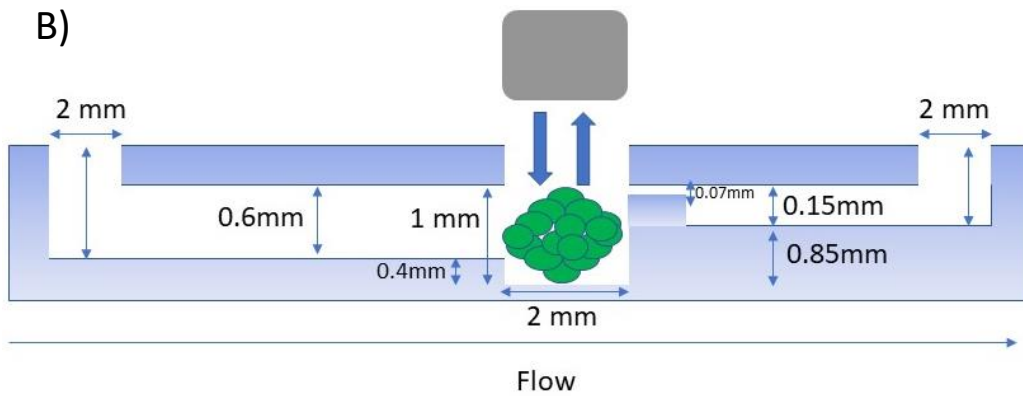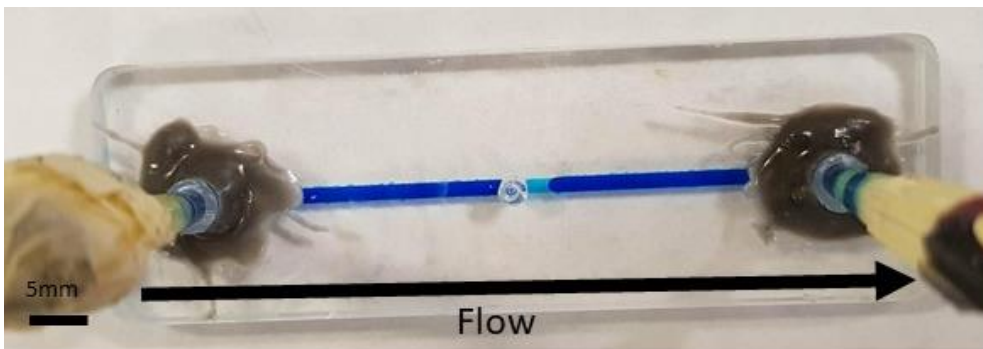
Figure 5.1: Generation 2 microfluidic device panel image (schematic, cross sectional drawing and photo)

Generation 2 microfluidic device schematic used for CNC milling purposes (in mm) (A), Generation 2 microfluidic device cross sectional drawing with an example spheroid in the micro-well and a grey PDMS plug with arrows denoting the removability of it (B) and a photo from above with brilliant blue dye flowing from the deep channel, through the micro-well and into the shallow channel. Scale bar represents 5 mm.

5.3.2   Silanisation and glass surface treatment

To prevent MCF7 and U-87 MG spheroids from breaking and becoming fragmented, as was seen in the generation 1 microfluidic device, the microfluidic device was silanised. Silanisation is the process of altering the glass properties, in this example from being a hydrophilic surface to a hydrophobic one. Once the glass was silanised it was coated with F108; to prevent the cells adhering to the glass surfaces. The cells were therefore unlikely to become unattached from the spheroid due to the microfluidic device material property. To demonstrate whether the silanisation and surface treatment of the glass surface were successful in increasing hydrophobicity, contact angles were measured. A glass slide untreated was used as a hydrophilic control, and a p-nitrile surface was used as a hydrophobic control. Three further conditions on microscope slides were tested: untreated slide; silanised slide (treatment with OTS alone); silanised slide with F108 treatment. The results in Figures 5.2 (example of the water droplets, and the contact angle results, respectively) show that the droplet of water on the untreated hydrophilic microscope slide is flat and has a high contact angle. This shows that the water is attracted to the glass surface (Figure 5.2). The water droplet on the OTS treated slide is dome-like in shape, with a lower contact angle (approximately 90º) than the untreated slide (Figure 5.3). This indicates that the silanisation has altered the glass hydrophobicity from being hydrophilic to hydrophobic. In the slide silanised and treated with F108, the dome shaped water droplet is still observed, but the contact angles are 14 degrees larger than when the glass slides are treated with OTS alone (Figure 5.3). This data shows that although the slides treated with F108 remain hydrophobic, they are less so than silanisation alone.

5.3.2.1 Silanisation confirmation within microfluidic devices

Upon confirmation of the successful silanisation and surface treatment of microscope slides, the microfluidic device microchannels were also treated in the same manner described in section 2. In brief a 1% v/v OTS solution was prepared and flowed in by hand using glass

syringes. The solution was further flowed and left within the devices to incubate for 20 mins before F108 was incubated within the microchannels for 12 h overnight.

The following day, water was added to the device microchannels at a variable flow rate, mainly driven by gravity at 9.81 m s^{-1}. Upon successful water flow within the microchannels, the devices were observed be eye to have a water-air interface and therefore the device was immediately imaged on a microscope (figure 5.4).

The images captured were then used to measure contact angles at the upper and lower junctions that water met the microchannel edge. These angles mirrored what was seen in the glass slide surface test. The contact angles of the water and microchannel edge was lower than 90 degrees. With the average angle across at least 4 devices being 85 degrees. This angle value is lower than the values found for the glass slides treated with OTS and F108, and similarly lower than the hydrophilic glass slide control previously used. The values denote that the microfluidic devices had their glass microchannel surfaces successfully treated from hydrophilic to hydrophobic (figure 5.5).

5.3.3   Testing of cell adhesion to F108 surfaces

The efficacy of F108 treatment needed to be determined prior to implementation in the microfluidic devices. Three microscope slides; one untreated, one polylysine-treated (which is known to promote better cell adhesion), and one silanised slide treated with F108 were placed in a tissue culture dish.
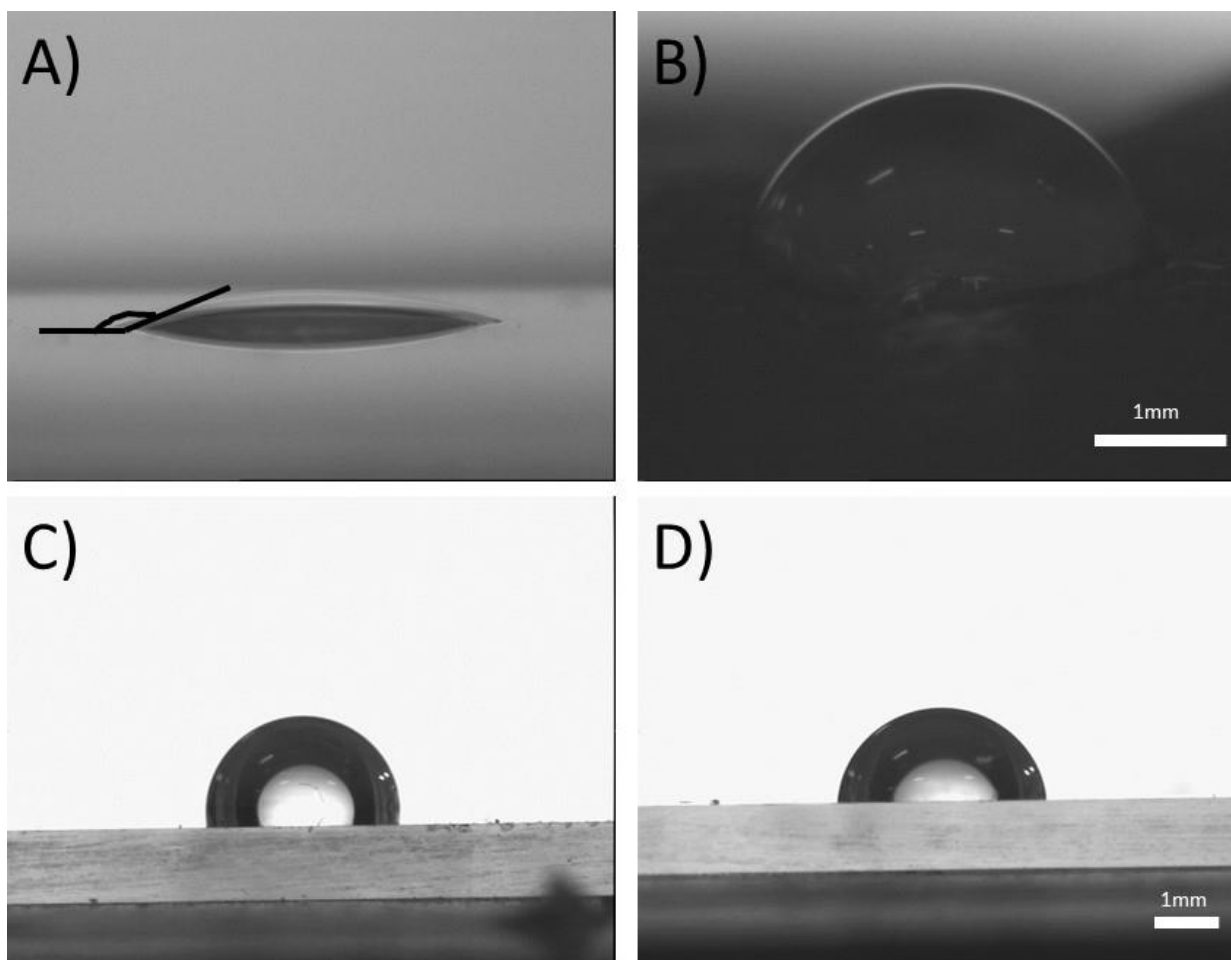
Figure 5.2: Representative images of water droplets used to measure contact angles on microscope slides after various surface treatments

Hydrophilic glass control slide with droplet of water (A) with example contact angle measurement, hydrophobic nitrile control with droplet of water (B), glass microscope slides with a droplet of water after being immersed in OST solution (C) and glass microscope slide with a droplet of water after being immersed in OTS solution and F108 for 24 h (D). Treatments were performed as noted in section 2.8. Images were obtained in using shape drop analyser (Kruss, UK). Scale = 1 mm. n=4 experimental repeats.
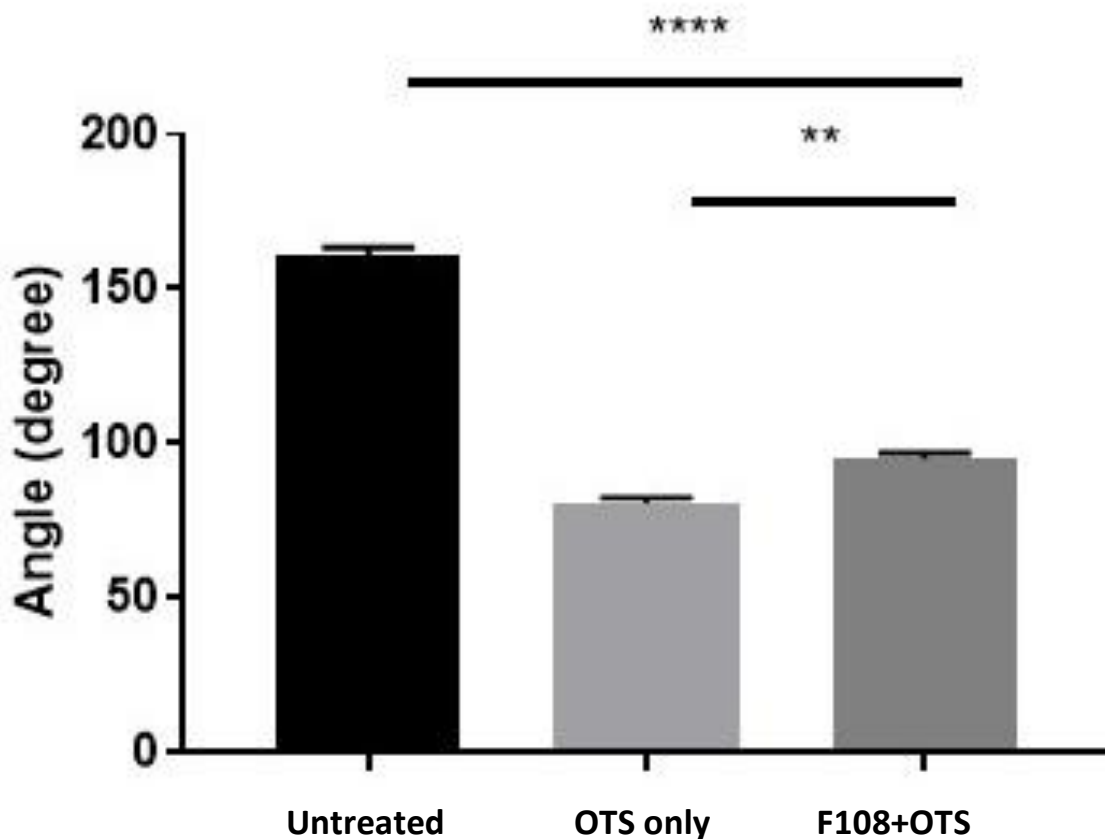
Figure 5.3: Contact angle hydrophobicity histogram

Histogram represents the average of contact angles measurements of at least four droplets of water on each of the three testing condition glass slides. In brief, 20 μl droplets of water were pipetted onto three differently treated glass microscope slides. The first slide was an untreated slide, naturally hydrophilic (UT). The second slide was a glass microscope treated with OTS only (OTS only). The third microscope slide was silanised with OTS and then incubated with F108 overnight (OTS + F108). Significance in differences between averages was determined using a 2 Way ANOVA. P *=<0.05, **=<0.01, ***=<0.001, ****=<0.0001. n=4 experimental repeats.
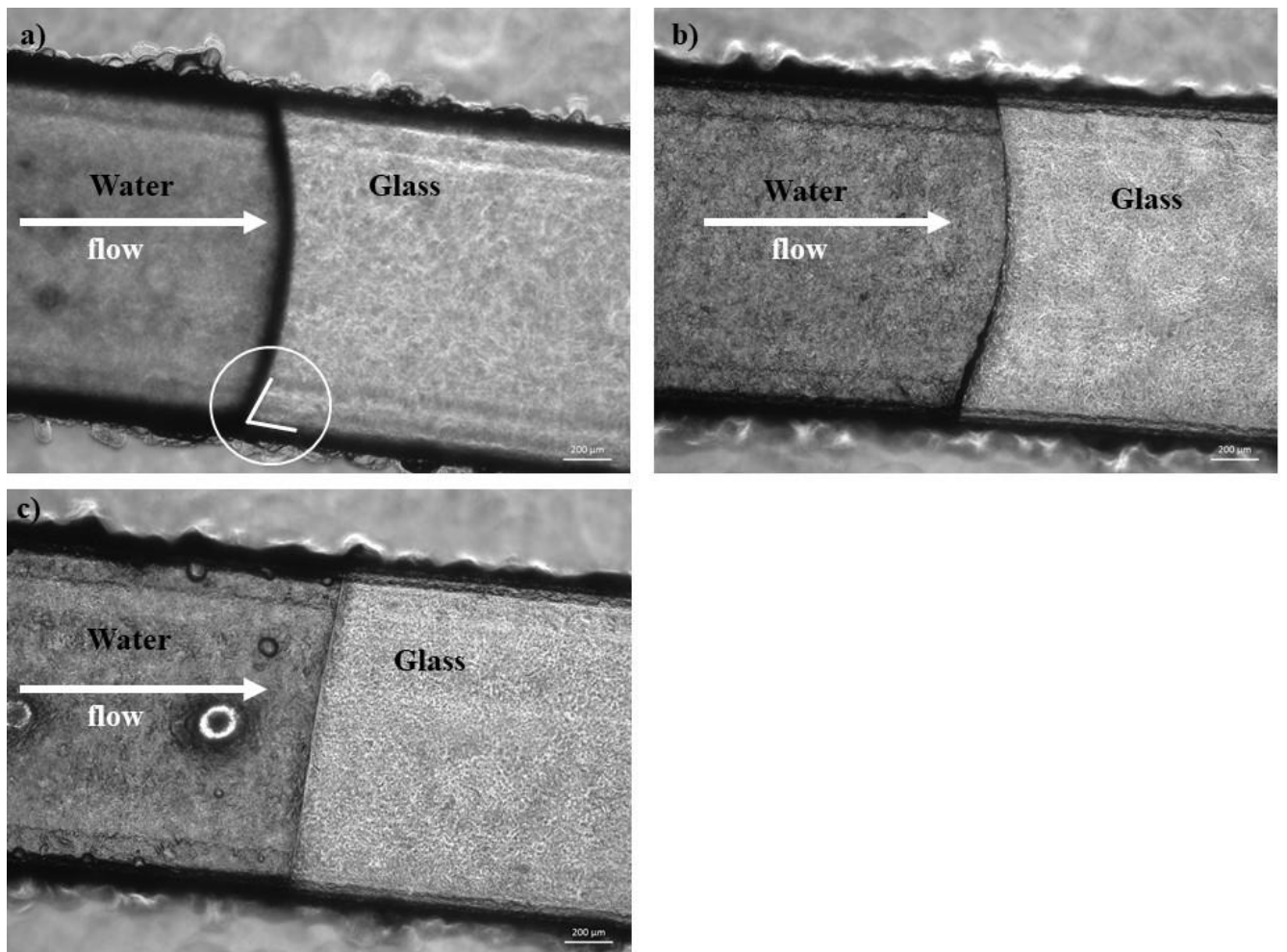
Figure 5.4: Representative images of water flowing within the microfluidic device microchannels. The water and glass angle was used to measure contact angles to prove surface treatments

Microfluidic devices (a, b and c) with water flowed in by hand to show that glass surface treatment has worked. The devices were immersed in OTS solution and F108 was added. Contact angles between the waters leading edge and microchannel edge were measured using computer software Treatments were performed as noted in section 2.8. Scale = 200 μm. n=4
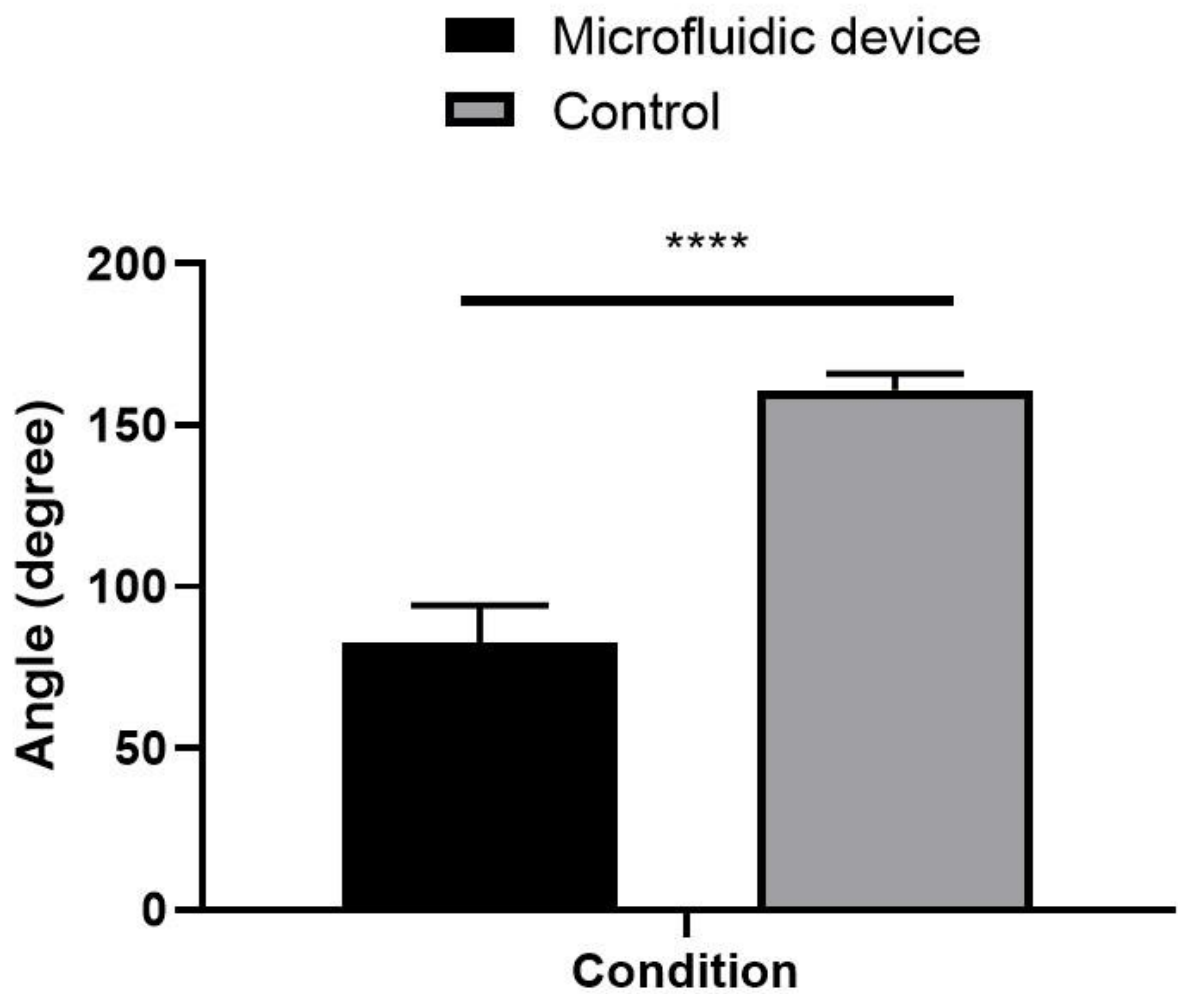
Figure 5.5: Contact angle hydrophobicity histogram

Histogram represents the average angle degree of contact angles measurements of water and the microchannel edge, at, at least eight sites on four different devices. The devices were silanised with OTS and then incubated with F108 overnight (OTS + F108). The measurement is compared to a hydrophilic glass control. Significance in differences between averages was determined using a 2 Way ANOVA. P *=<0.05, **=<0.01, ***=<0.001, ****=<0.0001. n=4.

Figure 5.4 shows the results. The results (figure 5.4) show that both cell lines (U-87 MG and MCF7) adhere and form monolayers on tissue culture plastic, untreated slides and poly-L-Lysine slides as expected (Figure 5.4). However, supporting the observations seen in the previous reports, a monolayer is not observed in the silanised F108 coated glass (Figure 5.4). These results validate the silanisation and F-108 treatment, and proves it is suitable to treat the microfluidic devices, so that cells are unable to adhere to the glass base.

5.3.4   Imaging and spheroids viability assessment in generation 2 device

Figure 5.7 and 5.8 shows spheroids are difficult to visualise, with the extremity of the mass not in focus like spheroids would be in standard tissue culture plastic. The spheroids appear to be a black mass, like the photos seen within the microwell in the generation 1 microfluidic device. Both magnifications, 5 x and 10 x, do not allow the spheroids to be clearly seen at the cellular detail. It is possible that this is due to the milling process. The glass microwell surface is rough due to milling and this could cause the light to refract and reflect internally resulting in the microscope not being able to focus on the spheroid cells, furthermore, the thickness of the glass base (1mm thick) below the microwell may also be an issue for the instruments. However, the Zeiss axio microscope used to image the microfluidic device has a focal length of 11mm at 5 x magnification, suggesting that the glass thickness is not the issue. Therefore, it is more likely that the milling process is causing the poor clarity images as shown above.

5.3.5   Staining pre-silanisation

To overcome this issue, FDA /PI staining on chip was conducted. FDA/PI staining would negate the issue of the glass reflecting and refracting the light internally within the microwell, as the cells are fluorescently labelled, not requiring reflected like, and would also allow the assessment of spheroid viability directly within the microwell. FDA/PI staining was conducted on the generation 2 microfluidic device on U-87 MG and MCF7 spheroids (2.5×10^4) and
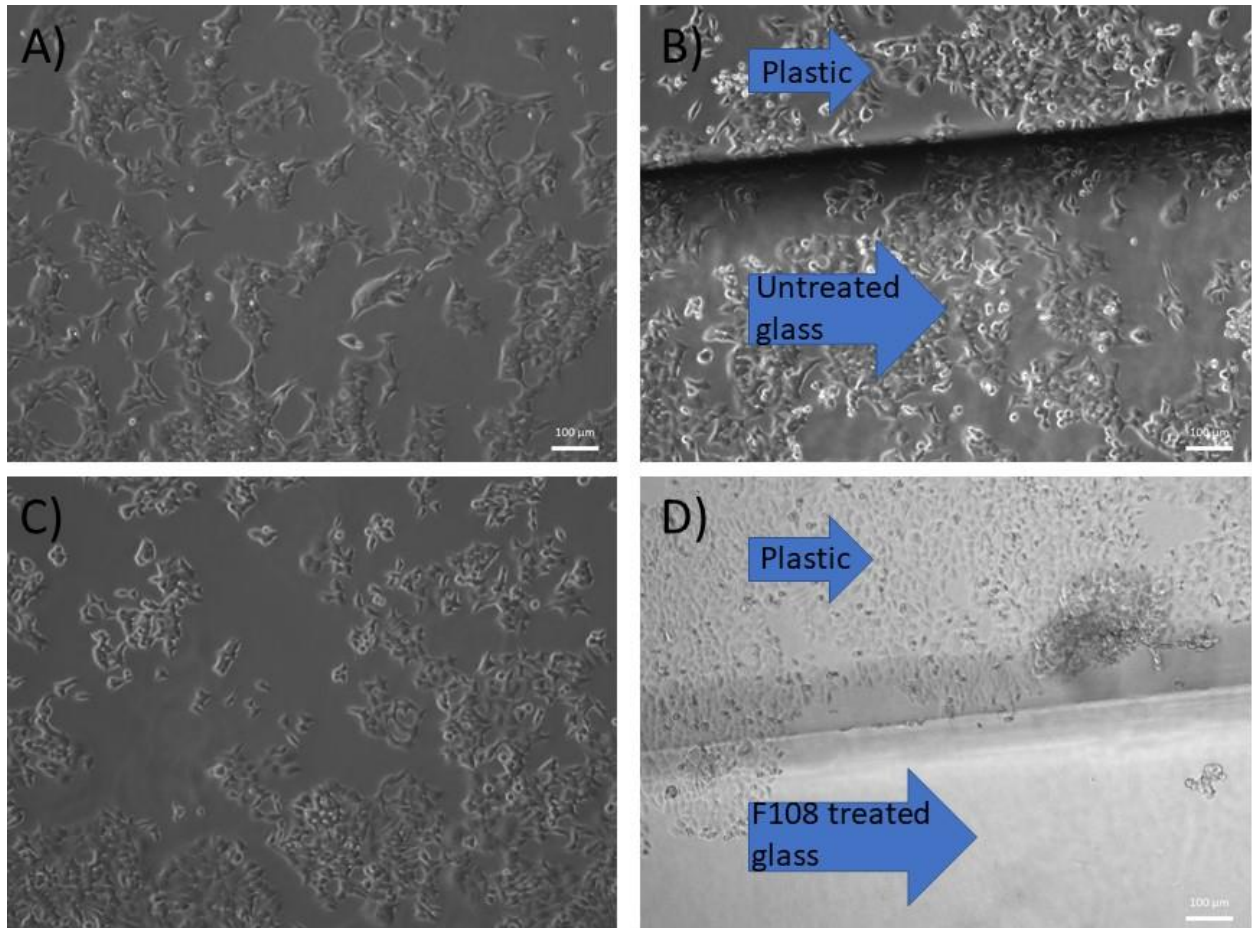
Figure 5.6: MCF7 monolayer formation on microscope slide using different surface treatments

MCF7 (2.5 x 10 ^{4}) monolayers were formed on four testing conditions surfaces - Untreated tissue culture plastics (A), an untreated glass microscope slide (B), polylysine glass microscope slide (C) OTS and F108 coated glass microscope slide the glass slide (D). Scale bar represents 100 μm. n=3 experimental repeats.
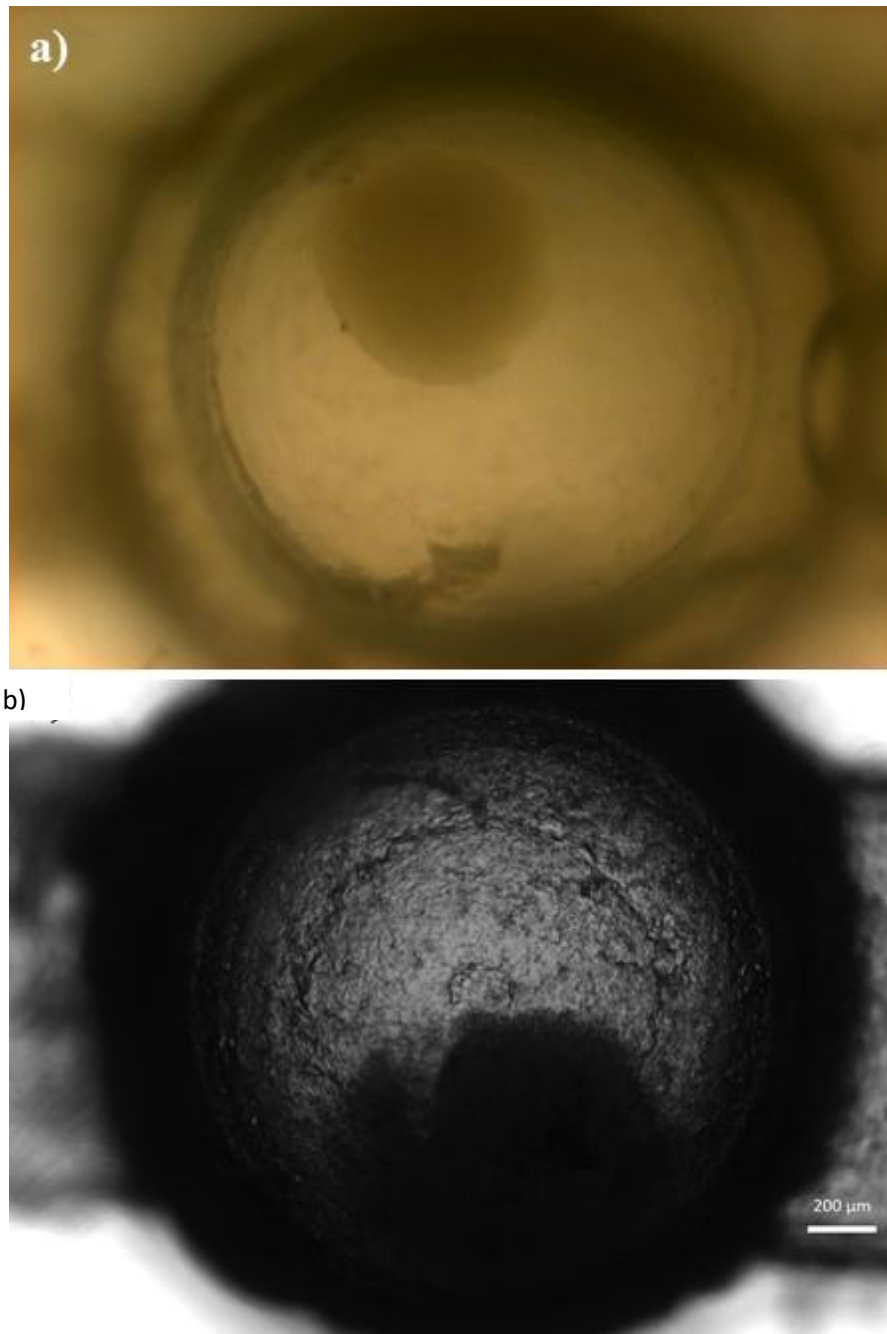
Figure 5.7: U-87 MG spheroids within a generation 2 microfluidic device

U-87 MG spheroids (2.5 x 10⁴) were formed following the protocol outlined previously and were incorporated into the microwell of the generation 2 microfluidic device via direct pipetting. The spheroids were imaged on a Ziess microscope using brightfield settings at 5 x magnification. Minimum of N= 3. Scale bar = 200 μm.
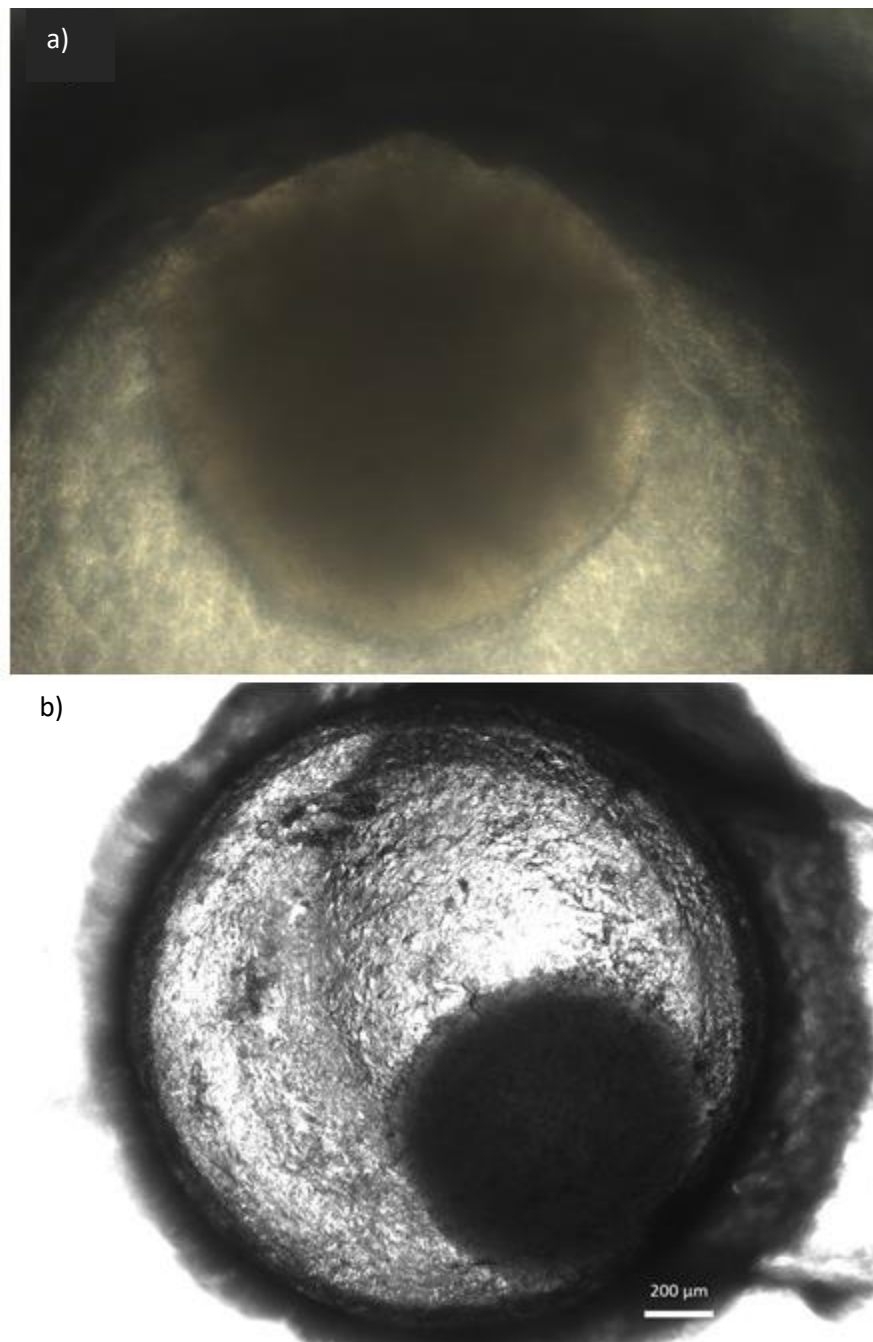
Figure 5.8: MCF7 spheroids within a generation 2 microfluidic device

MCF7 spheroids (2.5 x 10⁴) were formed following the protocol outlined previously and were incorporated into the microwell of the generation 2 microfluidic device via direct pipetting. The spheroids were imaged on a Ziess microscope using brightfield settings at b) 5 x magnification and 10 x magnification in a). Minimum of N= 3. Scale bar = 200 μm.

Figure 5.9 shows the results. It is possible to observe that, although staining on chip was observed, there were clear issues. The spheroids were disintegrated throughout the microwell and into the channels. This is possibly due to the rough channel surface as detailed before. The spheroid may have adhered to the microwell base and therefore were disintegrated during the FDA/PI staining process. Interestingly, there is very small evidence of PI staining within Figure 5.9. This could be explained through the staining process. If there were dead cells present, it would be possible that these cells were detached to the spheroid mass, meaning they were potentially washed away during the staining protocol.

5.3.6 Spheroid viability on a silanised and F108 treated generation 2 device

An adapted staining procedure was performed by staining the spheroids directly above the microwell. This was performed only using FDA solution, purely to demonstrate the spheroid location within the microwell. Figure 5.10 shows the results of the FDA stained MCF7 spheroids after 48 h within the silanised and treated generation 2 microfluidic device. The results show that spheroids can be stained within the device and can be done over a period of at least 48 h. However, the results still demonstrate the difficulties of the staining procedure. The spheroids appear misshapen to the off chip models. The spheroids FDA/PI staining was further amended, and figure 5.11 shows this. The results show the spheroids structure from the microfluidic device, the spheroids are more intact and representative of the off chip models structure. With the possibility to quantify the fluorescence intensity over unit area, which is shown in the histogram on figure 5.12. FDA fluorescence is higher on-chip being 50% better than the off-chip control, whilst PI fluorescence is 50% lower on-chip than off chip. Indicating more live cells and less dead cells on-chip.

Therefore, the microfluidic devices were all silanised to help maintain the spheroid structure whilst in the microfluidic device.
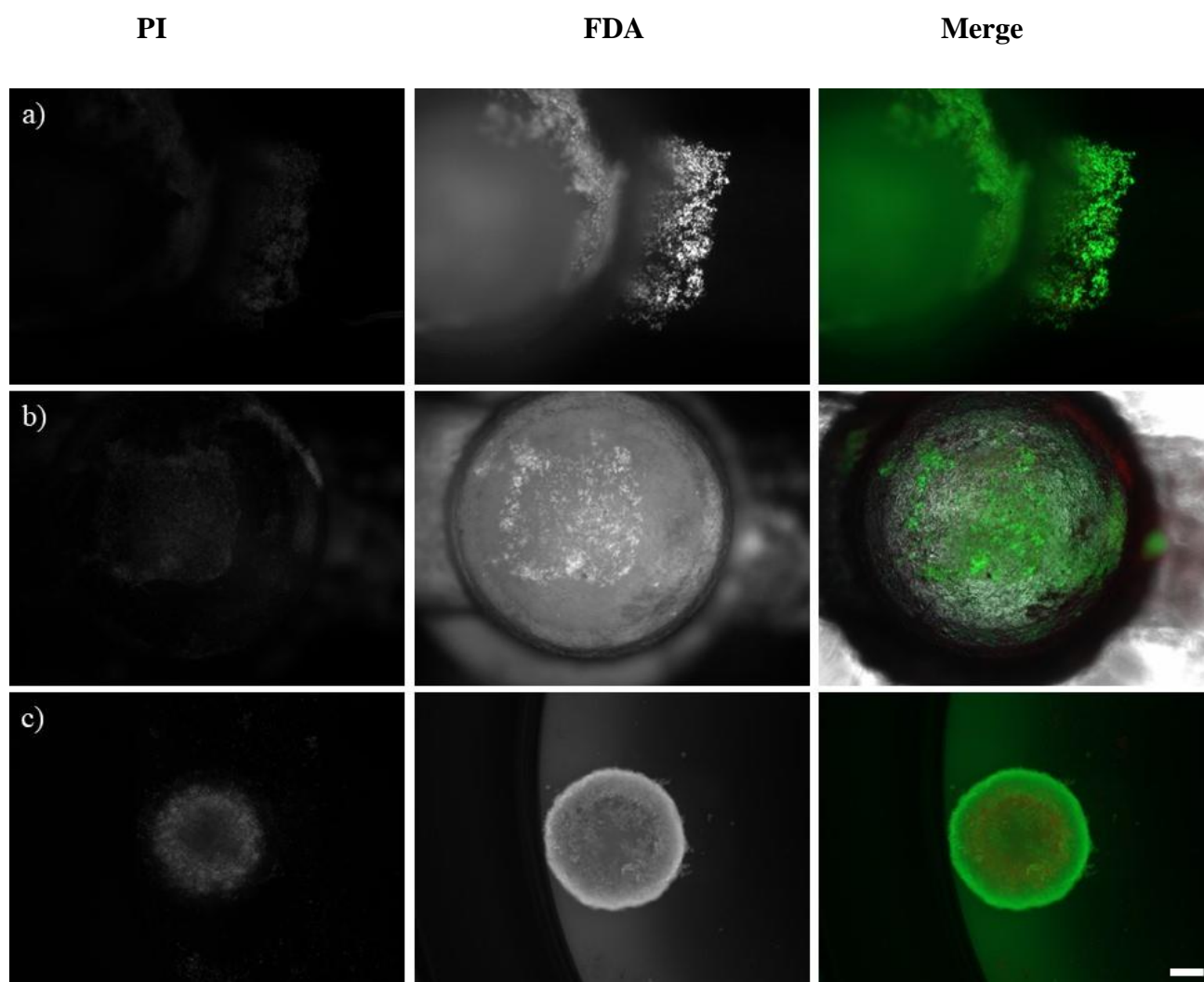
Figure 5.9: Example MCF7 spheroids within the generation 2 microfluidic device (a&b) and an off-chip spheroid (c) stained with FDA and PI solution

MCF7 (2.5 x 10 ^{4}) spheroids were incorporated into a generation 2 microfluidic device and perfused for 72 h with DMEM set at 3µl/min before being stained with FDA PI solution (a & b). An off chip MCF7 spheroid was stained with FDA PI solution (c). The first image shows PI staining, followed by FDA and finally a merge. All spheroids were imaged on a Zeiss microscope at 5x magnification using FITC and Texas Red filters. Scale bar = 200 µm. n=3 experimental repeats.
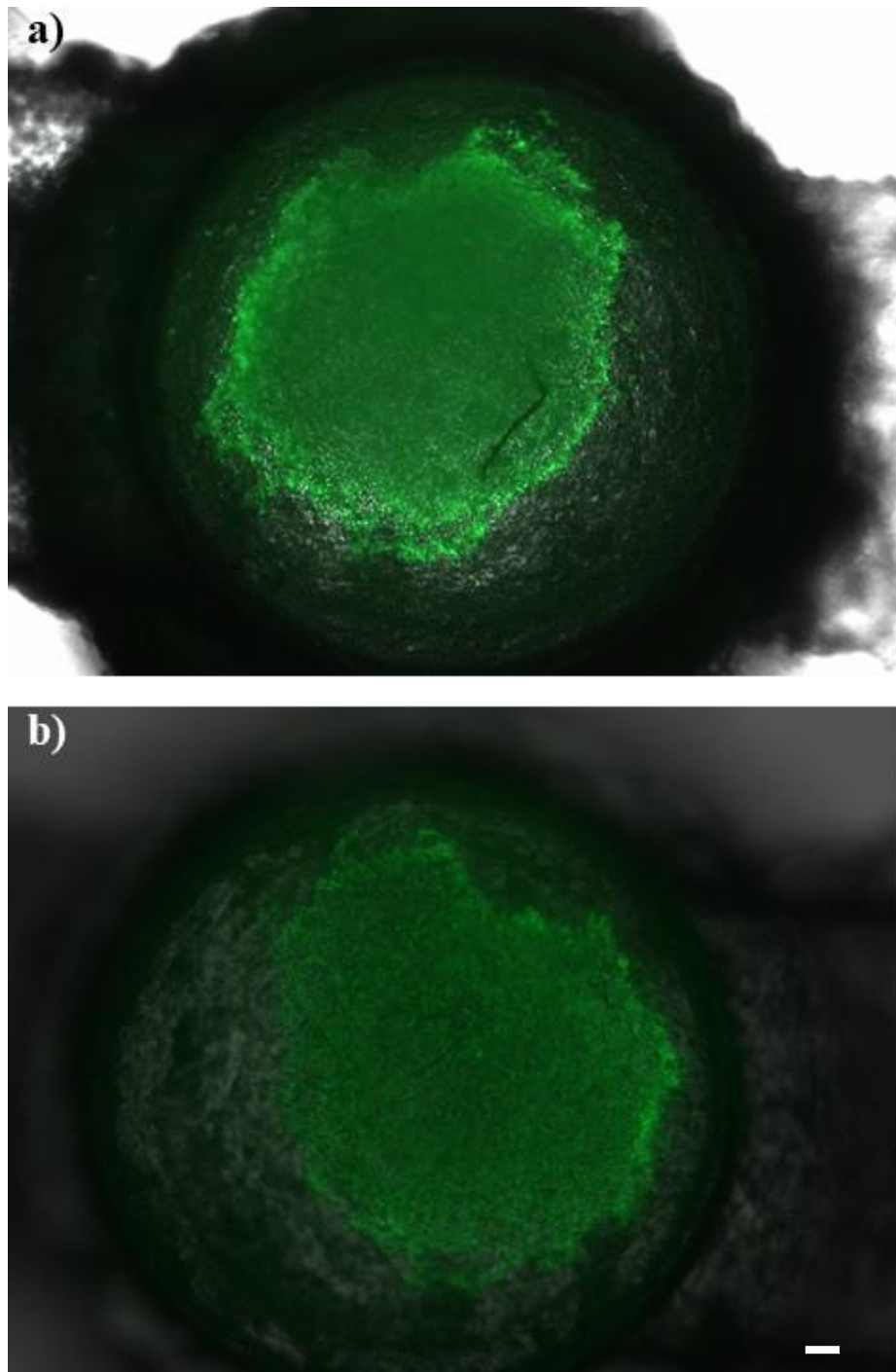
Figure 5.10: FDA stained MCF7 spheroids at a) 24 h and b) 48 h within a silanised generation 2 device

MCF7 spheroids (2.5 x 10⁴) were incorporated into two silanised and F108 treated generation 2 microfluidic devices and perfused for 24 h (a) and 48 h (b) with DMEM set at 3µl/min before being stained with FDA solution to demonstrate location within the microfluidic device. The spheroids were imaged on a Zeiss microscope at 5x magnification using FITC filters, to show presence within the microwell. N= 3 Scale bar = 200 µm

PI **FDA** **Merge**
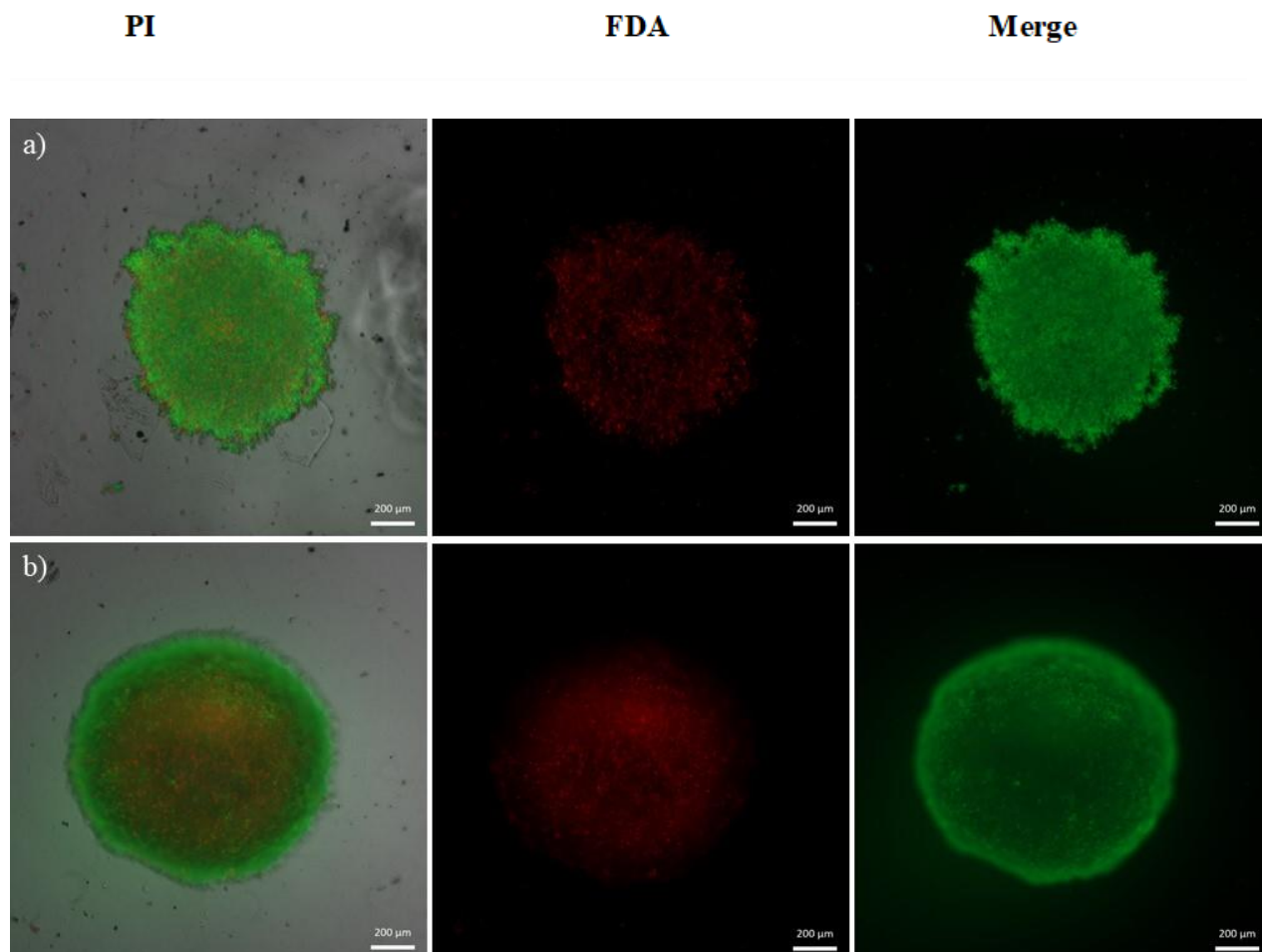
Figure 5.11: Representative images of FDA-PI stained MCF7 spheroids on-ship (silanised microfluidic device) vs off-chip

Representative FDA PI stain images of MCF7 spheroids (2.5 x 10^4 cells per well) at 72 h. (a) Spheroid on-chip; incorporated into a silanised microfluidic device for 72 h and subsequently removed for staining (b) off-chip spheroid. Red fluorescence represents PI incorporation, green fluorescence represents FDA incorporation. Scale bar represents 200 μm. n=3 experimental repeats.
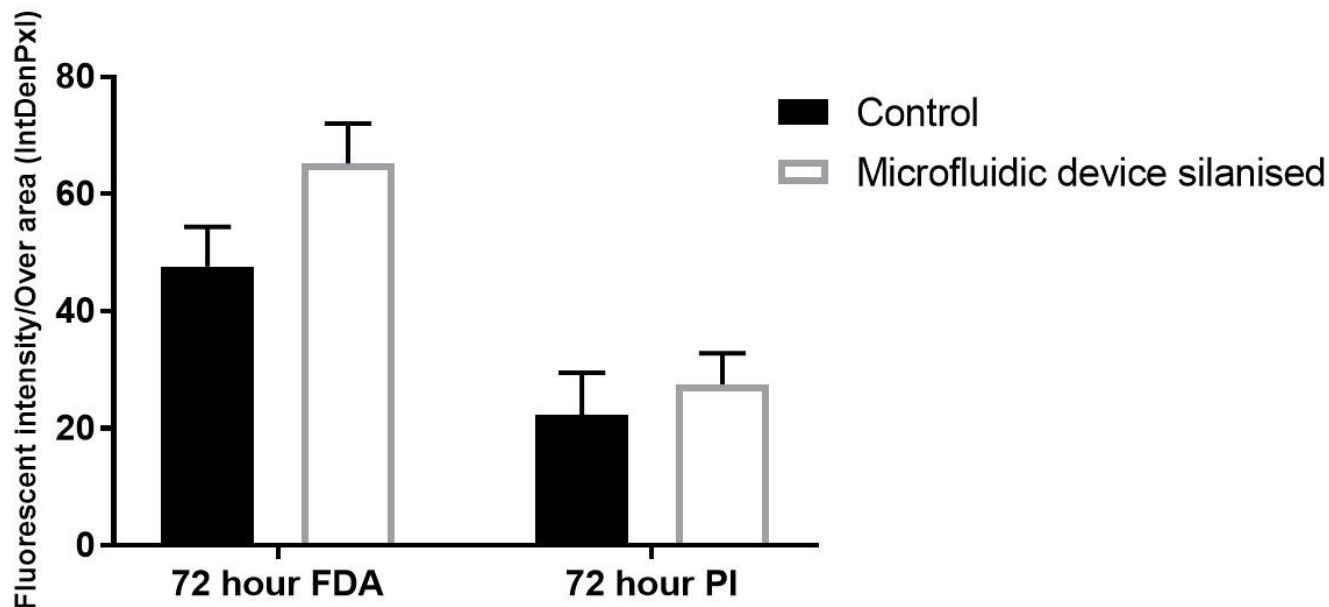
Figure 5.12: FDA PI fluorescent quantification histograms of spheroids comparing control vs silanised microfluidic device

Histograms show the average levels of FDA- and PI- associated fluorescence as a unit of intensity over area in spheroids off-chip (control) and spheroids incorporated to a silanised microfluidic device. Fluorescent intensity over area denotes the strength of signal produced from both FDA and PI greyscale images per area of the spheroid. Raw intensity of original grey scale images of the two conditions at 72 h is plotted over area. Error bars represent standard error of n=3. No significance was found using two way ANOVA.

5.3.7 Design and validation of Generation 3 spheroid-on-chip device

The second-generation device, although an improvement upon on the first design, still resulted in one problem: the device did not allow the spheroid to be imaged as clearly as required, which was a desired feature for analysis of cell migration from spheroids embedded in hydrogels.

Therefore, the design of the generation 2 device was improved upon, in order to allow clear visualisation of spheroids in the micro-well on chip. The upgraded design was again developed with the help and support of Dr Alex Iles. The device for generation three was designed with the same geometry as the generation two device and was again fabricated in Schott B270 glass. However, the microwell was complete drilled through, leaving a cylindrical access port (2 mm wide x 3 mm deep) through the device. A borosilicate glass coverslip was thermally bonded to the base to allow better clarity and imaging of the spheroids when inside the device. The generation 3 microfluidic device design is seen as a schematic (Figure 5.13a) and as a cross sectional side profile (figure 5.13b).

5.3.8 Spheroid incorporation

Following the fabrication of the generation 3 device, spheroids needed to be incorporated into it. The spheroids were added to the microwell via direct pipetting and figures 5.14/15 shows examples of the microfluidic device with spheroids within. The images show the spheroids at t=0, immediately after incorporation. The images show clear well defined spheroid masses within the microwell. The cells at the spheroid edge are clear and reflect the images able to be taken in an off chip model. The addition of a borosilicate base under the microwell allows the spheroid images to be clear, due to the smooth surface. Following confirmation of the clear spheroid images, the spheroids needed to be assessed for migratory and invasive capabilities. To do this the spheroids needed to be embedded within or lay over hydrogels, therefore hydrogel incorporation into the generation 3 microfluidic device was tested.
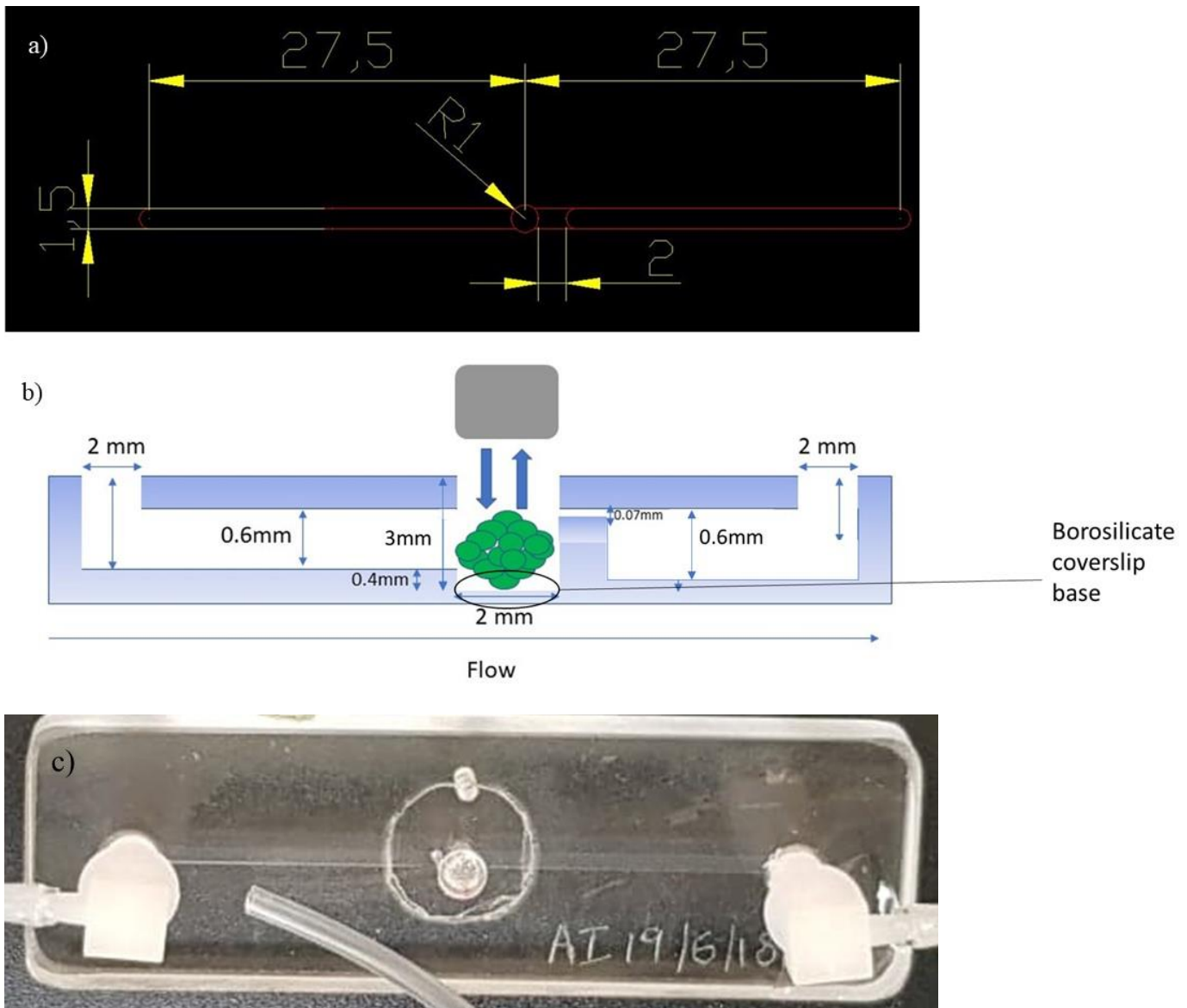
Figure 5.13: Generation 3 microfluidic device panel image (schematic and cross sectional)

Generation 3 microfluidic device schematic used for CNC milling purposes a), Generation 3 microfluidic device cross sectional drawing with an example spheroid in the micro-well and a grey PDMS plug with arrows denoting the removability of its b). The microwell base features a borosilicate glass coverslip bounded to the glass of the overall device. This allows direct better viewing of the spheroid mass.
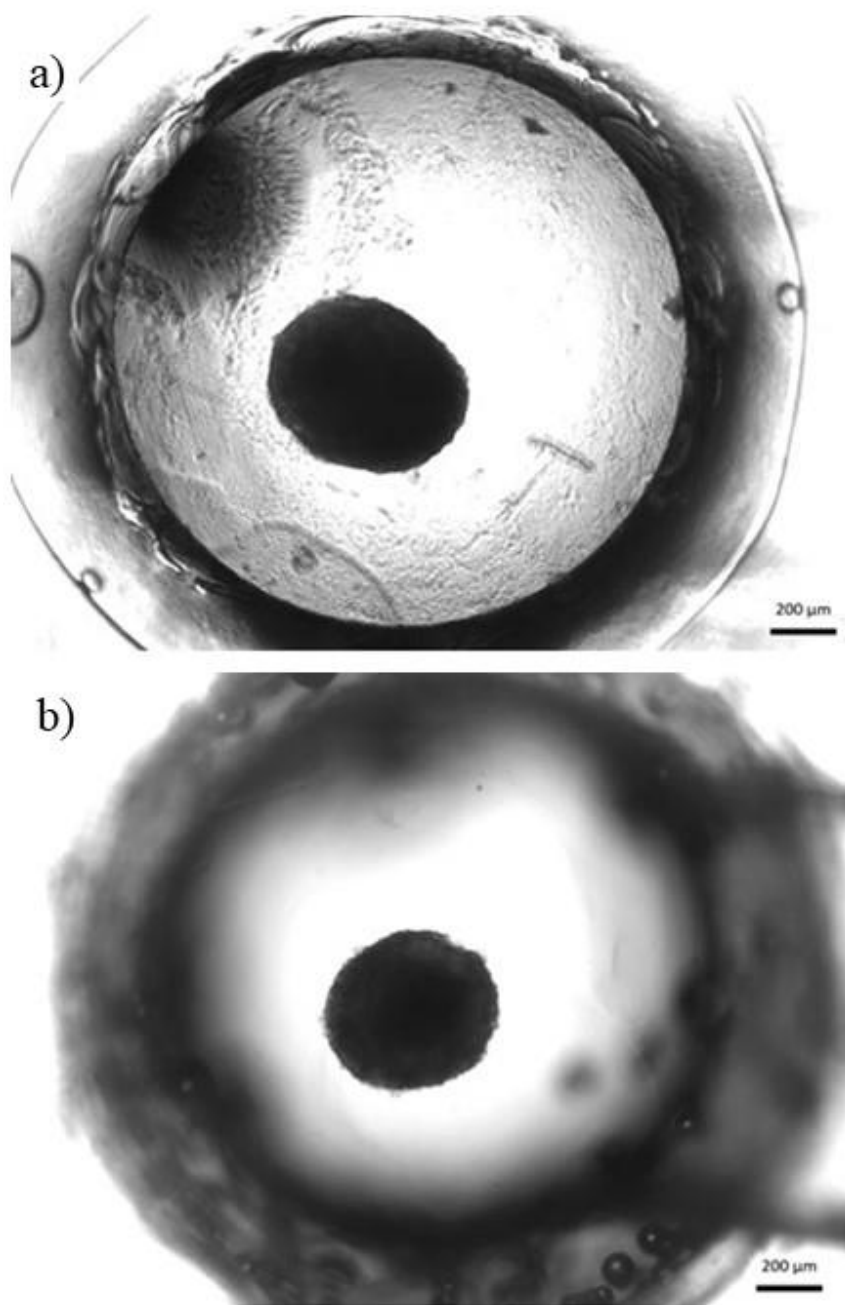
Figure 5.14: U-87 MG spheroids within a generation 3 microfluidic device

U-87 MG spheroids were seeded at 2.5 x 10⁴ cells per well as previously detailed. The spheroids were directly pipetted in the borosilicate coverslip base microwell before being images at 5 x on a Ziess microscope under brightfield settings. a and b) U-87 MG spheroids. Scale bar represents 200 μm. N=3 experimental repeats
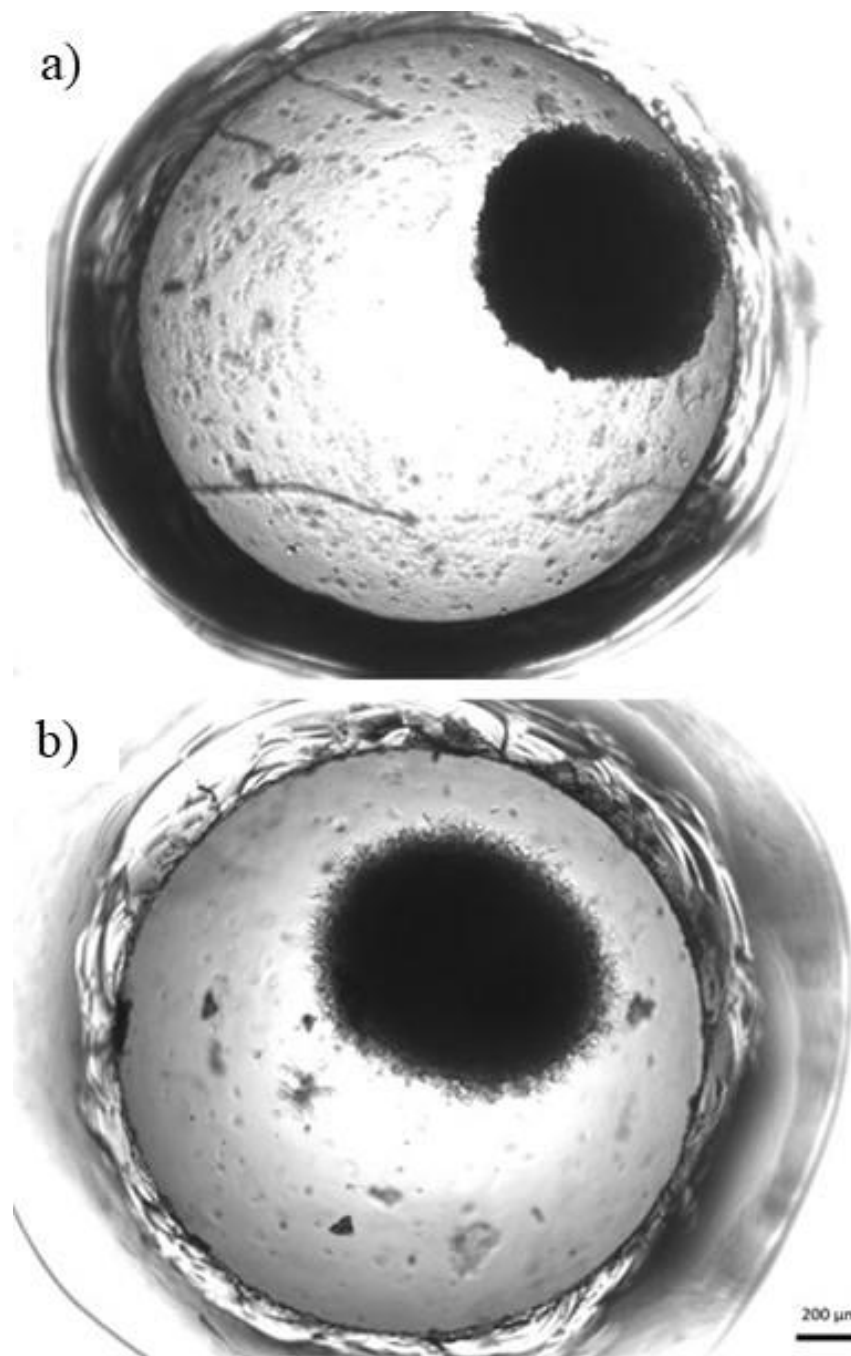
Figure 5.15: MCF7 spheroids within a generation 3 microfluidic device

MCF7 spheroids were seeded at 2.5 x 10^4 cells per well as previously detailed. The spheroids were directly pipetted in the borosilicate coverslip base microwell before being images at 5 x on a Ziess microscope under brightfield settings. a and b) MCF7 spheroids. Scale bar represents 200 μm. N= 3 experimental repeats

5.3.9   Hydrogel incorporation into the microfluidic device

Four hydrogels, fibronectin, Matrigel, collagen, and gelatin were tested for incorporation into a generation 3 microfluidic device. The hydrogels were formed and directly pipetted into the microwell before being left to set. Initially the hydrogels flooded through the microchannels and did not remain within the microwell as required, and examples of this unsuccessful incorporation can be seen in figures 5.16, 17 and 18. The method used here does not allow the through flow of medium as the hydrogels were blocking the passage of the channels. Moreover, the spheroids would not be able to be incorporated under these conditions as they would not be able to be continually perfused with media. Therefore, the method was amended by flushing the channels with medium first, prior to pipetting the hydrogels within the microwell. Examples of these can be seen in figure 5.17, where it is possible to see that the gelatin, Matrigel, and collagen hydrogels were successfully added to the generation 3 microfluidic device. Fibronectin was unsuccessful in its addition to the device, resulting in its flooding into the microchannels.

Following the addition of hydrogels, it would then be possible to add spheroids within the microwell to test the migrative and invasive capabilities of cancer spheroids. Following the incorporation of the hydrogel into the microwell, the viability of spheroids could be tested through FDA PI staining.

5.3.10   Spheroids viability assessment in the generation 3 microfluidic device

To assess spheroid viability within the generation 3 microfluidic device, the FDA/PI assay was conducted as before. The spheroids were stained within the microfluidic device following the adapted method used within the generation 2 device. Similarly, off chip controls were also used. Figure 5.19 shows an example of the spheroids stained on chip and the Figure 5.20 shows summary of the quantified values.
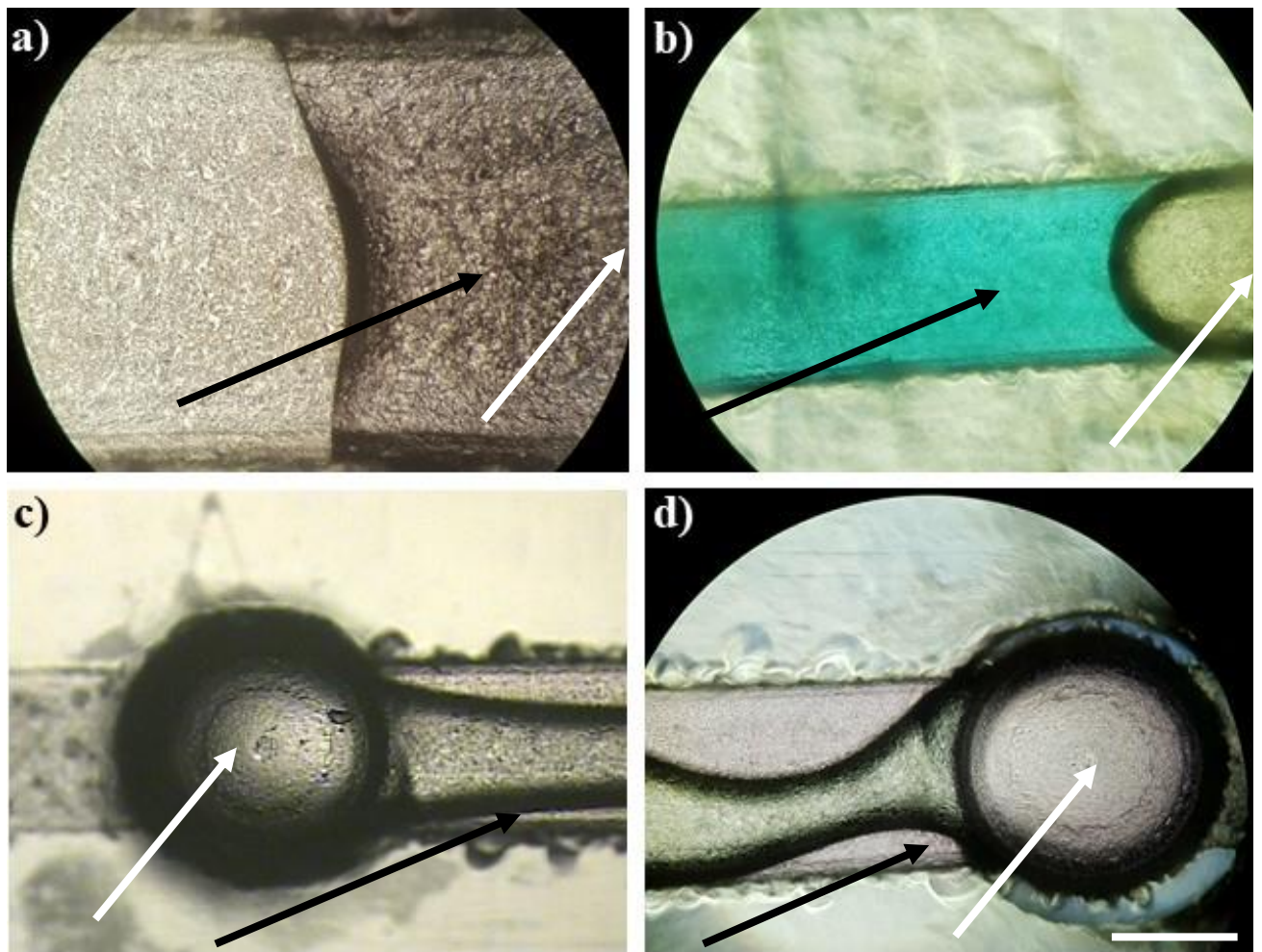
Figure 5.16: Hydrogel problems with incorporation within a generation 3 microfluidic device- fibronectin, Gelatin and Matrigel

Hydrogels were formed as previously detailed and were directly pipetted in the borosilicate coverslip base microwell before being images at 5 x on a Ziess microscope under brightfield settings, black arrows denote hydrogels and white arrows denote microwell location a) fibronectin b) gelatin stained with brilliant blue caught within the microchannel and c) Matrigel. Scale bar = 1 mm. n=3
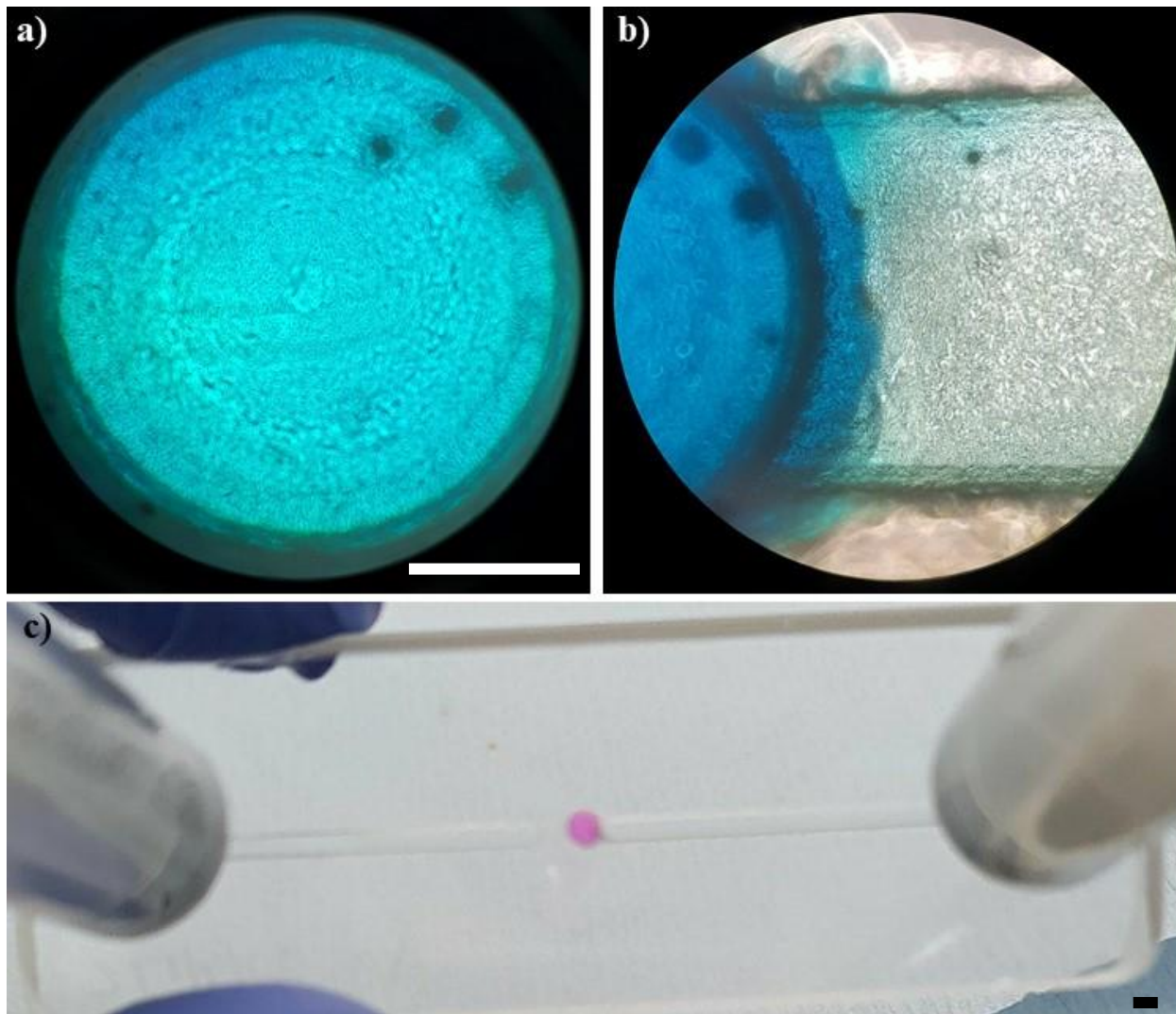
Figure 5.17: Successful hydrogel incorporation within a generation 3 microfluidic device

Hydrogels were formed as previously detailed and were directly pipetted in the borosilicate coverslip base microwell before being images at 5 x on a Ziess microscope under brightfield settings. a) gelatin stained with brilliant blue successfully placed and held within the microwell b) evidence of gelatin set within the microwell and not microchannel c) Matrigel successfully set within the microwell. White scale bar = 1 mm, black scale bar = 2 mm. n=3

MERGE	FDA	PI
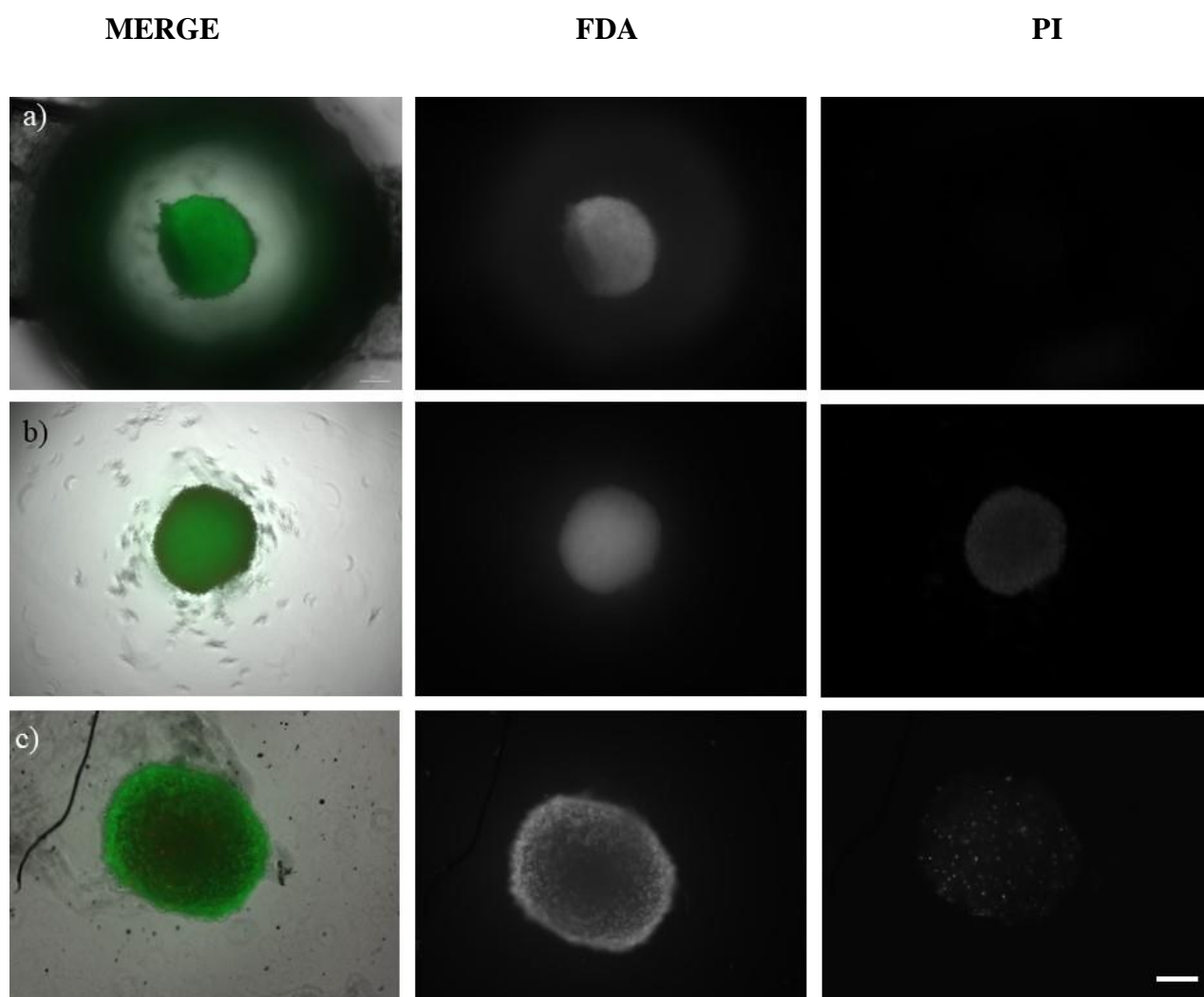
Figure 5.18: Representative images of FDA-PI stained U-87 MG spheroids on-chip (generation 3 microfluidic device)

Representative FDA PI stain images of U-87 MG spheroids (2.5 x 10^4 cells per well) at 72 h. a) Spheroid on-chip spheroid with FDA and PI greyscale images b) Spheroid on-chip spheroid with FDA and PI greyscale images to demonstrate variability between repeats c) control off-chip spheroid. Red fluorescence represents PI incorporation, green fluorescence represents FDA incorporation. Scale bar represents 200 μm. n=3 experimental repeats.
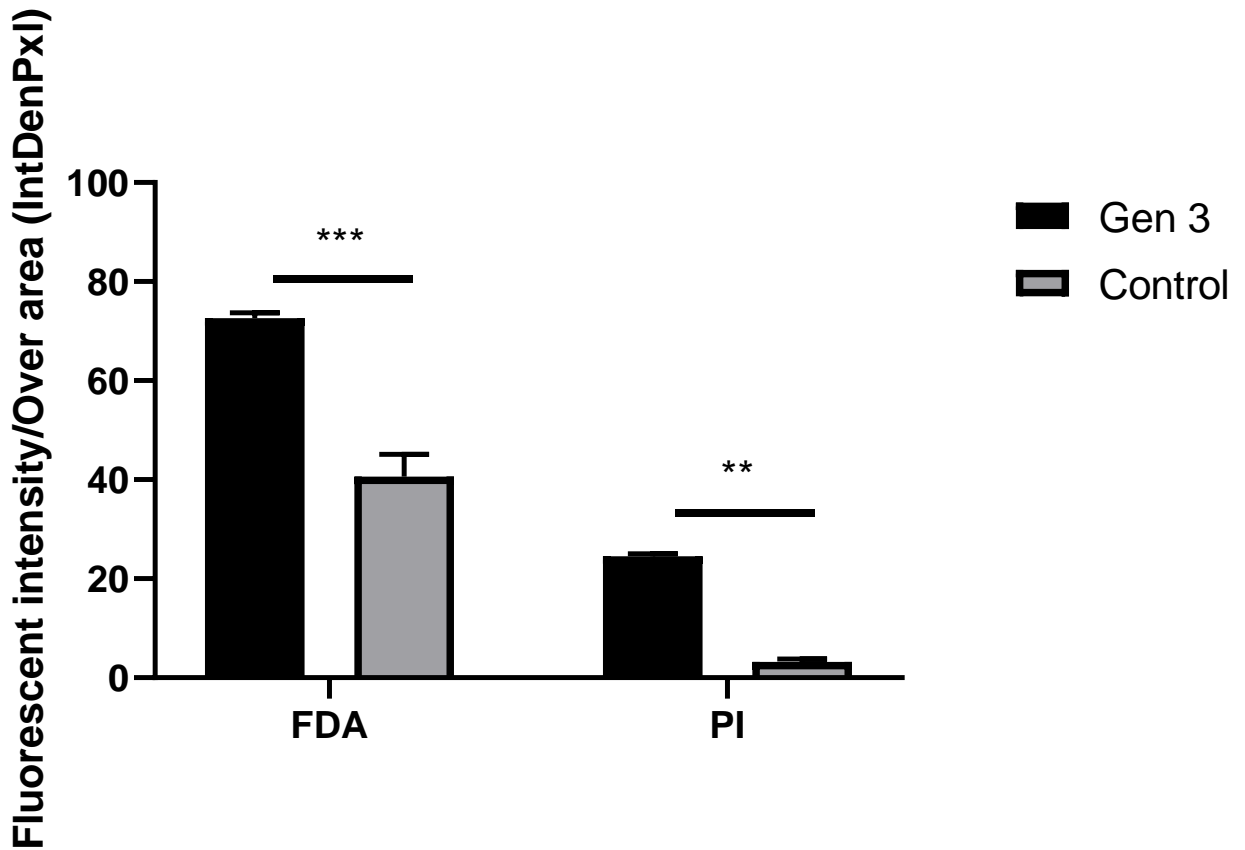
Figure 5.19: FDA PI fluorescent quantification histograms of spheroids comparing control spheroids vs generation 3 microfluidic device spheroid

Histograms show the average levels of FDA- and PI- associated fluorescence as a unit of intensity over area in spheroids off-chip (control) and spheroids incorporated to a generation 3 microfluidic device. Raw intensity of original grey scale images of the two conditions at 72 h is plotted over area. Error bars represent standard error of n=3. Two way ANOVA showed significance between FDA and PI in both conditions.

Figure 5.19 shows unexpected results. It shows that FDA (green) fluorescence intensity is higher in on-chip spheroids, being 46% higher than the off-chip spheroids. Indicating there are more cells live and viable than the off-chip models. However, the level of red fluorescence is also higher in the on-chip spheroids, being 8% of the off-chip spheroids. It is noteworthy however, there are large levels of variability between the fluorescent images. Figure 5.18 shows examples. Overall the results demonstrate that there are a large portion of cells which are alive and viable in the generation 3 microfluidic device. When compared to the previous two designs it shows that all devices are comparable to one another in terms of live and dead cells, with the generation 3 device having 5% higher portion of live cells over generation 1 and 2. Shown in Figure 5.20. Moreover, these results demonstrate that the microfluidic device allows spheroids to remain viable for at least 72 h and that investigations into cancer spread and migration within the device can be conducted.

5.3.11 Evaluation of metastasis potential on chip: markers of cancer spread in effluent

As previously detailed (Chapter 3) VEGF is critical in the migration and invasion of cancer in *in vivo* conditions, due to its promotion of angiogenesis and the release of proteolytic enzymes, such as MMPs (Lee *et al*., 2005; Egginton, 2011 Saharinen *et al*., 2011; Roberts *et al*., 2013; Vempati *et al*., 2013). Therefore, as for the generation 1 device, VEGF secretion within effluent of three conditions was assessed to represent an analogue of cancer spread and migration. To better replicate cancer migration and spread within *in vivo* conditions, ECM-like matrices type I collagen and Matrigel were incorporated into the device. These hydrogels were used as they replicate the basement membrane within mammals and closer resemble the natural tumour environment. The levels of VEGF secretion were quantified on the effluent of three conditions: off chip spheroids, on chip spheroids, and monolayers. All of these were tested for Matrigel, collagen, and media alone. Figure 5.21 shows the results of the ELISA on MCF7 cells and
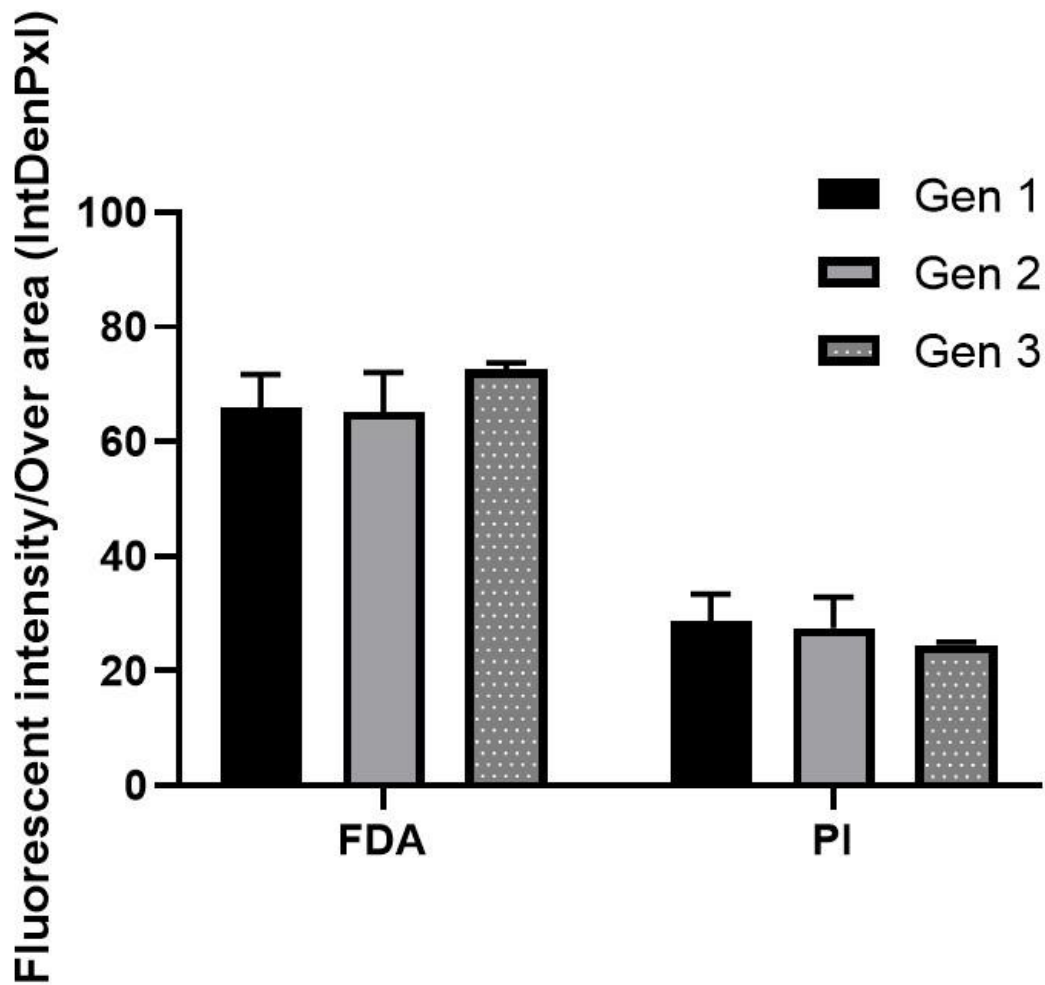
Figure 5.20: FDA PI fluorescent quantification histograms of spheroids, comparing generations 1, 2 and 3 microfluidic devices to one another

Histograms show the average levels of FDA- and PI- associated fluorescence as a unit of intensity over area in spheroids incorporated within a generation 1, 2 and 3 microfluidic devices. Raw intensity of original grey scale images of the two conditions at 72 h is plotted over area. Error bars represent standard error of n=3. Two way ANOVA showed no significance between FDA and PI in both conditions.
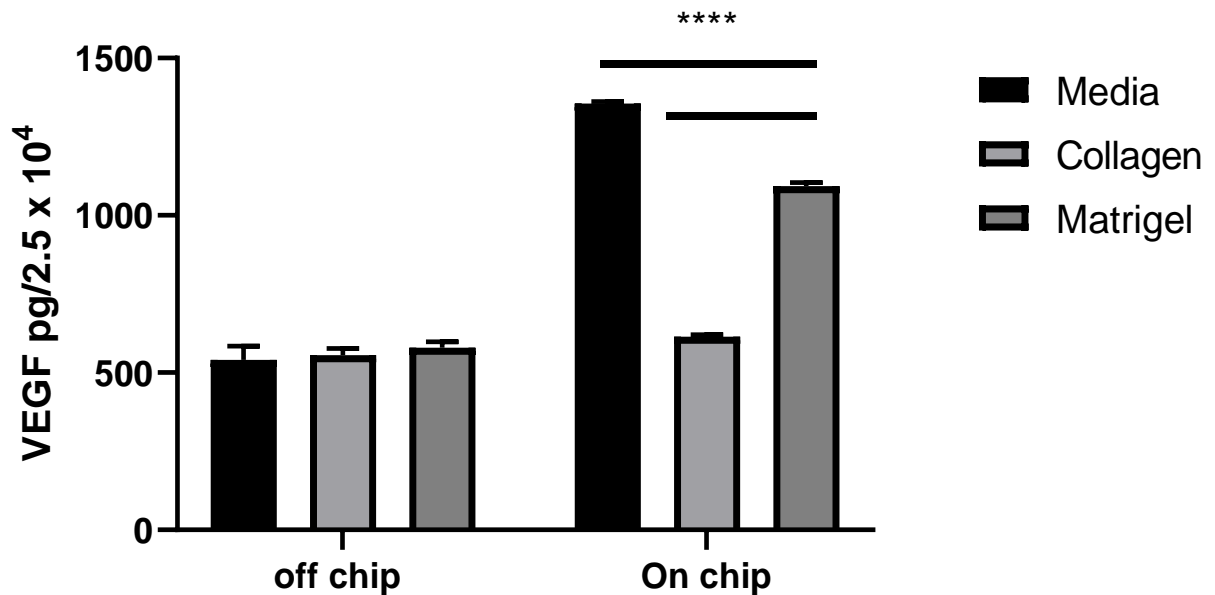
Figure 5.21: Comparison of VEGF secretion between 3D off-chip and 3D-on chip models at 72 h

MCF7 spheroids (2.5 x 10^4 cells per well) were formed. 3mg/ml of type I collagen, Matrigel and media alone was added to a generation 3 microfluidic device and ULA plate, on three separate occasions. Before one spheroid was incorporated into a generation 3 microfluidic device, and other spheroids were placed in a ULA plate. 200μl of media was collected at 72 h from the ULA plate spheroids. All 4.32 ml of media was collected every 24 h from the spheroid on a microfluidic device condition. The 72 h media was analysed for VEGF secretion using a VEGF ELISA. Histograms represent the media from n=3. Error bars are SE and two-way ANOVAs were performed to test for statistical significance. P *=<0.05, **=<0.01, ***=<0.001, ****=<0.0001.

spheroids. Here, it can be observed that VEGF levels were similar in conditioned media from the cell monolayer between each hydrogel and media alone. Similarly, no differences in VGEF levels are observed in conditioned media for the off-chip spheroid condition. Moreover, the VEGF levels in conditioned media for the monolayer and off-chip media and collagen conditions (Figure 5.21). VEGF levels in the effluent from spheroids in generation 3 microfluidic embedded in collagen are also comparable to the monolayer and off chip conditions.

Two interesting observations are the levels of VEGF secretion within the effluent from the generation 3 device when the spheroids are present within media alone and Matrigel. Firstly, when in Matrigel and within the device, VEGF secretion is increased to 1100 pg in comparison to the monolayer and off chip spheroid. Being 175% and 89% higher in the on-chip condition respectively. Whilst the VEGF secretion within the device in media alone is 165% and 150% higher in comparison to the monolayer and off chip conditions respectively.

5.3.11.1 IL-6 ELISA

A second ELISA was conducted to look at another marker of cellular spread and migration, IL-6. The IL-6 ELISA mirrored the VEGF ELISA, where ECM like matrices were included into the testing conditions, namely type I collagen and Matrigel. The levels of IL-6 secretion were tested within the effluent of three conditions, off chip spheroids, on-chip spheroids and monolayers, all of which were tested within Matrigel, collagen and media alone. Figure 5.22 shows the results of the ELISA. IL-6 expression is increased in all off chip spheroid conditions, as well as all on chip at every time point in comparison to the monolayers. The off chip static spheroids have higher IL-6 expression when in media, collagen and Matrigel, with the Matrigel being statistically significant, than the monolayer counterparts, something which was expected. Interestingly, when comparing the off chip IL-6 expression to on chip, it is seen that IL-6 is
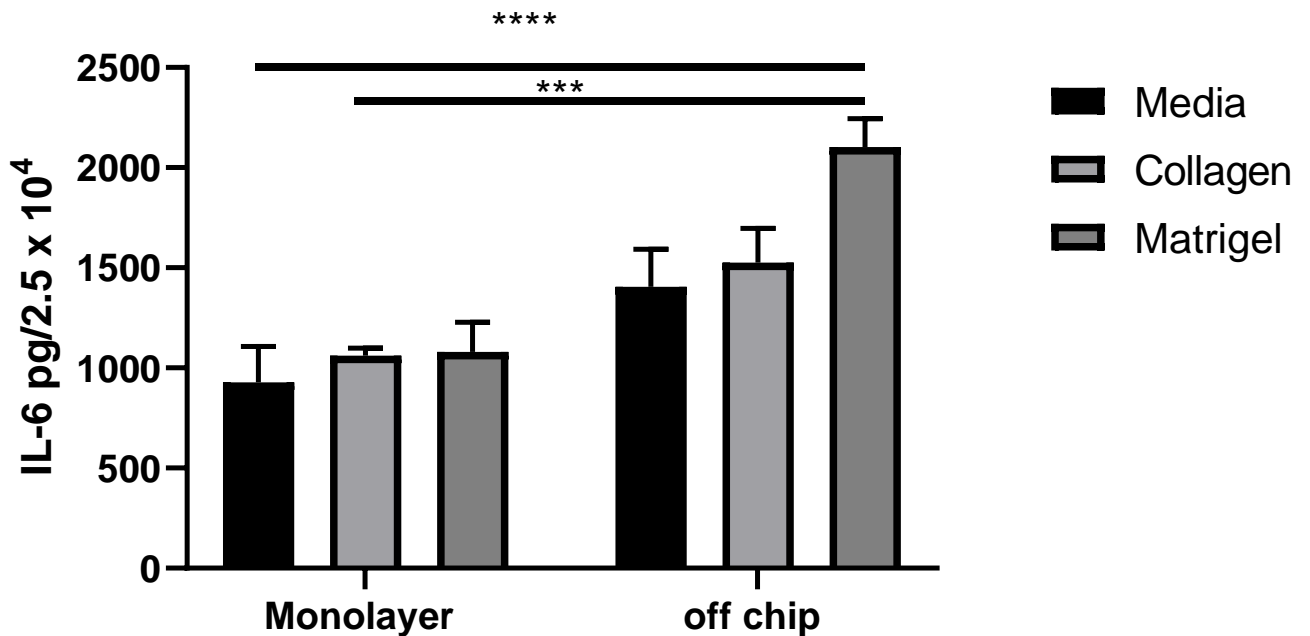
Figure 5.22: Comparison of IL-6 secretion between 2D monolayer and 3D-on chip models

MCF7 spheroids and monolayers (2.5 x 10⁴ cells per well) were formed. 3mg/ml of type I collagen, Matrigel and media alone was added to a flat bottom plate and ULA plate, on three separate occasions. Spheroids were placed in a ULA plate, and the monolayers in a flat bottom plate. 200µl of media was collected at 72 h from the monolayers and ULA plate spheroids. The 72 h media was analysed for IL-6 secretion using an IL-6 ELISA. Histograms represent the media from n=3 in duplicate. Error bars are SE and two-way ANOVAs were performed to test for statistical significance. P *=<0.05, **=<0.01, ***=<0.001, ****=<0.0001.
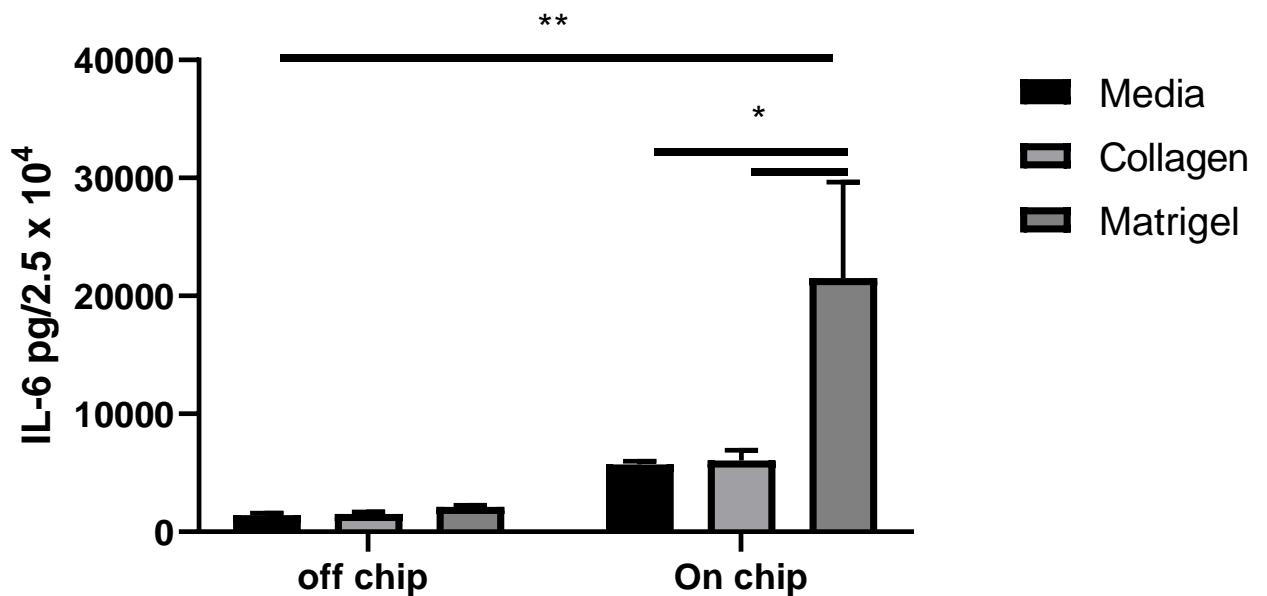
Figure 5.23: Comparison of IL-6 secretion between 3D off-chip and 3D-on chip models

MCF7 spheroids (2.5 x 10^4 cells per well) were formed as previously detailed. 3mg/ml of type I collagen, Matrigel and media alone was added to a generation 3 microfluidic device and ULA plate, on three separate occasions. Before one spheroid was incorporated into a generation 3 microfluidic device and other spheroids were placed in a ULA plate. 200µl of media was collected at 24 h from the ULA plate spheroids. All 4.32 ml of media was collected every 24 h from the spheroid on a microfluidic device condition. The 72 h media was analysed for IL-6 secretion using an IL-6 ELISA. Histograms represent the media from n=3 in duplicate. Error bars are SE and two-way ANOVAs were performed to test for statistical significance. P *=<0.05, **=<0.01, ***=<0.001, ****=<0.0001.

increased across all conditions on chip. The media IL-6 expression is higher, but so are the collagen and Matrigel, the latter two being statistically significant. VEGF secretion is higher on chip in the media only condition. Following the promising data of increased secretion of pro-metastatic markers in the on-chip model, a phenotypical analysis on-chip on the generation 3 device for evaluation of cell migration and invasion was performed.

5.3.11.2 *Evaluation of metastasis potential on chip: cell migration and invasion in situ*

To further investigate the ability of cancer spheroids to migrate and invade the local environment, direct imaging of spheroids on hydrogels was assessed. One of the objectives of this project was to investigate whether cells had a higher rate of migration or invasion on chip in comparison to the off chip models. U-87 MG, MCF7 and MDA-MB-231 spheroids (2.5 x 10^4) were formed and placed within media alone, collagen and Matrigel conditions. To demonstrate the invasive capabilities of the spheroids, spheroids were stained using FDA to highlight the invasive cell front in Matrigel after 72 h. From figure 5.24 it is possible to see that in 10 mg/ml of Matrigel MCF7 spheroids do not have any cells that are shed from the primary mass over 72 h. Likewise figure 5.24b and c show off-chip U-87 MG and MDA-MB-231 respectively. The spheroids both show clear masses of cells migrating away from the primary mass. The MDA-MB-231 spheroid is smaller than the other cell line spheroids but shows single cell and single cell aggregates surrounding the primary mass. Whilst the U-87 MG spheroid shows cells invading from the primary mass, where the cells appear to be attached to the primary mass and elongated in appearance. Overall these observations support the results seen in the literature and those previously shown within this report. Figure 5.25 shows an on-chip MCF7 spheroid within the microfluidic device. It demonstrates that the spheroid does not readily migrate and spread.

On-chip	Off-chip	Off-chip
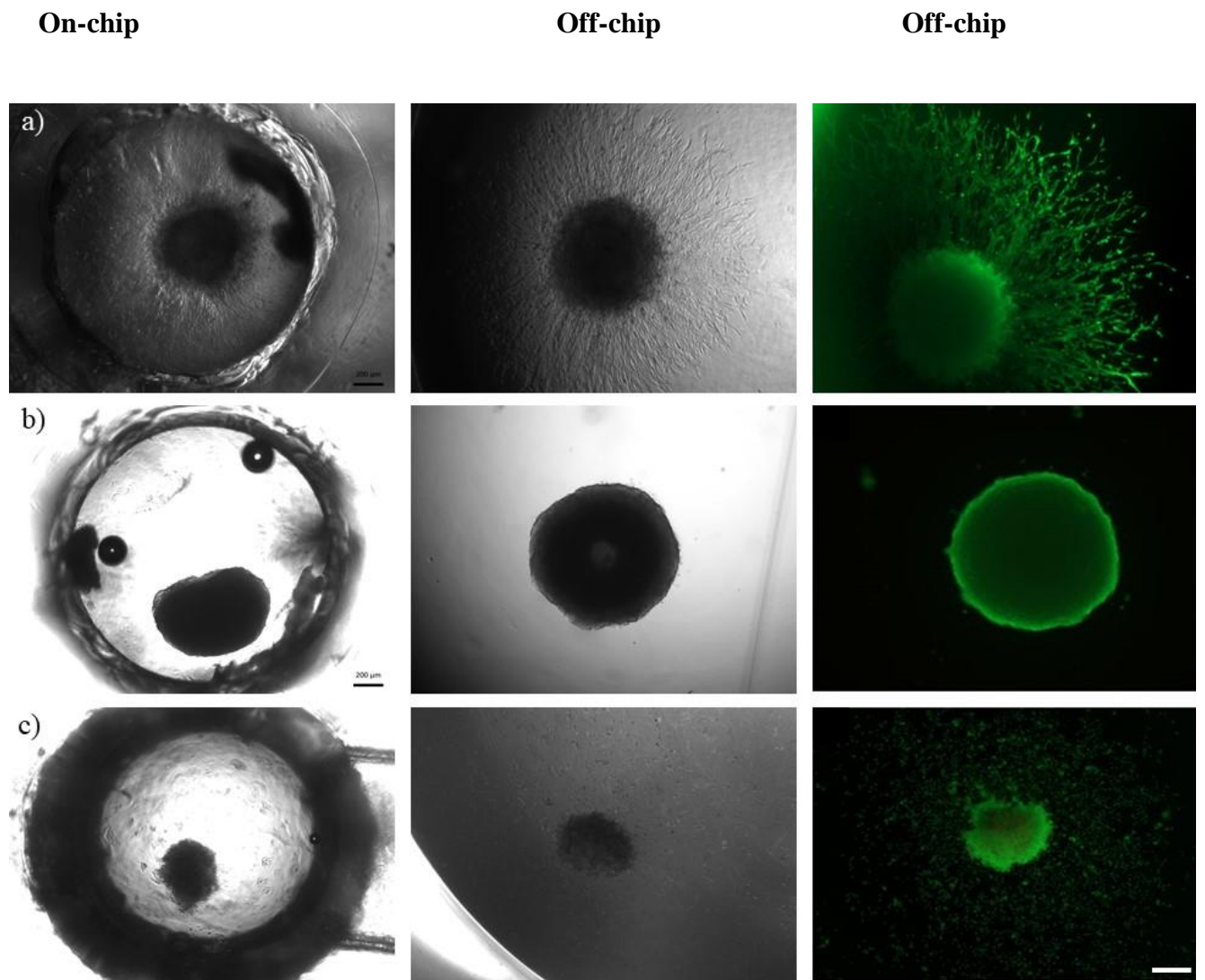
Figure 5.24: Brightfield and FDA stained spheroids to demonstrate migration and invasive capabilities

U-87 MG a) MCF7 b) MDA-MB-231 c) spheroid (2.5 x 10^4 cells per well) migration capabilities in Matrigel. Spheroids (2.5 x 10^4 cells per well) were formed as previously detailed. Matrigel added to a generation 3 microfluidic device and a ULA plate. Before one spheroid was incorporated into a generation 3 microfluidic device and other spheroids were placed in a ULA plate with Matrigel. The spheroids were stained with FDA at 72 h (third column) and imaged at 5 x magnification on a Ziess microscope using FITC settings to demonstrate the levels of cellular spread across different cell lines. First column is an on-chip spheroid, second is an off-chip spheroid, third is off-chip spheroid stained with FDA at 72 h. Scale bar = 200 μm. n=3 in triplicate.

Therefore, to assess the migratory potential within the microfluidic device U-87 MG spheroids were used. U-87 MG spheroids were used to test the migrative and invasive capabilities of cancer models within the generation 3 microfluidic device. Matrigel and collagen was added to the microwell (on separate occasions) before a U-87 MG spheroid was placed within the hydrogel and relevant off chip controls were also used. The spheroids were imaged over 72 h, and the results are shown as representive images below (two Matrigel examples, figure 5.25 and 5.26) and as a histogram (Figure 5.27). These data demonstrates that the spheroids are able to be incorporated into the device and migration fronts imaged *in situ* overtime. The representative images show that the spheroids appear to have a migratory front of cells, which over time appear to increase throughout the mass over time. These observations support the results shown previously (chapter 3, section 4.6) and observations of U-87 MG cells ability to migrate. From the histograms, it is possible to see that U-87 MG spheroid invasion in Matrigel, is the lowest in the media and on-chip conditions at 24 h. Being 20% less than the static spheroids (off-chip). Whilst at 48 h, the on-chip spheroid has 20% increased invasion over the media alone conditioned spheroid. Finally at 72 h, the highest invasion is seen in the static spheroid (off-chip) over the on-chip and media alone condition, being 100% higher than both.

At 24 and 48 h, the migration rate is the highest in the on-chip spheroid, being 100 % more than the off-chip spheroid and monolayer. Similarly this increased migration rate is reflected at 72 h, where the on-chip spheroid shows 76% and 46 % more migration than the monolayer and off-chip spheroid respectively.

Importantly, the invasion and migration analysis on Matrigel between conditions shows that the on chip models are comparable to the off chip (static) conditions and have higher migration rates than the monolayer conditions. Furthermore, the microfluidic models demonstrate it is possible to assess migration and invasion on chip and off chip.
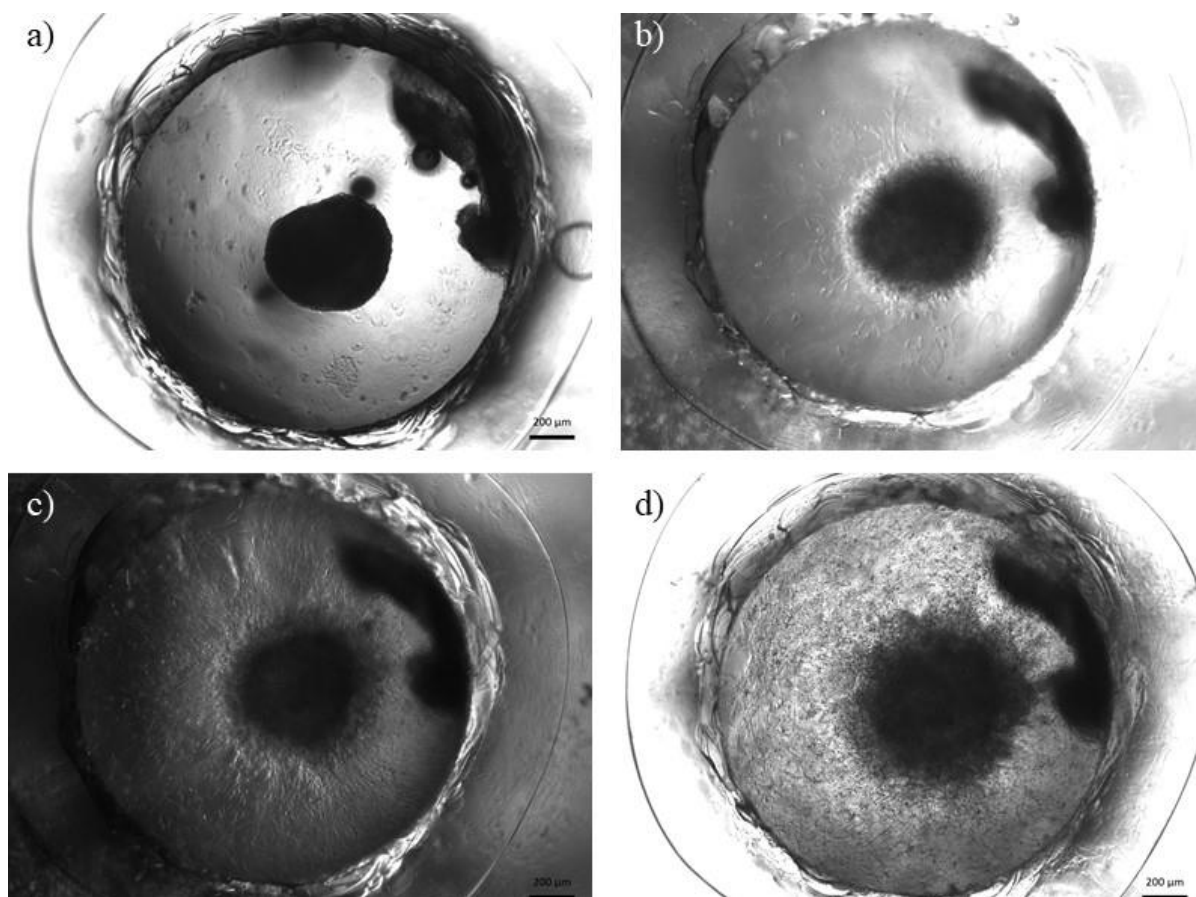
Figure 5.25: U-87 MG spheroids within a generation 3 microfluidic device with Matrigel over 72 h (example 1)

U-87 MG spheroids were seeded at 2.5 x 10^4 cells per well as previously detailed. 10 mg/ml Matrigel was added to the microwell within the generation 3 device before the spheroids were directly pipetted in the borosilicate coverslip base microwell. The images were taken over 72 h at 5 x on a Ziess microscope under brightfield settings at a flow rate of 3μl/min. a) 0 h, b) 24 h, c) 48 h d) 72 h. Scale bar represents 200 μm. n=3 in duplicate
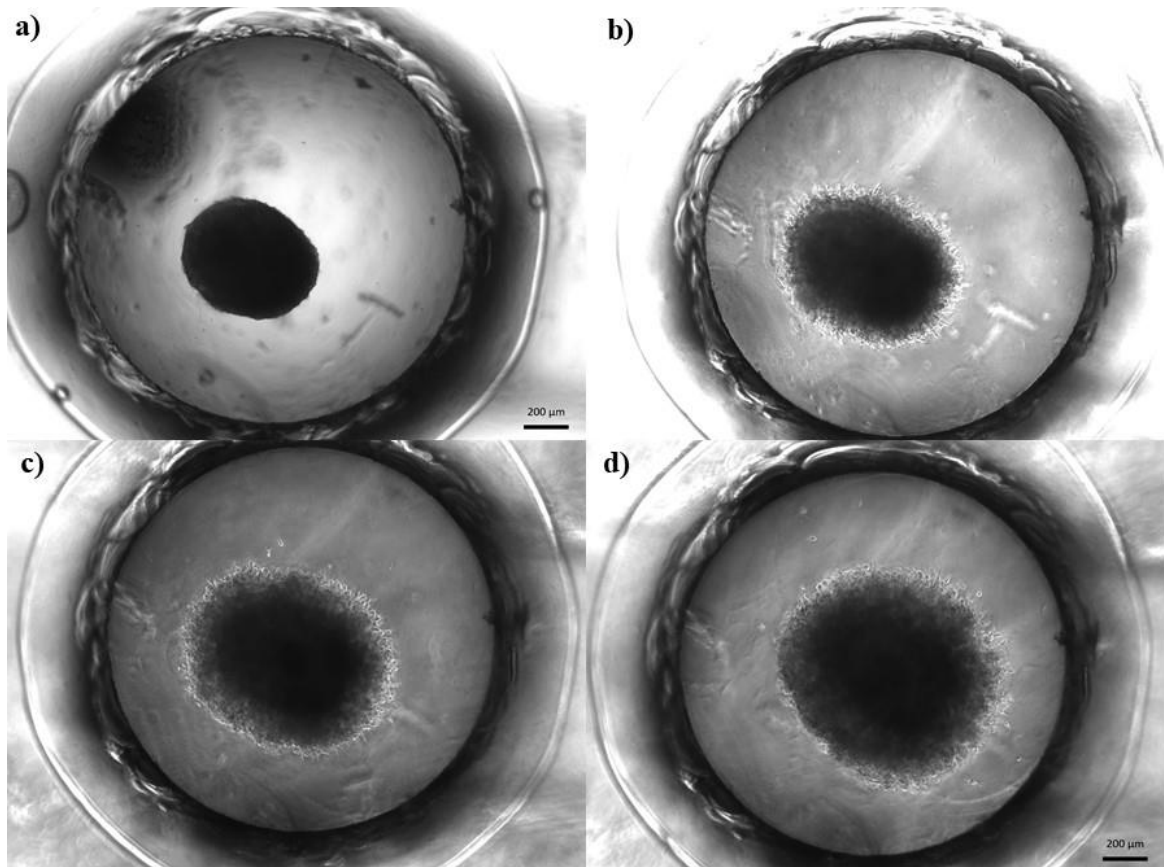
Figure 5.26: U-87 MG spheroids within a generation 3 microfluidic device with Matrigel over 72 h (example 2)

U-87 MG spheroids were seeded at 2.5 x 10⁴ cells per well as previously detailed. 10 mg/ml Matrigel was added to the microwell within the generation 3 device before the spheroids were directly pipetted in the borosilicate coverslip base microwell. The images were taken over 72 h at 5 x on a Ziess microscope under brightfield settings at a flow rate of 3μl/min. a) 0 h, b) 24 h, c) 48 h d) 72 h. Scale bar represents 200 μm. n=3 in duplicate

Matrigel migration
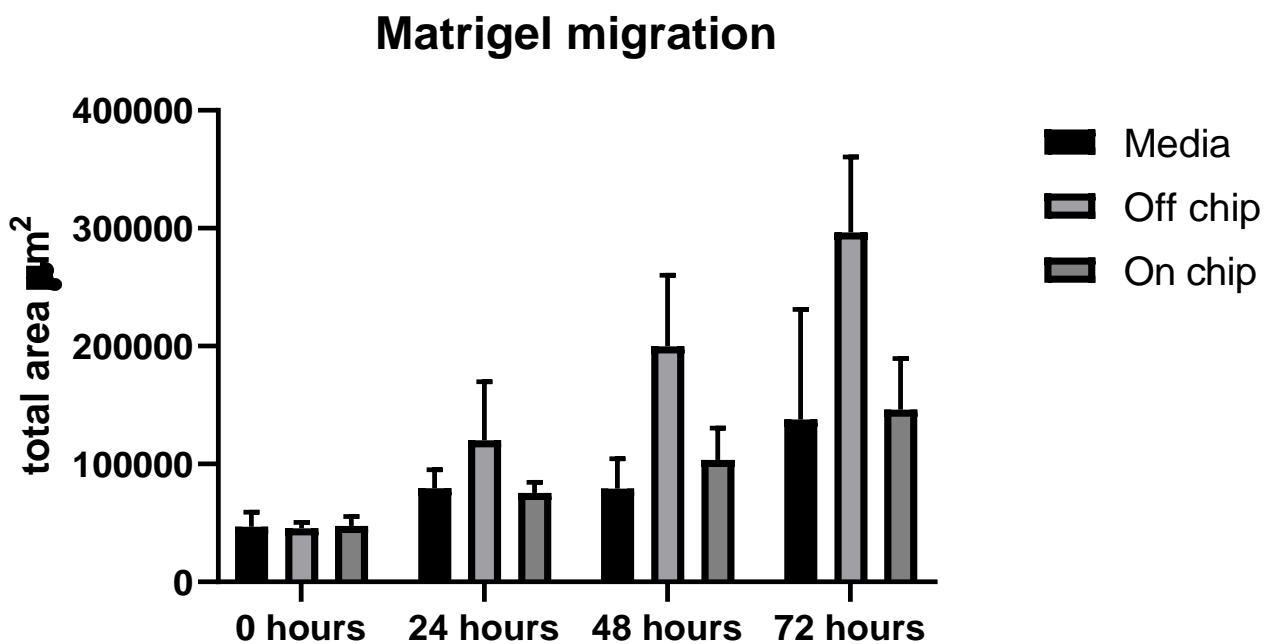
Figure 5.27: Comparison of media and Matrigel migration between 3D off-chip and 3D-on chip models

U-87 MG spheroids (2.5 x 10^4 cells per well) were formed as previously detailed. 10 mg/ml of Matrigel was added to a generation 3 microfluidic device and a ULA plate. Before one spheroid was incorporated into a generation 3 microfluidic device and other spheroids were placed in a ULA plate with Matrigel and no base (media alone). The spheroids were imaged at 0, 24, 48 and 72 h before being imaged at 5 x magnification on a Ziess microscope using brightfield settings. Histograms represent the media from n=7 for all conditions. Error bars are SE and two-way ANOVAs were performed to test for statistical significance.
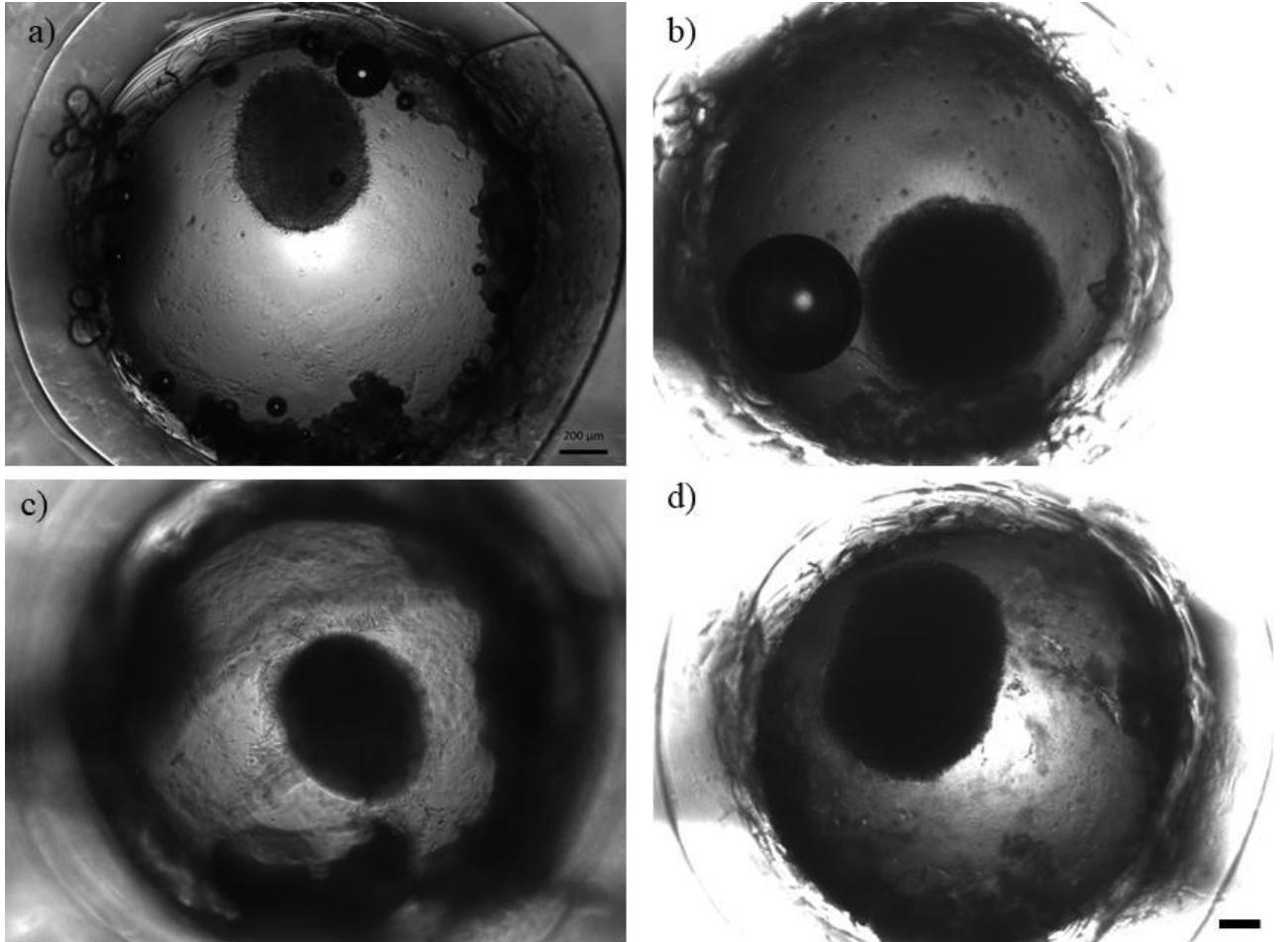
Figure 5.28: U-87 MG spheroids within a generation 3 microfluidic device with Type II Collagen over 72 h (example 2)

U-87 MG spheroids were seeded at 2.5 x 10^4 cells per well as previously detailed. 3 mg/ml Type II Collagen was added to the microwell within the generation 3 device before the spheroids were directly pipetted in the borosilicate coverslip base microwell. The images were taken over 72 h at 5 x on a Ziess microscope under brightfield settings at a flow rate of 3μl/min. a) 0 h, b) 24 h, c) 48 h d) 72 h. Scale bar represents 200 μm. n=3 in duplicate

Collagen migration
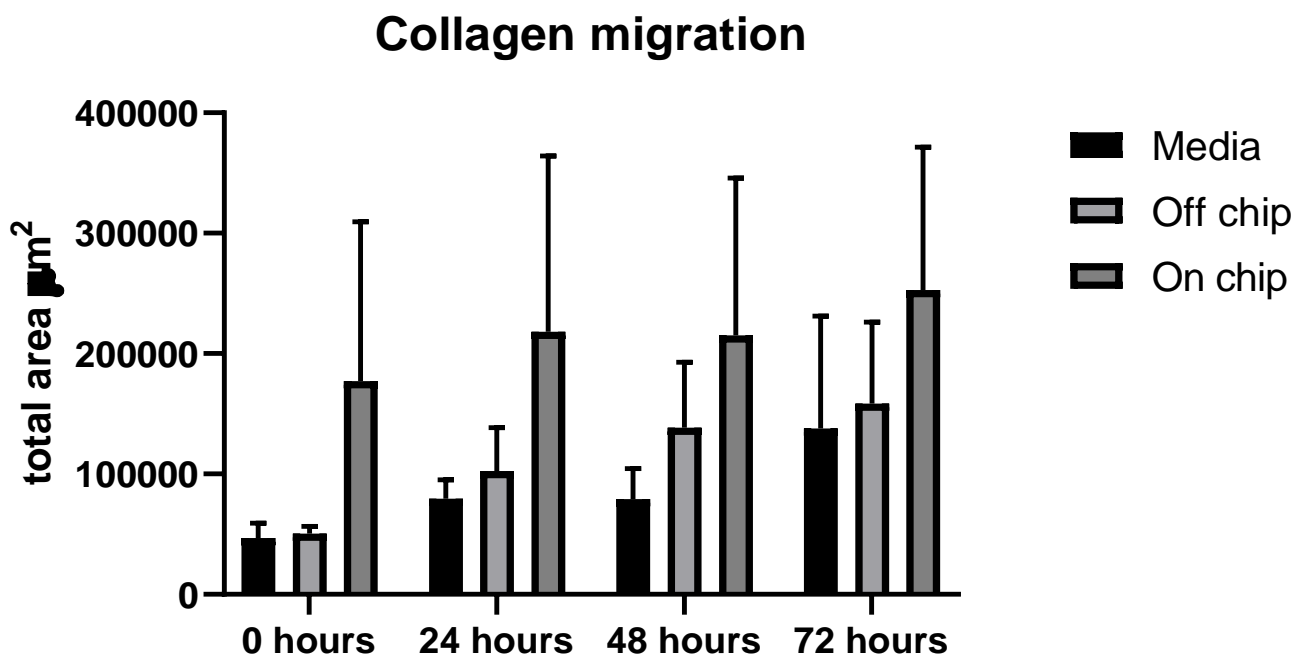
Figure 5.29: Comparison of Collagen migration between 2D, 3D off-chip and 3D-on chip models

U-87 MG spheroids (2.5 x 10⁴ cells per well) were formed as previously detailed. 3 mg/ml of collagen was added to a generation 3 microfluidic device and a ULA plate. Before one spheroid was incorporated into a generation 3 microfluidic device and other spheroids were placed in a ULA plate with collagen and no base (media alone). The spheroids were imaged at 0, 24, 48 and 72 h before being imaged at 5 x magnification on a Ziess microscope using brightfield settings. Histograms represent the media from n=7 for all conditions. Error bars are SE and two-way ANOVAs were performed to test for statistical significance.

5. 4   Discussion

5.4.1   Key findings

The key findings of this chapter were: a further advancement of the microfluidic device was developed well and allowed U-87 MG and MCF7 spheroids to be added within the microwell without being disaggregated and broken. However, the spheroids were unable to be imaged well. FDA/PI staining did not show an intact spheroid; therefore, the device was silanised and a PEG tri-copolymer added to render the surface resistant to cell adhesion. The resistance to cell adhesion using the PEG tri-copolymer was confirmed externally to the device, where cells were shown not to adhere to a treated surface. FDA/PI staining was further conducted to spheroids within a silanised device. This showed that spheroids were viable but again needed to be removed from chip. A final advancement to the device was constructed. The final device had a coverslip base and allowed hydrogels to be added within. It was shown that both Type I collagen and Matrigel were able to be added well and contained within the microwell. FDA/PI staining of spheroids then showed that the spheroids were viable and comparable to off-chip models, showing good levels of live cell fluorescence. Finally, the effluent was collected from three hydrogel conditions on-chip and assessed for VEGF and IL-6. Both ELISAs showed that levels were increased in the on-chip conditions than the off-chip counterparts. The spheroids were also able to be imaged on-chip and quantified for invasion and migration. Which showed that migration was increased on-chip and invasion was comparable to off-chip models.

The aims of this chapter were:

To improve the microfluidic device design for analysis of pro-metastatic phenotypes in spheroids

- *Advance design to allow easier access to microwell*

- *Advance design to image spheroids directly on-chip*

- *Incorporate hydrogel(s) into microfluidic device and embed spheroids*

- *Investigation of potential secreted biomarkers of cell migration/invasion, such as VEGF and IL-6*

- *Evaluate cell migration patterns of spheroids on-chip*

5.4.2 Advance design to allow easier access to microwell

The advancement of the design to allow easier access to the microwell was achieved. An access port, made through milling, was added, resulting in the spheroids being able to be pipetted in. This resulted in the spheroids maintaining their structure and integrity. However, upon trying to image the spheroids, it was concluded that the device needed to be altered, as the rough microwell edge resulted in poor clarity and the spheroids potentially being ripped and disaggregated when trying to fluorescently image them.

5.4.3 Surface treatment

Therefore, the surface treatment through silanisation and subsequent addition of F108 PEG was conducted. The spheroid would therefore likely remain intact as it could not become in contact with the rough surface, resulting in a more trustworthy and accurate measure of fluorescence. To prevent the adherence of cells to the microfluidic device glass surface, glass modification experiments were performed (Tarn 2011), which would be beneficial to both the current and future microfluidic device design and functionality (Corey *et al*. 2010). Silanisation is the process of covering (surface treating) a surface (glass) with organofunctional molecules to prevent the absorption of solute to glass surfaces, resulting in the increasing of its hydrophobicity (Seed 2001). The silanisation step is necessary as F018 can only bind to hydrophobic surfaces (Corey *et al*. 2010). F108 PEG tri co polymer treatment has been shown to lead to decreased cell adhesion and has been used in multiple other studies to prevent cell adhesion to the surface to allow the formation of spheroids on chip (Corey *et al*., 2010; Cheng *et al*., 2016; Zhang *et al*., 2018). To silanise the glass surface OTS was chosen, as it has been shown to render the glass surface hydrophobic (Lee and Sung 2005, Tarn 2011).OTS features

a silane group with four substituents and a -R group responsible for causing the glass to become hydrophobic, the chlorine present reacts with the hexane in the solvent to produce an alkoxy silane and hydrochloric acid, meaning the silanizing agent works due to hydrolysis. The chlorine (-Cl) present in OTS was used to link the silane to the surface. Following the silanisation of the surface, F108 was added to prevent cell adhesion.

5.4.4   Contact angle measurements

To confirm the silanisation process worked and F108 surfactant was present, contact angles were measured. The contact angle of a water droplet in relation to the glass surface can denote the levels of hydrophobicity present (Cras *et al*. 1999). Therefore, where a contact angle is greater than 90°, it indicates a hydrophilic surface. Where it is less than 90°, the surface is hydrophobic. The results showed that the surfaces were altered, and these results validate the silanisation and F-108 treatment. Proving it is suitable to treat the microfluidic devices. as shown by Corey *et al* and others (Corey *et al*., 2010; Cheng *et al*., 2016; Zhang *et al*., 2018).

5.4.5   FDA/PI staining on silanised devices

Following surface treatment, spheroids needed to be assessed for live/dead cells. The results demonstrated that the spheroids appeared to be viable at a comparable level to pre-silanised devices. Suggesting that although the spheroid structure appears to be more intact after silanisation, the silanisation process does not affect the viability of the cells within the spheroids when compared to an un-silanised microfluidic device. However, the stain showed little PI presence, this could be explained through the staining process itself. If there were dead cells present it would be likely that these cells were unbound to the spheroid mass, meaning they were potentially washed away during the staining protocol. Therefore, an adaption to the protocol was made, allowing a stain to be added from above the microwell. Although the treatment was shown to be effective, the spheroids themselves still had poor optical clarity and needed to be removed from the device to allow them to be stained and assessed for live and

dead cells. It is possible that the poor clarity was due to the milling process. The glass microwell surface is rough as was shown previously. This could cause the light to refract and reflect internally resulting in the microscope not being able to focus on the spheroid cells, furthermore, the thickness of the glass base below the microwell may also be an issue for the instruments, meaning that the focusing would not be possible. However, the Zeiss axio microscope used to image the microfluidic device has a focal length of 11mm at 5 x magnification, suggesting that the glass thickness is not the issue. Therefore, it is more likely that the milling process is causing the poor clarity images. The rough microwell would prevent the analysis of spheroid and cell migration/invasion on chip in real time through microscopy. To amend this issue, a borosilicate coverslip base was thermally bonded to the base of the generation 3 microfluidic device. Borosilicate was chosen as this is the material used when IF experiments were conducted off chip, offering similar material properties to the Schott B270 glass used to fabricate the device.

5.4.6 Hydrogel incorporation

After clear spheroid images were confirmed on-chip. Hydrogel incorporation into the microfluidic device was critical to replicating the *in vivo* environment of cancer. This would allow the investigation of cancer migration throughout different hydrogels, continuous perfusion and different culture techniques. Type I collagen and Matrigel were used as they replicate the basement membrane within mammals and closer resemble the natural tumour environment, which has been shown previously in other studies. The successful implementation of hydrogels into the microwell could be accounted due to the wetting of the microwell and channels. This wetting of the surfaces would reduce the capillary action on the hydrogels and draw of fluid, due to the hydrophilic nature of the microchannel surfaces. Therefore, following the addition of liquid buffer, the hydrogels would be able to remain present within the microwell for a period, allowing the gel to set. As detailed Type I collagen

and Matrigel were the most suitable ECM-matrices to proceed with. The spheroids were able to be clearly imaged, stained and incorporated into the hydrogels and therefore assessments on cell migration and invasion were performed as outlined in the final objective of the thesis project.

5.4.7 Assessment of cancer migration on chip

5.4.7.1 VEGF ELISA

ELISA for VEGF and IL-6 were used to assess the media from on chip, off chip and monolayer conditions. Importantly, to model metastasis and spread potential on chip, VEGF and IL-6 were used on chip over other factors. VEGF was chosen as vascular endothelial growth factor is a key factor in cancer angiogenesis and vascular-genesis. The four splice variants play critical roles in pathways promoting cell survival (PI3K), cell differentiation, migration and angiogenesis (Ras) and proliferation (p38MAPK) (Roberts *et al*., 2013). Furthermore, it promotes the secretion of proteolytic enzymes (MMP) which degrade the ECM and basement membrane (Vempati *et al*., 2013). It is also important as active VEGF assists in the proliferation and migration of endothelial cells, enabling the formation of immature vasculature (Roberts *et al*., 2013). VEGF is also important as the increased levels of shear stress on chip have been shown to be linked to cell remodelling and detachment, specifically in endothelial cells (Cezeaux JL *et al*., 1991; Egginton, 2011; Roberts *et al*., 2013). Furthermore, its ability to assist in proliferation and migration of endothelial cells and its role in vascularisation demonstrates how influential VEGF is in cancer spread and migration (Lee *et al*., 2005; Egginton, 2011 Saharinen *et al*., 2011; Roberts *et al*., 2013; Vempati *et al*., 2013).

The media assessment showed that VEGF was increased in the Matrigel and media on chip conditions significantly, whilst the VEGF trend was also higher in collagen than the off chip and monolayer conditions. As spheroids contain a region of hypoxia within their central region and areas 200µm away from the spheroid edge, then HIF would be induced. This in turn could

upregulate expression of VEGF, resulting in the values and trends seen. However, the differences are not statistically significant which could potentially account due to the smaller levels of hypoxia present within the off chip models in comparison to the monolayer conditions. The increase in levels of VEGF seen in the Matrigel testing condition on chip could show that the spheroids are moving to a more invasive phenotype, due to the increased levels of shear stress, the presence of continued nutrients and waste removal and continuous perfusion. The constituent of Matrigel could be interacting with the cells within the spheroids, where more MMPs and proteins are being required to break down the ECM matrices, allowing the cells to migrate and invade throughout. In the media on chip conditions, VEGF is increased to the highest level. It is explainable that VEGF should be increased when the spheroids are in the device, as they are coupled with continuous perfusion culture and shear stress. Increased levels (but low levels) of shear stress have been shown to be linked to cell remodelling and detachment, specifically in endothelial cells (Cezeaux JL *et al*., 1991; Egginton, 2011). Therefore, the cells could be remodelled to a more invasive and metastatic phenotype under shear stress, something which correlates to increased VEGF expression (Roberts *et al*., 2013). Moreover, the cells within the spheroid mass contain regions of hypoxia, and from the simulations shown in Chapter 4, areas of the device also contain regions of low oxygen. The lower oxygen concentrations within and around the spheroid (hypoxia) will result in VEGF being upregulated (Saharinen *et al*., 2011; Zanoni *et al*., 2016). However, the extent of the VEGF increase on chip, in comparison to the hydrogel condition, namely Matrigel, is surprising. It is expected that the VEGF expression should be higher within the Matrigel conditions, due to the reasons explained above, but also as VEGF should increase expression of proteolytic enzymes and MMPs, causing more VEGF to be upregulated and expressed. It is something unexpected, that requires further investigation.

5.4.7.2 IL-6 ELISA

IL-6 expression was investigated as it is a pleiotropic cytokine which is released and overexpressed in inflammation through interactions within the NF- κβ and TNF-α pathways. IL-6 effects tumour cell survival, proliferation and angiogenesis and is highly expressed in several cancers including breast (Ashizawa *et al*., 2005;Browning *et al*., 2018). IL-6 can stimulate cell growth, increases the expression of Bcl-2 and XL, and survivin, resulting in cancer cell survival (Tawara *et al*., 2011). IL-6 is also releasing during infection and injury. IL-6 effects bone metabolism and has a strong activity within tumours. IL-6 effects tumour cell survival, proliferation and angiogenesis through its interactions and roles in PI3K, JAK and MAPK signalling pathways(Ashizawa *et al*., 2005; Browning *et al*., 2018). Moreover, IL-6 is highly expressed in several cancers including breast, colon, hepatic, ovarian and prostate, all through autocrine signalling. It is therefore a clinically relevant prognostic marker (Ashizawa *et al*., 2005; Browning *et al*., 2018). As stated, it plays key roles in cancer progression and bone metastasis. IL-6 can stimulate cell growth and proliferation by activating Raf and MEK. It also increases the expression of Bcl-2 and XL, and survivin, resulting in cancer cell survival (Tawara *et al*., 2011). Furthermore, IL-6 is integral in bone metastasis as it can induce RANKL production, resulting in STAT-3 and subsequent osteoclast maturation (Tawara *et al*., 2011). It can also inhibit anti-osteoclast activity, resulting in further osteolysis, specifically in breast cancer. Furthermore, it has been shown that IL-6 expression is increased in serum of patients with bone and breast cancer metastasis, as well as those of a worse prognosis (Ara & DeClerck, 2010). Breast cancer cells that have metastasised to bone have been shown to overexpress CXCR4 ligand, which is thought to direct cells to the bone and other metastatic sites. IL-6 increases CXCR4 expression in breast cancer cells, and subsequent STAT-3 activation (Tawara *et al*., 2011). Moreover, when within the circulation after intravasation, IL-6 can help protect cancer cells from the immune response. IL-6 has inhibitory effects on expression of IL-2, resulting in inhibition of immune cells and prevention of immune surveillance on tumour cells.

A further example of IL-6's influence on cancer migration is an increase in IL-6 expression also increases VEGF and MMPs, specifically MMP-9. These cause the breakdown of ECM and further expression of VEGF (Browning *et al*., 2018). Finally it has shown that, in breast cancer specifically, IL-6 acts as a regulator in estrogen synthesis, contributing to increased EMT, cell invasion and migration (Abana *et al*., 2017). As previously detailed IL-6 is integral in bone metastasis inducing RANKL and STAT-3, and can inhibit anti-osteoclast activity, specifically in breast cancer. As IL-6 has been correlated with worse patient prognosis and is elevated within patients with bone and breast metastasis(Ara & DeClerck, 2010).

IL-6 was increased in all on chip conditions within each hydrogel. The results could be due to cancer cell interactions with the hydrogels, especially Matrigel. This interaction could be causing the cells to release components such as MMPs, ADAMs or other enzymes used to break down the ECM-like matrices. Henceforth the ECM will be broken down by proteolytic enzymes and thus able to release the factors embedded within, such as VEGF, which is at 5.0 – 7.5 ng/mL (Corning, 2012). The increased levels of VEGF and factors released from the ECM matrices would further upregulate MMP expression and act in a positive feedback loop, resulting in more VEGF and IL-6 release, being shown in the ELISAs. The increase in expression in Matrigel is expected as breast cancer cells over express IL-6 naturally (Abana *et al*., 2017). Therefore, the genetic and protein profile in spheroids are more like *in vivo* tumours (Weiswald *et al*., 2015) and therefore they will release more IL-6 than the monolayer. When the spheroids are within Matrigel, they need to invade the local environment, meaning that MMPs and other proteolytic enzymes are required to breakdown the ECM (Bartsch *et al*., 2003; Lima *et al*., 2016). IL-6 secretion will cause MMPs to be released, allowing the cells to breakdown the Matrigel. This will further result in more IL-6 being upregulated and VEGF release (Browning *et al*., 2018). Coupling the IL-6 expression with VEGF secretion, which is also higher in the Matrigel conditions shown in Figure 5.20, then increased IL-6 is expected.

The increase in IL-6 is expected as both factors interact with signalling pathways which will cause one another to be upregulated and expressed, meaning an increased level over time (Tawara *et al.*, 2011). As the media alone condition on chip is higher, then the collagen and Matrigel would be expected to also be higher. The increased shear stress and continuous perfusion results in the spheroid cells being potentially remodelled and subsequently releasing more IL-6 (Egginton, 2011). However, a plausible explanation for the increased IL-6 in the media condition is due to the VEGF secretion. Looking at the previous ELISA data, this increase in VEGF could influence the secretion of IL-6 within the IL-6 ELISA data set. More interestingly, the increase in IL-6 within the collagen and Matrigel could be a result of not only the VEGF, as was shown in the previous ELISA data, but also the increase in shear stress and continuous perfusion, and the production of MMPs (Browning *et al.*, 2018). The increase in shear stress (even if low) has been shown to increase the invasive potential of cells and cell remodelling through affecting cell adhesion and thus metastatic progression, therefore the IL-6 and VEGF secretion increase in the Matrigel is expected (Cezeaux *et al.*, 1991; Kumar , 2009; Kraning Rush *et al.*, 2012; Jain *et al.*, 2014). Furthermore, the increase in MMPs as a result will cause more IL-6 production as was seen in the Matrigel condition (Tawara *et al.*, 2011).

5.4.7.3 Spheroid migration on chip

Spheroids were incorporated into two different hydrogels and investigated for cellular migration and invasion. The results showed that the invasion on chip through Matrigel was lower but comparable at certain time points (0, 24 h) to the off chip models, whilst the migration on collagen was higher in the on chip conditions in comparison to the off chip model. Both results are explainable; as (following on from the work conducted in Chapter 3) MCF7 cells are not as migratory as MDA-MB-231 counterparts, being shown to invade less, migrate more, due to their epithelial nature over the mesenchymal nature of MDA-MB-231 cells. Similarly, U-87 MG cells have been shown to migrate readily within hydrogels. Therefore, both the

observations of decreased migration of MCF7 spheroids in hydrogels and increased migration of U-87 MG spheroids are expected. In the media alone conditions, the lack of ECM means that the spheroids do not have any induced signals, meaning that they are less likely to have any cells migrating away from the primary mass. Moreover, any cells which are released from the spheroids within the media alone controls would not have any base to remain within and could be removed when media is replenished in the ULA plate and washed away in the microfluidic device conditions. The previous results show there are increased levels of VEGF and IL-6 in the off chip Matrigel models in comparison to media alone. As there are an increased level of VEGF and IL-6 in the off chip Matrigel model, then these could induce cell proliferation and spread. With the increased level of hydrogel (in comparison to media alone) then increased VEGF induces increased expression of MMPs, allowing the cells and subsequent spheroids to breakdown the ECM-matrices. This will further perpetuate the cells to gain a more invasive and migratory ability, resulting in increased invasion and migration over time. The increased migration on chip in collagen is also explainable. The increased levels of shear stress and continuous flow. As the on chip models have higher levels of shear stress than the off chip counterparts, then this can potentially cause an increased level of cell shedding/migration as increased shear stress has been shown to increase invasion, specifically through the promotion of synthesis of cAMP, IL-1β and VEGF (Vempati *et al*., 2013). The relatively low values of shear stress shown in this device could cause increased VEGF expression, which is shown in the ELISA on chip data across all conditions. This increased VEGF promotes the secretion of proteolytic enzymes, including the matrix metalloproteinases (MMP), which can cleave and degrade the ECM and basement membrane, further secreting and releasing VEGF (Vempati *et al*., 2013), furthering the increased levels of migration seen in the device in collagen. Moreover, cancer cells under low shear stress, which is seen within the device, have been shown to have increased migration *in vivo* and *in vitro,* suggesting a

further reason for increased migration (Mitchell & King., 2013; Huang *et al*., 2018). In comparison to the increased migration on-chip in collagen. the decreased invasion on-chip may be due the size constraints of the culture conditions. The 96 well plates used are Corning 96 well ULA plates, which have a well diameter of 6.4 mm. This size is triple the size of the microwell within the generation 3 microfluidic device, which has a diameter of 2 mm. Therefore, the ULA plates have an microwell volume of 68.63 mm^3 and the microfluidic device has a volume of 2.0944 mm ^{3}, meaning that when assessing the invasion and migration of spheroids within the hydrogels, the potential for migration and invasion analysis within the 96 well plate (off chip) is 3 times higher than the on chip conditions.

5.5   Conclusion

Overall, the results showed that the chip modification and advancement progressed the chip to a point in which relevant biological readouts, namely ELISA for biomarkers and realtime spheroid analysis, were possible. The results demonstrated that both VEGF and IL-6 secretion was increased on chip, as was migration within the on chip collagen model. Moreover, the results showed U-87 MG invasion on-chip was comparable across all three testing, whilst migration was increased on-chip over cell monolayers and static spheroids.

Therefore, the work presented in this chapter has fulfilled the aims of:

- *Advance design to allow easier access to microwell*

- *Advance design to image spheroids directly on-chip*

- *Incorporate hydrogel(s) into microfluidic device and embed spheroids*

- *Investigation of potential secreted biomarkers of cell migration/invasion, such as VEGF and IL-6*

- *Evaluate at cell migration patterns of spheroids on-chip*

Meaning that this work offers a novel and promising foundation into investigation cancer *in vitro*, whilst modelling aspects of *in vivo* tumours.

6 General Discussion

6.1 Summary of work presented in previous chapters

The **novelty** of this work is the formation of **spheroids externally**, allowing them to be grown to a **relevant size**, which replicates what is seen *in vivo*; in terms of the hypoxic, necrotic and anoxic regions. This is something that is not commonly done. Secondly, this work did not want to assess the effects of drugs on the spheroid masses to assess whether it is possible to reduce their size and kill the tumour cells. Instead wanting to keep the spheroids **alive and viable** to allow the assessment of the cancer on chip, allowing us to study the biology of the spheroids overtime. Thirdly, the project wanted to use **shear stress and continuous perfusion** to identify **key factors secreted** from the spheroid mass to identify whether a trend was seen in comparison to off chip models. Finally, the project wanted to generate an easy to use **glass microfluidic device**, which would allow the user to monitor migration and invasion of cancer spheroids in **real time, through hydrogels and ECM-like matrices**. Allowing us to understand trends and biomarkers that may offer insight into the early stage interactions of cells and the external microenvironment within metastasis.

There is a clear gap in the research which this project aims to fill. The current gap in the research is a lack of understanding and knowledge regarding the early stages of the metastatic cascade and how external factors such as shear stress, the tumour microenvironment and continuous perfusion contribute to cancer spread *in vitro*. This research aims to use a glass microfluidic device to replicate *in vivo* conditions within an *in vitro* environment. The device will be used to look at both brain and breast cancer spheroids to investigate the early metastatic spread of tumours.

MCF7 and U-87 MG spheroids were formed off-chip and incorporated into the device by pipetting, before being perfused with complete media at 3 µL min^{-1} for 72 h. Cell viability was assessed in effluent, using the CytoTox Glo assay, demonstrating spheroid viability is robustly

maintained on-chip. *In situ* analysis of cell viability indicated an increased proportion of viable cells and decreased dead cells on-chip compared to off-chip. ELISA showed that VEGF secretion, as evaluated by its presence in conditioned media, was comparable across all testing conditions. The chip model has been further developed to allow spheroids to be embedded in ECM (extracellular matrix)-like matrices. VEGF ELISA and IL-6 ELISA showed that both VEGF and IL-6 secretion, as evaluated by its presence in conditioned media, was comparable across all testing conditions. ELISA also showed that IL-6 and VEGF was increased in the on-chip models within hydrogel conditions. The device has also allowed the direct imaging of spheroids on chip over 72 h. The analysis of U-87 MG spheroids on chip showed that invasion through Matrigel was comparable to the off-chip static models. Whilst migration on chip, through collagen analysis, was increased over the off-chip counterparts. The work shown offers a novel insight into cancer metastasis; on a more replicative model than the current conventional *in vitro* techniques.

This study **hypothesised**, that it was possible to mirror the early stages of metastasis in a microfluidic device and it would be possible to recreate and drive EMT and invasion of cells in spheroids within a microfluidic device.

The main **aim** of this study was to design and optimise a microfluidic device capable of harbouring a characterised cancer spheroid, in order to mirror characteristics that are linked to metastatic potential and spread. The aims were furthered to allow the investigation of metastatic biomarkers released from the primary spheroid mass will be identified.

Specifically, the objectives of each research chapter were to:

1 **To generate and characterise the best cancer spheroids to incorporate in a microfluidic device**

2 **To design and validate a microfluidic device for spheroid incorporation and maintenance**

3 **To improve the microfluidic device design for analysis of pro-metastatic phenotypes in spheroids**

The research shown and reported here demonstrated good viability over the period of 72 h when compared to the off-chip and monolayer counterparts. This was both confirmed through the CytoTox glo assay and fluorescent cell staining for the generation 1 device. Likewise, live/dead staining showed good viability over 72 h in the generation 2 microfluidic device, over off-chip counterparts. Finally, the generation 3 microfluidic device also showed good levels of live cell intensity on chip, in comparison to the off-chip counterparts, being 46% higher. This data proves, like is seen with previous literature, that large populations of live cells within the spheroids were able to be maintained on-chip for at least 72 h.

Vinci and colleagues detailed spheroid formation and composition from a variety of cell lines, and chapter 3 supported the observations, that U-87 MG and MCF7 spheroids were reproducibly and routinely produced (Vinci *et al*., 2013). Moreover, it showed that MDA-MB-231 spheroids were 'grape-like' and larger than their same sized counterparts (Vinci *et al*., 2013). Growth kinetics were then assessed and spheroids followed a four phase pattern of growth over time (Mehta *et al*., 2012). The percentage of the spheroids core and G0/proliferative rim over time was performed on two seeding densities, and showed the core percentage of the total spheroid increased over time (Sutherland, 1988; Gong *et al*., 2015; Rodriguez *et al*., 2015). Staining of both H & E and Ki-67, as a marker of cellular spread, showed expected trends, supporting those seen within the literature (Sutherland, 1988; Scholzen, 2000; Mehta *et al*., 2012; Zanoni M *et al*., 2016). Hypoxyprobe (Pimonidazole) IF staining of spheroid sections showed a hypoxic core within the spheroids, as expected (Varia *et al*, 1998; Mehta *et al*., 2012; Zanoni M *et al*., 2016).

The first generation device used within this study was previously used at the University of Hull Shear stress and flow rates proved ideal for spheroids to be added to the device, but this was not as robust, reproducible and uniform as first desired. However, it was shown that multiple cell lines could be added without the spheroids being disaggregated and thus were usable. By using the spheroids which were added successfully, the viability could be analysed. This showed fresh samples were preferential, and the spheroids remained viable on chip over off chip and monolayer counterparts. FDA PI supported the initial observations. ELISA showed that the levels of a marker of spread, VEGF, was comparable, if not elevated, in the on chip conditioned spheroid effluent over the off chip and monolayer conditions. To further assess migration, western blot of spheroids for EMT markers were performed. They showed E-cadherin, appeared to be cleaved in the on-chip spheroids over many repeats. However, acknowledging the issues with spheroid shape potentially accounting for this alteration, simulations were performed. The simulations showed that oxygen levels were lower on chip than first thought. Resulting in higher hypoxic regions throughout the spheroid. Moreover, this combined with structural analysis through H&E presented the spheroid as a 'compressed' shape, meaning opportunities for the advancements of the microfluidic device were required. By adding an access port above the microwell, direct pipetting of the spheroid and hydrogel into the generation 2 device was possible. To further prevent the issue of misshapen spheroids, surface modifications were performed. The glass surface was silanised using OTS, and the PEG surfactant was added. The successful addition and prevention of cell adhesion was confirmed, reproducibly and accurately. Once the glass surface was modified to prevent cell adhesion, cell imaging was performed on chip. Similarly, to the first generation microfluidic device, the spheroids had poor optical clarity and were not at a desired focus. To combat this, FDA/PI staining was conducted and showed spheroids were maintained at a viable level on chip over a 72 h period. Meaning there was no loss in cell viability over time.

A final adjustment to the chip was conducted. A borosilicate coverslip, which is 0.4 mm in depth, was bound, underneath the microwell. After the glass coverslips were added to the microwell base, hydrogel incorporation was attempted. The incorporation of hydrogels would allow the system to mirror what is seen *in vivo*. The results demonstrated that type I collagen and Matrigel were successfully incorporated, and all spheroids used were able to be incorporated well into the hydrogels. The spheroids were then also able to be imaged well through brightfield microscopy. FDA PI stain for live dead cells showed viability was maintained on chip; with large percentages of live cells over dead cells. The observations found mirror those within the literature; spheroid cells being live on chip over time.

In order to investigate the final aims and objectives; VEGF and IL-6 ELISAs were measured. VEGF was used as it is critical in the migration and invasion of cancer *in vivo*, namely due to its promotion of proteolytic enzyme and ability to assist in proliferation and migration (Lee *et al*., 2005; Egginton, 2011 Saharinen *et al*., 2011; Roberts *et al*., 2013; Vempati *et al*., 2013). Whilst IL-6 was assessed, as it has been shown to effect bone metabolism and has been correlated with strong activity within tumours, moreover it is linked tumour cell survival, proliferation and angiogenesis, and is highly expressed in several cancers including breast, colon, hepatic, ovarian and prostate, all through autocrine signalling (Ashizawa *et al*., 2005; Browning *et al*., 2018). The ELISA results showed that VEGF expression was increased in all conditions on chip, with significant differences in media and Matrigel, in comparison to the off chip and monolayer testing conditions. Similarly, IL-6 expression was increased to a larger significance in collagen and Matrigel in the on chip conditions, over the other two counterparts. The results could be due to cancer cell interactions with the hydrogels, especially Matrigel. This interaction could be causing the cells to release components such as MMPs, ADAMs or other enzymes used to break down the ECM-like matrices. Henceforth the ECM will be broken down by proteolytic enzymes and thus able to release the factors embedded within, such as

VEGF, which is at 5.0 – 7.5 ng/mL (Corning, 2012). The increased levels of VEGF and factors released from the ECM matrices would further upregulate MMP expression and act in a positive feedback loop, resulting in more VEGF and IL-6 release, being shown in the ELISAs. Further to this point, is these results could be due to the increased levels of shear stress on chip, something known to increase migration and invasion potential. Similarly, the continuous perfusion and flow, allowing more nutrient acquisition to on chip spheroids, could allow cells to produce more signals resulting in increased expression of VEGF and IL-6 in the effluent. To test and to reflect what was seen in the effluent, on chip spheroid imaging of invasion and migration was conducted over time.

MCF7 spheroids did not migrate or invade within any conditions tested. Therefore, U-87 MG spheroids were used to identify if there were any differences in migration and invasion between on-chip and off-chip conditions. The on chip imaging results showed that invasion, in the on chip conditions within Matrigel was lower but comparable to the off chip models, whilst migration on chip in collagen was higher than the off chip counterparts. This could be a result of shear stress, continuous perfusion, hypoxia or cell remodelling. Meaning the model shows that migration is increased on chip and invasion on chip is comparable, but it needs to be further investigated.

6.2 Future directions

6.2.1 Single cell spheroids

As this work offers a solid foundation for further investigations into cancer migration and spread, there are many avenues that future work could progress towards. Firstly, it must be noted, as detailed in chapter 3, that cancer cell line spheroids are limited in terms of their application, as they are not fully replicative of *in vivo* tumours, due to their homogenous cell populations (MacGowan *et al*., 2001; Holen *et al*., 2017). Cancer cell spheroids only contain singular cells from the cell line used, for example MCF7 or U-87 MG cells, as is the case with this research. Therefore, to overcome this caveat, and to make the populations more

realistic spheroids could be co-culture with other cells. This first improvement can be seen in other works (Blaha *et al*., 2017; Bersini *et al*., 2018; Yuan *et al*., 2019), however, not all these examples use co-cultured spheroids within a microfluidic device and the models are not used to identify metastasis in the manner proposed in this research. The cocultured spheroids need to be cultured with other variants of stromal cells, immune cells and primary cells (such as HUVECs, fibroblasts and macrophages). This would allow the user to investigate and identify cell-cell interactions to see how these influence the migratory and invasive potential of cancer spheroids in 3D. Further to this point is that when using both co-cultured and singular culture spheroids, it would better to add different components of *in vivo* cells within the ECM-like matrices to identify key interactions between cells and the basement membrane in a more realistic environment. By using the single cell spheroids, it would be possible to add the cell variants to the ECM like matrices. This would better mirror those conditions seen *in vivo* and the addition of cells to the ECM-like matrices is something which has been done previously (Peela *et al*., 2017). The cells which could be used are cancer associated fibroblasts and primary cells such as HUVECs or endothelial cells. This would replicate the lining which cancer cells need to breakdown and simulate the conditions seen within humans(Sung KE *et al*., 2013; Bersini *et al*., 2014).

6.2.2   *Metastatic niches*

To further advance this model, whilst still using single cell type spheroids, it would be interesting to add micrometastases niches and tropisms on chip. For example, developing locations on chip that replicate bone, lung and bladder microenvironments, using cyto and chemo kines, cells and ECM-like matrices. The single cell spheroids would then be attracted to one of the different locations (over the others) and this would then allow the researchers to see how and where cancer cells migrate towards over one another (Hao *et al*., 2018).

Moreover, it would then be possible to look at which biomarkers and factors are released, to both prime the premetastatic niche and to increase migration and invasion.

6.2.3   Multi-chip model

In comparison to using a singular microfluidic device to investigate singular cellular spheroids. A multi-chip approach could be a possible avenue to investigate the whole metastatic cascade. Each chip could mirror each individual stages of the metastatic cascade. An example being, one chip being used with a co-cultured spheroid on a cell embedded ECM – matrix to look at local invasion through the basement membrane mix (stage 1 and 2), whilst a further chip could be used to multiplex the microfluidic device. Using multiple spheroids on chip would allow more cells to migrate and spread from the primary spheroids, these could all collect in one central location on chip, and form spheroid models within the device. The secondary cells would be able to be compared to the primary mass to assess genetic aberrations and alterations from the original tumour source. Such as looking at markers of cancer stem cells through techniques including flow cytometry. Useful markers to look at would be CXCR4, CD44, specifically v9 and v8-10, to be variants different from normal cell surface markers or CD117 when looking at the ability of self-renewal of cancers (Kim & Ryu, 2017; Wang *et al*., 2018b). The device would replicate the formation of micrometastases *in vitro*. To further this design, chemokines and cytokines would be used to replicate *in vivo* environments, such as was seen with Hao (Hao *et al*., 2018). Downstream of the multiplexed spheroids would be collecting microwells. Each microwell would replicate a different *in vivo* tropism of cancer, such as brain, bone and bladder. The spheroid shed cells would then move towards one and this would allow the researcher to identify which location appears preferable for the tumour cells. Using this style of device there are three directions that the research would follow. Firstly, the primary mass would have its secretome analysed. There would be factors that are being released by the primary mass to break down the

basement membrane and to prime the secondary site, in preparation for the micrometastases, identifying factors such as MMPs, ADAMs, Interleukins and heat shock proteins 27, 70 and 90 (Chatterjee & Burns, 2017). This would lead onto the second task, where the media should be collected to look for CTCs and identify any factors priming the pre-metastatic niche, this would be done through RNA sequencing focusing on miRNA 19a, 138 and 200, all shown to lead to increased motility of primary cancers, inducing EMT and enhancing angiogenesis (Wang *et al*., 2018a). Finally, the 'secondary' shed cells could be have its proteome analysed as was previously suggested, to look for markers of both stem cells or EMT and MET, including factors shown in this report such as E-cadherin, β-catenin, Vimentin (Brabletz *et al*., 2018).

6.2.4   *Current advancement*

An advancement on this research is something which is currently being investigated and is being done. The original generation 3 device is being used, with a more reproducible and robust tubing set up. The outlet tubing is connected to a 'newer' second device, holding an oxygen plasma treated microscope slide with tiny microwells within. The cells shed from the spheroid in the initial microwell on the generation 3 microfluidic device can migrate into the second device, allowing the cells to sediment and form secondary masses. These would then be looked at to assess differences to the primary mass.

6.2.5   *Open scope*

In the future, microfluidics has a key role to play in medical and cancer research. The technology offers a unique ability to provide point of care diagnosis, and specifically being able to take a tumour sample from patients, run molecular analysis on it, before allowing the treatment to be specifically tailored to the tumour subtype. The excised patient tumour could be subdivided into multiple devices, before trying different chemotherapeutics on them. This would then dictate which treatment should be used for maximum efficiency by the clinicians.

This strategy is something I can actively see the field progressing towards and is actively being pursued.

In a situation undeterred by accessibility and financial constraints, it would unique and novel to build a patient on a microfluidic device. The building of a human on chip is something currently underway, however, that is not unique as stated here. It would be interesting to build each patient on a microfluidic device individually, using their cells, components and samples. This would then allow clinicians and scientists to screen mutations, identify trends and have a rapid, microscale system which could allow better treatment further in the future.

6.2.6 Concluding remarks

Overall, as detailed, this work offers a foundation and platform to identify early stage biomarkers of metastasis and is something that needs to be furthered upon by using the suggestions described within the future work section.

6.3   Conclusion

Overall, the results showed that the project aims, and objectives outlined were achieved. The chip modifications and advancement progressed the chip to a point in which relevant biological readouts were possible, such as ELISA for biomarkers of cellular spread, western blot of proteins for EMT and ICC analysis. Furthermore, the results offer a novel insight into the hypothesis detailed; it is possible to recreate and model the tumour microenvironment within a microfluidic device to investigate cellular spread. Supporting that it is potentially possible to mirror the early stages of metastasis in a microfluidic device, increasing the level of invasion and migration over conventional models. This work offers a foundation and platform to identify early stage biomarkers of metastasis and is something that needs to be furthered upon.

Chapter 7   Appendix
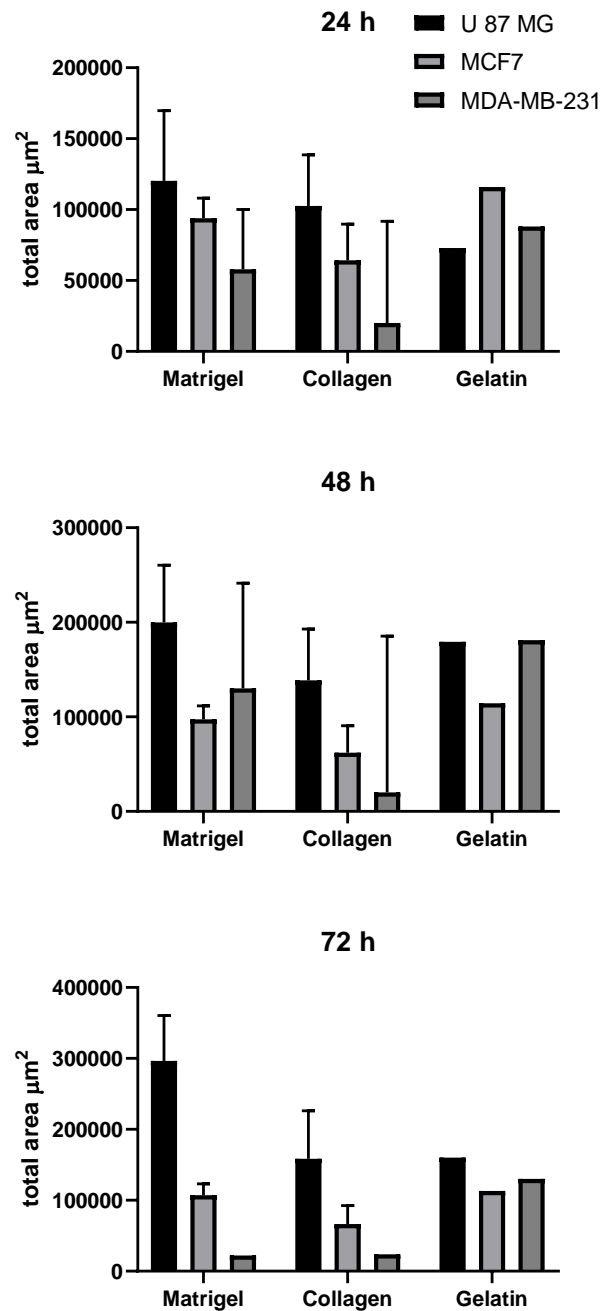
Figure 7.1: U-87 MG, MCF7 and MDA-MB-231 spheroid migration on three hydrogels, ANOVA comparison

24 h a), 48h b) and 72h c) spheroids (seeded at 2.5 x 10^4) placed on three hydrogels; Matrigel, collagen and gelatin, and measured for migration (total area in μm^2) over a period of 72 h. Migration times equate to t=0, t=24, t= 48 and t=72. SE of n=3 (for Matrigel and collagen). Two way ANOVA shows no significance at t=24, 48 or 72 across any cell type or hydrogel.
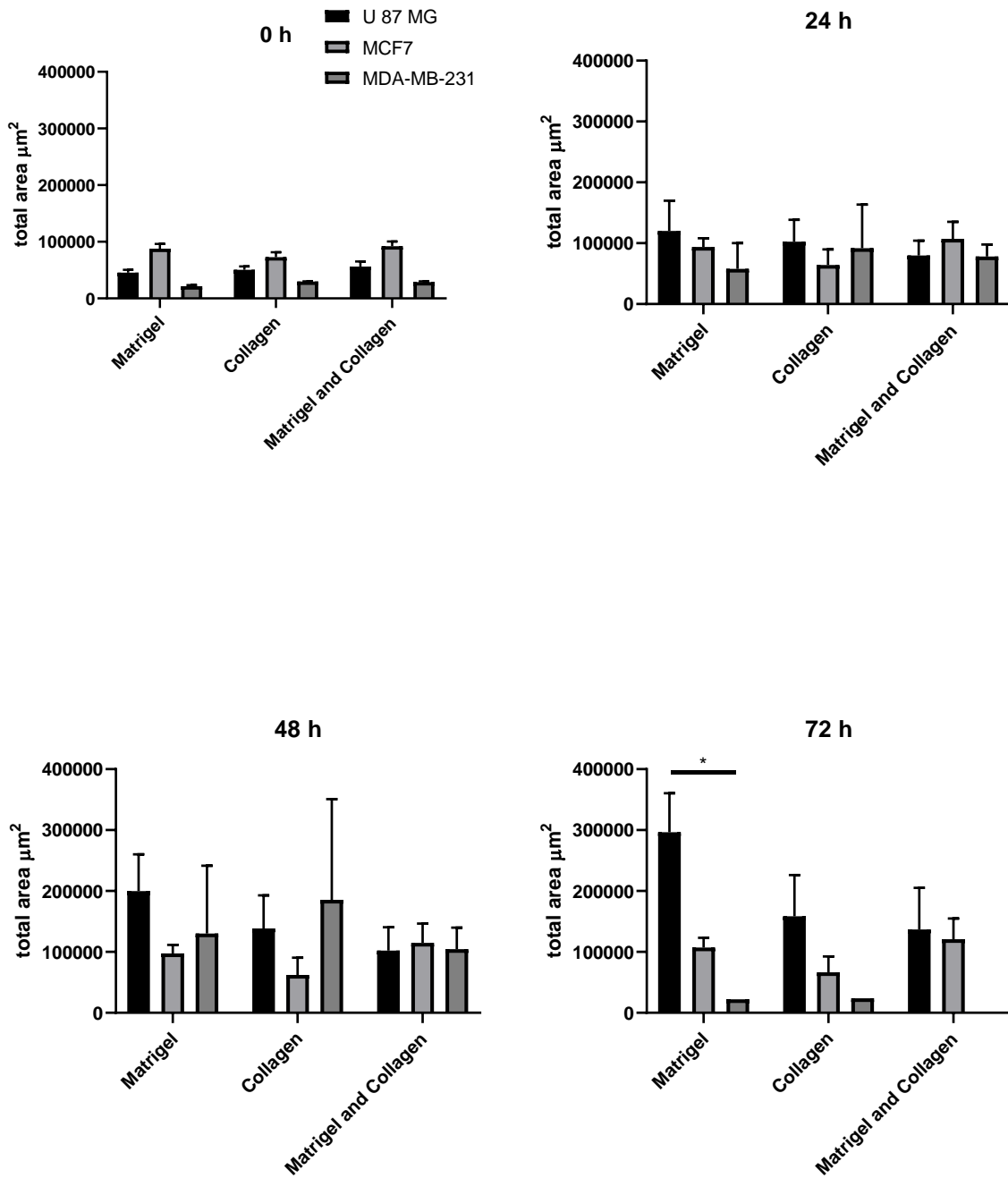
Figure 7.2: U-87 MG, MCF7 and MDA-MB-231 spheroid migration on three concentrations of collagen, ANOVA comparison

U-87 MG a), MCF7 b) and MDA-MB-231 c) spheroids (seeded at 2.5 x 10⁴) placed on various hydrogels; Matrigel, collagen and Matrigel with collagen. Spheroids were measured for migration (total area) over a period of 72 h. Migration times equate to t=0, t=24, t= 48 and t=72. Two way ANOVA was conducted and showed no significance except for 1 * significance between U-87 MG and MDA-MB-231 spehroids at 72 h.. n=3 experimental repeats in triplicate.
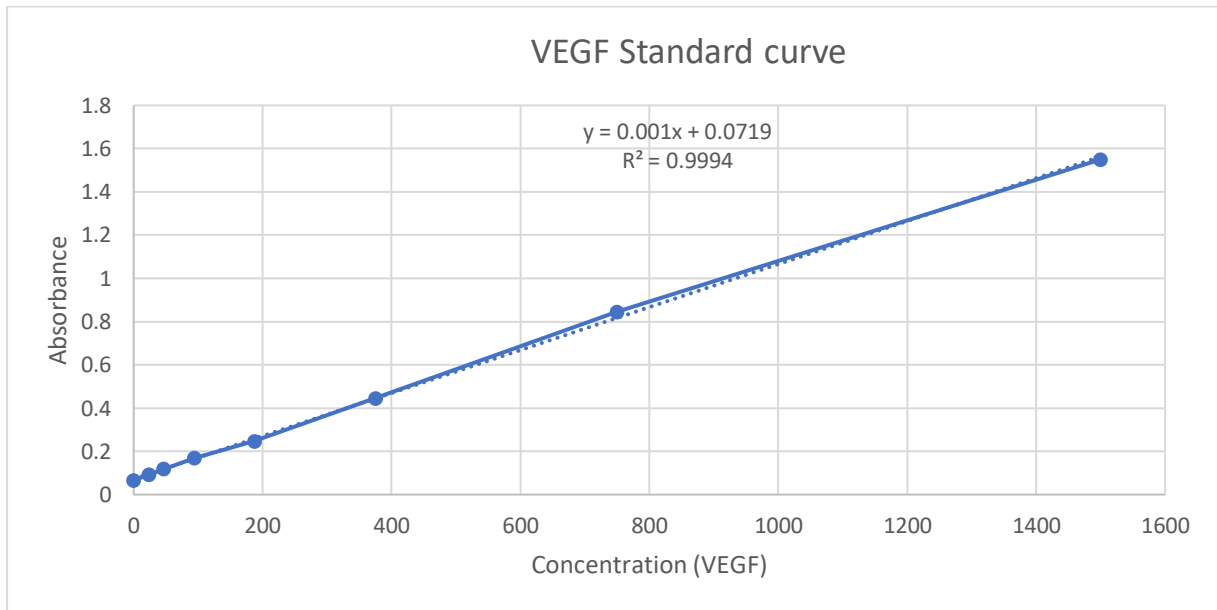
Figure 7.3: Standard curve of ELISA - VEGF concentration and absorbance

A standard curve was produced for VEGF, using kit procedures, to determine the levels of absorbance for VEGF present at different concentrations. This straight line equation was used to determine the unknown concentration of IL-6 present in effluent samples.

Worked Example, using VEGF standard curve on figure 7.3:

Standard curve data

Conc.	Measure 1	Measure 2	Average
1500	1.61	1.49	1.55
750	0.849	0.841	0.845
375	0.471	0.42	0.4455
187.5	0.256	0.24	0.248
93.75	0.179	0.158	0.1685
46.875	0.12	0.117	0.1185
23.4375	0.096	0.088	0.092
0	0.068	0.065	0.0665

Example absorbance, next to effluent amount

	effluent amount	72 hours	72 hours	average	STD dev	SE
Y	800 µl	1.097	1.079	1.088	0.012728	0.009001
Y	600 µl	0.849	0.901	0.875	0.03677	0.026004
Y	4500 µl	0.138	0.152	0.145	0.009899	0.007001

Equation rearranged for X: X=y-0.0719/0.001

Average values – 0.0719

cell monolayer	1.0161
static spheroid	0.8031
microfluidic device	0.0731

Values divided by 0.001

cell monolayer	1016.1
static spheroid	803.1
microfluidic device	73.1

Values normalised to volume

before normalisation		after volume normalisation
1016.1	(already at 800 ul)	1016.1
803.1	X 1.3 (difference between 600 and 800 ul)	1070.797323
73.1	x7.5 (difference between 4.32 ml and 200 ul)	548.25

Values divided by cell number

cell number			72 hours
140000		monolayer	254.025
105000		static	356.9333
35000		microfluidic	548.25

Final value

	72 hours	SE
monolayer	254.025	2.25034
static	356.9333	11.5573
microfluidic	548.25	52.50793
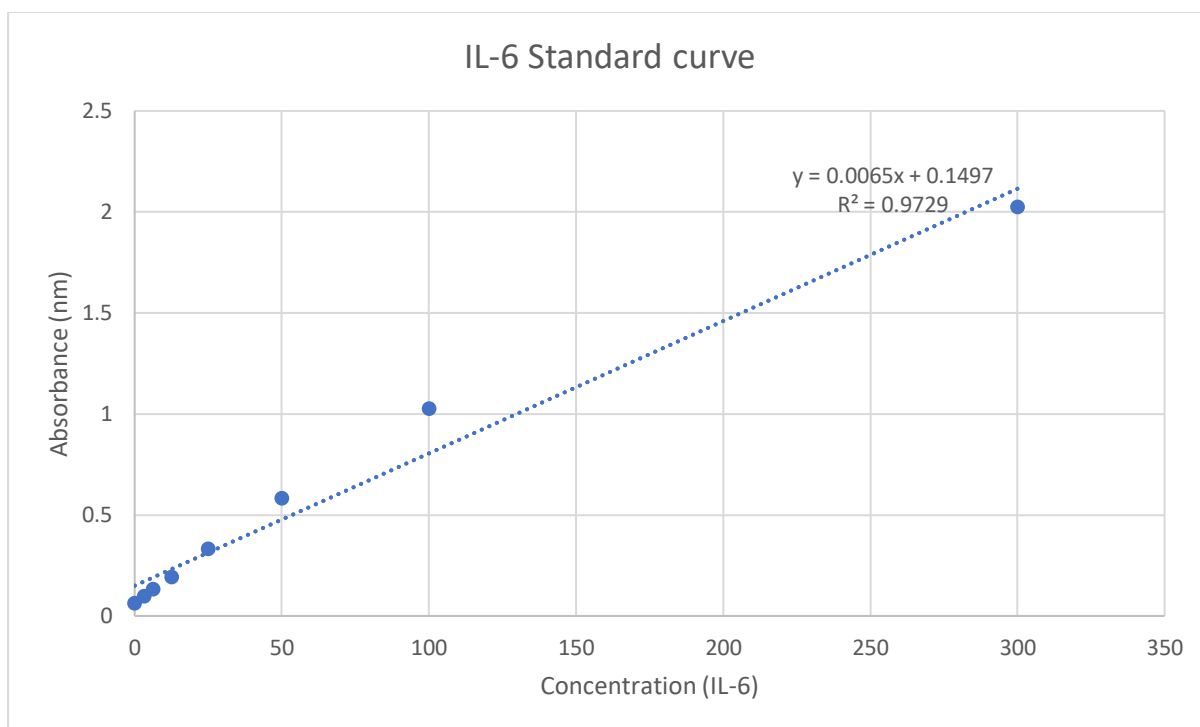
Figure 7.4: Standard curve of ELISA - IL-6 concentration and absorbance

A standard curve was produced for IL-6, using kit procedures, to determine the levels of absorbance for IL-6 present at different concentrations. This straight line equation was used to determine the unknown concentration of IL-6 present in effluent samples. Worked example shown below.

Raw data in duplicate

	n=1	n=1	n=2	n=2	n=3	n=3	Average	Std Dev	SE
monolayer media	2.04	2.02	2.22	2.04	6.16	4.5	3.163333	1.759973	0.586658
monolayer collagen	3.86	3.22	3.4	3.32	3.58	4.2	3.596667	0.371681	0.123894
monolayer matrigel	3.58	3.08	4.68	1.16	4.42	5.06	3.663333	1.426235	0.475412
static media	3.98	8.4	4.14	4.1	3.72	3.98	4.72	1.808779	0.602926
static collagen	3	4.8	3.62	6.8	5.26	7.18	5.11	1.669239	0.556413
static matrigel	5.78	7.58	5.56	6.4	9.28	7.3	6.983333	1.381675	0.460558
on-chip media	1.58	1.52	2.02	2.1	2.04	1.96	1.87	0.252587	0.084196
on-chip collagen	1.14	1.12	1.9	2.02	2.76	2.9	1.973333	0.762592	0.254197
on-chip matrigel	1.22	1.14	14.32	17.6	2.7	2.76	6.623333	7.339029	2.446343

Using the straight line equation to rearrange for X, raw data is -0.1479

|	n=1	n=1	n=2	n=2	n=3	n=3	Average	Std Dev	SE
monolayer	1.8903	1.8703	2.0703	1.8903	6.0103	4.3503	3.163333	1.759973	0.586658
monolayer	3.7103	3.0703	3.2503	3.1703	3.4303	4.0503	3.596667	0.371681	0.123894
monolayer	3.4303	2.9303	4.5303	1.0103	4.2703	4.9103	3.663333	1.426235	0.475412
static med	3.8303	8.2503	3.9903	3.9503	3.5703	3.8303	4.72	1.808779	0.602926
static colla	2.8503	4.6503	3.4703	6.6503	5.1103	7.0303	5.11	1.669239	0.556413
static matr	5.6303	7.4303	5.4103	6.2503	9.1303	7.1503	6.983333	1.381675	0.460558
on-chip me	1.4303	1.3703	1.8703	1.9503	1.8903	1.8103	1.87	0.252587	0.084196
on-chip co	0.9903	0.9703	1.7503	1.8703	2.6103	2.7503	1.973333	0.762592	0.254197
on-chip ma	1.0703	0.9903	14.1703	17.4503	2.5503	2.6103	6.623333	7.339029	2.446343

After the subtraction, to find normalised values for X, the data is divided by 0.0065

	n=1	n=1	n=2	n=2	n=3	n=3	Average	Std Dev	SE
monolayer media	290.8154	287.7385	318.5077	290.8154	924.6615	669.2769	3.163333	1.759973	0.586658
monolayer collagen	570.8154	472.3538	500.0462	487.7385	527.7385	623.1231	3.596667	0.371681	0.123894
monolayer matrigel	527.7385	450.8154	696.9692	155.4308	656.9692	755.4308	3.663333	1.426235	0.475412
static media	589.2769	1269.277	613.8923	607.7385	549.2769	589.2769	4.72	1.808779	0.602926
static collagen	438.5077	715.4308	533.8923	1023.123	786.2	1081.585	5.11	1.669239	0.556413
static matrigel	866.2	1143.123	832.3538	961.5846	1404.662	1100.046	6.983333	1.381675	0.460558
on-chip media	220.0462	210.8154	287.7385	300.0462	290.8154	278.5077	1.87	0.252587	0.084196
on-chip collagen	152.3538	149.2769	269.2769	287.7385	401.5846	423.1231	1.973333	0.762592	0.254197
on-chip matrigel	164.6615	152.3538	2180.046	2684.662	392.3538	401.5846	6.623333	7.339029	2.446343

The data was then normalised to volume before being graphed, multiplied by difference of sample volume - 200μl (all cell numbers were the same), such as x21.6 to get to 4.32ml for on-chip samples

	n=1	n=1	n=2	n=2	n=3	n=3	Average	Std Dev	SE
monolayer media	581.6308	575.4769	637.0154	581.6308	1849.323	1338.554	927.2718	541.5303	180.5101
monolayer collagen	1141.631	944.7077	1000.092	975.4769	1055.477	1246.246	1060.605	114.3633	38.12111
monolayer matrigel	1055.477	901.6308	1393.938	310.8615	1313.938	1510.862	1081.118	438.8416	146.2805
static media	1178.554	2538.554	1227.785	1215.477	1098.554	1178.554	1406.246	556.5473	185.5158
static collagen	877.0154	1430.862	1067.785	2046.246	1572.4	2163.169	1526.246	513.6121	171.204
static matrigel	1732.4	2286.246	1664.708	1923.169	2809.323	2200.092	2102.656	425.1309	141.7103
on-chip media	4752.997	4553.612	6215.151	6480.997	6281.612	6015.766	5716.689	839.3648	279.7883
on-chip collagen	3290.843	3224.382	5816.382	6215.151	8674.228	9139.458	6060.074	2534.152	844.7174
on-chip matrigel	3556.689	3290.843	47089	57988.69	8474.843	8674.228	21512.38	24388.16	8129.386

Chapter 8   References

Aaberg-Jessen, C., Nørregaard, A., Christensen, K., Pedersen, C., Andersen, C. & BW, K. (2013) Invasion of primary glioma- and cell line-derived spheroids implanted into corticostriatal slice cultures. *International Journal of Clinical and Experimental Patholgy*, 6(4), 546-560.

Abana, C., Bingham, B., Cho, J., Graves, A., Koyama, T., Pilarski, R., Chakravarthy, A. & Xia, F. (2017) IL-6 variant is associated with metastasis in breast cancer patients. *Plos One*, 1-15.

Acosta, M., Jiang, X., Huang, P., Cutler, K., Grant, C., Walker, G. & Gamcsik, M. (2014) A microfluidic device to study cancer metastasis under chronic and intermittent hypoxia. *Biomicrofluidics,* 8(5).

Ahmad, A., Ormiston-Smith, N. & Sasieni, P. (2015). Trends in the lifetime risk of developing cancer in Great Britain: comparison of risk for those born from 1930 to 1960. *British journal of cancer*, 112(5), 943–947

Alkatout, I., Wiedermann, M., Bauer, M., Wenners, A., Jonat, W. & Klapper, W. (2013) Transcription factors associated with epithelial-mesenchymal transition and cancer stem cells in the tumor centre and margin of invasive breast cancer. *Experimental and molecular pathology,* 94(1), 168-173.

Ara, T. & DeClerck, Y. (2010) Interleukin-6 in Bone Metastasis and Cancer Progression. *European Journal of Cancer,* 46(7), 1223-1231.

Ashizawa, T., Okada, R., Suzuki, Y., Takagi, M., Yamazaki, T., Sumi, T., Aoki, T., Ohnuma, S. & Aoki, T. (2005) Clinical significance of interleukin-6 (IL-6) in the spread of gastric cancer: role of IL-6 as a prognostic factor. *Gastric Cancer*, 8(2), 124-131.

Au, S., Storey, B., Moore, J., Tang, Q., Chen, Y., Javaid, S., Sarioglu, A., Sullivan, R., Madden, M., O'Keefe, R., Haber, D., Maheswaran, S., Langenau, D., Stott, S. & Toner, M. (2016) Clusters of circulating tumor cells traverse capillary-sized vessels. *Proceedings of the National Academy of Sciences of the United States of America*, 113(18), 4947-4952.

Avraham-Chamik, L., Elad, D., Zaretsky, U., Kloog, Y., Jaffa, A. & Grisaru, D. (2013) Fluid-Flow Induced Wall Shear Stress and Epithelial Ovarian Cancer Peritoneal Spreading. *Plos One*. 4(8) e60965

Ayuso, J., Truttschel, R., Gong, M., Humayun, M., Virumbrales-Munoz, M., Vitek, R., Felder, M., Gillies, S., Sondel, P., Wisinski, K., Patankar, M., Beebe, D. & Skala, M. (2019) Evaluating natural killer cell cytotoxicity against solid tumors using a microfluidic model. *OncoImmunology,* 8(3).

Babahosseini, H., Strobl, J. & Agah, M. (2017) Microfluidic Iterative Mechanical Characteristics (iMECH) Analyzer for Single-Cell Metastatic Identification. *Analytical Methods,* 5(9), 847-855.

Bardella, C., Pollard, P. & Tomlinson, I. (2011) SDH mutations in cancer. *Biochimica et Biophysica Acta (BBA) - Bioenergetics*, 1807(11), 1432–1443.

Barsoum, I., Smallwood, C., Siemens, D. & Graham, C. (2013) A mechanism of hypoxia-mediated escape from adaptive immunity in cancer cells. *Cancer Research*, 74(3), 665-674.

Bartsch, J., Staren, E. & Appert, H. (2003) Matrix metalloproteinase expression in breast cancer. *Journal of Surgical Research,* 110(2), 383-392.

Bender, B. F., Aijian, A. P. & Garrell, R. L. (2016) Digital microfluidics for spheroid-based invasion assays. *Lab Chip*, 16(8), 1505-13.

Bernhart, E., Damm, S., Wintersperger, A., DeVaney, T., Zimmer, A., Raynham, T., Ireson, C. & Sattler, W. (2013) Protein kinase D2 regulates migration and invasion of U87MG glioblastoma cells in vitro. *Experimental Cell Research*, 319(13), 2037-2048.

Bersini, S., Jeon, J. S., Dubini, G., Arrigoni, C., Chung, S., Charest, J. L., Moretti, M. & Kamm, R. D. (2014) A microfluidic 3D in vitro model for specificity of breast cancer metastasis to bone. *Biomaterials*, 35(8), 2454-61.

Bersini, S., Miermont, A., Pavesi, A., Kamm, R., Thiery, J. P., Moretti, M. & Adriani, G. (2018) A combined microfluidic-transcriptomic approach to characterize the extravasation potential of cancer cells. *Oncotarget, 9*(90), 36110-36125.

Bhave, M., Hassanbhai, A., Anand, P., Luo, K. & Teoh, S. (2015) Effect of Heat-Inactivated Clostridium sporogenes and Its Conditioned Media on 3-Dimensional Colorectal Cancer Cell Models. *Scientific Reports*, 5(15681).

Blaha, L., Zhang, C., Cabodi, M. & Wong, J. (2017) A Microfluidic Platform for Modeling Metastatic Cancer Cell Matrix Invasion. *Biofabrication,* 9(4).

Boyd, V., Cholewa, O. & Papas, K. (2008) Limitations in the Use of Fluorescein Diacetate/Propidium Iodide (FDA/PI) and Cell Permeable Nucleic Acid Stains for Viability Measurements of Isolated Islets of Langerhans. *Current trends in Biotechnology and Pharmacology,* 2(2), 6-8.

Brabletz, T., Kalluri, R., Nieto, M. & Weinberg, R. (2018) EMT in cancer. *Nature Review: Cancer,* 18, 128-134.

Brem, S., Cotran, R. & Folkman, J. (1972) Tumor Angiogenesis: A Quantitative Method for Histologic Grading. *Journal of the National Cancer Institute*, 48, 347-356.

Browning, L., Patel, M., Horvath, E., Tawara, K. & Jorcyk, C. (2018) IL-6 and ovarian cancer: inflammatory cytokines in promotion of metastasis. *Cancer Management and Research*, 10, 6685—6693.

Cai, Y., Wu, J., Xu, S. X. & Li, Z. Y. (2013) A Hybrid Cellular Automata Model of Multicellular Tumour Spheroid Growth in Hypoxic Microenvironment. *Journal of Applied Mathematics,* 10. 519895.

Carreau, A., El Hafny-Rahbi, B., Matejuk, A., Grillon, C. & Kieda, C. (2011) Why is the partial oxygen pressure of human tissues a crucial parameter? Small molecules and hypoxia. *Journal of Cellular and Molecular medicine*, 15(6), 1239-1253.

Cezeaux JL, Austin V, Hosseinipour MC, Ward KA &., Z. S. (1991) The effects of shear stress and metastatic phenotype on the detachment of transformed cells. *Biorheology*, 28(3-4), 195-205.

Chafe, S. & Dedhar, s. (2015) Carving out its niche: A role for carbonic anhydrase IX in pre-metastatic niche development. *OncoImmunology*, 4(12), 1048955.

Chafe, S., Lou, Y., Sceneay, J., Vallejo, M., Hamilton, M., McDonald, P., Bennewith, K., Moller, A. & Dedhar, S. (2015) Carbonic anhydrase IX promotes myeloid-derived suppressor cell mobilization and establishment of a metastatic niche by stimulating G-CSF production. *Cancer Research*, 75(6), 996-1008.

Chandrasekaran, S. & King, M. R. (2012) Gather Round: In vitro tumor spheroids as improved models of in vivo tumors. 109 editions.: *Journal of Bioengineering & Biomedical Science,* 2: e109

Chatterjee, S. & Burns, T. (2017) Targeting Heat Shock Proteins in Cancer: A Promising Therapeutic Approach. *International Journal of Molecular science*, 18(9), 1987.

Chaw, K., Manimaran, M., Tay, F. & Swaninathan, S. (2007) Matrigel coated polydimethylsiloxane based microfluidic devices for studying metastatic and non-metastatic cancer cell invasion and migration. *Biomedical Microdevices,* 9(4), 597–602.

Chen, J., Imanaka, N., Chen, J. & Griffin, J. (2010) Hypoxia potentiates Notch signaling in breast cancer leading to decreased E-cadherin expression and increased cell migration and invasion. *British Journal of Cancer*, 102(2), 351–360

Chen, M., Shah, M., Shelper, T., Nazareth, L., Barker, M., Velasquez, J., Ekberg, J., Vial, M. & St John, J. (2019) Naked liquid marbles: a robust threedimensional low-volume cell culturing system. *Applied Materials and Interfaces,* 11 (10), 9814-9823.

Chen, Y., Gao, D., Liu, H., Lin, S. & Jiang, Y. (2015) Drug cytotoxicity and signaling pathway analysis with three-dimensional tumor spheroids in a microwell-based microfluidic chip for drug screening. *Anal Chim Acta*, 898, 85-92.

Cheng, Y., Chen, Y., Brien, R. & Yoon, E. (2016) Scaling and automation of a high-throughput single-cell-derived tumor sphere assay chip. *Lab on a chip*, 16(19), 3708-17.

Choi, Y., Hyun, E., Seo, J., Blundell, C., Kim, H., Lee, E., Lee, S., Moon, A., Moon, W. & Huh, D. (2015) A microengineered pathophysiological model of early-stage breast cancer. *Lab on a chip,* 16(15), 3350-7.

Christensen, M. (2019) *Modelling, design and characterisation of liver-on-chip models*. Chemistry PhD University of Hull.

Christoffersson, J., Meier, F., Kempf, H., Schwanke, K., Coffee, M., Beilmann, M., Zweigerdt, R. & Mandenius, C. (2018) A Cardiac Cell Outgrowth Assay for Evaluating Drug Compounds Using a Cardiac Spheroid-on-a-Chip Device. *Bioengineering (Basel),* 5(2), 36.

Corey, J., Gertz, C., Sutton, T., Chen, Q., Mycek, K., Wang, B., Martin, A., Johnson, S. & Feldman, E. (2010) Patterning N-type and S-type Neuroblastoma Cells with Pluronic F108 and ECM Proteins. *Journal of Biomedical Materials Research Part A*, 93(2), 673-686

Cosma, S., Cimpean, A. & Raica, M. (2015) The Story of MCF-7 Breast Cancer Cell Line: 40 years of Experience in Research. *Anticancer research*, 35(6).

Cox, T., Bird, D., Baker, A., Barker, H., Ho, M., Lang, G. & Erler, J. (2013) LOX-mediated collagen crosslinking is responsible for fibrosis-enhanced metastasis. *Cancer Research*, 73(6), 1721–1732.

Cras, J., Rowe-Taitt, A., Nivens, D. & Ligler, F. (1999) Comparison of chemical cleaning methods of glass in preparation for silanization. Biosensors and Bioelectronics, 14(8-9), 683-688.

CRUK (1981) Spheroids in Cancer Research. *Cancer Research,* 41 (7).

Das, T., Meunier, L., Barbe, L., Provencher, D., Guenat, O., Gervais, T. & Mes-Masson, A. M. (2013) Empirical chemosensitivity testing in a spheroid model of ovarian cancer using a microfluidics-based multiplex platform. *Biomicrofluidics*, 7(1), 11805.

David, J. & Rajasekaran, A. (2012) Dishonorable Discharge: The Oncogenic Roles of Cleaved E-cadherin Fragments. *Cancer Research,* 72(12), 2917-2923.

Daw, R. & Finkelstein, J. (2006) Introduction Lab on a chip. *Nature*. 442, (7071) 367

Eaton, S., Roche, S., Hurtado, M., Oldknow, K., Farguharson, C., Gillingwater, T. & Wishart, T. (2013) Total Protein Analysis as a Reliable Loading Control for Quantitative Fluorescent Western Blotting. *Plos One*, 8(8), 72457.

Edmondson, R., Broglie, J., Adcock, A. & Yang, L. (2014) Three-Dimensional Cell Culture Systems and Their Applications in Drug Discovery and Cell-Based Biosensors. Assay *Drug Development Technology,* 12(4), 207–218

Egginton, S. (2011) In Vivo shear stress response. *Biochemical Society Transactions*, 39(6), 1633-1638.

Fernekorn, U., Hampl, J., Weise, F., Klett, M., Läffert, A., Friedel, K. & Schober, A. (2015) Microfluidic 3D HepG2 cell culture: Reproducing hepatic tumor gene and protein expression in in vitro scaffolds. *Engineering in Life Sciences*, 15(3), 340-350.

Gale, B., Jafek, A., Lambert, C., Goenner, B., Moghimifam, H., Nze, U. & Kamarapu, S. (2018) A Review of Current Methods in Microfluidic Device Fabrication and Future Commercialization Prospects. *Inventions,* 3(60), 1-25.

Geng, F., Zhu, W., Anderson, R., Leber, B. & Andrews, D. (2012) Multiple post-translational modifications regulate E-cadherin transport during apoptosis. *The Journal of Cell Science*, 125, 2615-2625.

GL., S. (2014) Oxygen sensing, hypoxia-inducible factors, and disease pathophysiology. *Annual Review of Pathology*, 9, 47–71

Gong, X., Lin, C., Cheng, J., Su, J., Zhao, J., Zhao, H., Liu, T., Wen, X. & Zhao, P. (2015) Generation of multicellular tumour spheroids with microwell based agarose scaffolds for drug testing. *Plos One*. 10 (6), e0130348

Greer, S., Metcalf, J., Wang, Y. & Ohh, M. (2012) The updated biology of hypoxia-inducible factor. *The EMBO journal*, 31(11), 2448-60.

Grimes, D., Kelly, C., Bloch, K. & Partridge, M. (2014) A method for estimating the oxygen consumption rate in multicellular tumour spheroids. *Royal Society*, 11(92)

Günther, W., Pawlak, E., Damasceno, R., Arnold, H. & Terzis, A. (2003) Temozolomide induces apoptosis and senescence in glioma cells cultured as multicellular spheroids. *British Journal of Cancer,* 88(3), 463–469.

Halldorsson, S., Lucumi, E., Gomez-Sjoberg, R. & Fleming, R. (2015) Advantages and challenges of microfluidic cell culture in polydimethylsiloxane devices. *Biosensors and Bioelectronics*, 63, 218-231.

Hamilton, G. (1998) Multicellular Spheroids as an in vitro tumour model. *Cancer Letters*, 131(11), 29-34.

Han, C., Takayama & Park (2015) Formation and manipulation of cell spheroids using a density adjusted PEG/DEX aqueous two phase system. *Scientific Reports*, 5, 11891.

Hao, S., Ha, L., Cheng, G., Wan, Y., Xia, Y., Sosnoski, D., Mastro, A. & Zheng, S. (2018) A Spontaneous 3D Bone-On-a-Chip for Bone Metastasis Study of Breast Cancer Cells. *Nano Micro Small*, 14(12).

Health, National. Institute. (2015) gemcitabine hydrochloride National Cancer Institute.November].

Heerboth, S., Housman, G., Leary, M., Longacre, M., Byler, S., Lapinska, K., Willbanks, A. & Sarkar, S. (2015) EMT and tumor metastasis. *Clinical Translation Medicine*, 4(6).

Hesse, E., Hefferan, T., Tarara, J., Haasper, C., Meller, R., Krettek, C., Lu, L. & Yaszemski, M. (2010) Collagen type I hydrogel allows migration, proliferation, and osteogenic differentiation of rat bone marrow stromal cells. *Journal of Biomedical Materials Research*, 94(2), 442-449.

Hockemeyer, K., Janetopoulos, C., Terekhov, A., Hofmeister, W., Vilgelm, A., Costa, L., Wikswo, J. P. & Richmond, A. (2014) Engineered three-dimensional microfluidic device for interrogating cell-cell interactions in the tumor microenvironment. Biomicrofluidics, 8(4), 044105.

Hoeben, A., Landuyt, B., Highley, M., Wildiers, H., Oosterom, A. & De Bruijn, E. (2004) Vascular Endothelial Growth Factor and Angiogenesis. *Pharmacological Reviews*, 56(4).

Holden, P. & Horton, W. (2009) Crude subcellular fractionation of cultured mammalian cell lines. *BMC Research Notes*, 2(243).

Holen, I., Speirs, V., Morrissey, B. & Blyth, K. (2017) In vivo models in breast cancer research: progress, challenges and future directions. *Disease models and mechanisms*, 10(4), 359–371.

Hollborn, M., Stathopoulos, C., Steffen, A., Wiedemann, P., Kohen, L. & Bringmann, A. (2007) Positive feedback regulation between MMP-9 and VEGF in human RPE cells. *Invest Ophthalmol Vis Sci.*, 48(9), 4360-7.

Holliday, D. & Speirs, V. (2011) Choosing the right cell line for breast cancer research. Breast *Cancer Research*, 13 (4), 215.

Hongzhou, H., Ying, D., Xiuzhi, S. S. & Thu, A. N. (2013) Peptide Hydrogelation and Cell Encapsulation for 3D Culture of MCF-7 Breast Cancer Cells. *Plos One*, 8(3), 59482.

Horning, J., SK, Vijayaraghavalu, SDimitrijevic, SVasir, JKJain, TKPanda, JK, Labhasetwar, V (2008) 3-D tumor model for in vitro evaluation of anticancer drugs. *Molecular Pharmacuetics,* 5(5).

Hsiao, A., Toisawa, Y.-s., Tung, Y.-C., Sud, S., Taichman, R., Pienta, K. & Takayama, S. (2009) Microfluidic system for formation of PC-3 prostate cancer co-culture spheroids. *Biomaterials*, 30(16), 3020-3027.

Iglesias, J., Beloqui, I., Garcia-Garcia, F., Leis, O., Vazquez-Martin, A., Eguiara, V., Cufi, S., Pavon, A., Menendez, J., Dopazo, J. & Martin, A. (2013) Mammosphere Formation in Breast Carcinoma Cell Lines Depends upon Expression of E-cadherin. *Plos One,* 8(10), e77281.

Iliescu, C., Taylor, H., Avram, M., Miao, J. & Franssila, S. (2012) A practical guide for the fabrication of microfluidic devices using glass and silicon. *Biomicrofluidics*, 6(1), 16505-1650516.

Imamura, Y., Mukohara, T., Shimono, Y., Funakoshi, Y., Chayahara, N., Toyoda, M., Kiyota, N., Takao, S., Kono, S., Nakatsura, T. & Minami, H. (2015) Comparison of 2D- and 3D-culture models as drug-testing platforms in breast cancer. *Oncol Rep*, 33(4), 1837-43.

Imaninezhad, M., Hill, L., Kolar, G., Vogt, K. & Zustiak, S. (2019) Templated Macroporous Polyethylene Glycol Hydrogels for Spheroid and Aggregate Cell Culture. *Bioconjugate Chemistry*, 30(1), 34-46.

Ip, C. K., Li, S. S., Tang, M. Y., Sy, S. K., Ren, Y., Shum, H. C. & Wong, A. S. (2016) Stemness and chemoresistance in epithelial ovarian carcinoma cells under shear stress. *Scientific Reports,* 6, 26788.

Irimia, D. & Toner, M. (2009) Spontaneous migration of cancer cells under conditions of mechanical confinement. *Integrative Biology*, 1, 506-512.

Ivascu A &., K. M. (2007) Diversity of cell-mediated adhesions in breast cancer spheroids. *International Journal of Oncology*, 31(6), 1403-1413.

Jabłońska-Trypuć, A., Matejczyk, M. & Rosochacki, S. (2016) Matrix metalloproteinases (MMPs), the main extracellular matrix (ECM) enzymes in collagen degradation, as a target for anticancer drugs. *Journal of Enzyme Inhibition and Medicinal Chemistry*. 31.

Jain RK, Martin JD & T, S. (2014) The role of mechanical forces in tumor growth and therapy. *Annual Review of Biomedical Engineering*.16, 321-346.

Jeanes, A., Gottardi, C. & Yap, A. (2008) Cadherins and cancer: how does cadherin dysfunction promote tumor progression? *Oncogene*, 27(55), 6920-6929.

Jiang, T., Munguia-Lopez, J., Flores-Torres, S., Grant, J., Vijayakumar, S., De Leon-Rodriguez, A. & Kinsella, J. (2018) Bioprintable Alginate/Gelatin Hydrogel 3D In Vitro Model Systems Induce Cell Spheroid Formation. *Journal of Visualized Experiments* (137).

Johnson, S., Chen, H. & Lo, P. (2013) In vitro Tumorsphere Formation Assays. *Bio-protocol*, 3(3), 325.

Jones KH & JA, S. (1985) An improved method to determine cell viability by simultaneous staining with fluorescein diacetate-propidium iodide. *The Journal of histochemistry and cytochemistry: official journal of the histochemistry society*, 3(1), 77-79.

Justus, C., Leffler, N., Echevarria, M. & Yang, L. (2014) In vitro Cell Migration and Invasion Assays. *Journal of Visualized Experiments* (88).

Kangning R, Zhou J & H, W. (2012) Materials for Microfluidic Chip Fabrication. *Accounts of Chemical Research*, 46(11), 2396- 2406.

Katt, M., Placone, A., Wong, A., Xu, Z. & Searson, P. (2016) In Vitro Tumor Models: Advantages, Disadvantages, Variables, and Selecting the Right Platform. *Frontiers in Bioengineering and Biotechnology*, 4(12).

Khaitan, D., Chanda, S., Arya, M. & Dawarkatha, B. (2006) Establishment and characterization of multicellular spheroids from a human glioma cell line; Implications for tumor therapy. *Journal of Translational Medicine*. 4, (12). 1-13

Khan, Z. & Vanapalli, S. (2013) Probing the mechanical properties of brain cancer cells using a microfluidic cell squeezer device. *Biomicrofluidics*, 7(1) 11806.

Khawar, I., Park, J., Jung, F., Lee, M., Chang, S. & Hyo-Jeung, K. (2018) Three Dimensional Mixed-Cell Spheroids Mimic Stroma-Mediated Chemoresistance and Invasive Migration in hepatocellular carcinoma. *Neoplasia*, 20(8), 800-812.

Kim, W.-T. & Ryu, C.-J. (2017) Cancer stem cell surface markers on normal stem cells. *BMB reports,* 50(6), 285–298.

Kleinman, H. & Martin, G. (2005) Matrigel: basement membrane matrix with biological activity. *Seminars in Cancer Biology*, 15(5), 378-86.

Kraning Rush C, Califano JP & Reinhart-King C (2012) Cellular Traction Stresses Increase with Increasing Metastatic Potential. *Plos One*. 7(2), e32572

Kuijper, A., van der Groep, P., van der Wall, E. & van Diest, P. J. (2005) Expression of hypoxia-inducible factor 1 alpha and its downstream targets in fibroepithelial tumors of the breast. *Breast Cancer Research*, 7(5), 808-818.

Kulasinghe, A., Zhou, J., Kenny, L., Papautsky, I. & Punyadeera, C. (2019) Capture of Circulating Tumour Cell Clusters Using Straight Microfluidic Chips. *Cancers*, 11(1), 89.

Kumar S & V, W. (2009) Mechanics, malignancy, and metastasis: The force journey of a tumor cell. *Cancer and Metastasis Review*, 28(1), 113-127.

Kuo, C. T., Chiang, C. L., Chang, C. H., Liu, H. K., Huang, G. S., Huang, R. Y., Lee, H., Huang, C. S. & Wo, A. M. (2014) Modeling of cancer metastasis and drug resistance via biomimetic nano-cilia and microfluidics. *Biomaterials*, 35(5), 1562-71.

Kwak, B., Lee, Y., Lee, J., Lee, S. & Lim, J. (2018) Mass fabrication of uniform sized 3D tumor spheroid using high-throughput microfluidic system. *Journal of Controlled Release*, 275, 201-207.

Kwapiszewska, K., Michalczuk, A., Rybka, M., Kwapiszewski, R. & Brzozka, Z. (2014) A microfluidic-based platform for tumour spheroid culture, monitoring and drug screening. *Lab Chip*, 14(12), 2096-104.

Kühlbach, C., Luz, S., Baganz, F., Hass, V. & Mueller, M. (2018) A Microfluidic System for the Investigation of Tumor Cell Extravasation. *Bioengineering*, 5(2).

Labelle, M. & Hynes, R. (2012) The initial hours of metastasis: the importance of cooperative host-tumor cell interactions during hematogenous dissemination. *Cancer Discovery*, 2(12), 1091–1099.

Lake, M., Narciso, C., Cowdrick, K., Storey, T., Zhang, Z., Zartman, J. & Hoelzle, D. (2015) Microfluidic device design, fabrication, and testing protocols. *Nature*, 1-26.

Lee, B. H. & Sung, M. M. (2005) Effect of Island Size on the Packing Density in the Early Stages of Alkylsilane-Based Monolayer Self Assembly. *Bulletin of the Korean Chemical Society* 26, 127-130.

Lee, C., Boss, M. & Dewhirst, M. (2014) Imaging Tumor Hypoxia to Advance Radiation Oncology. *Antioxidants and redox signalling*, 21(2), 313-337.

Lee, D. & Cha, C. (2018) The Combined Effects of Co-Culture and Substrate Mechanics on 3D Tumor Spheroid Formation within Microgels Prepared via Flow-Focusing Microfluidic Fabrication. *Pharmaceutics*, 10(4), 229.

Lee, J., Kim, S., Khawar, I., Jeong, S., Chung, S. & Kuh, H. (2018) Microfluidic co-culture of pancreatic tumor spheroids with stellate cells as a novel 3D model for investigation of stroma-mediated cell motility and drug resistance. *Journal of Experimental and Clinical Cancer Research*, 37(1), 4.

Lee, S., Jilani, S., Nikolova, G., Carpizo, D. & Iruela-Arispe, M. (2005) Processing of VEGF-A by matrix metalloproteinases regulates bioavailability and vascular patterning in tumors. *Journal of Cell Biology,* 169(4).

Li, X. J., Valadez, A. V., Zuo, P. & Nie, Z. (2012) Microfluidic 3D cell culture: potential application for tissue-based bioassays. *Bioanalysis,* 4(12), 1509-25.

Liang, C., Park, A. & Guan, J.-L. (2007) In vitro scratch assay: a convenient and inexpensive method for analysis of cell migration in vitro. *Nature Protocol*, 2 pages, 329 – 333.

Lim, W., Hoang, H., You, D., Han, J., Lee, J., Kim, S. & Park, S. (2018) Formation of size-controllable tumour spheroids using a microfluidic pillar array (µFPA) device. *The Analyst*, 143(23), 5841-5848.

Lima, J., Nofech-Mozes, F., Bayani, J. & Bartlett, J. (2016) EMT in Breast Carcinoma—A Review. *Journal of Clinical Medicine*, 5(7), 65.

Liu, W. S., J.Du, X.Zhou, Y.Li, Y.Li, R.Lyu, L.He, Y.Hao, J. Ben, J.Wang, W.Shi, H.Wang, Q. (2019) AKR1B10 Promotes Brain Metastasis of Lung Cancer Cells in a Multi-Organ Microfluidic Chip Model. *Acta Biomaterialia*, 27, 195-208.

Liu, Z., Lee, Y., Jang, J., Li, Y., Han, X., Yokoi, K., Ferrari, M., Zhou, L. & Qin, L. (2015) Microfluidic cytometric analysis of cancer cell transportability and invasiveness. *Scientific Reports,* 5, 14272.

Loessner, D., Stok, K., Lutolf, M., Hutmacher, D., Clements, J. & Rizzi, S. (2010) Bioengineered 3D platform to explore cell-ECM interactions and drug resistance of epithelial ovarian cancer cells. *Biomaterials*, 31(32), 8494-506.

Lu, H., Forbes, R. & Verma, A. (2002) Hypoxia-inducible factor 1 activation by aerobic glycolysis implicates the Warburg effect in carcinogenesis. *The Journal of Biological Chemistry*, 277(26), 23111-23115.

Lu, X. & Kang, Y. (2010) Hypoxia and Hypoxia-Inducible Factors: Master Regulators of Metastasis. *Clinical Cancer Research*, 16(24).

Ma, Y. M., K. Lidan You, L. Sun, Y (2018) A review of microfluidic approaches for investigating cancer extravasation during metastasis. *Microsystems and Nanoengineering*.

Ma, J. Y., Zhang, X., Liu, Y., Yu, H. B., Liu, L. Q., Shi, Y., Li, Y. F. & Qin, J. H. (2016) Patterning hypoxic multicellular spheroids in a 3D matrix - a promising method for anti-tumor drug screening. *Biotechnology Journal*, 11(1), 127-134.

MacGowan, A., Rogers, C. & Bowker, K. (2001) In Vitro Models, In Vivo Models, and Pharmacokinetics: What Can We Learn from In Vitro Models? *Clinical Infectious Diseases*, 33(Supplement 3), S214-S220.

Mak, M., Reinhart-King, C. & Erickson, D. (2013) Elucidating mechanical transition effects of invading cancer cells with a subnucleus-scaled microfluidic serial dimensional modulation device. *Lab on a Chip*, 13, 340-348.

Marimuthu, M., Rousset, N., St-George-Robillard, A., Lateef, M., Ferland, M., Mes-Masson, A. & Gervais, T. (2018) Multi-size spheroid formation using microfluidic funnels. *Lab on chip*, 18(2) 304-314.

Masoud, G. & Li, W. (2015b) HIF-1α pathway: role, regulation and intervention for cancer therapyHIF-1α pathway: role, regulation and intervention for cancer therapy. *Acta Pharmaceutica Sinica B*, 5(5), 378–389.

Masson, N. & Ratcliffe, P. (2014) Hypoxia signaling pathways in cancer metabolism: the importance of co-selecting interconnected physiological pathways. *Cancer Metabolism*, 2, 3.

McDonald, P., Chafe, S. & Dedhar, S. (2016) Overcoming Hypoxia-Mediated Tumor Progression: Combinatorial Approaches Targeting pH Regulation, Angiogenesis and Immune Dysfunction. *Frontiers in cell and developmental biology*, 4(27).

McKeown, S. (2014) Defining normoxia, physoxia and hypoxia in tumours—implications for treatment response. *British Journal of Radiology*, 87(1035), 20130676.

Mehlen, P. & Puisieux, A. (2006) Metastasis: a question of life or death. *Nature Reviews cancer*, 6, 449-458.

Mehta, G., Hsiao, A. Y., Ingram, M., Luker, G. D. & Takayama, S. (2012) Opportunities and Challenges for use of Tumor Spheroids as Models to Test Drug Delivery and Efficacy. *Journal of Control Release*. 164(2), 192-204.

Mi, S. D., Z. Yuanyuan, X. Wu, Z. Qian, X. Zhang, M. Sun, W. (2016) Microfluidic co-culture system for cancer migratory analysis and anti-metastatic drugs screening. *Scientific Reports* (6), 1-11.

Michael, I., Kumar, S., Oh, J., Kim, D., Kim, J. & Cho, Y. (2018) Surface-Engineered Paper Hanging Drop Chip for 3D Spheroid Culture and Analysis. *ACS Applied Materials & Interfaces*, 10(40), 33839–33846.

Miller, M., Robison, P., Wagner, C. & O'Shannessy, D. (2018) The Parsortix™ Cell Separation System—A Versatile Liquid Biopsy Platform. *Cytometry*, 1-6.

Mina, S., Huang, P., Murray, B. & Mahler, G. (2017) The role of shear stress and altered tissue properties on endothelial to mesenchymal transformation and tumor-endothelial cell interaction. *Biomicrofluidics*, 4(11) 044104.

Mitchell, M. & King, M. (2013) Fluid Shear Stress Sensitizes Cancer Cells to Receptor-Mediated Apoptosis via Trimeric Death Receptors. *New Journal of Physics*, 15 015008.

Monazzam A, Razifar P, Lindhe O, Josephsson R, Langstrom B & M, B. (2005) A new, fast and semi-automated size determination method (SASDM) for studying multicellular tumor spheroids. *Cancer Cell International*, 5(32) 1-16.

Mueller-Klieser W, Freyer JP & RM, S. (1986) Influence of glucose and oxygen supply conditions on the oxygenation of multicellular spheroids. *British Journal of Cancer*, 53(3), 345–353.

Munson, J. & Shieh, A. (2014) Interstitial fluid flow in cancer: implications for disease progression and treatment. *Journal of Cancer Management and Research*, 6, 317–328.

Murphy, R. (2016) *Cancer Registration Statistics*, England: 2014. Found at https://www.ons.gov.uk/peoplepopulationandcommunity/healthandsocialcare/conditionsanddiseases/bulletins/cancerregistrationstatisticsengland/2014

Muthna, D., Tomsik, P., Havelek, R., Kohlerova, R., Kasilingam, V., Cermakova, E., Stibal, D., Rezacova, M. & Suss-Fink, G. (2016) In-vitro and in-vivo evaluation of the anticancer activity of diruthenium-2, a new trithiolato arene ruthenium complex (eta(6)-p-MeC6H4Pri)(2)Ru-2(mu-S-p-C6H4OH)(3) Cl. *Anti-Cancer Drugs*, 27(7), 643-650.

Nagaraju, S., Truong, D., Mouneimne, G. & Nikkhah, M. (2018) Microfluidic Tumor-Vascular Model to Study Breast Cancer Cell Invasion and Intravasation. *Advanced Healthcare Materials*, 9(7) 1701257.

Noman, M., Hasmim, M., Messai, Y., Terry, S., Kieda, C., Janji, B. & Chouaib, S. (2015) Hypoxia: a key player in antitumor immune response. A Review in the Theme: Cellular Responses to Hypoxia. *American journal of cell physiology*, 309(9) 569-579.

Nunes, A., Barros, A., Costa, E., Moreria, A. & Correia, I. (2018) 3D tumor spheroids as in vitro models to mimic in vivo human solid tumors resistance to therapeutic drugs. *Biotechnology and Bioengineering*. 116(1), 206-226.

Obermayr, F., Martischnegg, F., Agreiter, C., Pecha, N., Speiser, P., Helmy-Bader, S., Danzinger, S., Krainer, M., Singer, C. & Zeillinger, R. (2017) Efficient leukocyte depletion by a novel microfluidic platform enables the molecular detection and characterization of circulating tumor cells. *Oncotarget*, 9(1), 812-823.

Olive, P., Vikse, C. & Trotter, M. (1992) Measurement of oxygen diffusion distance in tumor cubes using a fluorescent hypoxia probe. *International journal of radiation oncology, biology, physics*, 22(3) 397- 402.

Ong, L., Islam, A., Dasgupta, R., Iyer, N., Leo, H. & Toh, Y. (2017) A 3D printed microfluidic perfusion device for multicellular spheroid cultures. *Biofabrication*, 4(9) 045005.

Onishi, M., Ichikawa, T., Kurozumi, K. & Date, I. (2011) Angiogenesis and Invasion in Glioma. *Brain Tumour Pathology*, 28(1), 13-24.

Organisation, World. Health. (2018) Newsroom, Factsheet*Cancer. Accessed:* August 2019, available at: https://www.who.int/news-room/fact-sheets/detail/cancer.

Palazon, A., Goldrath, A., Nizet, V. & Johnson, R. (2014) HIF Transcription Factors, Inflammation, and Immunity. *Immunity*, 41(4), 518-528.

Panisova, E., Kerv, M., Sedlakova, O., Brisson, L., Debreova, M., Sboarina, M., Sonveaux, P., Pastorekova, S. & Svastova, E. (2017) Lactate stimulates CA IX expression in normoxic cancer cells. *Oncotarget*, 8(44), 77819-77835.

Park, S., Eom, S., Hong, H., Seong, J., Seong, J., Bum, C., Hyung, W. & Dong, S. (2019) Reconstruction of in vivo-like in vitro model: Enabling technologies of microfluidic systems for dynamic biochemical/mechanical stimuli. *Microelectronic Engineering*, 203-204, 6-24.

Patra, B., Peng, Y. S., Peng, C. C., Liao, W. H., Chen, Y. A., Lin, K. H., Tung, Y. C. & Lee, C. H. (2014) Migration and vascular lumen formation of endothelial cells in cancer cell spheroids of various sizes. *Biomicrofluidics*, 8(5), 052109.

Peela, N., Barrientos, E., Truong, D., Mouneimne, G. & Nikkhah, M. (2017) Effect of suberoylanilide hydroxamic acid (SAHA) on breast cancer cells within a tumor–stroma microfluidic model. *Integrative Biology,* 9(12), 988-999.

Percival, R., Marsh, P., Devine, D., Rangarajan, M., Aduse-Opoku, J., Shepherd, P. & MA, C. (1999) Effect of Temperature on Growth, Hemagglutination, and Protease Activity of Porphyromonas gingivalis. *Infection and Immunity*, 67(4), 1917–1921.

Perez, T. & Nelson, W. (2004) Cadherin Adhesion: Mechanisms and Molecular Interactions. *Handbook of Experimental Pharmacology*, 165, 3-21.

Plunkett W, Huang P, Xu YZ, Heinemann V, Grunewald R &., G. V. (1995) Gemcitabine: metabolism, mechanisms of action, and self-potentiation. *Seminars in Oncology*, 22(4), 3-10.

Raghavan, S., Mehta, P., Horst, E., Ward, M., Rowley, K. & Mehta, G. (2016) Comparative analysis of tumor spheroid generation techniques for differential in vitro drug toxicity. *Oncotarget,* 7(13), 16948-16961.

Ramis, G., Thomas-Moya, E., Fernandez de Mattos, S., Rodriguez, J. & Villalonga, P. (2012) EGFR Inhibition in Glioma Cells Modulates Rho Signaling to Inhibit Cell Motility and Invasion and Cooperates with Temozolomide to Reduce Cell Growth. *Plos One*.7(6)e38770

Rankin, E. & Giaccia, A. (2016) Hypoxic control of metastasis. *Science*, 352(6282), 175

Ren, K., Zhou, J. & Wu, H. (2013) Materials for microfluidic chip fabrication. *Accounts of Chemical Research*. 46(11), 2396-2406.

Reneman, R. & Hoeks, A. (2008) Wall shear stress as measured in vivo: consequences for the design of the arterial system. *Medical & Biological Engineering & Computing*, 46(5), 499–507

Riss, T., Moravec, R., Niles, A., Duellman, S., Benink, H., Worzella, T. & Minor, L. (2014) Cell Viability Assays. Bethesda: Eli Lilly & Company and the National Center for Advancing Translational Science, available from: https://www.ncbi.nlm.nih.gov/books/NBK144065/

Roberts, E., Cossigny, D. & Quan, G. (2013) The Role of Vascular Endothelial Growth Factor in Metastatic Prostate Cancer to the Skeleton. *Prostate Cancer*. 2013, 418340

Rodriguez, C., Reidel, S., Bal de kier Joffe, E., Jasnis, M. & G, F. (2015) Autophagy Protects from Trastuzumab-Induced Cytotoxicity in HER2 Overexpressing Breast Tumor Spheroids. *Plos One* 10(9), e0137920

Rogers, M. S., T. Schaffer, DK. Samson, PC. Johnson, AC. Owens, P. Codreanu, SG. Sherrod, SD. McLean, JA. Wikswo, JP. Richmond, A. (2018) Engineered microfluidic bioreactor for examining the three-dimensional breast tumor microenvironment. *Biomicrofluidics*, 3(12).034102

Rommerswinkel, N., Niggemann, B., Keil, S., Zänker, K. & Dittmar, T. (2014) Analysis of Cell Migration within a Three-dimensional Collagen Matrix. *Journal of visualized experiments* (92), 51963.

Rundhaug, J. (2003) Matrix Metalloproteinases, Angiogenesis, and Cancer. *Clinical Cancer Research* .9(2), 551-554

Sabhachandani, P., Sarkar, S., McKenney, S., Ravi, D., Evens, A. & Konry, T. (2019) Microfluidic assembly of hydrogel-based immunogenic tumor spheroids for evaluation of anticancer therapies and biomarker release. *Journal of Controlled Release*, 21-30.

Saharinen, P., Eklund, L., Pulkki, K., Bono, P. & Alitalo, K. (2011) VEGF and angiopoietin signaling in tumor angiogenesis and metastasis. *Trends in molecular medicine*, 17(7), 347–362.

Sarker, P., Talukdar, S., Deb, P. & Mohsina, K. (2013) Optimization and partial characterization of culture conditions to produce alkaline protease from Bacillus licheniformis P003. Springer Plus, 2(1), 506.

Scanlon, S. & Glazer, P. (2015) Multifaceted Control of DNA Repair Pathways by the Hypoxic Tumor Microenvironment. *DNA repair*, 32, 180-189.

Scholzen, T. G., J. (2000) The Ki-67 protein: from the known and the unknown. *Journal of cellular physiology*, 182(3).

Seed, B. (2001) Silanizing Glassware. *Current Protocols in Immunology*, 21, A3K.1–A.3K.2.

Senkowski, W., Xiaonan, Z., Hagg Olofsson, M., Isacson, R., Hoglund, U., Gustafsson, M., Nygren, P., Linder, S., Larsson, R. & Fryknas, M. (2015) Three-Dimensional Cell Culture-Based ScreeningIdenti fi es the Anthelmintic Drug Nitazoxanide as a Candidate for Treatment of Colorectal Cancer. *Molecular Cancer Therapuetics*.

Shang, M., Soon, R., Lim, C., Khoo, B. & Han, J. (2019) Microfluidic modelling of the tumor microenvironment for anti-cancer drug development. *Lab on Chip* (19), 369-386.

Shields, J., Fleury, M., Yong, C., Tomei, A., Randolph, G. & Swartz, M. (2007) Autologous chemotaxis as a mechanism of tumor cell homing to lymphatics via interstitial flow and autocrine CCR7 signaling. *Cancer Cell*, 11(6), 526-538.

Shirazi, F., Zarghi, A., Kobarfard, F., Zendehdel, R., Nakhjavani, M., Arfaiee, S., Tannaz, Z., Mohebi, S., Anjidani, N., Ashtarinezhad, A. & Shoeibi, S. (2011) Remarks in Successful Cellular Investigations for Fighting Breast Cancer Using Novel Synthetic Compounds. *InTech*, 85-102.

Sleeboom, J., Toonder, J. & Sahlgren, C. (2018) MDA-MB-231 Breast Cancer Cells and Their CSC Population Migrate Towards Low Oxygen in a Microfluidic Gradient Device. *International journal of molecular sciences* 19(10) e3047.

Soldati, G., Del Ben, F., Brisotto, G., Biscontin, E., Bulfoni, M., Piruska, A., Steffan, A., Turetta, M. & Della Mea, V. (2018) Microfluidic droplets content classification and analysis through convolutional neural networks in a liquid biopsy workflow. *American Journal of Translational research,* 10(12), 4004–4016.

Solinas, M., Massi, P., Cinquina, V., Valenti, M., Bolognini, D., Gariboldi, M., Monti, E., Rubino, T. & Parolaro, D. (2013) Cannabidiol, a Non-Psychoactive Cannabinoid Compound,

Inhibits Proliferation and Invasion in U87-MG and T98G Glioma Cells through a Multitarget Effect. *PlosOne*, 8(10) e76918.

Song, J., Cavnar, S., Walker, A., Luker, K., Gupter, M., Tung, Y., Luker, G. & Takayama, S. (2009) Microfluidic Endothelium for Studying the Intravascular Adhesion of Metastatic Breast Cancer Cells. *Plos One*, 4(6) e5756

Stewart, D., Nunez, M., Behrens, C., Liu, M., Lee, J., Roth, J., Heymach, J., Swisher, S., Hong, W. & Wistuba, I. (2014) Membrane carbonic anhydrase IX (CAIX) expression and relapse risk in resected stage I-II non-small cell lung cancer. *Journal of Thoracic Oncology*, 9(5), 675-684.

Sung KE, Su X, Berthier E, Pehlke C, Friedl A & DJ, B. (2013) Understanding the Impact of 2D and 3D Fibroblast Cultures on In Vitro Breast Cancer Models. 10 editions.: *Plos one*.8(10) e76373

Sutherland (1988) Cell and environment interactions in tumor microregions: the multicell spheroid model. *Science*, 240(4849), 177-184.

Talmadge, J. & Fidler, I. (2010) AACR Centennial Series: The Biology of Cancer Metastasis: Historical Perspective. *Cancer Research*, 70(14), 5649-5669.

Tarn, M. (2011) Continuous Flow Processes on Single Magnetic and Diamagnetic Particles in Microfluidic Devices. Doctor of Philosophy University of Hull. Available online: https://hydra.hull.ac.uk/assets/hull:4915a/content [Accessed: February 2019]

Tawara, K., Oxford, J. & Jorcyk, C. (2011) Clinical significance of interleukin (IL)-6 in cancer metastasis to bone: potential of anti-IL-6 therapies. *Cancer Management Research*, 3, 177-189.

Thurston, G. (1976) Viscosity and viscoelasticity of blood in small diameter tubes. *Microvasular Research* 11, 133 146

Toh, Y., Raja, A., Yu, H. & van Noort, D. (2018) A 3D Microfluidic Model to Recapitulate Cancer Cell Migration and Invasion. *Bioengineering* (Basel), 5(10).

Vaithilingam IS, Stroude EC, McDonald W & RF, D. M. (1991) General protease and collagenase (IV) activity in C6 astrocytoma cells, C6 spheroids and implanted C6 spheroids. *Journal of Neuro-Oncology*, 10(3), 203-212.

Valastyan, S. & Weinberg, R. (2011b) Tumor Metastasis: Molecular Insights and Evolving Paradigms. *Cell*, 147(2), 275-292.

van de Merbel , A., van der Horst, G., van der Mark, M., van Uhm, J., van Gennep, E., Kloen, P., Beimers, L., Pelger, R. & van der Pluijm, G. (2018) An ex vivo Tissue Culture Model for the Assessment of Individualized Drug Responses in Prostate and Bladder Cancer. *Frontiers in Oncology*, 8(400).

Vempati, P., Popel, A. & Gabhann, F. (2013) Extracellular regulation of VEGF: isoforms, proteolysis, and vascular patterning. *cytokine growth factor review*.25(1) 1-19

Vinci, M., Box, C., Zimmermann, M. & Eccles, S. A. (2013) Tumor spheroid-based migration assays for evaluation of therapeutic agents. *Methods Mol Biol,* 986, 253-66.

Vinci, M., Gowan, S., Boxall, F., Patterson, L., Zimmermann, M., Court, W., Lomas, C., Mendiola, M., Hardisson, D. & Eccles, S. (2012) Advances in establishment and analysis of threedimensional tumor spheroid-based functionalassays for target validation and drug evaluation. *Journal of Biology*, 10(29).

Wagner, B., Venkataraman, S. & Buettner, G. (2011) The rate of oxygen utilization by cells. *Free radical biology and medicine*, 51(3), 700-712.

Wang, G. L. & Semenza, G. L. (1993) General involvement of hypoxia-inducible factor 1 in transcriptional response to hypoxia. *Proceedings of the National Academies of Science U. S. A.*, 90, 4304–4308.

Wang, J., Tang, Y., Fan, C., Guo, C., Zhou, Y., Li, Z., Li, X., Li, Y., Li, G., Xiong, W., Zeng, Z. & Xiong, F. (2018a) The role of exosomal non-coding RNAs in cancer metastasis. *Oncotarget,* 9(15), 12487–12502.

Wang, L., Zuo, X., Xie, K. & Wei, D. (2018b) The Role of CD44 and Cancer Stem Cells. *Methods in Molecular Biology*, 1692, 31-42.

Wei, L., Shao-Ming, S., Xu-Yun, Z. & Guo-Qiang, C. (2012) Targeted genes and interacting proteins of hypoxia inducible factor-1. *International Journal of Biochemistry   and Molecular Biology*, 3(2), 165-178.

Weinberg, R. & Hanahan, D. (2011) Hallmarks of Cancer: The Next Generation. *Cell*, 144(5), 646–674.

Weinberg, R. (2013) *Biology of Cancer*. New York: Garland Science.

Weiswald, L. B., Bellet, D. & Dangles-Marie, V. (2015) Spherical cancer models in tumor biology. *Neoplasia*, 17(1), 1-15.

West, C. (1989) Size-dependent resistance of human tumour spheroids to photodynamic treatment. 4 editions.: *British Journal of Cancer,* 59(4), 510-514

Whitesides, G. M. (2006) The origins and the future of microfluidics. *Nature*, 442(7101), 368-73.

Wilson, W. R. & Hay, M. P. (2011) Targeting hypoxia in cancer therapy. *Nat Rev Cancer*, 11(6), 393-410.

Wu, L. Y., Di Carlo, D. & Lee, L. P. (2008) Microfluidic self-assembly of tumor spheroids for anticancer drug discovery. *Biomed Microdevices*, 10(2), 197-202.

Yokota, J. (2000) Tumor progression and metastasis. *Carcinogenesis*, 21(3), 497-503.

Young, E. W. (2013) Cells, tissues, and organs on chips: challenges and opportunities for the cancer tumor microenvironment. *Integr Biol (Camb)*, 5(9), 1096-109.

Yuan, T., Gao, D., Shangfu, L. & Yuyang, J. (2019) Co-culture of tumor spheroids and monocytes in a collagen matrix-embedded microfluidic device to study the migration of breast cancer cells. *Chinese Chemical Letters*, 30(2), 331-336.

Zanoni M, Piccinini F, Arienti C, Z. A., Santi, SPolico R, Belivacqua A, & A, T. (2016) 3D tumor spheroid models for in vitrotherapeutic screening: a systematic approach to enhance the biological relevance of data obtained. *Scientific Reports*, 6 (11) 19103.

Zhang, W., Kai, K., Choi, D., Iwamoto, T., Nguyen, Y., Wong, H., Landis, M., Ueno, N., Chang, J. & Qin, L. (2012) Microfluidics separation reveals the stem-cell–like deformability of tumor-initiating cells. *Proceedings of the National Academy of Sciences of the United States of America*, 46(109), 18707–18712.

Zhang, Z., Chen, Y., Urs, S., Chen, L., Simone, D. & Yoon, E. (2018) Scalable Multiplexed Drug-Combination Screening Platforms Using 3D Microtumor Model for Precision Medicine. *Nano Micro Small*, 14(42).

Zhou, Y. (2016) Understanding the cancer/tumor biology from 2D to 3D. *Journal of Thoracic Disease,* 8(11), 1484–1486.

Ziello, J., Jovin, I. & Huang, Y. (2007) Hypoxia-Inducible Factor (HIF)-1 Regulatory Pathway and its Potential for Therapeutic Intervention in Malignancy and Ischemia. *Yale Journal of Biology and Medicine,* 8(2), 51-60.

Zijl, F., Krupitza, G. & Miklutis, W. (2011) Initial steps of metastasis: Cell invasion and endothelial transmigration. *Mutation Research*, 728(23-34).